

Investigation of Biological Macromolecules Using Atomic Force Microscope-Based Techniques

Dissertation

zur Erlangung des akademischen Grades

Doctor rerum naturalium

(Dr. rer. nat.)

vorgelegt der

Fakultät Mathematik und Naturwissenschaften

an der Technischen Universität Dresden

von

Christian A. Bippes

geboren am 19.11.1978 in Karlsruhe

Datum der Einreichung: 18.05.2009

1. Gutachter: Prof. Dr. Daniel J. Müller

2. Gutachter: Prof. Dr. Dimitrios Fotiadis

Datum der Disputation: 18.08.2009

Meinen Eltern.

SUMMARY

The atomic force microscope (AFM) provides a powerful instrument for investigating and manipulating biological samples down to the subnanometer scale. In contrast to other microscopy methods, AFM does not require labeling, staining, nor fixation of samples and allows the specimen to be fully hydrated in buffer solution during the experiments. Moreover, AFM clearly compares in resolution to other techniques.

In general, the AFM can be operated in an imaging or a force spectroscopy mode. In the present work, advantage was taken of this versatility to investigate single biomolecules and biomolecular assemblies.

A novel approach to investigate the visco-elastic behavior of biomolecules under force was established, using dextran as an example. While a molecule tethered between a solid support and the cantilever tip was stretched at a constant velocity, the thermally driven oscillation of the cantilever was recorded. Analysis of the cantilever Brownian noise provided information about the visco-elastic properties of dextran that corresponded well to parameters obtained by alternative methods. However, the approach presented here was easier to implement and less time-consuming than previously used methods.

A computer controlled force-clamp system was set up, circumventing the need for custom built analogue electronics. A commercial PicoForce AFM was extended by two computers which hosted data acquisition hardware. While the first computer recorded data, the second computer drove the AFM bypassing the manufacturer's microscope control software. To do so, a software-based proportional-integral-differential (PID) controller was implemented on the second computer. It allowed the force applied to a molecule to be held constant over time. After tuning of the PID controller, response times obtained using that force-clamp setup were comparable to those of the recently reported analogue systems. The performance of the setup was demonstrated by force-clamp unfolding of a pentameric Ig25 construct and the membrane protein NhaA. In the latter case, short-lived unfolding intermediates that were populated for less than 10 ms, could be revealed.

Conventional single-molecule dynamic force spectroscopy was used to unfold the serine:threonine antiporter SteT from *Bacillus subtilis*, an integral membrane protein. Unfolding force patterns revealed the unfolding barriers stabilizing structural

segments of SteT. Ligand binding did not induce new unfolding barriers suggesting that weak interactions with multiple structural segments were involved. In contrast, ligand binding caused changes in the energy landscape of all structural segments, thus turning the protein from a brittle, rigid into a more stable, structurally flexible conformation. Functionally, rigidity in the ligand-free state was thought to facilitate specific ligand binding, while flexibility and increased stability were required for conformational changes associated with substrate translocation. These results support the working model for transmembrane transport proteins that provide alternate access of the binding site to either face of the membrane.

Finally, high-resolution imaging was exploited to visualize the extracellular surface of Cx26 gap junction hemichannels (connexons). AFM topographs reveal pH-dependent structural changes of the extracellular connexon surface in presence of HEPES, an aminosulfonate compound. At low pH (< 6.5), connexons showed a narrow and shallow channel entrance, which represented the closed pore. Increasing pH values resulted in a gradual opening of the pore, which was reflected by increasing channel entrance widths and depths. At pH > 7.6 the pore was fully opened and the pore diameter and depth did not increase further. Importantly, coinciding with pore gating a slight rotation of the subunits was observed. In the absence of aminosulfonate compounds, such as HEPES, acidification did not affect pore diameters and depths, retaining the open state. Thus, the intracellular concentration of taurine, a naturally abundant aminosulfonate compound, might be used to tune gap junction sensitivity at low pH.

TABLE OF CONTENTS
CHAPTER 1**INTEGRAL MEMBRANE PROTEINS.....1**

1.1	CELLULAR MEMBRANES.....	1
1.2	MEMBRANE PROTEINS	3
1.2.1	On the Importance of Membrane Protein Folding and Assembly.....	5
1.2.1.1	<i>Progress in Protein Folding</i>	5
1.2.1.2	<i>Membrane Protein Folding</i>	7
	<i>Translocon-Assisted Membrane Protein Folding and Insertion.....</i>	7
	<i>The "Two-Stage" Model.....</i>	8
	<i>The "Four-Step" Model</i>	9
1.2.1.3	<i>Membrane Protein Misfolding</i>	11
1.2.2	Hurdles in Membrane Protein Studies	12
1.2.3	Methodological Approaches in Membrane Protein Research	13
1.3	MEMBRANE PROTEINS FULLFIL SPECIFIC FUNCTIONS.....	15
1.3.1	Gap Junctions.....	15
1.3.2	Amino Acid Transporters	18
1.3.2.1	<i>How Cells Perform Transport Across Membranes</i>	18
1.3.2.2	<i>L-Amino Acid Transport.....</i>	19

CHAPTER 2**ATOMIC FORCE MICROSCOPY.....21**

2.1	HISTORY.....	21
2.2	PRINCIPLE	21
2.2.1	AFM Setup.....	21
2.2.2	Cantilevers.....	23
2.2.2.1	<i>General Considerations</i>	23
2.2.2.2	<i>Forces Acting on the Cantilever</i>	24
2.2.2.3	<i>Force Sensitivity.....</i>	26
2.2.2.4	<i>Cantilever Calibration.....</i>	27
	<i>Detector Calibration.....</i>	27
	<i>Spring Constant Calibration – Added Mass.....</i>	28
	<i>Spring Constant Calibration – Sader Method</i>	29
	<i>Spring Constant Calibration – Thermal Fluctuation Analysis</i>	29
2.3	OPERATION MODES	30
2.3.1	Surface Imaging.....	31
2.3.1.1	<i>Contact Mode</i>	31
2.3.1.2	<i>Tapping Mode</i>	32
2.3.2	Force Measurement	33
2.3.2.1	<i>AFM-Based Single-Molecule Force Spectroscopy.....</i>	35

Constant Velocity Force Spectroscopy.....	35
Constant Force Force Spectroscopy.....	36
2.3.2.2 Polymer Extension Models.....	36
Freely Jointed Chain Model.....	37
Wormlike Chain Model.....	37
2.3.2.3 Model Systems.....	38
Dextran.....	39
27 th Immunoglobulin Domain from the Giant Muscle Protein Titin.....	40
Bacteriorhodopsin.....	41
2.3.2.4 Kinetic Interpretation of SMFS Experiments.....	41
2.4 WHY USE ATOMIC FORCE MICROSCOPY TO STUDY MEMBRANE PROTEINS?..	44
2.4.1 Imaging Membrane Protein Surfaces at High Resolution.....	44
2.4.2 Force as an Alternative Denaturant.....	44
CHAPTER 3	
VISCO-ELASTICITY OF SINGLE DEXTRAN MOLECULES UNRAVELED BY BROWNIAN NOISE ANALYSIS.....	47
3.1 INTRODUCTION.....	47
3.2 EXPERIMENTAL PROCEDURES.....	48
3.2.1 Sample Preparation.....	48
3.2.2 AFM Instrumentation.....	48
3.2.3 Extracting Visco-Elastic Properties.....	49
3.3 RESULTS AND DISCUSSION.....	50
3.3.1 Extraction of Visco-Elastic Parameters.....	50
3.3.2 Measurement Noise Depends on Window Size and Cantilever Type.....	51
3.3.3 Visco-Elasticity of Dextran.....	54
3.4 CONCLUSIONS.....	56
CHAPTER 4	
DIGITAL FORCE-FEEDBACK FOR SINGLE-MOLECULE FORCE-CLAMP SPECTROSCOPY ON PROTEINS.....	57
4.1 INTRODUCTION.....	57
4.2 EXPERIMENTAL PROCEDURES.....	58
4.2.1 Support Preparation.....	58
4.2.2 Sample Preparation.....	59
4.2.3 Force Spectroscopy Measurements.....	59
4.2.4 Data Analysis.....	61
4.2.5 Software-Based PI(D) Controller.....	61
4.3 RESULTS AND DISCUSSION.....	62
4.3.1 PI(D)-Controller.....	62
4.3.2 System Stability.....	64
4.3.3 Force-Clamp Unfolding of Ig27 ₅	65

4.3.4	Force-Clamp Unfolding of NhaA	65
4.4	CONCLUSIONS.....	68
CHAPTER 5		
LIGAND BINDING TRIGGERS ENERGY LANDSCAPE AND MECHANICAL PROPERTIES OF THE AMINO ACID ANTIPORTER SteT		
<hr/>		
5.1	INTRODUCTION.....	69
5.2	EXPERIMENTAL PROCEDURES.....	71
5.2.1	Cloning, Overexpression, Purification, and Reconstitution into Proteoliposomes of SteT.....	71
5.2.2	SMFS and DFS.....	71
5.2.3	Data Selection and Analysis.....	72
5.2.4	Compensation for Hydrodynamic Drag.....	73
5.2.5	Calculation of x_u and k_0 from DFS Data	74
5.2.6	Calculation of Transition Barrier Heights and Rigidity	74
5.3	RESULTS	75
5.3.1	Interactions of SteT In Presence and Absence of Substrates	75
5.3.2	Direction of Unfolding.....	78
5.3.3	Probability of Interactions.....	78
5.3.4	Substrate Binding Changes the Dynamic Energy Landscape of SteT.....	79
5.3.5	Correlation of x_u , k_0 , and ΔG^\ddagger	83
5.3.6	Mechanical Properties of SteT	84
5.4	DISCUSSION	85
5.4.1	Amino Acid Binding by SteT Lacks Detectable Localized Interactions	85
5.4.2	SteT Unfolds Differently Compared to Other Membrane Proteins	86
5.4.3	Substrate Binding Changes the Energy Landscape of SteT	88
5.4.4	Hammond-Like Behavior Reflects Ground State Effects	89
5.5	CONCLUSIONS.....	90
CHAPTER 6		
PH-INDUCED CONFORMATIONAL CHANGES IN CX26 HEMICHANNELS MODULYTED BY AMINOSULFONATES.....		
<hr/>		
6.1	INTRODUCTION.....	93
6.2	EXPERIMENTAL PROCEDURES.....	95
6.2.1	Cx26 Gap Junction Preparation.....	95
6.2.2	AFM Imaging	95
6.2.3	Image Processing and Averaging	96
6.3	RESULTS	96
6.3.1	High-Resolution Imaging of the Extracellular Connexon Surface.....	96
6.3.2	Observing pH-Induced Conformational Changes.....	98
6.3.3	Conformational Changes Are Not Dependent on HEPES Concentration	101

6.3.4	No Conformational Change Occurs in the Absence of Aminosulfonates	102
6.3.5	Quantitative Analysis of the Channel Closure	103
6.4	DISCUSSION.....	104
6.4.1	Aminosulfonates Are Required to Induce Closure During Acidification in Isolated Cx26 Gap Junction Hemichannels	105
6.4.2	pH Gating of Connexins.....	106
6.4.3	Mechanism of Channel Closure at the Extracellular Surface Gate.....	107
6.4.4	Connexon Extracellular Surface Is More Rigid When the Extracellular Gate Is Closed.....	109
6.4.5	The Relevance of pH Gating in Tissues and Organs	109
6.4.6	The Importance of Taurine in Tissues and Organs and Co-Expression with Cx26 110	
6.5	CONCLUSIONS.....	111
CHAPTER 7		
OUTLOOK		113
<hr/>		
7.1	EFFECT OF LIGANDS AND INHIBITORS ON TRANSPORT PROTEINS	114
7.2	MEMBRANE PROTEIN FOLDING	114
CHAPTER 8		
APPENDIX		117
<hr/>		
GLOSSARY OF ABBREVIATIONS		117
GLOSSARY OF SYMBOLS.....		120
PUBLICATION LIST.....		123
ACKNOWLEDGEMENTS		125
CHAPTER 9		
BIBLIOGRAPHY		127
<hr/>		

INTEGRAL MEMBRANE PROTEINS

1.1 CELLULAR MEMBRANES

The cell is the building block of all organisms. In its simplest form, a cell can be described as a balloon filled with various macromolecules and chemicals that are essential for life, e.g. proteins, nucleic acids, carbohydrates, and small organic and inorganic molecules [1]. That balloon is called the outer or plasma membrane and is universal to all cells on earth.

In the early prebiotic environment, various simple organic molecules formed, which then reacted to form more and more complex molecules. In the course of time, intricate catalytic and self-replicating polymeric systems developed¹. While these systems coexisted, they also had to compete for available resources in the primordial pond. The development of the plasma membrane was the advent of the first cell-like structures and a milestone in evolution [1]. Improvements in the "cellular" machinery, which proved beneficial in the struggle for survival, did not have to be shared with competing, free-floating systems. Nutrients could be gathered from the environment and products of the cell's metabolic machinery could be retained within the cell. Thus, the plasma membrane promoted further growth and evolution of the cell. Even "simple" prokaryotes, containing only a simple plasma membrane, which is often surrounded by a cell wall, performs various metabolic tasks in different regions of the cytoplasm. In more complex eukaryotes, membranes define different organelles, such as endoplasmic reticulum, Golgi apparatus, mitochondria, chloroplasts, lysosomes, peroxisomes, or vacuoles [1]. In all cases compartmentalization preserves the (bio)chemical and physical characteristics of organelles.

Most probably, spontaneous self-assembly of lipids present in the primordial pond lead to formation of the first plasma membrane [2]. However, it is intrinsic to

¹ The first self-replicating systems are believed to be ribonucleic acids. Although they show limited catalytic activities compared to proteins, they can easily provide for exact (complementary) copies of themselves [2].

these first and all later membranes that they are dynamic, thin, self-healing, and insulating boundaries. Generally, such boundaries are established by a lipid bilayer². The exact lipid composition of membranes strongly depends on cell type, organelle, and organism [5]. Nature has developed a variety of different saturated and unsaturated lipids with different headgroups to tailor membranes with physical and chemical properties that match the needs of the cell.

In most cellular membranes, phospholipids are the major constituents found. However, many membranes also contain large amounts of cholesterol³ and glycolipids [5,6]. Interestingly, the different types of lipids are not equally distributed within the two leaflets of a membrane, resulting in a vertical asymmetry [7]. The paradigm for this asymmetry is the plasma membrane of eukaryotic cells, where phosphatidylserine (PS) and phosphatidylethanolamine (PE) are enriched in the cytoplasmic leaflet and phosphatidylcholine (PC) and sphingomyeline (SM) are primarily and glycolipids exclusively located on the exoplasmic leaflet [6,8]. This asymmetry is of functional importance, since some proteins specifically bind or recognize certain headgroups [9,10]. Moreover, PC, PE, and SM lipids exhibit zwitterionic headgroups that are neutral at physiological pH, while PS lipids are negatively charged. Hence, the enrichment of PS lipids in the cytosolic leaflet causes a marked charge difference between the two faces of the membrane. This difference might be helpful in determining the transmembrane topology of a membrane protein, as depicted by the "positive-inside" rule [11-14]. Lipids and their distribution within membranes are important for protein folding, assembly [15] and activity [16,17].

The exact structure of cellular membranes is still an exciting mystery. In 1972, Singer and Nicolson proposed, in their "fluid mosaic model", that membranes are an oriented, dynamic, two dimensional, and viscous solution of proteins and lipids [18]. Since then, it turned out that "membranes are more mosaic than fluid" [19]. Proteins were shown to undergo confined or directed motion within the membrane [20] and organize in functionally relevant supramolecular complexes, some of which are gap junctions [21], complexes I, III, and IV of the respiratory chain [22], and photosystems I

² Some archaeal lipids are bipolar and capable of spanning both membrane leaflets [3]. The unusual lipid design allows the archaea to withstand the harsh environmental conditions of their habitats [4].

³ Cholesterol strengthens the impermeability of membranes. Its rigid steroid ring structure immobilizes in neighboring lipids the first few methylene groups close to the headgroups. Thus the membrane is more rigid and less deformable, resulting in decreased permeability of small water-soluble molecules [6].

and II [23]. Moreover, cholesterol and sphingolipids may transiently associate to form microdomains, lipid rafts, that host certain membrane proteins [24].

All lipid bilayers, regardless of their composition, form an impermeable barrier for almost all water-soluble molecules. The structure of the fluid liquid-crystalline (L_{α}) phase of a 1,2-dioleoyl-*sn*-glycero-3-phosphocholine (DOPC) bilayer comprises 15 Å thick interface regions⁴ which on both sides flank a 30 Å thick hydrophobic hydrocarbon core region that sets the permeability barrier [25]. For unabated growth, however, cells need to gather raw material from the environment and secrete (toxic) waste. So, specific transport systems spanning the membrane are indispensable.

1.2 MEMBRANE PROTEINS

Numerous processes crucial for cell viability, such as specific solute transport, signal transduction, and energy conversion are performed or catalyzed by proteins embedded into cellular membranes⁵. The fact that 20-30 % of all open reading frames in the genome of cells encode integral membrane proteins [27] highlights the importance of this class of proteins and reflects the diversity of functions they fulfill. In contrast, the knowledge about membrane protein structures and functional mechanisms is poor. As structural studies of integral membrane proteins have progressed slowly in the past [28], membrane proteins are with less than 1 % of the total records significantly underrepresented in the Protein Data Bank (PDB) [29]⁶. Analysis of the known integral membrane protein structures revealed that the diversity of secondary structure elements capable of passing the membrane is low as only two motifs have been observed [31]: α -helical bundles and β -barrels composed of antiparallel β -strands (Figure 1.1). α -helical membrane proteins are widely distributed in cellular membranes, where they are involved in e.g. active solute transport, signaling, and intercellular communication. In contrast, β -barrel membrane proteins emerge from the outer membrane of Gram-positive bacteria, mitochondria, or chloroplasts, where they

⁴ The interface region is defined as the headgroups' water of hydration [25]. It is chemically highly heterogeneous, rich in possibilities for non-covalent contacts with peptides, and can easily accommodate folded or unfolded polypeptides [26].

⁵ Besides spanning the membrane, proteins can be associated to the membrane by partitioning an amphipathic helix to the cytosolic leaflet or by inserting a covalently bound anchor (fatty acid chains, glycosylphosphatidylinositol (GPI)) into the membrane [6].

⁶ As of January 13, 2009, the coordinates of 868 membrane protein / peptide structures from 224 unique membrane proteins/peptides from 126 unique protein families [30] were in the PDB. At that time, the PDB contained 53289 protein structures (soluble and membrane proteins).

fulfill numerous functional tasks (Refs. [32-36] reviewed structure and folding of β -barrel membrane proteins in detail). Moreover, some bacterial toxins also form β -barrel membrane pores [37,38].

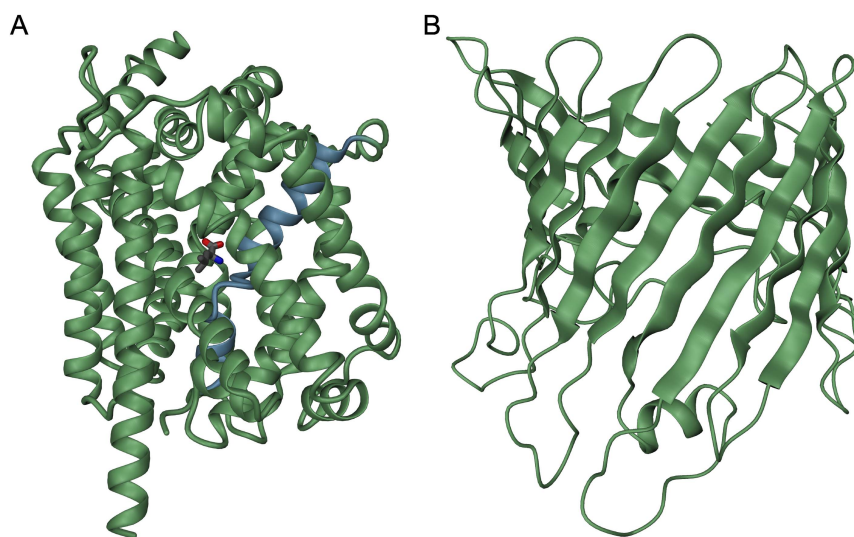


Figure 1.1 Major structural motifs found in transmembrane proteins. (A) LeuT_{Aa} from *Aquifex aeolicus* is a bacterial homologue of eukaryotic neurotransmitter sodium symporters (NSS). LeuT_{Aa} contains 12 transmembrane α -helices connected by relatively short extramembrane loops [39]. LeuT_{Aa} is shown in complex with its substrate leucine (represented as sticks). Transmembrane α -helix VI is discontinuous (shown in blue) and amino acids located in the elongated peptide segment are involved in leucine binding. PDB ID: 2A65 [39]. (B) Porin from *Rhodobacter capsulatus* is a β -barrel protein formed by 16 antiparallel β -strands [40]. The central pore allows passage of molecules up to ~ 600 Da. PDB ID: 2POR [40]. Both proteins are presented in side-view.

Lipid bilayers establish a hydrophobic environment to be passed by transmembrane proteins. The only permissible structural motifs are α -helices and β -barrels [26,41], because intra- and intersegment hydrogen bonding compensates for dehydration of the peptide bonds in the apolar milieu.

Non-polar amino acid residues such as alanine, valine, leucine, and isoleucine are enriched in transmembrane α -helices [42] that are usually formed by ~ 20 amino acid (aa) long segments that pass the entire membrane [43,44]. In the hydrophobic core, unstructured loops and shorter helical segments⁷ are energetically unfavorable, due to uncompensated helix dipoles and a lack of backbone hydrogen bonding. However, α -helical transmembrane segments are not always straight, rod-shaped structures. Distortions, π -interactions [44], and discontinuities [46] (Figure 1.1A) are frequently observed. Also helices protruding half way through the bilayer have been revealed

⁷ There is no absolute value for the length of transmembrane α -helices, rather the length of helices varies significantly from less than 14 to more than 40 aa residues [45]. It is necessary to consider helices in the context of the whole transmembrane protein and, thus, the interactions established to the lipid matrix and the protein.

[47,48]. These deviations from a perfect α -helical shape are important for protein folding and function.

Polar and charged residues accumulate in extramembrane loops and domains. These segments can both provide additional stability, assist folding, and be important for correct helix packing and serve as environmental sensors involved in protein activity [44,49]. Some amino acids, namely tyrosine, tryptophan, histidine, arginine, and lysine, are preferentially located in the interface region, presumably because their side chains exhibit both hydrophilic and hydrophobic regions [42,50]. Further, arginine and lysine residues, which carry a positive charge, are more abundant at the cytoplasmic face of membrane proteins [11,42].

1.2.1 On the Importance of Membrane Protein Folding and Assembly

Why is membrane protein folding such an interesting and important research area? The answer is quite simple. Membrane proteins are located at the boundaries of cells. As a consequence, they are involved in all processes that require signal transmission from outside the cell to the inside or *vice versa*. Moreover, they are responsible for extrusion of toxic compounds, import of nutrients, energy conversion, and cell adhesion. Thus, membrane proteins are attractive targets for drugs and, indeed, about 70 % of all drug targets are membrane proteins [51,52]. Mutations in membrane proteins can result in misfolding, mistargeting, or misassembly of those, which in turn might cause severe diseases, such as cystic fibrosis, retinitis pigmentosa, non-syndromic deafness, and diabetes. To understand the molecular mechanisms behind these diseases and to develop of new drugs, it is of utmost importance to gain insight into the functional mechanisms of membrane proteins. Therefore, we have to extend our knowledge of the fundamental processes that lead to membrane protein structure, which determines function. Unquestionably, *in vitro* protein folding studies will be required to do so.

The following sections will provide an overview of protein folding in general. They will focus on water-soluble proteins, the process of membrane protein folding *in vivo*, current models of membrane protein folding, and membrane protein associated maladies.

1.2.1.1 Progress in Protein Folding

Protein folding describes the process of converting linear information, the amino acid sequence, into three dimensional structure. Although research has already

been going on for decades, many fundamental questions still remain to be answered. However, protein folding research has made great progress within the last two decades. Advances in molecular biology in conjunction with various, highly developed techniques⁸ unveiled structural, dynamic, kinetic, and thermodynamic properties of the folding process and lead to an enormous increase in our knowledge about protein structure and its dynamics down to the (sub-)nanosecond time-scale [68,73,74]. In combination with theoretical progress [75] and atomic-resolution computational modeling [76], these data opened the way to a highly advanced understanding of forces that drive and determine folding and structure of water-soluble proteins [77,78].

The first experiments showing reversible unfolding of a protein by Anfinsen [79-81] lead to the conclusion, that protein folding is a process guided by the information stored in the amino acid sequence of the protein, simply because folding of a protein by randomly exploring all possible conformations would take longer than the age of the universe⁹. Thus, proteins were thought to follow specific pathways circumventing random search [84]. In the 1990s, Ken A. Dill introduced an appealing theoretical framework describing protein folding and dynamics [85-89] – the concept of energy landscapes and folding funnels, which is often called the "new view" of protein folding. Each point on a multidimensional energy landscape relates the free energy of a conformation to its degrees of freedom, its entropy. Since the free energy is minimized during folding, the final structure should correspond to the deepest valley on the globally funnel-shaped energy landscape (Figure 1.2). While folding, the polypeptide chain follows the energy gradient to reach its folded state and, as a result, avoids unproductive conformations. One implication of the energy landscape model is, however, that no predefined pathways to the native state exist. The protein is free to explore different routes to the minimum. Experimentally observed folding intermediates correspond to meta-stable conformations trapped in local minima. To further proceed to the folded state, activation energy is required for the intermediate to overcome the energy barrier separating the local from the global minimum [86,90,91].

⁸ Methods applied in protein folding studies are for example (real-time) NMR [53,54], X-ray crystallography, conventional optical spectroscopy [55-57], circular dichroism (CD) spectroscopy [58,59], Förster resonance energy transfer (FRET) [60,61], calorimetry [62], and Fourier-transform infrared (FTIR) spectroscopy [63,64] as well as triplet-triplet energy transfer techniques [65,66] and (ultra)fast perturbation methods, such as temperature (*T*)- [67,68] and pressure (*p*)-jump [69-72].

⁹ This notion became known as 'Levinthal's paradox' [82,83].

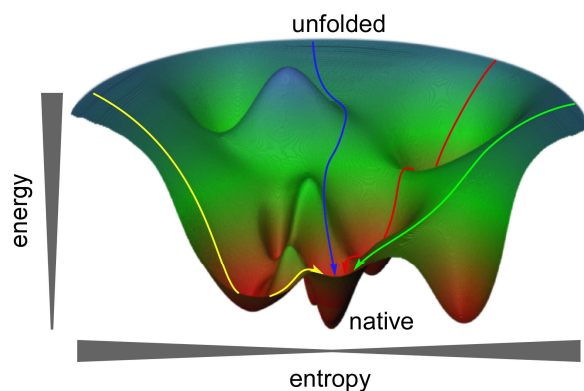


Figure 1.2 Energy landscape of a polypeptide chain. The unfolded polypeptide chain contains the highest energy due to intensive solvent contacts. Energy minimization is driving the polypeptide chain to its final, folded (native) conformation. The protein can choose different routes to reach the energy minimum. Following some routes, the polypeptide is transiently trapped in local minima corresponding to folding intermediates (red and yellow routes).

1.2.1.2 Membrane Protein Folding

Translocon-Assisted Membrane Protein Folding and Insertion

In vivo, folding and insertion of constitutive membrane proteins is facilitated and controlled by a proteinaceous machinery resident in the membrane, the so-called translocon¹⁰ [95]. The structure of an archaebacterial protein-translocating SecYEG channel [96] and exhaustive functional studies on both eukaryotic and bacterial homologues have resulted in significant progress in understanding the molecular mechanisms guiding membrane protein folding and insertion [95,97-99]. The translocon molds a hydrophilic cavity with a diameter of a few tens of Ångströms and displays a ribosome binding site towards the cytoplasm. A signal sequences in the N-terminal portion of the nascent polypeptide chain of membrane proteins¹¹ targets the peptide-ribosome complex to the translocon. Upon binding, the ribosome caps the translocon and the nascent peptide is directly expelled from the ribosomal exit tunnel into the translocon pore. The translocon can accommodate peptides of ~ 20 aa length, which is sufficient for a transmembrane α -helical segment to form. The peptide exits the translocon through a lateral gate that might open and close periodically [100] to allow the peptide segment to sense and partition into the lipid bilayer if sufficiently hydrophobic [101]. The size of the pore indicates that the transmembrane segments laterally exit the translocon one by one or pairwise [102,103]. Subsequent hydrophilic sequences pass through the aqueous pore or emerge between the translocon and the

¹⁰ Some nonconstitutive membrane proteins, such as melittin [92], colicins [93], and diphtheria toxin [94] bypass the translocon and insert spontaneously into the membrane from the aqueous phase.

¹¹ Except membrane proteins also soluble proteins, which have to be secreted, possess signal peptides. Soluble proteins are targeted to the translocon either co- or posttranslationally [95].

ribosome, while hydrophobic sequences are inserted into the membrane following the same mechanism¹².

The "Two-Stage" Model

The process of translocon-assisted membrane protein folding and insertion is at the spotlight of current research. However, other studies aiming to reveal the forces and interactions that govern protein folding and assembly [104-106] have used synthetic peptides [107] and a few model proteins. Based on the refolding experiments on bacteriorhodopsin (bR) performed by Khorana and co-workers [108,109], Popot and Engelman showed, that fully denatured bR could recover its functionality in absence of denaturants without the aid of a translocon. Moreover, they demonstrated that fragments of bR refolded separately and, after mixing, associate to form functional bR [110]. Based on these observations, Popot and Engelman introduced the first general model for membrane protein folding [111]. The model separates membrane protein folding into two distinct phases: (i), the folding and insertion of individually stable α -helices into the lipid membrane and, (ii), the lateral association of helices to form the native, functional structure of the protein (Figure 1.3). In the first stage, α -helices are assumed to be autonomously folding stable units. In the second stage, interactions between individual domains are established leading to the final tertiary structure. Recently, oligomerization, formation of additional structured elements, and co-factor binding were introduced as a third stage [112].

Although the two-stage model is a simple approximation of the processes taking place, it successfully describes data from *in vitro* and *in vivo* folding

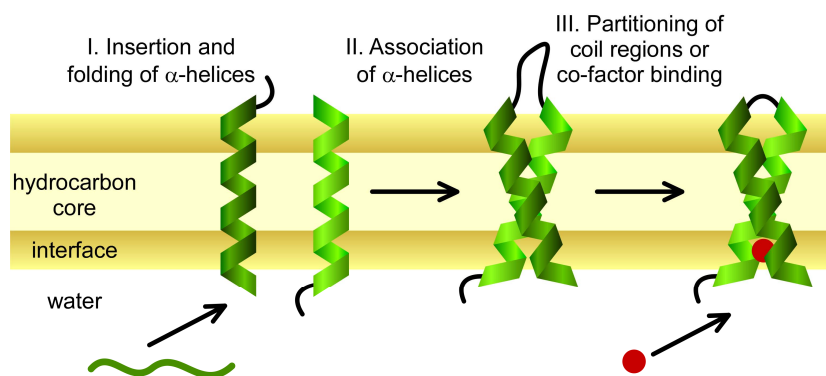


Figure 1.3 The two-stage model. It describes insertion of helical domains and subsequent association [111]. The model was lately extended into a three-stage model accounting for co-factor binding, oligomerization, and extramembrane domain folding [112].

¹² Interestingly, the topology of the first transmembrane segment determines the topology of all following transmembrane segments of a membrane protein.

experiments. In fact, individual transmembrane segments or pairs thereof leave the translocon, thus representing individual, stable domains embedded into the lipid bilayer. Only in a following step, these domains associate. Assembly of functional membrane proteins from independently refolded or synthesized fragments supports this notion and has been shown for bR, lactose permease (LacY), a voltage-gated chloride channel, and other proteins [44]. NMR studies on glycophorin A (GpA) fragments shed light on the molecular basis for helix-helix interactions that determine the assembly and oligomerization of transmembrane proteins [113]. In combination with dimerization assays [114], and statistical analysis of transmembrane helix sequences [115], these experiments revealed a short peptide sequence (GxxxG) that mediates dimerization through optimized packing. Thus, dimerization (or lateral association) is driven by van der Waals forces [113]. However, even at the early stage of translocon-mediated insertion [116], inter-helical hydrogen-bonding between polar/charged side chains seems to be involved in helix-helix packing [117-119]. Possibly important for *in vivo* folding [120], the overall energetic gain by inter-helix hydrogen bonds is rather small [121].

The "Four-Step" Model

Although the two-stage model nicely explains most results on membrane protein folding, it only deals with the compaction of transmembrane structures from pre-formed transmembrane segments. Yet, it neglects the important question, how, when, and why transmembrane segments are formed. At about the same time as the two-stage model has been proposed, Jacobs and White introduced a three-step model [122], which was lately developed into a more elaborate four-step thermodynamic cycle [26]. In contrast to the more phenomenological two-stage model, the four-step model is based on brilliant systematic biophysical measurements with synthetic peptides or small proteins, thus describing the thermodynamic context within which *in vivo* folding must proceed. The four-step model includes: (i), partitioning of the polypeptide chain in the membrane interface region, (ii), folding of α -helices, (iii), insertion into the bilayer, and, (iv), association of transmembrane segments (Figure 1.4). Importantly, the folding and association of α -helices can proceed along an interfacial or a water pathway or a combination of both¹³. Because the process is spontaneous, each step is coupled to a decrease in free energy. The driving force

¹³ Recent all-atoms molecular dynamics simulations suggested that short peptides can insert into the lipid membrane prior to secondary structure formation [123].

behind all steps is the minimization of the free energy cost of burying polar groups (especially the backbone peptide bond) [26], which is also responsible for maintaining the secondary structure in the folded protein. The propensity of different amino acids to promote membrane protein folding was described by a hydrophobicity scale, which was obtained from measurements of the transfer energies of small peptides from water to non-polar environments like 1-octanol or 1-palmitoyl-2-oleoyl-*sn*-glycero-3-phosphocholine (POPC) lipids [124,125]. According to the Wimley-White hydrophobicity scale, the gain in free energy for individual α -helices is 10-20 kcal/mol and corresponds well to the stabilization energy of small water-soluble proteins. Nevertheless, the presence of single or multiple charged or polar residues can render the hydrophobicity of an α -helix insufficient for membrane insertion. If the hydrophobicity of the following or preceding α -helix is high enough to compensate partitioning of charged and polar residues, the two α -helices insert together as a helical pair [121,126,127].

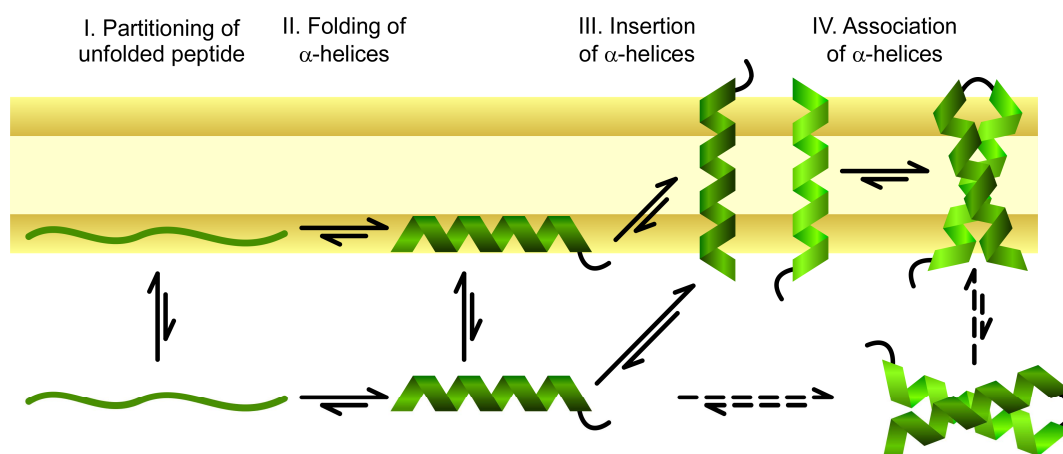


Figure 1.4 The four step model of membrane protein folding. The four-step thermodynamic cycle for membrane protein folding describes partitioning, folding, insertion, and association of helical domains. It is based on biophysical experiments and modeling [26].

Using an astute approach, von Heijne and co-workers established a biological hydrophobicity scale that agrees well with the Wimley-White scale [101]. They inserted each of the 20 proteinogenic amino acids into test peptides and quantified the insertion efficiency *in vivo*. Thus, they could calculate an apparent biological ΔG for partitioning to the lipid bilayer for each amino acid. Recently, the same authors showed that the contribution of certain amino acids to the overall free energy change is highly dependent on their position within the test peptide [128]. Indeed, the position dependence remarkably mirrors the statistical distribution of amino acids in transmembrane α -helices deduced from known three-dimensional (3D) structures [42].

1.2.1.3 Membrane Protein Misfolding

The "new view" of protein folding permits a polypeptide to acquire several low energy conformations, although only one defines the correct, functional fold [86]. It is well known, that water-soluble proteins can adopt both functional native and non-functional aberrant conformations, of which the latter can be induced *in vitro* by the environmental conditions [129-136]. These misfolded proteins often adopt a β -sheet structure that is prone to aggregation. These aggregates are known as amyloids¹⁴ and accumulate within cells or in the extracellular space [139]. However, misfolding is not an exclusive property of water-soluble proteins. Membrane proteins are also susceptible to misfolding, which is often caused by mutations and, thus, related to inherited diseases, some of which are cystic fibrosis [140-142], retinitis pigmentosa [143-145], diabetes [146,147], cystinuria [148,149], and non-syndromic deafness [150].

One of the best-studied disease related membrane proteins is the cystic fibrosis transmembrane conductance regulator (CFTR), a chloride channel that causes cystic fibrosis if its function is lost. Curiously, *in vivo* folding of wild-type (wt) CFTR is highly ineffective, as only 30-40 % of the synthesized protein reach the plasma membrane [151]; the majority of the protein shows impaired folding, which is recognized by the quality control machinery of the endoplasmic reticulum [152]. Misfolded molecules are targeted to the proteasome for degradation [153]. However, the amount of functional CFTR is sufficient to exercise its proper function. Interestingly, the efficiency of folding of wt and mutants of a variety of membrane proteins can be altered by changes in the "environmental" conditions like temperature or composition of the solvent or the lipid membrane [15,140,154-159].

In over 90 % of the individuals suffering from cystic fibrosis, a single amino acid deletion (Δ F508) has been identified [160]. This deletion causes biosynthetic arrest and the quality control system to prevent Δ F508-CFTR from entering the secretory pathway although Δ F508-CFTR exhibits reduced but significant functionality [159]. This way, Δ F508-CFTR is completely sequestered from the plasma membrane, which in turn causes the pathological phenotype [161]. In total, about 1600 different mutations affecting CFTR folding and targeting have been identified [162]. Among these mutations, many are non-conservative replacements (polar \rightarrow apolar and *vice versa*) in transmembrane α -helices [160]. As discussed in section 1.2.1.2, hydrophobicity as well

¹⁴ Amyloids are observed in a variety of human diseases including Alzheimer's, Parkinson's, and Creutzfeldt-Jakob disease, type II diabetes, and Huntington's disease; this field of research has recently been reviewed by Chiti and Dobson [137,138].

as hydrogen bonding between polar side chains can be critical for membrane protein folding. Consequently, non-conservative replacements disrupting native interactions may severely promote misfolding.

The two membrane proteins that have been mainly investigated within the frame of this thesis, connexin 26 (Cx26) and the serine:threonine antiporter (SteT), are both directly and indirectly disease related. The first protein, Cx26, oligomerizes *in vivo* to form hexameric connexons, which dock end-to-end to connexons of adjacent cells to establish gap junctions (for details on gap junctions see section 1.3). Mutations in Cx26 lead to either inefficient trafficking of Cx26 to the plasma membrane or impaired oligomerization, both resulting in a loss-of-function phenotype [163]. As Cx26 is the main connexin expressed in the cochlea of the inner ear, loss-of-function mutations result in deafness. The second protein, SteT, is a membrane protein from *Bacillus subtilis*. SteT is homologous to the light subunit of eukaryotic heteromeric amino acid transporters (HATs), which are involved in a variety of aminoacidurias and are overexpressed in some primary human tumors. Consequently, deciphering the mechanisms regulating and stabilizing these (and other) proteins is of major interest in understanding the molecular basis of diseases.

1.2.2 Hurdles in Membrane Protein Studies

Although membrane proteins are of scientific interest, as they are involved in a multitude of vital processes, our knowledge about their structure, function, and folding is fairly limited. What makes membrane proteins so difficult to study? Compared to soluble proteins, they show a similarly dense packing and hydrophobicity of their interior [164]. In contrast to soluble proteins, membrane proteins expose a hydrophobic surface, thus adjusting to the environmental constrictions set by the lipid bilayer. It is this surface hydrophobicity that makes it difficult to work with membrane proteins in aqueous solution [165]. Intuitively, the best suited environment for handling membrane proteins would be the native membrane. However, biophysical techniques used for studying membrane proteins often require purified and solubilized protein [166]. In general, several bottlenecks have to be overcome to reveal a membrane protein's secrets: production of sufficient amounts, purification, solubilization, and reconstitution or crystallization of the desired protein [167]. For soluble proteins reliable methods have been established for each of these steps. For membrane proteins, the repertoire is still limited.

Membrane proteins are usually present in the native membrane at very low concentration and accompanied by a plethora of other proteins¹⁵, which calls for overexpression approaches [166,171,172]. However, accumulation of overexpressed proteins in the membrane can induce stress response mechanisms or become toxic for the cell [172]. Heterologous expression of eukaryotic membrane proteins in bacteria might be further hampered by the need for specific glycosylation [172,173] or membrane lipid composition [17,167], both of which cannot be provided by bacteria. Moreover, differences in the translation rate and the translocation channel between prokaryotes and eukaryotes might lead to aggregation and misfolding [171]. Thus, especially for mammalian membrane proteins homologous expression systems are used to produce functional protein [171].

Purification of functional membrane proteins is complicated by the complexity of the cellular membrane. The use of detergents is necessary for solubilization and will at best result in slight destabilization of the membrane protein [165,174]. Indeed, one of the most important decisions to make is the choice of the detergent and/or lipid system for solubilization as the (long-term) stability of membrane proteins depends on the nature of the solubilizing agents [166,175].

Folding and unfolding studies of α -helical membrane proteins are hampered by their resistance to chemical unfolding by standard chaotrops, such as urea or guanidinium hydrochloride, at neutral pH [165,176]. Likewise, membrane proteins exhibit a high thermal stability. Calorimetric and spectroscopic observations unveiled that, even at high temperatures, a considerable fraction of secondary structure is retained. These results suggest that solvent-exposed extramembrane loops and domains unfold similar to water-soluble proteins but that the transmembrane α -helices maintain their secondary structure [176-178]. Moreover, even if membrane proteins can be (partially) denatured this way, they are prone to irreversible aggregation. Even strong polar detergents like SDS only induce a compact denatured state rendering proteins non-functional, although a significant amount of α -helical structure is retained [165].

1.2.3 Methodological Approaches in Membrane Protein Research

As summarized in the previous section, membrane protein research is still a challenge, especially for structural biologists. The limited stability of solubilized

¹⁵ Some proteins like cytochrome c oxidase [168], bR [169], and aquaporin-1 [170] can be purified from natural sources, as they are available in large quantities from cellular membranes.

membrane proteins and the enormous number of crystallization conditions that have to be screened, make the growth of well-diffracting 3D crystals of membrane proteins still a matter of years. That resulted in under-representation of membrane protein structures in the PDB. Although new approaches like the lipid cubic phase [179], fusion with large hydrophilic domains [180], and the use of antibody fragments [181] have been introduced, the pace of structure determination is still low. The problem of crystallization can be overcome by approaching 3D structures using electron microscopy (EM) [182], which requires proteins to be arranged in two-dimensional (2D) arrays [183]. Freezing these samples (cryo-EM [184]) increases the resolution to near-atomic level [185] and lets electron crystallography compete with X-ray crystallography. Even if 2D crystals are not available, single-particle EM techniques yield medium resolution (8-30 Å), which allows functionally related conformational changes to be observed [186].

Even with development of the TROSY (transverse relaxation optimized spectroscopy) technique [187], solution nuclear magnetic resonance (NMR) is still of limited use, especially for α -helical membrane proteins¹⁶. The huge size of the protein-micelle complexes results in band broadening and signal loss [188]. However, different solid-state NMR methods (oriented sample NMR and magic angle spinning NMR) are becoming popular [189].

In the absence of 3D structural information other methods are sought. Site-directed spin labeling electron paramagnetic resonance (SDSL-EPR) provides information about the secondary structure [190], immersion depth of a residue [94,191], and distances between different labels [192-195]. Using different EPR methods, it is possible to measure distances of up to 50 Å [196]. Site-specific infrared dichroism (SSID) [197] is another method that can reveal secondary structure and, moreover, yields tilt and rotational orientation of α -helices within the lipid bilayer. Thus, using a series of different labeling sites, three-dimensional information can be obtained. Results from SDSL-EPR and SSID can be used as constraints for modeling or refinement of NMR structures.

Besides these new technologies, "classical" methods such as circular dichroism (CD) [58,198], (time-resolved) Fourier transform infrared (FTIR) spectroscopy [199,200], different types of fluorescence spectroscopy [198,201], calorimetry [202,203], and

¹⁶ In contrast to the signals of β -barrel membrane proteins, the signals obtained from α -helical membrane proteins overlap and are significantly less dispersed.

electrophysiological techniques [204-206] are applied to study structure-function relationships of membrane proteins. Site-directed cross-linking studies [194] and functional assays [207-210] also provide valuable data. Noteworthy, advanced molecular biology is a prerequisite for most of the above mentioned methods because either site-specific labels have to be introduced or mutational analysis is required for meaningful interpretation of the results.

Apart from *in vivo* and *in vitro* experiments, computational methods are gaining importance. One of today's simple tasks is prediction of transmembrane protein topology based on sequence analysis. The power of more demanding molecular dynamics simulations is illustrated through modeling of structure and function of GPCRs [211,212], ligand binding [213], proton exclusion from aquaporin1 [214], or unfolding of bR [215,216].

1.3 MEMBRANE PROTEINS FULLFIL SPECIFIC FUNCTIONS

Located at the border between the interior and exterior of cells, membrane proteins provide specific functionalities vital for the cell. Two projects presented in this theses (chapters 5 and 6) deal with membrane proteins of different classes. In the following, these proteins will be briefly introduced.

1.3.1 Gap Junctions

Gap junction communication channels exist in all multicellular organisms¹⁷, play an important role in direct cell-to-cell communication and have recently been proposed to participate in cell adhesion [218]. Each gap junction is created by the non-covalent end-to-end docking of two hemichannels resident in the plasma membrane of the neighboring cells (Figure 1.5A). Hemichannels, the so-called connexons, are hexameric, ring-shaped assemblies of connexin proteins (Figure 1.5A, Figure 1.6A). *In vivo*, gap junctions cluster in large two-dimensional, semi-crystalline arrays, and thus give rise to specialized areas in the plasma membrane. The channels form a small aqueous pore (Figure 1.6A) that connects the cytosol of the participating cells and allows exchange of nutrients, metabolites, ions, and small molecules of up to ≈ 1000 Da [219].

¹⁷ Gap junctions are found in all multicellular animals. Nevertheless, gap junctions composed of connexins are a feature exclusive to vertebrates. Gap junctions in invertebrates are made from the evolutionary older innexins that exhibit an analogous topology but belong to a different protein family. Innexin relatives found in mammals are termed pannexins [217].

At present, 20 different connexin isoforms have been identified [220,221]. All share a common topology with four transmembrane domains, two extracellular loops (E1 and E2), one cytosolic loop, and the N- and C-terminal domains residing in the cytosol (Figure 1.5B) [222].

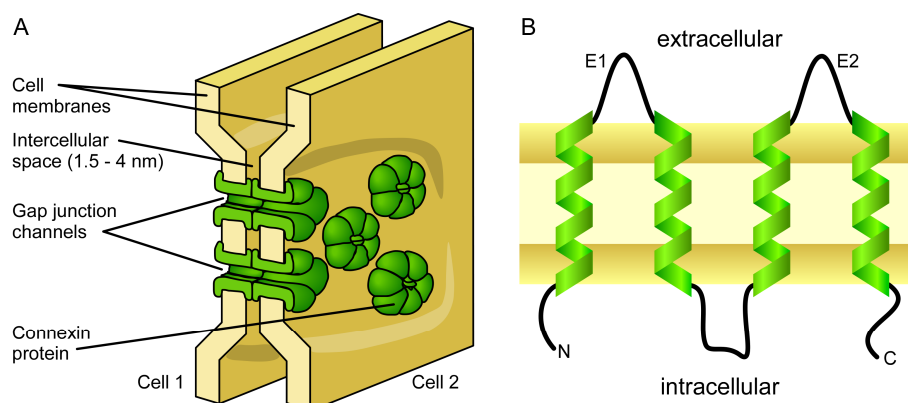


Figure 1.5 Schematic illustration of connexins and gap junctions. (A) Connexin hexamers, connexons, dock to connexons of adjacent cells and thus form gap junction communication channels that bridge the intercellular space. Gap junctions assemble into large two-dimensional arrays. (B) Membrane topology common to connexin molecules. For details on the secondary structure of the extracellular loops E1 and E2 see Figure 1.6B, C.

First cryo-EM studies showed that connexons are highly ordered and that the transmembrane domains adopt an α -helical structure [223,224]. Although the extracellular loops along with the transmembrane domains are highly conserved among connexin isoforms, the structure of the two extracellular loops stayed obscure until very recently the 3D structure of wt Cx26¹⁸ (Figure 1.6) was solved at 3.5 Å by X-ray crystallography [225]. In this structure, the E1 contains a 3_{10} -helix in the beginning and a short α -helix in the C-terminal half. The short β -strand between the helical elements of E1 forms a small β -sheet in concert with the β -strands located in E2 (Figure 1.6B, C). Three indispensable disulfide bonds connect E1 and E2 (Figure 1.6C). In docked connexons, interactions among the charged and polar residues in E1 and E2 structures of adjacent connexins establish a sealed double-layered wall¹⁹.

Differences among the connexin family primarily arise within the cytosolic loop and the C-terminal domain, which varies in size and sequence [217]. Thus, connexin isoforms are specified simply by their molecular weight: Cx26 and Cx37 are connexin isoforms with molecular weights of 26 and 37 kDa, respectively.

¹⁸ The gap junction is assumed to be in its open state, since no obstruction of the permeation pathway had been observed at the resolution achieved and blocking conditions had been avoided during crystallization [225].

¹⁹ The inner wall is formed by interactions between E1 structures, while interchannel contacts within E2 set up the outer wall.

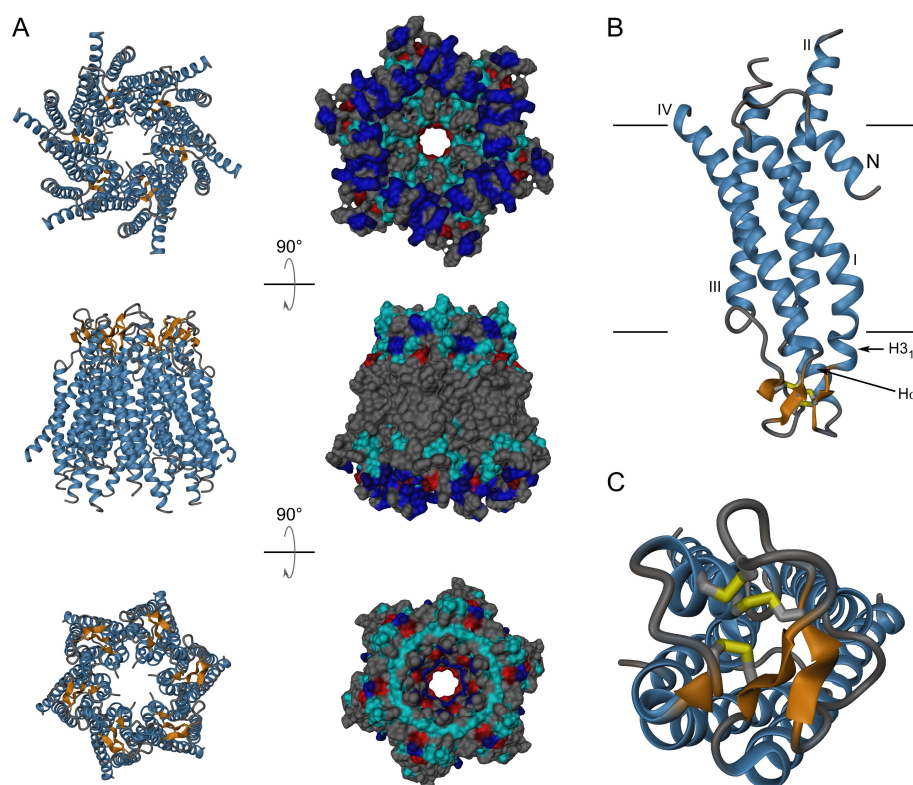


Figure 1.6 Structure of wt Cx26. (A) Structure of a Cx26 connexon from a Cx26 gap junction represented in bottom- (cytosolic side, top row), side- (along the membrane plane, middle row), and top-view (extracellular side, bottom row). The structure is shown as a cartoon (left column, blue: helices, orange: β -strands, grey: coil) and as a space-fill model (right column). Red, blue, and cyan colored surfaces in the space-fill model represent acidic, basic, and polar residues, respectively. (B) Single Cx26 monomer represented as a cartoon in side-view. Transmembrane α -helices are marked with I-IV. The short N-terminal helix (N) inserts into the cytosolic pore entrance and forms the pore funnel. The extracellular loops E1 and E2 consist of both helical (marked as H3₁₀ and H α) and β -strand structures. The black bars indicate the borders of the transmembrane region. (C) Single Cx26 monomer viewed from the extracellular surface, showing the arrangement of the conserved and essential disulfide bridges interconnecting loops E1 and E2. PDB ID: 2ZW3 [225].

Structural studies on gap junctions have been carried out using electron microscopy, X-ray diffraction [225-229], and NMR [230-234]. However, lacking a high-resolution structure²⁰, biochemical, mutagenic, and electrophysiological techniques have been exploited to gain information on gap junctions. It was disclosed that gap junctions are involved in development, maintenance of homeostasis, and signal transduction pathways. Consequently, the channels are tightly regulated and modulated by several small molecules and physiological conditions [235-238]. However, connexin isoforms respond differently to modulating stimuli [239,240].

²⁰ Although gap junctions, similar to bR, assemble in large two-dimensional arrays, efforts in structure determination have not been successful. In particular, large-scale expression and purification of these delicate structures have proved very challenging.

In combination with the ability of connexins to produce connexons composed of different isoforms, differential expression of isoforms might be a mechanism by which the functionality of gap junctions is shaped in a tissue-specific manner [240-242]. Consequently, single point mutations in different connexin genes can lead to tissue-specific breakdown of gap junction function [243]. Mutations in Cx26 have been shown to cause non-syndromic deafness [150,244-247], skin lesions, and vascularising keratitis [248]. Not less than 130 different mutations in Cx32 are the basis of the X-linked Charcot-Marie-Tooth syndrome [249], which is a neurodegenerative disease of the peripheral nervous system. Although Cx32 is also expressed in the central nervous system, it is not affected by these mutations. Moreover, mutations in other connexins are associated with cataract (Cx46 and Cx50), several skin diseases (Cx30 and Cx31), and various heart diseases (e.g. Cx37, Cx40, Cx43, and Cx45) [250]. As outlined in section 1.2.1.3, these diseases are based on either impaired trafficking or altered function, i.e. pore gating in the case of connexins.

1.3.2 Amino Acid Transporters

1.3.2.1 How Cells Perform Transport Across Membranes

Lipid membranes establish tight diffusion barriers for small polar, water-soluble molecules. For this reason, cells had to establish specific systems, the transport proteins, to catalyze uptake, excretion, and exchange of ions and small organic molecules. In multicellular organisms, transporters are also involved in recycling of neurotransmitters at synaptic membranes. The importance of these tasks is underscored by the fact that 15-30 % of all membrane proteins are dedicated transport processes [6]. Specificity for a single or a small number of solutes is common to all transport proteins.

Nature has established different mechanisms to perform and fuel transport. Passive transport occurs "downhill" along the electrochemical gradient and can be facilitated by channels (Figure 1.7A) or carriers (Figure 1.7B). Active transport, on the other hand, requires "uphill" transport against an electrochemical gradient. The required free energy is supplied by light absorption, ATP hydrolysis (Figure 1.7C), or coupling to "downhill" transport of a co-solute. The co-solute can be transported in the same (symport, Figure 1.7D) or the opposite direction (antiport, Figure 1.7E) of the main solute. Coupled transport is also referred to as secondary transport, because the

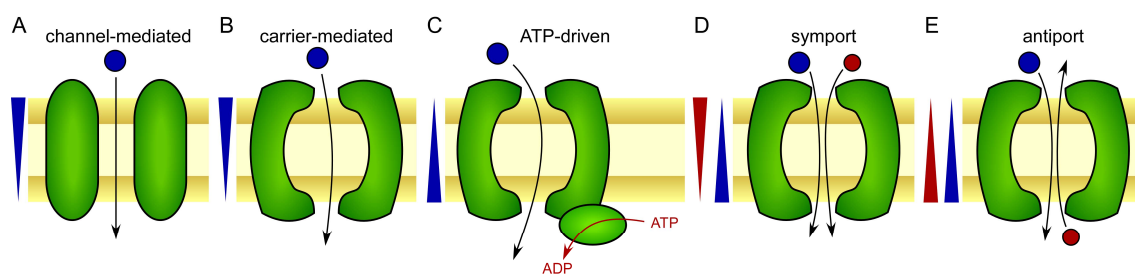


Figure 1.7 Different transport mechanisms. (A) A channel provides an aqueous pore and allows selected solutes to pass by diffusion. (B) The solute binds to a carrier that undergoes a conformational change and releases the solute on the opposite side before switching back to the initial conformation. (C) ATP-hydrolysis is used to fuel solute transport against the electrochemical gradient. (D), (E) Solute and co-solute are transported in the same (D) or opposite (E) direction. Transport of the co-solute provides the energy for the translocation of the solute. Active transporters, i.e. ATP-driven (C) and solute-coupled (D and E) transporters, alternate between different conformations during transport cycles. Solute and co-solute as well as the corresponding electrochemical gradients are depicted in blue and red, respectively.

electrochemical gradient that provides the free energy has to be established in a preceding step, usually by an ATP-driven pump.

1.3.2.2 L-Amino Acid Transport

Transport of L-amino acids is crucial for both prokaryotes and eukaryotes. Despite being the raw material for protein biosynthesis, amino acids play an important role in a multitude of processes. Prokaryotes use amino acids as a carbon and nitrogen source, for pH homeostasis [251-254], osmoprotection, generation of electrochemical ion gradients [255,256], and many more processes [257,258]. In eukaryotes, e.g. in man, amino acid transporters absorb amino acids from blood and, moreover, take part in signaling [259] and assimilation of essential amino acids²¹ in the intestine.

Amino acid transport is facilitated by ATP binding cassette (ABC)-type transporters and secondary transporters. In ABC-type systems, transport is driven by ATP hydrolysis. In contrast, secondary transporters mainly exploit Na^+ or H^+ gradients across the membrane to energize transport, i.e. Na^+ or H^+ serve as co-solute. However, also antiport of two amino acids or of amino acids and other small organic compounds occurs [258].

As amino acids serve a huge number of functions, amino acid transporters are in general specific for one or a small set of amino acids. Moreover, several differently regulated transport systems are available for each amino acid. Therefore, it is not astounding that amino acid transporters are found among different secondary

²¹ Certain amino acids, the essential amino acids, cannot be synthesized by humans. Thus, these amino acids have to be taken up with food [260].

transporter families [258]. Most transporter families contain members of prokaryotic and eukaryotic origin. One such family is the amino acid/polyamine/organocation (APC) superfamily, which occurs in all phyla and whose members catalyze solute:cation symport or solute:solute antiport [261].

The L-amino acid transporter (LAT) family is a member of the APC superfamily. Members of the LAT family match the light subunits of HATs found in eukaryotes [262,263]. The heavy subunit of HATs is an N-glycosylated type II membrane protein that is covalently linked to the light subunit by a single disulfide bond and that is responsible for plasma membrane localization of the transporter system. The light subunit, on the other hand, is a multipass transmembrane protein that has transport activity. Genetic defects in either subunit cause a number of human diseases. Mutations in the light as well as the heavy subunit of system $b^{0,+}$ cause cystinuria [148,149], whereas mutations in the light subunit y^+ LAT1 account for lysinuric protein intolerance [264,265]. Another light subunit, xCT, facilitates cysteine uptake and glutamate efflux [266,267] and is involved in cocaine relapse and maintenance of the plasma redox balance [268,269]. LAT1, the light subunit of system L, is overexpressed in certain primary human tumors. It is responsible for transport of essential neutral amino acids with long, branched, or aromatic side chains. These amino acids are required by tumor cells to support their unabated growth [270]. Therefore, amino acid transporters like LAT1 are attractive drug targets.

The only prokaryotic representative of the LAT family known is the serine:threonine exchange transporter SteT [271]. Due to its high homology to the eukaryotic LAT members and the problems associated with studying these proteins, SteT is an appealing model system for studying structure and function of LAT family members.

ATOMIC FORCE MICROSCOPY

2.1 HISTORY

In 1986, Binnig, Quate, and Gerber introduced the atomic force microscope (AFM) as an innovative method to image both conducting and non-conducting²² surfaces [273]. Unlike light and electron microscopes, the AFM exploits the interaction forces between a sharp tip and the surface (for details see section 2.2.2.2) to generate a topographic image. Consequently, the AFM belongs to the family of scanning probe microscopes (SPM), which all use a sharp tip to probe the surface. However, each SPM technique relies on a different measurable quantity like tunneling currents in the scanning tunneling microscope (STM) [272], potential offset between sample and tip in the Kelvin probe microscope [274], magnetic forces in the magnetic force microscope [275], or light in the scanning near field microscope (SNOM) [276] (Ref. [277] provides a technical review of several SPM techniques). AFM impresses by its high spatial resolution, although true atomic resolution is only possible under ultrahigh vacuum and with atomically flat surfaces [278].

2.2 PRINCIPLE

2.2.1 AFM Setup

The AFM setup fascinates by its simplicity. Only a few components are needed to set up an AFM – a cantilever with a sharp stylus or tip, a piezoelectric actuator or transducer, a laser diode, a position sensitive photo detector (PSPD), and (computer) hardware for control and visualization (Figure 2.1). The sample is usually immobilized on a piece of mica or glass glued onto a steel disc, which can be mounted on top of the piezoelectric actuator. The actuator provides 3D sample positioning and movement

²² The previously developed scanning tunneling microscope [272], which allows atomic resolution imaging, is limited to conducting surfaces, since it relies on tunnel currents between the tip and the surface.

with sub-nanometer accuracy. The cantilever "feels" the interaction forces between its tip and the surface during imaging or force spectroscopy (for details see sections 2.3.1 and 2.3.2, respectively). These forces result in deflection of the cantilever from its force-free resting position. The cantilever itself is fixed in a quartz glass fluid cell (not shown in Figure 2.1), which in turn is placed inside the AFM head. The AFM head also houses the optical beam deflection detection system consisting of a red light ($\lambda = 625 \text{ nm}$) emitting laser diode and a four quadrant PSPD²³ [280]. The laser beam is focused onto the end of the cantilever, reflected onto a mirror (which is not shown in Figure 2.1), and finally onto the PSPD. Forces acting on the cantilever cause its bending and thus a change in the angle at which the laser is reflected onto the PSPD. As a consequence, the position of the laser spot on the PSPD is altered, resulting in a change of the deflection signal. In contact mode imaging (see section 2.3.1.1), the deflection signal is transferred to the controller and fed into a feedback loop, which moves the piezoelectric actuator to keep the deflection constant.

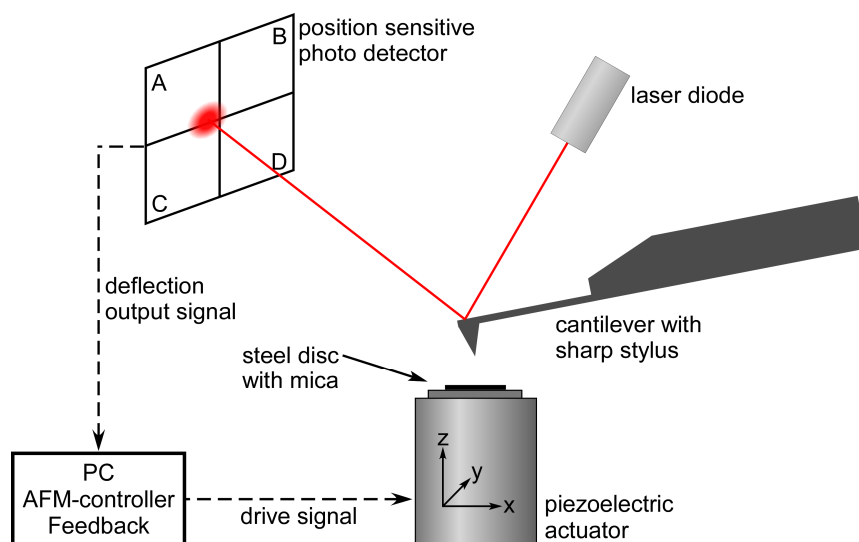


Figure 2.1 Illustration of a typical AFM setup. The sample is mounted on top of the piezoelectric actuator, which allows sub-nanometer positioning. For AFM imaging (for details see section 2.3.1), the sample is raster-scanned below a sharp tip mounted at the end of a soft cantilever. For force spectroscopy (see section 2.3.2.1 for details), the sample is repeatedly approached and retracted from the cantilever tip. Vertical cantilever deflection results in a change of the position of the laser spot on the PSPD (quadrants A-D) that is quantified by calculating the signal difference between the upper and lower halves of the PSPD.

By using an optical beam deflection detection system, the cantilever deflection is amplified and the PSPD finally provides a measurable voltage signal (U_{PSPD}) that is proportional to cantilever bending. This signal is converted into an absolute deflection

²³ Alternative detection systems rely on interferometry [279] or capacitance. Originally, a scanning tunneling microscope (STM) was used to measure the cantilever deflection [273].

(measured in nanometers). Because the cantilever can be described as a Hookean spring, deflection is subsequently converted into force (measured in Newton). This force is acting between the cantilever tip and the surface.

For the techniques and applications described and used within the frame of this thesis, only the vertical deflection of the cantilever is of importance. For that reason, from now on the terms deflection and deflection signal will be always used to mean vertical deflection of the cantilever and the corresponding signal on the PSPD. The latter is expressed as the signal difference between the upper and lower halves of the PSPD²⁴.

2.2.2 Cantilevers

2.2.2.1 General Considerations

Cantilevers are the most important part of an AFM – it is the cantilever tip that is in contact with the sample and that senses the forces in its vicinity. Today's cantilevers are usually micro-fabricated using various techniques, such as photo lithography, dry and wet etching, or thin film deposition. It is possible to create small and sharp tips at the end of a cantilever. Cantilevers are usually made from silicon or silicon nitride (Si_3N_4) and covered with thin layers of gold or aluminum to increase reflectivity of the backside²⁵. Magnetic coatings are employed for applications, where the cantilever is oscillated within a magnetic field. For standard cantilevers, the tip is either made from silicon or silicon nitride, just as the entire cantilever. However, in order to tune the cantilevers' surface properties, tips can be coated with a thin layer of oxide and various precious metals (e.g. gold, silver, and platinum). Moreover, tips can be modified using carbon nanotubes, magnetic coatings, and various chemicals to introduce desired functional groups on the surface. Depending on the coating, tips can be conductive or non-conductive. The tip base is most often conical or pyramidal and terminates in a sharp apex of 2 to 50 nm radius. Typical tip heights range from 2 to several tens of micrometers. Cantilevers are either V-shaped (triangular) or rectangular and exhibit a thickness range of less than 200 nm up to 2 μm . Typical cantilevers vary in length between 100 and 200 μm , but commercially available small cantilevers as short as 38 μm are becoming more and more popular. Compared to regular cantilevers,

²⁴ The deflection signal is $U_{\text{PSPD}}=(U_{\text{A}}+U_{\text{B}})-(U_{\text{C}}-U_{\text{D}})$, where $U_{\text{A}}, U_{\text{B}}, U_{\text{C}}$, and U_{D} correspond to the voltage measured from each of the four quadrants for the PSPD.

²⁵ The backside of a cantilever is the tip-less side of the cantilever, onto which the laser is focused and which is not contacting the sample surface. The tip is located on the frontside.

small cantilevers exhibit higher resonance frequencies and thus lower noise levels at the same measurement bandwidth [281]. The V-shaped geometry minimizes torsion resulting from lateral friction while scanning the sample, which makes them a good choice for purely topological imaging. The higher susceptibility to torsion of rectangular cantilevers does not influence the capability to be used in force spectroscopy experiments.

Regardless of the shape, all cantilevers can be described as springs using Hooke's law²⁶. The applied or experienced force, F , is proportional to the vertical displacement, Δx_z , of the cantilever

$$F = -\kappa_{cant} \Delta x_z \quad 2.1$$

where κ_{cant} , the spring constant of the cantilever, is the scaling factor. Cantilever spring constants depend on their geometry and material. Determined by the application, cantilevers with different spring constants should be used. For contact mode imaging of biological samples, spring constants typically range from 60-100 pN/nm. Cantilevers used for force spectroscopy are slightly softer (5-100 pN/nm) while in tapping mode imaging harder cantilevers (0.3–40 nN/nm) are employed.

2.2.2.2 Forces Acting on the Cantilever

As mentioned above (section 2.1), AFM is based on interactions between the cantilever tip and the sample surface. The most common interactions between tip and surface are (i), steric forces, (ii), van der Waals forces, and, (iii), electrostatic forces (e.g. Coulomb, ionic, or double layer forces).

Hard core steric forces are repulsive and extremely short-ranged (≤ 0.1 nm). The force is caused by overlapping electron clouds and a result of the Pauli exclusion principle. Empirically, the distance dependence of steric repulsion can be described by a $1/d^{12}$ power law, where d is the distance between the two surfaces [282].

Van der Waals forces result from fluctuations of electric dipole moments of molecules, which influence dipole moments of molecules close by. The resulting forces can be attractive or repulsive over a range of a few nanometers and depend on the shape of macroscopic bodies such as AFM cantilever tips [282].

Biological macromolecules as well as most common AFM supports (e.g. mica, glass, silicon, and graphite) and cantilever surfaces (e.g. Si_3N_4 , silicon, gold, oxide)

²⁶ Modeling of cantilevers as Hookean springs is only valid for small deflection of several tens of nanometers. At higher deflections, cantilevers do not behave as linear springs.

exhibit a net surface charge and, thus, a surface potential (ψ_0). Sign and magnitude of the surface charges depend on the pH of the buffer solution and the pK values of functional groups. Charges on surfaces immersed in aqueous solution are screened by counterions, thus giving rise to a diffuse electrical double-layer (EDL). According to Boltzmann's law, the counterion concentration decays exponentially with the distance from the surface, and so does the potential

$$\psi_d = \psi_0 e^{-d/\lambda_D} \quad 2.2$$

where ψ_d is the potential at a distance d from the surface. The characteristic length scale of the decay, also understood as the thickness of the EDL, is given by the Debye length, λ_D ,

$$\lambda_D = \sqrt{\frac{\epsilon_e \epsilon_0 k_B T}{e^2 \sum_i c_{e,i} z_i^2}} \quad 2.3$$

where e is the electronic charge, k_B is the Boltzmann constant, T the absolute temperature, ϵ_e and ϵ_0 are the permittivity of the solute and vacuum, respectively, and $c_{e,i}$ and z_i are the concentration and valency of the i^{th} electrolyte component. Obviously, λ_D strongly depends on the concentration and valency of the electrolyte ions [282].

When a cantilever tip approaches a surface, the EDLs of both surfaces overlap and give rise to electrostatic double-layer forces, F_{el} , which can be significant up to the micrometer range [282]. When coming closer to the surface, van der Waals forces, F_{vdW} , have to be considered. The Derjaguin-Landau-Verwey-Overbeek (DLVO) theory describes the interplay between the two forces. However, it does not account for steric forces, specific interactions, and hydration forces [282].

Both F_{vdW} and F_{el} depend on the shape and area of the interacting surfaces. To calculate the DLVO forces (F_{DLVO}), an estimate of the cantilever geometry is required. The global radius (R_g) of a cantilever tip has been estimated to be in the range of 40-200 nm [283,284]. However, such a huge tip radius is not compatible with the sub-nanometer resolution topographs recorded from two-dimensional protein crystals [285], suggesting small protrusions from the global tip that interact with the surface and contour the topography. The radius of such a local tip (R_l) has been estimated to be ≈ 2 nm [286]. For high-resolution imaging, consequently, interactions between the macroscopic tip (R_g) and the flat sample surface as well as interactions between the local tip (modeled as a half sphere) and a protein of the same radius (R_l) have to be considered, resulting in the overall F_{DLVO}

$$\begin{aligned}
 F_{DLVO}(d) &= F_{DLVO}^s(d) + \frac{1}{2}F_{DLVO}^l(d) = F_{el}^s(d) + F_{vdW}^s(d) + \frac{1}{2}[F_{el}^l(d) + F_{vdW}^l(d)] \\
 &= \frac{4\pi\sigma_s\sigma_tR_g\lambda_D}{\epsilon_e\epsilon_0}e^{-(d+R_l)/\lambda_D} - \frac{H_aR_g}{6(d+R_l)^2} + \frac{\pi\sigma_s\sigma_tR_l\lambda_D}{\epsilon_e\epsilon_0}e^{-d/\lambda_D} - \frac{H_aR_l}{24d^2}
 \end{aligned} \tag{2.4}$$

where σ_s and σ_t are the surface charge densities of sample and tip, H_a is the Hamaker constant, and d is the distance between the two surfaces²⁷. Based on Equation 2.4 and underscored by experimental evidence, Müller *et al.* have shown that careful adjustment of pH and electrolyte concentrations are a prerequisite for high-resolution topographic images [283,288]. Calculations assuming a local tip with a radius of 2 nm and a global tip with a radius of 100 nm revealed that, at low electrolyte concentrations and imaging forces, the local protrusion would be separated about 9 nm from the surface of purple membrane due to electrostatic repulsion of the macroscopic tip. High imaging forces would be required to bring the small tip into contact with the surface. However, such high forces might destroy the sample. Lowering of the electrostatic repulsion by increasing the electrolyte concentration would allow the local tip to be about 1 nm from the surface. Van der Waals attraction compensates the remnant electrostatic repulsion. However, electrostatic repulsion is required for stable imaging. In absence of electrostatic repulsion van der Waals forces would pull the tip into the sample and lead to deformation of the soft biomolecules [288].

2.2.2.3 Force Sensitivity

For force measurements high force sensitivity of the cantilever is desirable. However, noise from thermal excitation and/or components of the instrument may reduce sensitivity [280,289]. Modern instruments offer advanced mechanical, optical, and electronic components, so that the deflection of the cantilever is limited to the thermal motion. The equipartition theorem [290] provides the basis for an estimation of the minimal detectable force. The energy associated with each degree of freedom (e.g. with each elastic mode²⁸) of the cantilever equals $k_B T/2$. Thus, using the equipartition

²⁷ Similarly, the F_{DLVO} between sample and support can be calculated using $F_{DLVO}(d) = F_{el}(d) + F_{vdW}(d) = \frac{2\sigma_s\sigma_p}{\epsilon_e\epsilon_0}e^{-d/\lambda_D} - \frac{H_a}{6d^3}$, where σ_p is the surface charge density on the sample [287]. This calculation can be used to adjust the pH and electrolyte concentration of adsorption buffers.

²⁸ In a first approximation, a cantilever can be regarded as a simple harmonic oscillator with one degree of freedom. The higher elastic modes of the cantilever exhibit much higher spring constants than the first mode and, therefore, do not significantly contribute to the deflection at the end of the cantilever [289].

theorem, Hutter and Bechhoefer [289] correlated the fluctuations of the cantilever to the thermal energy by

$$\frac{1}{2} \langle x_z^2 \rangle \kappa_{cant} = \frac{1}{2} k_B T \quad 2.5$$

where $\langle x_z^2 \rangle$ is the time-averaged mean-square displacement of the cantilever. Thus, the root-mean-square (RMS) displacement, $x_{z,RMS}$, can be estimated by

$$x_{z,RMS} = \sqrt{\frac{k_B T}{\kappa_{cant}}} \quad 2.6$$

Applying Hooke's law, the minimal detectable force can be approximated by the thermal RMS force, F_{RMS} , as

$$F_{RMS} = \sqrt{k_B T \kappa_{cant}} \quad 2.7$$

According to Equation 2.7, spring constant and thermal energy determine the force sensitivity of the measurement, which can be improved by choosing a soft cantilever. However, as evident from Equation 2.6, the use of soft cantilevers results in large fluctuations in the position of the cantilever tip. Moreover, flexible tips tend to relax slowly [291].

Viscous damping and measurement bandwidth are considered in a more sophisticated description of the minimal detectable force, F_{min} [292]

$$F_{min} = \sqrt{\frac{4k_B T B \kappa_{cant}}{\omega_0 Q}} \quad 2.8$$

where ω_0 is the angular resonance frequency of the cantilever, Q its quality factor²⁹, and B the measurement bandwidth. In single-molecule force spectroscopy (SMFS) experiments, force traces are usually recorded with a fixed number of data points. An increase of the pulling velocity, v_p , consequently results in an increased measurement bandwidth. According to Equation 2.8, higher pulling velocities thus cause increased noise levels.

2.2.2.4 Cantilever Calibration

Detector Calibration

The deflection of a cantilever can be measured with a resolution as high as 0.05 Å [289]. The optical deflection system used in most AFMs detects the position

²⁹ Q is a measure for the energy dissipation of an oscillating system (e.g. a cantilever); $Q = \frac{\kappa}{\omega_0 \gamma}$, where γ is the damping coefficient.

change of a laser spot on a PSD, which sends a position-dependent voltage to the AFM controller. Consequently, the detector has to be calibrated in order to convert the voltage signal into a value for the cantilever deflection.

Calibration of the PSD requires a well calibrated piezoelectric transducer, a clean cantilever tip, and a clean and hard surface. The cantilever is approached towards the surface until and beyond the point at which it comes into contact with the surface. As the surface is hard and the cantilever cannot indent it, the deflection signal (U_{PSPD}) obtained beyond the contact point linearly depends on the distance (z_p) traveled by the transducer:

$$U_{\text{PSPD}} = \frac{1}{\chi} z_p \quad \mathbf{2.9}$$

where χ is the optical lever deflection sensitivity. Butt and Jaschke [293], however, pointed out that U_{PSPD} is strictly only proportional to the angular changes in the cantilever position and not to the displacement of the end of the cantilever, the first depending on the elastic modes of the cantilever. Using beam theory, these authors proposed a correction factor of ≈ 1.09 for rectangular cantilevers.

To quantitatively apply forces to the cantilever it is crucial to know κ_{cant} (Equation 2.1). Manufacturers provide a nominal κ_{cant} . However, experience shows that actual values may differ more than 50 % from the nominal value. Accordingly, each cantilever has to be calibrated before performing experiments. In the following, some of the common methods used to measure κ_{cant} will be explained.

Spring Constant Calibration – Added Mass

The added mass method was introduced by Cleveland *et al.* in 1993 [294]. The cantilever is approximated as a single harmonic oscillator, for which the resonance frequency, ν_0 , is given by

$$\nu_0 = \frac{1}{2\pi} \sqrt{\frac{\kappa_{\text{cant}}}{m}} \quad \mathbf{2.10}$$

where m is the mass of the cantilever. Thus, the resonance frequency of the cantilever changes, when mass is added. Measurement of ν_0 before and after adding a known mass M^* is sufficient to calculate κ_{cant} according to

$$\kappa_{\text{cant}} = 4\pi^2 \frac{M^*}{\nu_1^{-2} - \nu_0^{-2}} \quad \mathbf{2.11}$$

where ν_1 is the resonance frequency after the mass was added. For precise measurements, it is crucial to place the additional mass M^* as close as possible to the

end of the cantilever, because its effect on the resonance frequency will be diminished the closer it is to the cantilever base. However, measuring the distance of the added mass from the end of the cantilever allows correcting for this effect [295]. Probably the most critical variable is the method by which the mass is added and determined. Usually small tungsten spheres are used, whose mass is calculated from the specific density of tungsten and their diameter, which is measured with an optical microscope. However, the tungsten particles are in general not perfect spheres, which results in uncertainties in mass determination.

Spring Constant Calibration – Sader Method

The Sader method [296] bases on modeling the dynamic deflection of a cantilever immersed in a viscous fluid (e.g. air). The method relies on the determination of the unloaded resonance frequency of the cantilever, ω_0 , a quantity, which is readily available. Moreover, it requires the length (L_{cant}), width (w_{cant}), and Q of the cantilever to be measured. *A priori* knowledge of the cantilever thickness and density, two quantities whose estimation is difficult and associated with large errors, is not necessary. Moreover, the method accounts for the effects of the surrounding environment. Finally, Sader's considerations resulted in

$$\kappa_{cant} = 0.1906\rho_f w_{cant}^2 L_{cant} \omega_0 Q \Gamma_i(\text{Re}) \quad 2.12$$

where ρ_f is the density of the fluid and Γ_i is the imaginary part of the complex hydrodynamic function. Γ_i depends on the Reynolds number, Re , which is given by [297]

$$\text{Re} = \frac{\rho_f \omega_0 w_{cant}^2}{4\eta_f} \quad 2.13$$

where η_f is the viscosity of the fluid³⁰. As the cantilever should not be highly damped, which means $Q \gg 1$, measurements of Q and ω_0 have to be performed in air. The method is limited to rectangular cantilevers, which must not narrow towards the end.

Spring Constant Calibration – Thermal Fluctuation Analysis

Calibration using the thermal fluctuation analysis is probably the most convenient and often used way to measure κ_{cant} . Hutter and Bechhoefer [289] modeled the cantilever as a single harmonic oscillator and correlated the thermal motion of the first elastic mode to its thermal energy (Equation 2.5). Solving for κ_{cant} results in

³⁰ Sader placed a calculator on his web site for convenient calculation of κ_{cant} [298].

$$\kappa_{cant} = \frac{k_B T}{\langle x_z^2 \rangle} \quad 2.14$$

The power spectral density (PSD) of the thermal fluctuations of the cantilever has a peak at the cantilever's resonance frequency (Figure 2.2). The area below that peak equals $\langle x_z^2 \rangle$. For precise measurement of $\langle x_z^2 \rangle$, it is important to use a properly calibrated PSPD and to apply the corresponding correction factor to compensate for the error introduced by the optical detection system (see section 2.2.2.4 – Detector Calibration).

However, the cantilever does not behave like a perfect spring and thus modeling it as a single harmonic oscillator results in an error that has to be corrected. Butt and Jaschke [293] derived a formula that takes the deviations into account

$$\kappa_{cant} = 0.971 \frac{k_B T}{\langle x_{z,1}^2 \rangle} \quad 2.15$$

where $\langle x_{z,1}^2 \rangle$ is the time-averaged mean-square displacement attributed to the first elastic mode of the cantilever, which equals the area under the peak in the PSD.

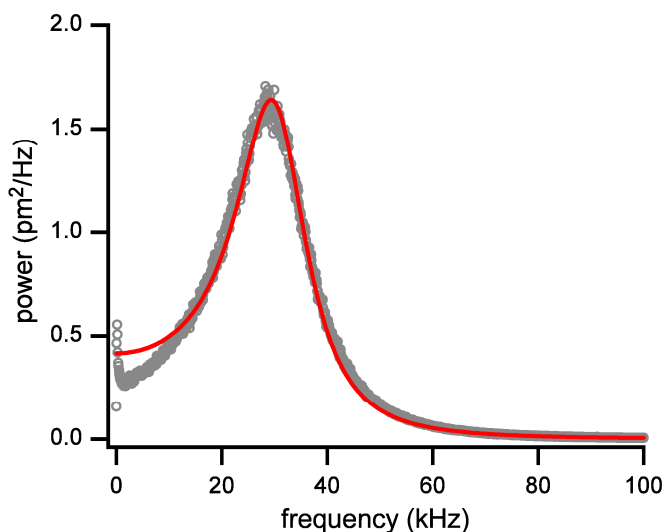


Figure 2.2 Power spectral density of an Olympus BioLever mini. PSD calculated from the thermal oscillation of a cantilever far from the surface. The PSD shows a clear peak at the cantilever's resonance frequency at ≈ 30 kHz. The red line shows a fit to Equation 3.2, which represents the theoretical power spectral density that was derived from modeling the cantilever as a harmonic oscillator.

2.3 OPERATION MODES

The AFM is a versatile instrument. It can not only be used to produce topographic images but is also capable of measuring force-distance (F-D) relationships using the so-called force spectroscopy mode. In this section, two imaging techniques will be introduced, which are routinely used to investigate biomolecules and details on AFM-based force measurements will be given.

2.3.1 Surface Imaging

In all SPM-based imaging applications, the piezo raster-scans the sample relative to the probe in the x,y -plane and simultaneously extends or retracts vertically (z direction) to keep the interaction between the sample and the tip constant. However, different imaging techniques differ in how the probe interacts with the sample, how the contrast is generated, and the information that can be extracted from the images. One of the most important advantages of AFM imaging is the fact that it can be performed with an outstanding signal-to-noise ratio. Neither sample staining nor dehydration or freezing are required for (sub-)nanometer resolution imaging. Thus, AFM can clearly compete with other techniques (Figure 2.3A) and provide complementary information.

Since AFM images are generated by a cantilever tip contouring the surface, resolution depends on tip geometry (Figure 2.3B). Tips with a smaller radius can protrude deeper into surface depressions. Moreover, tip convolution, i.e. surface structures appearing broader than they are, is reduced using sharper tips.

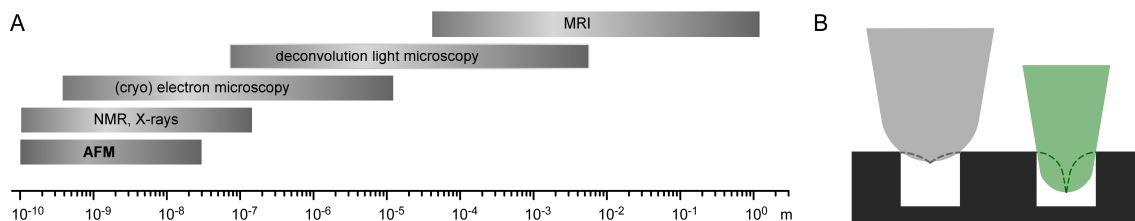


Figure 2.3 Resolution in AFM. (A) Comparison of the spatial resolution obtained by different techniques. (B) Resolution in AFM is limited by the cantilever tip geometry. Tips with smaller tip radii (green) allow higher lateral resolution, indent deeper into surface depressions, and cause less tip convolution (indicated by the dashed lines) than tips with larger radii (grey).

2.3.1.1 Contact Mode

During raster-scanning a surface, the tip is in contact with the surface and a user-defined low, non-destructive imaging force of ≤ 100 pN is applied³¹. A feedback loop is used to maintain the interaction force throughout the imaging process. If a topographic feature of the sample causes the cantilever to bend, the feedback loop adjusts the position of the piezoelectric actuator to reset the cantilever deflection to its pre-defined setpoint (Figure 2.4A). The x,y , and z -position of the piezo at each point

³¹ Higher contact forces can deform or disrupt soft samples. Moreover, due to increased tip-sample contact area resolution decreases [288].

of the image is used to generate the topographic height image. The error signal³², which is calculated by the feedback loop, provides information about the edges of surface features. True high-resolution contact mode height imaging requires careful adjustment of the feedback parameters to minimize the error signal.

In a special case, the so-called error signal mode, x,y -scanning is operated without any feedback and, thus, sample topography can be inferred from the cantilever deflection. However, high non-constant vertical and lateral forces are applied causing deformation or even disruption of the specimen.

True contact mode height imaging is suited best for well immobilized samples like membrane proteins densely packed into proteoliposomes or arranged in 2D arrays [299-302]. In these particular cases, dense packing reduces the lateral mobility of single molecules.

2.3.1.2 Tapping Mode

Tapping mode imaging is an approach to circumvent sample disruption and displacement by the lateral forces exerted during contact mode imaging. In tapping mode, the cantilever is acoustically oscillated. The tip touches the surface only once during an oscillation cycle, which reduces lateral forces that are applied to the sample. Several oscillation parameters are sensitive to interaction with the surface: resonance frequency, oscillation amplitude, and the phase shift. Any of these can be used as a feedback parameter to contour the surface topography [303]. The most common tapping mode used in biology is amplitude-modulated tapping mode AFM. In this mode, the cantilever is excited close to its resonance frequency and the RMS amplitude of the oscillation is detected by the PSPD. The amplitude is damped, when the tip is close to or in contact with the surface. The feedback maintains a constant, pre-defined amplitude by adjusting the piezo position vertically (Figure 2.4B). The topographic image is generated from the piezo movement, just like in contact mode imaging.

Frequently, a phase shift between the driving and the measured oscillation is observed, which originates from dissipative tip-sample interactions (Figure 2.4B, blue and green curves). From the phase shift, information about the mechanical properties of the sample surface can be deduced [303].

³² The error signal is the difference between the actual cantilever deflection and the pre-defined setpoint.

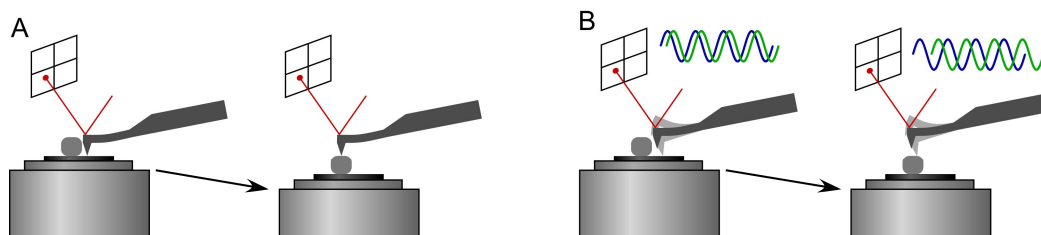


Figure 2.4 AFM imaging modes. (A) The cantilever is quasi-static and the surface topography is contoured by maintaining the cantilever deflection at the setpoint value through repositioning of the piezo in z-direction. (B) In tapping mode, the cantilever is oscillated close to its resonance frequency. Maintaining the oscillation amplitude constant reveals topographic height information. Mechanical properties of the surface can be extracted from the phase shift between the drive signal (blue sine waves) and the detected cantilever oscillation (green sine waves).

Compared to contact mode AFM, tapping mode imaging usually results in lower-resolution images. Often, the height information obtained by tapping mode AFM is not as accurate as that from contact mode AFM [304]. However, it can be used to image soft and fragile specimens such as cells or fibrillar macromolecular assemblies [305,306], where contact mode imaging fails due to sample deformation or destruction.

2.3.2 Force Measurement

Force plays a pivotal role in all fields of biology. This holds true for macroscopic bodies and systems (e.g. muscle contraction generates a force), but also and maybe especially on the microscopic level as force is involved in phenomena like cell adhesion [307], molecular recognition [308], DNA mechanics [309], motor protein movement [310], and protein folding and stabilization [311-316]. The forces experienced and generated by biological molecules are of manifold nature and can range from the sub-piconewton range up to several nanonewton (Table 2.1) [317].

Type of Force	Approximate Magnitude (pN)
Elastic	1-100
Covalent	10 000
Viscous	1-1000
Collisional	10^{-12} to 10^{-9} for 1 collision/s
Thermal	100-1000
Electrostatic / van der Waals	1-1000
Magnetic	$\ll 10^{-6}$

Table 2.1 Forces relevant on the molecular level and their approximate magnitude.

Measuring these forces with high precision in both force and position provides information on structure, dynamics, intra- and intermolecular interactions, and mechanical properties of molecules and complexes and thus sheds light on the molecular basis of various biological phenomena [313,315,318-323]. Different

techniques have been developed to approach this task, especially at the single molecule level. Each of these techniques may be used for different force ranges (Figure 2.5).

However, the way force is measured is different among these methods. In AFM, deflection of the cantilever is detected (Figure 2.5A). Both the biomembrane force probe (BFP) [324] and the laser optical tweezers (LOT) [325,326] measure the displacement of a small bead that is either attached to a micropipette-aspirated membrane sac (Figure 2.5E) or trapped in a highly focused laser beam (Figure 2.5C), respectively. The "spring" of BFP is the membrane sac, whose stiffness can be tuned by suction into the micropipette [324]. LOT use the restoring force generated by the photonic gradient of the laser that traps the bead.

Another single molecule method is magnetic tweezers (MT) [328]. In contrast to AFM, LOT, and BFP, which measure force changes, MT by definition exert constant forces on the sample. The force is generated through magnetic beads trapped in a magnetic field (Figure 2.5D) and can be tuned by bead size and material. As a constant-force technique, MT measure the time-dependence of length changes of the sample.

The surface force apparatus (SFA) [282,329], measures the F-D relationship of a sample between two cylinders (Figure 2.5B), e.g. the two components of an adhesive system. However, the interacting surfaces are macroscopic (a few μm^2) and thus, a large number of molecules and interactions are probed, making it well suited for determining surface or adhesion energies [330].

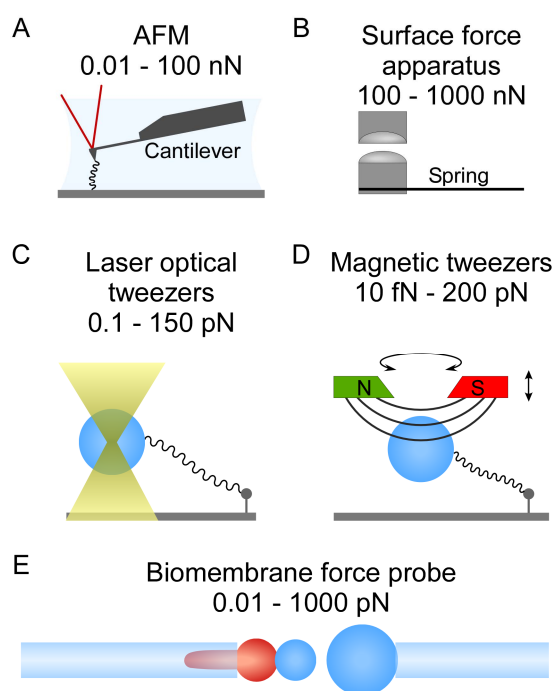


Figure 2.5 Different force probes used to measure interaction forces. (A) AFM in which the tip is attached to the force-transducing cantilever (immersed in liquid). (B) SFA with two crossed cylinders and a force-transducing spring. (C) LOT with a bead trapped in the photonic gradient. (D) MT with a magnetic bead in the magnetic field of a strong magnet. (E) BFP with a micropipette-aspirated membrane vesicle (left) that is used as a spring of adjustable stiffness. Figure adapted from [327].

2.3.2.1 AFM-Based Single-Molecule Force Spectroscopy

Constant Velocity Force Spectroscopy

In SMFS, the cantilever is used as a tool that can pick up single surface-anchored molecules from the specimen by approaching the surface to the cantilever and allowing it to rest while in physical contact. Subsequently, the surface is retracted from the cantilever at a constant velocity and if a molecule adhered to the tip, it is mechanically stretched by a force that is transmitted from the cantilever through the molecule to the sample surface. This force deflects the cantilever vertically, causing a change in the deflection signal, which is acquired alongside with the distance traveled by the piezo (Figure 2.6). However, the distance moved by the piezo does not represent the extension of the molecule, which is the tip-sample separation (tss), because the cantilever bends towards the surface. Knowing the cantilever deflection and the piezo movement allows tss to be calculated by

$$tss = z_p - \Delta x_z \quad 2.16$$

Plotting the force as a function of tss yields a F-D trace (Figure 2.6, inset). F-D traces contain information about structural transitions of the molecule when stretched (see also section 2.3.2.3). The constant velocity approach is widely used because it is simple and has a wide range of applications.

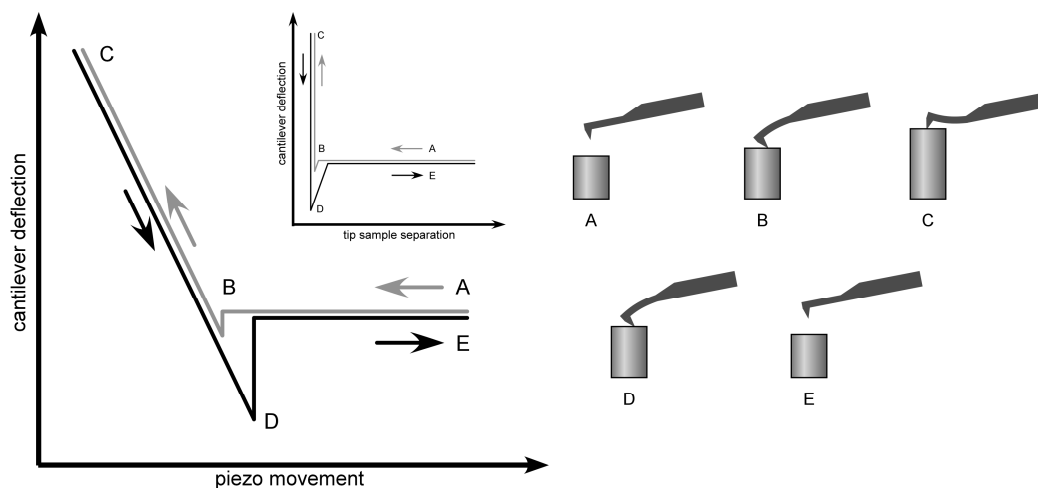


Figure 2.6 SMFS approach-retract cycle. The surface is approached to the cantilever until a certain contact force is reached (A-C). During approach, close to the surface, attractive forces pull the cantilever towards the surface ("snap in", B). After allowing the tip to establish interactions with the sample (C) the surface is retracted from the cantilever. If tip-sample interactions were formed, an increasing stretching force is generated with retraction and the cantilever is bent towards the surface. As soon as the force suffices to break the interaction (D), the cantilever relaxes to its unbent position and is further separated from the surface (E). The inset shows an approach-retract cycle, where the force is plotted *versus* the extension of the molecule (tss , Equation 2.8), thus representing a F-D trace.

Constant Force Force Spectroscopy

In contrast to the constant velocity approach, where the cantilever deflection is a function of time, the constant force approach aims to keep the cantilever deflection and thus the strain on the bond or molecule constant over time [331-333]. As a result of the quick relaxation of the molecule and the cantilever upon unfolding of a protein or a domain thereof the piezo rapidly moves in a non-linear fashion to restore the strain on the molecule. Consequently, information is obtained from the time-dependent piezo position. Each step in the piezo movement *versus* time diagram reflects an unfolding event and is associated with a characteristic step size. This approach allows direct measurement of force-dependent life-times of proteins and their domains. As the applied force is virtually constant during the experiment, the molecule is not subjected to changes in the applied load. The advantage of the so-called force-clamp spectroscopy is counterbalanced by the fact that these machines are in general made up from custom-built analogue electronics [332,333], which hampered the spread of this technique. In chapter 4, this issue will be addressed by implementation of a computer-controlled digital force-feedback, which is easy to set up.

2.3.2.2 Polymer Extension Models

Some of the most important components of a cell, namely proteins, DNA, and RNA, are of polymeric nature, consisting of hundreds to millions of monomers (amino acids or nucleotides). Similarly, polysaccharides, which are used as energy storage and structure-stabilizing components, are polymers composed of sugar molecules. All these polymers are involved in almost every facet of processes that define a living organism. As force is quasi omnipresent, it is tempting to describe polymers, with their large number of degrees of freedom by means of statistical physics to elucidate the restoring forces set up upon tensile stress.

A free polymer in solution tends to acquire a non-structured random coil configuration, which maximizes conformational entropy. Application of force reduces the conformational entropy by aligning the molecule along the direction of force. In the simplest case, backbone bonds are unaffected and work is performed against pure entropic restoring forces. The molecule behaves like an ideal spring, whose spring constant solely depends on the length of a monomer, the Kuhn length (l_K), and the contour length (L_c) of the polymer [334]

$$F(x_{mol}) = 3 \frac{k_B T}{l_K L_c} x_{mol} \quad \mathbf{2.17}$$

where x_{mol} is the extension of the molecule. L_c describes the length of the linearly extended molecule without stretching the polymer backbone [323]. However, this Gaussian model is true for very small extensions $x_{mol} \ll L_c$ and low forces. Different models describe polymer extension at larger extensions and take backbone stretching into account.

Freely Jointed Chain Model

When subjected to a stretching force, the molecule loses its random coil conformation and aligns along the direction of the applied force. This decreases the conformational entropy of the molecule. In the freely jointed chain (FJC) model [335], a polymer is regarded as a chain composed of n independent rigid elements of length l_K that are connected by perfectly flexible hinges (Figure 2.7A). For extensions $x_{mol} < L_c$, Equation 2.18 describes the non-linear extension of a polymer [335]

$$x_{mol}(F) = nl_K \left[\coth\left(\frac{Fl_K}{k_B T}\right) - \frac{k_B T}{Fl_K} \right] \quad 2.18$$

At large extensions ($x_{mol} \approx L_c$) Equation 2.18 fails to describe the extension of the polymer. At increasing forces, bonds and bond angles become distorted and contribute to the overall elasticity. In the extended freely jointed chain (eFJC) model, the rigid segments of the FJC model are replaced by springs with identical spring constants, $\kappa_{segment}$. Thus, Equation 2.18 is extended by an additional term to account for enthalpic restoring forces [336]:

$$x_{mol}(F) = nl_K \left[\coth\left(\frac{Fl_K}{k_B T}\right) - \frac{k_B T}{Fl_K} \right] + \frac{nF}{\kappa_{segment}} \quad 2.19$$

The freely jointed chain model has been successfully applied to model the extension of polysaccharides and synthetic polymers [319,323,337,338].

Wormlike Chain Model

In a more realistic approach, the polymer is modeled as a continuous, elastic curve, a wormlike chain (WLC) [339], without fine structure (Figure 2.7B). The WLC model includes entropic and enthalpic (bending) contributions in the description of the force-extension relationship. It is accurate up to several hundreds of pN and given by [315,320,340]

$$F(x_{mol}) = \frac{k_B T}{l_p} \left[\frac{1}{4} \left(1 - \frac{x}{L_c} \right)^{-2} + \frac{x}{L_c} - \frac{1}{4} \right] \quad 2.20$$

where l_p is the persistence length of the polymer, which describes the rigidity of the polymer and the distance over which the chain orientation is lost [341]. Typically, values for l_p and l_k are specific for each polymer and must be experimentally determined [342]. These parameters also depend on the solvating medium [343]. For polypeptides, a persistence length of 4 Å has been successfully applied to describe the extension at forces larger than 50 pN [313,315]. Although the WLC model accounts for bending elasticity, polymers cannot be stretched beyond their contour length [343]. At elevated forces, chain stiffness has to be considered. In the extended WLC (eWLC), a linear elastic term is introduced [344]

$$F(x_{mol}) = \frac{k_B T}{l_p} \left[\frac{1}{4} \left(1 - \frac{x}{L_c} + \frac{F}{\Phi} \right)^{-2} + \frac{x}{L_c} - \frac{1}{4} - \frac{F}{\Phi} \right] \quad 2.21$$

where Φ is the specific stiffness of the polymer. The wormlike chain model has been used to describe the F-D relationship of polypeptides [315] and DNA ($l_p \approx 50$ nm) [320,340].

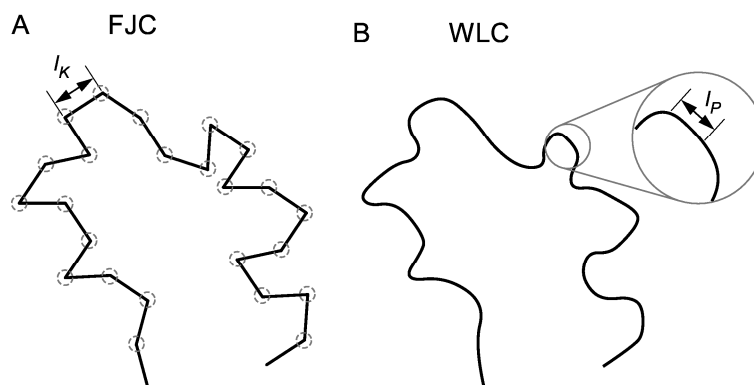


Figure 2.7 Polymer chain models. (A) Freely jointed chain and (B) wormlike chain models of polymer mechanics. The FJC is modeled as a chain of discrete rigid segments connected by flexible hinges. The WLC, in contrast, is described as a continuous elastic medium.

2.3.2.3 Model Systems

Both the FJC and the WLC model predict a monotonically rising force with increasing extension. Discontinuities or deviations from the models point towards rupture of non-covalent inter- and intramolecular bonds or conformational changes of the polymer. Several biological macromolecules, such as DNA, water-soluble and membrane proteins, and polysaccharides as well as synthetic polymers (e.g. polyethylene glycol), have been extensively studied by SMFS. In the following, model systems relevant for this thesis will be described, which are: dextran, the 27th immunoglobulin domain from titin (Ig27), and bR.

Dextran

Dextran is produced by some bacteria and forms slimy capsules surrounding the cells. It commonly consists of $\alpha 1 \rightarrow 6$ glycosidic linked α -D-glucopyranose rings resulting in polymers of largely varying lengths. In a first study, Rief *et al.* showed that dextran molecules exhibit a large enthalpic component in their elasticity, which is marked by a prolonged plateau in the F-D trace (Figure 2.8) [319]. At small extensions (here < 60 nm), almost all pyranose rings are in a 4C_1 chair conformation, which exhibits intrinsic flexibility [345] (Figure 2.8, red eFJC fit with $l_K = 4.7$ Å and $\kappa_{segment} = 13.7$ N/m). As the force reaches ≈ 800 pN the pyranose rings start switching from a chair-like to a boat-like conformation [338]. This chair-boat transition leads to an about 19 % elongation of the dextran monomer and causes the characteristic plateau. After most pyranose rings achieved the boat-like conformation a steep increase in force is detected (Figure 2.8, blue eFJC fit with $l_K = 5.6$ Å and $\kappa_{segment} = 56.8$ N/m) prior to detachment of the molecule. The obtained values for Kuhn length and segment elasticity correspond to previously published data [319,338]. The shapes of F-D traces from dextran but also from other polysaccharides exhibit unique fingerprints, which allow identification of different molecules just by their F-D trace [337].

Since the first experiments, dextran has become an important model system [346-349], because dextran samples can be easily prepared on glass surfaces and F-D traces can be acquired routinely.

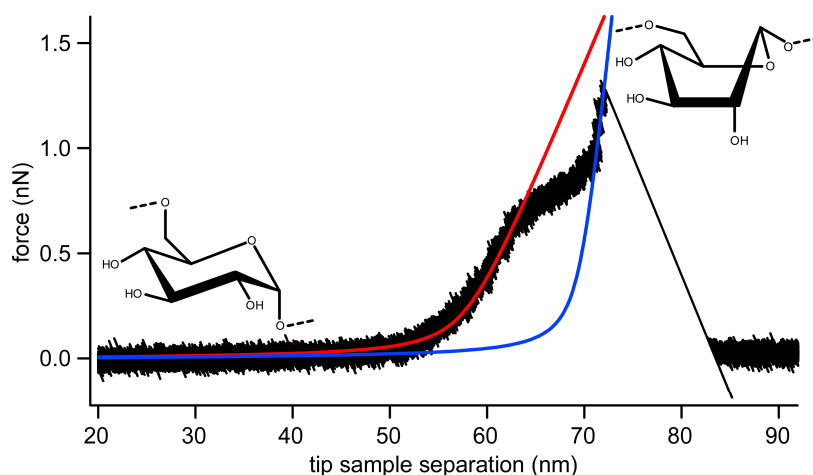


Figure 2.8 Characteristic F-D trace of the polysaccharide dextran. Typical F-D trace recorded while stretching a single dextran molecule. The curve reveals the chair-to-boat transition of the pyranose ring that results in the plateau between 60 and 70 nm extension. The curve is well described by the eFJC model before (red line) and after the transition (blue line) with Kuhn lengths of 4.7 and 5.7 Å and segment elasticities of 13.7 and 56.8 N/m, respectively. The stretched dextran segment comprised 122 monomers. The F-D trace was recorded in PBS at 160 nm/s.

27th Immunoglobulin Domain from the Giant Muscle Protein Titin

The giant muscle protein titin (~3-4 MDa) is composed of long repeats of immunoglobulin-like and fibronectin type III domains. Titin is found in the muscle sarcomere, provides muscle elasticity, and generates passive tension (for recent reviews on titin's physiological function see Refs. [350,351]). In 1997, Rief *et al.* demonstrated in a pioneering experiment force-induced unfolding and subsequent refolding of titin [315]. Rief *et al.* genetically engineered multidomain protein constructs, in which identical domains, Ig27, are repeated. The stretching of such a polypeptide chain at a constant velocity resulted in an increasing force. At a sufficient high force, the structural integrity of one domain breaks, because the hydrogen bond network between two force-bearing β -strands is distorted [352]. This transition from a folded protein domain to an unfolded peptide results in sudden chain elongation and relaxation of the cantilever. In such a multidomain construct, each unfolding event can be attributed to the unfolding of a single domain. F-D traces of multimeric Ig27 exhibit a characteristic saw-tooth pattern with evenly spaced peaks (Figure 2.9).

Since the first experiments, Ig27 has been the protein domain, whose response to force has been the most extensively studied by SMFS [315,332,353-355] and molecular dynamics simulations [352]. Thus, it became the paradigm model for SMFS [356]. Recently, multi-domain proteins, composed of Ig27 or other well studied protein domains, were used to host several proteins for SMFS experiments [357-361].

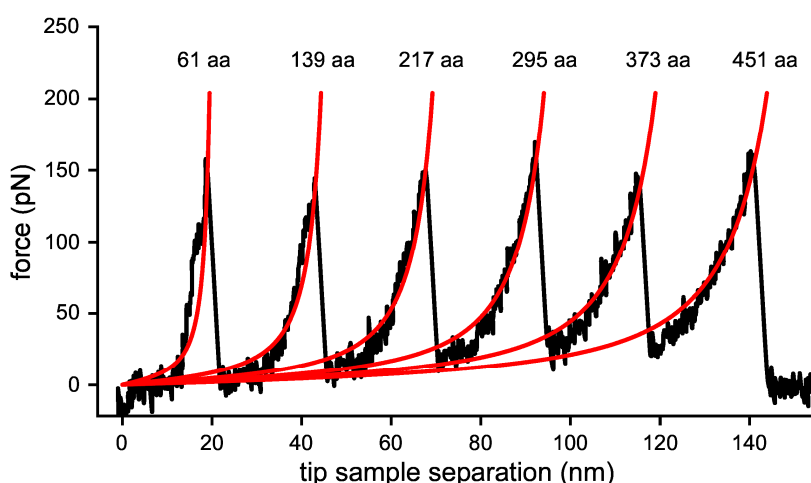


Figure 2.9 Characteristic F-D trace of a multi-domain Ig27 construct. The F-D trace shows unfolding of a pentameric Ig27 construct. Each peak was fitted using the WLC model with a persistence length of 4 Å and an amino acid monomer length of 3.6 Å (red curves); contour lengths of the peaks are given above each fit and are in amino acids. Each peak, except the last one, denotes unfolding of an individual Ig27 domain, which is associated with a contour length increase of 78 aa (28 nm). The last peak represents stretching of the completely unfolded polypeptide and final detachment of the polypeptide from the tip. Sample was adsorbed to freshly exposed template-stripped gold in PBS. Data was recorded at 440 nm/s in PBS. Pentameric Ig27 was a kind gift from A. Smith, Leeds, UK.

Bacteriorhodopsin

In 2000, bR was the first membrane protein studied by SMFS [313]. bR is a light-driven proton pump from *Halobacterium salinarium*, an archaeal organism which lives in high salinity environments [362,363]. Due to a known atomic structure [179,364], an enormous amount of function-related biochemical data [365], and its high availability, bR was an ideal model for this new approach. In these SMFS experiments, single bR molecules withstood forces of up to 200 pN before structural segments unfolded cooperatively [366]. Mechanically induced unfolding occurred along a few highly reproducible, temperature-dependent pathways [366,367]. In combination with further studies of bR mutants [368,369], these SMFS experiments provided valuable information about the interactions that stabilize individual transmembrane segments and fragments thereof. Consequently, this approach has been applied to other integral membrane proteins [311,312,314,370-372].

2.3.2.4 Kinetic Interpretation of SMFS Experiments

SMFS experiments measure the force at which a bond or a protein breaks or unfolds. But what can be extracted from this rather abstract measure about kinetics of the underlying dissociation reaction? Conceptually, SMFS experiments are far from equilibrium, because rebinding or refolding are prevented by rapid separation of the system's constituents. Moreover, unbinding depends on the rate at which force is applied and the duration of loading [373]. Unfolding or unbinding can be considered a two state process, which involves a low energy conformation (e.g. the native state of a protein) and a high energy state (e.g. an unfolded protein) separated by a single energy barrier (Figure 2.10A, black line). The folding and unfolding of many water-soluble proteins can be well explained by such a two state model [374,375]. Unfolding, thus, can be described as a thermally driven over-damped first-order kinetic process in liquid [376,377], whose rate in the absence of force, k_0 , is given by

$$k_0 = \frac{1}{\tau_D} e^{\frac{-\Delta G_0^\ddagger}{k_B T}} \quad \mathbf{2.22}$$

where τ_D is the diffuse relaxation time³³ and ΔG_0^\ddagger is the activation free energy.

Based on Bell's phenomenological model for the off-rate [379], Evans and Ritchie [291,373] showed that the transition rate over a potential barrier depends on the

³³ The exact value of τ_D for protein folding is not known. However, values of 10^{-7} - 10^{-9} s⁻¹ obtained from experiments seem to provide a reasonable estimate [378]. For calculations in this thesis a value of 10^{-8} s⁻¹ was used.

rate of force application. Proteins are, in general, stabilized by non-covalent intramolecular bonds. These bonds have finite life times and will fail under any force (including no force) if given sufficient time. Slow pulling velocities, v_p , result in long life-times but low rupture forces, and high v_p reveal high rupture forces but short life-times [291,380]. Moreover, the location and shape of the transition state are insensitive to force [373], while the height of the energy barrier is lowered according to [379]

$$\Delta G^\ddagger(\mathbf{F}) = \Delta G_0^\ddagger - \mathbf{F}x_\beta \quad 2.23$$

where x_β is the characteristic length scale along the reaction coordinate, with $x_\beta = x_u \cos(\theta)$ (Figure 2.10A). x_u is the distance between the native state and the transition state and θ is the deviation of the reaction coordinate from the direction of force. For small deviations, which are usually the case in AFM experiments, $\cos(\theta) \approx 1$ and $x_\beta \approx x_u$. Combining Equations 2.22 and 2.23 gives

$$k(\mathbf{F}) = \frac{1}{\tau_D} e^{\frac{-(\Delta G_0^\ddagger - \mathbf{F}x_u)}{k_B T}} \quad 2.24$$

where $k(\mathbf{F})$ is the force-dependent dissociation rate which exponentially increases with force scaled by $\frac{x_u}{k_B T}$.

As mentioned before, the rupture force of a bond depends on the rate at which it is loaded with force. The force applied to a bond, in turn, tilts the corresponding energy landscape. Consequently, the force applied to the bond over time (t) has to be described. In the simplest case, a linearly rising force is assumed, where the slope is the loading rate, r_f , which is given by

$$r_f = \frac{d\mathbf{F}}{dt} \quad 2.25$$

Ultra-sensitive force probes allow such a force ramp to be applied to a sample. A force probe (e.g. a cantilever) with a spring constant lower than that of the handles connecting the molecule to tip and surface applies a load that increases at a constant rate and is equal to the product of κ_{cant} and v_p . However, in most cases long flexible linkers, polymer spacers, or already unfolded polypeptide segments, are used as handles to connect molecules to the cantilever tip [315,381]. This results in a non-linear loading of the targeted bond. Still, the loading rate can be approximated from a linear fit to the F-D trace before the rupture event.

Evans and Ritchie showed that the most probable unfolding force, F^* , is a function of $\ln(r_f)$ [291,373]

$$F^* = \frac{k_B T}{x_u} \ln \frac{r_f x_u}{k_B T k_0}$$

2.26

The insets in Figure 2.10 show theoretical dynamic force spectra. Experiments require the most probable rupture force at different loading rates, i.e. pulling velocities, to be measured. Such experiments are known as dynamic force spectroscopy (DFS). Fitting experimental data with Equation 2.26 yield x_u and k_0 , parameters that characterize the energy landscape underlying the unfolding or unbonding reaction.

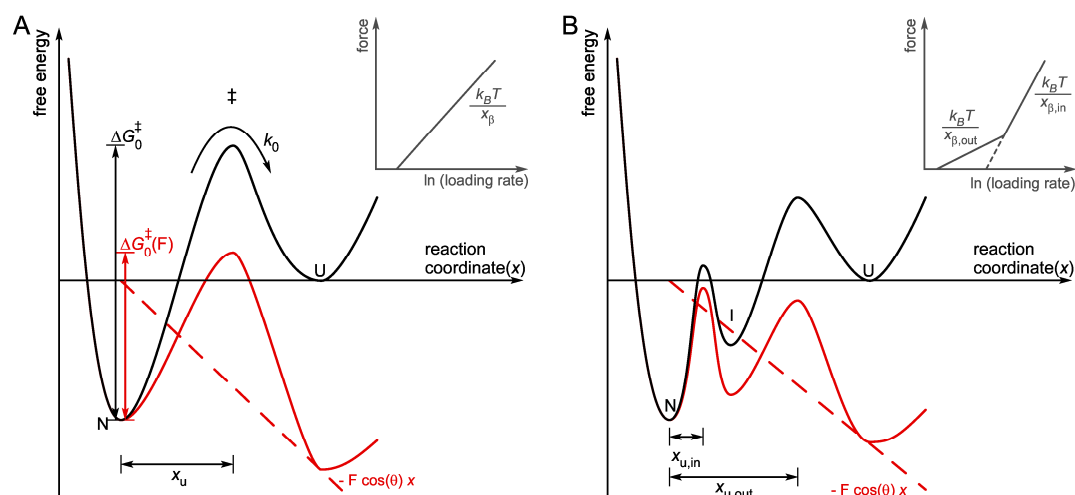


Figure 2.10 Energy landscape projections under externally applied force. (A) Energy landscape of a two state protein (black line). The energy landscape is characterized by a sharp potential barrier separating native (N) and unfolded state (U). The activation energy of unfolding is given by ΔG_0^\ddagger , while x_u represents distance between the native and the transition state (\ddagger) along the reaction coordinate x and provides information about the width of the potential barrier. The energy barrier is spontaneously crossed at a rate k_0 . Application of an external force F adds a mechanical potential $-F \cos(\theta) x$ (dashed red line) that tilts the energy landscape (solid red line). Therefore, the energy barrier is lowered according to Equation 2.23. The inset sketches the theoretical dependence of the rupture force on the loading rate, the dynamic force spectrum, which is governed by a single linear regime, with a slope proportional to $1/x_u$. **(B)** Energy landscape for a three state protein, which passes an intermediate state (I) during unfolding. Two energy barriers at $x_{u,in}$ and $x_{u,out}$ have to be crossed on the way from the native to the unfolded protein. Again, an external potential (dashed red line) tilts the energy landscape (solid red line). At sufficient high force, the outer barrier is suppressed and the inner barrier determines the transition kinetics. The inset shows the corresponding dynamic force spectrum, which has two linear regimes. At slow pulling velocities (and thus lower forces), the outer barrier determines the unfolding kinetics, while at higher pulling velocities (and thus higher forces) the inner barrier becomes dominant.

The smooth energy landscape sketched in Figure 2.10A is an oversimplification. Macromolecular complexes are stabilized by a vast number of individually weak interactions. As a consequence, the energy landscape is rough with energy barriers of different height and width [85,86,89,382]. Dynamic force spectra locate the most prominent energy barriers along the reaction coordinate [291,318]. Figure 2.10B shows the energy landscape of a three state process in which an intermediate state is populated. Along the reaction coordinate, two energy barriers separate the native from

the unfolded state. Similar to the two state process depicted in Figure 2.10A, an external potential tilts the more complex energy landscape. At high loading rates, the outer barrier is lower than the inner barrier, which then governs the unbinding rate. Such an energy landscape results in two regimes in the dynamic force spectrum (Figure 2.10B, inset). Due to the logarithmic dependences of unbinding force on loading rate, it is necessary to cover many orders of magnitude in loading rate, to get a description of the energy landscape.

2.4 WHY USE ATOMIC FORCE MICROSCOPY TO STUDY MEMBRANE PROTEINS?

2.4.1 Imaging Membrane Protein Surfaces at High Resolution

In contrast to other methods used to get structural information about membrane proteins, AFM does not require neither 3D crystallization nor freezing or staining of the sample. Indeed, AFM allows the sample topology to be monitored down to sub-nanometer resolution in a physiological buffer environment at ambient temperature. High-resolution AFM has been extensively used to characterize the surface topology of a variety of membrane proteins, including aquaporins [299,383,384], rhodopsin [385], the bacteriophage $\phi 29$ head-tail connector [302], various archaeal rhodopsins [314,372,386], and photosynthetic complexes [387,388]. High-resolution AFM has been employed to elucidate the stoichiometry of F_1F_0 ATP synthase c-rings from various organisms [389-394] and the diffusion of membrane proteins within the lipid bilayer [395]. Moreover, gating events associated with conformational changes induced by various stimuli have been revealed for OmpZ [396] and gap junction hemichannels [397,398] (chapter 6). High-resolution AFM with its outstanding signal-to-noise ratio allows valuable information that cannot be as easily accessed by other experimental techniques.

2.4.2 Force as an Alternative Denaturant

Protein stability is classically studied using heat or denaturants, such as guanidinium hydrochloride or urea. Pressure and acidification are exploited to shift the equilibrium towards the unfolded state. Force as a "denaturant" is appropriate for "mechanical" proteins, polymers, and complexes, which are under load *in vivo*. Moreover, as outlined in section 1.2.2, methods commonly used to denature water-soluble proteins usually fail to completely unfold membrane proteins, as significant

amounts of secondary structure often remain. In contrast, SMFS drives membrane proteins from their folded into a well defined stretched conformation that lacks secondary structure. Moreover, as a single-molecule technique, SMFS allows unfolding trajectories of individual molecules and rare unfolding intermediates, which are averaged out in ensemble measurements, to be found.

What can we learn from SMFS experiments? SMFS unveils the mechanical stability of (membrane) proteins and stable structural segments within the protein [313,354,360,399]. Moreover, different unfolding pathways and their relative likelihood were determined [311,313,314,367]. Comparative studies allowed interaction sites of ligands and inhibitors to be mapped on transporter proteins [311,400,401]. Similarly, stabilization due to heterodimer formation was detected [371,402]. DFS was used to elucidate the energy landscape of protein unfolding [403-405] or ligand-receptor unbinding [318] and trace changes therein for effects of ligand binding [406] (chapter 5) and point mutations [368,369]. In a further approach the roughness of the unfolding energy landscape of bR was estimated [407]. SMFS has also been applied to study re- and misfolding of water-soluble and membrane protein [312,315,316,355,399,404,408].

A modified SMFS approach, the so-called force-clamp force spectroscopy, subjects a molecule or complex to a constant force. It is used to measure force-dependent life-time distributions. The method has been employed to study unfolding and refolding of water-soluble proteins [331,409,410], the kinetics of disulfide reduction [411,412], and the visco-elastic properties of dextran [348]. Since expensive and complicated custom built electronics are commonly used to achieve fast force-feedback, an easy to build but comparable computer-based solution is desirable (chapter 4).

SMFS measures the stability of single molecules by the resistance to force. But which factors contribute to the stability? Most biomolecular interactions exhibit elastic and viscous forces that sum up to the measured force. The approaches that have been used to decipher the contribution of conservative (elastic) and dissipative (viscous) effects in the unfolding of proteins and stretching of polymers [346-348,413-416] (chapter 3) revealed that (intramolecular) viscosity significantly contributes to molecular elasticity.

VISCO-ELASTICITY OF SINGLE DEXTRAN MOLECULES UNRAVELED BY BROWNIAN NOISE ANALYSIS

3.1 INTRODUCTION

As outlined in chapter 2, the mechanical properties of biological macromolecules play an important role in many fundamental biological processes, including cell adhesion, muscle function, and gene transcription [317,417]. Consequently, optical and magnetic tweezers as well as AFM have been extensively used to address the mechanics of single biomolecules [330]. In conventional force-extension experiments (see section 2.3.2.1), the molecule is tethered between tip and support, and the elastic response of the molecule upon continuous stretching is determined. Importantly, most biomolecular interactions exhibit conservative (elastic) and dissipative (viscous) forces that should be analyzed independently to allow a deeper understanding of their contribution to dynamic biological processes. Extended AFM force spectroscopy experiments have been developed to measure such visco-elastic responses of a wide class of (bio)molecules, including nucleic acids [418], receptor-ligand complexes [419], proteins [415,420], polysaccharides [346,416], and synthetic polymers [421]. In these experiments, the AFM cantilever is sinusoidally oscillated while a single molecule is extended between the tip and the surface. Analysis of amplitude and phase response of the cantilever provides information about resulting elastic and viscous forces. In contrast to the stretching of unfolded proteins, nucleic acids, and poly(ethylene glycol), which is governed by purely elastic interactions [415,418,420,421], the unfolding of secondary structure elements within bR and Ig27 as well as the chair-to-boat transitions in the polysaccharide dextran indicated dissipative interactions [346,415,416,420].

Recently, an alternative approach to determine the visco-elastic properties of single molecules was proposed by Kawakami and co-workers [348]. Instead of using a continuous extension protocol, single dextran molecules were subjected to pre-defined

forces using a feedback loop. Then, the thermal motion of the AFM cantilever during a few seconds was analyzed to obtain the molecules' visco-elasticity as a function of the applied tension. In this chapter, measurement of visco-elastic parameters from the thermal cantilever motion during conventional force-extension measurements will be presented. Dextran was chosen as a model system for this study because its visco-elastic properties have been extensively studied [346-348,416].

3.2 EXPERIMENTAL PROCEDURES

3.2.1 Sample Preparation

Dextran (average molecular weight 2 MDa) was purchased from Sigma. 200 μ l of a 5 % (w/w) dextran solution in nanopure water (≥ 18 M Ω , purelab ultra, ELGA LabWater) were allowed to dry in air at 37 °C on glass cover slips which were glued to 12 mm diameter steel discs. Samples were then rinsed for 1 minute under a flow of nanopure water. Experiments were performed in 150 mM KCl, 10 mM Tris, pH 7.8 at 160 nm/s pulling velocity.

3.2.2 AFM Instrumentation

A commercial AFM (Nanoscope IIIa equipped with PicoForce scanner and module, Veeco, Santa Barbara, CA, USA) was extended with a PC equipped with 16-bit data acquisition electronics (E-6052, National Instruments, Munich, Germany). The cantilever deflection signal was first low-pass filtered at 100 kHz by a passive hardware filter to avoid aliasing and then digitized at 300 kHz using IgorPro (Wavemetrics, Lake Oswego, OR, USA) (Figure 3.1). Spring constants of the cantilevers, k_{cant} , were calibrated in buffer using thermal fluctuation analysis (section 2.2.2.4). The cantilevers used were the short thin-legged NP-S and Microlever B from Veeco, the short OMCL-TR 400, the BioLever A (BL-RC150 VB), and the "BioLever mini" (BL-AC40TS) [422] from Olympus (Tokyo, Japan). Cantilever specifications are given in Table 3.1.

cantilever	shape*	length (μ m)	width (μ m)	thickness (μ m)	approx. k_{cant} (N/m)	approx. ν_0 (kHz)**
NP-S	v	115	17	0.6	0.31	13
MCLT-B	r	200	20	0.6	0.04	3.5
OMCL-TR 400	v	100	15	0.4	0.10	8
BioLever A	r	60	30	0.18	0.05	10
BioLever mini	r	38	16	0.2	0.12	30

Table 3.1 Specifications of the cantilevers used for experiments. * Cantilevers were either V-shaped (v) or rectangular (r). ** The approx. resonance frequency of the cantilever in buffer solution is given.

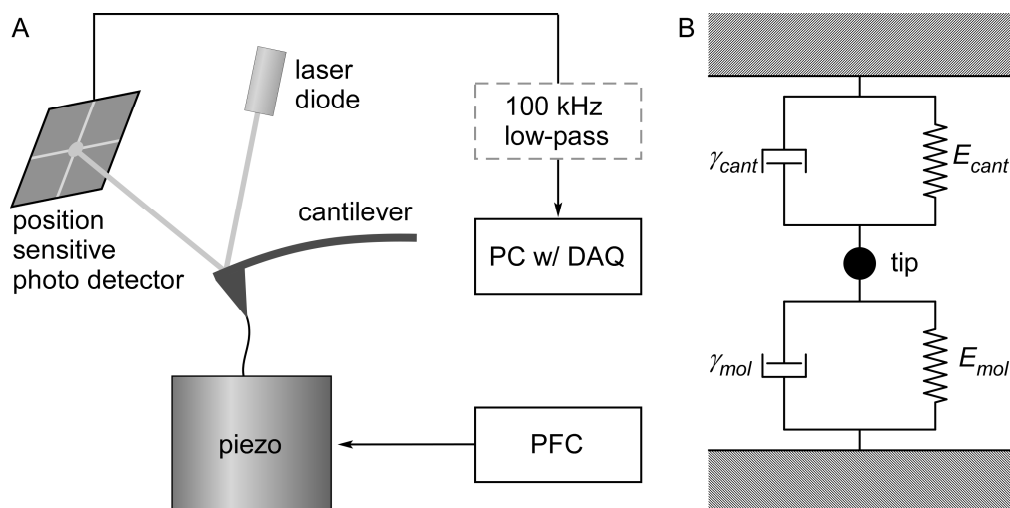


Figure 3.1 Scheme of the extended AFM setup. (A) A commercial PicoForce AFM (PFC) with a beam deflection detection system was extended with a PC and additional data acquisition hardware (DAQ). The signal was low-pass filtered prior to acquisition. The PFC was used to drive the piezo during conventional force-extension experiments. (B) Molecule and cantilever were treated as two independent Voigt-Kelvin elements (each composed of a spring and a dashpot) acting in parallel on the AFM tip, where the cantilever motion is monitored.

3.2.3 Extracting Visco-Elastic Properties

Deflection curves were analyzed using custom macros and built-in features of IgorPro. The curves were first high-pass filtered at 400 Hz (also to reduce contributions of $1/\nu$ noise) and then divided into windows of equal length. Each window was processed by calculating the power spectral densities (PSD) from segments of 512 points applying a Hanning-type window function and allowing a 50 % overlap of the segments. Thus nine Fourier spectra were averaged for each 8.3 ms raw data window (Figure 3.2 and Figure 3.6) and the resulting PSD were fitted with Equation 3.2. Calculation and fitting of the PSD was independently double-checked using the thermal tune function of the AFM and Origin software (Northampton, MA, USA). To obtain the molecular visco-elastic response according to Equations 3.3-3.5, the visco-elasticity curves recorded during surface approach were smoothed and subtracted from the corresponding visco-elasticity curves recorded during surface retract as has been recently described [415].

3.3 RESULTS AND DISCUSSION

3.3.1 Extraction of Visco-Elastic Parameters

In contrast to the force-clamp technique recently introduced by Kawakami and co-workers [348], here the thermal cantilever motion was analyzed as a function of tip-sample separation while a molecule was stretched between the tip of the cantilever and the sample surface. A schematic of the AFM setup used is shown in Figure 3.1A. The force curve shown in Figure 3.2A was recorded while stretching a dextran molecule and, thus, exhibited the characteristic force-extension pattern [319,338] discussed in section 2.3.2.3 - Dextran. Briefly, the plateau at forces around 0.8 nN is caused by a force-induced chair-boat transition of the glucopyranose rings, which leads to elongation of the whole molecule.

As a first step in the analysis, the thermal cantilever motion was extracted from the force curve using offline high-pass filtering. Then the curve was divided into small windows (Figure 3.2B, boxes) and for each window the thermal noise PSD was calculated (Figure 3.2C, D). According to the simple harmonic oscillator model [297,423], the motion of a thermally excited AFM cantilever can be described by the following differential equation

$$E\ddot{x}_z + \gamma\dot{x}_z + m\ddot{x}_z = F_{thermal}(t) \quad 3.1$$

in which $F_{thermal}(t)$ is the stochastic thermal force, x_z denotes the tip displacement, E is the elasticity, γ the damping coefficient, and m the effective mass of the cantilever-molecule system. This simple model then allows E , γ , and m to be obtained from the PSD according to [423,424]

$$\langle |x(\nu)|^2 \rangle = \frac{4k_B T \gamma}{[E - m(2\pi\nu)^2]^2 + \gamma^2 (2\pi\nu)^2} \quad 3.2$$

where $\langle |x(\nu)|^2 \rangle$ is the frequency (ν) dependent PSD. Since the motion of the cantilever is detected at its tip, the cantilever and the molecule were considered as two independent Voigt-Kelvin elements acting in parallel (Figure 3.1B) [425]. Consequently, the visco-elastic properties of the system can be expressed by

$$E = E_{cant} + E_{mol} \quad 3.3$$

$$\gamma = \gamma_{cant} + \gamma_{int} \quad 3.4$$

$$m = m_{cant} + m_{mol} \quad 3.5$$

where the index *cant* denotes the quantities associated with the untethered, free cantilever. The molecule contributes linearly (E_{mol}) to the system's elastic modulus E , and with its effective mass m_{mol} to the total mass m . The damping coefficient is

decomposed into the initial contribution of the cantilever γ_{cant} , and the contribution γ_{int} arising from the interaction. Conceptually, γ_{int} contains the dissipation by the molecule itself as well as damping induced by the altered boundary conditions at the tip (partially clamped end) [426]. It was shown that E_{cant} , γ_{cant} , and m_{cant} are readily extracted from the motion of a free cantilever and allow hydrodynamic and surface effects to be excluded [415,424]. Thus, by applying Equations 3.2-3.5, E_{mol} , γ_{int} , and m_{mol} are obtained. In the following, the discussion will focus on the visco-elastic response of the molecule (elastic modulus and damping coefficient) since a change in effective mass is not detected in single-molecule manipulation experiments³⁴ [347,348,425].

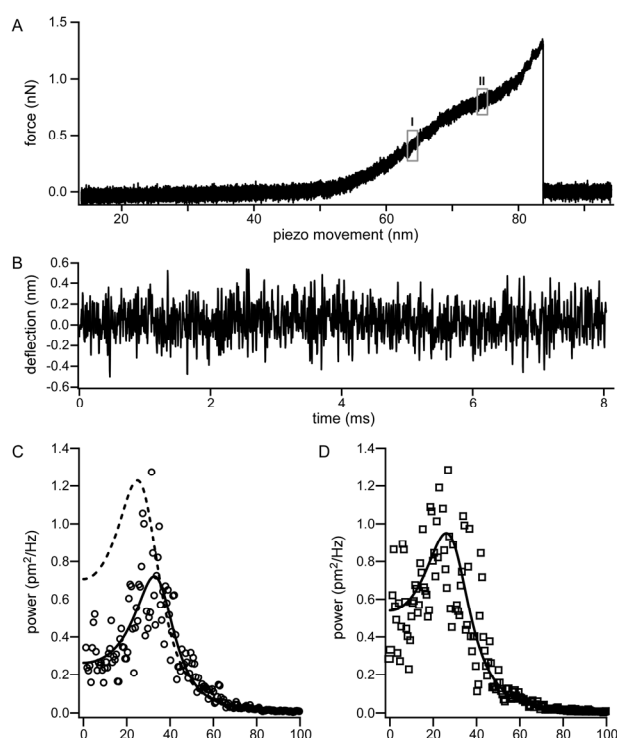


Figure 3.2 Analysis of thermal cantilever motion in a force-extension experiment. (A) Typical force trace of a single dextran molecule recorded with a BioLever mini, exhibiting the characteristic plateau at forces of ≈ 0.8 nN. As an example, the analysis of two segments (marked I and II) is shown in (B-D). (B) Time-series of the deflection signal of window I after high pass filtering. (C), (D) PSDs calculated from the deflection in windows I (circles in C) and II (squares in D). The PSDs are well described by fitting with Equation 3.2 (solid lines) and reveal the visco-elastic properties of the system at that specific instance. The dashed line in C represents a fit to a PSD calculated from the deflection of a free cantilever 160 nm above the surface.

3.3.2 Measurement Noise Depends on Window Size and Cantilever Type

To evaluate the effect of the window size on the signal-to-noise (S/N)-ratio of the experiments, force-extension curves, where no molecule had attached to the AFM tip, were analyzed. For these curves, the peak noise in the elasticity and damping coefficient was measured along the tip-sample separation in a range between 0 and 160 nm. One should note that there is a negligible dependence of the elasticity and damping coefficient on tip-sample separation in this range (Figure 3.3). As expected, this analysis showed that the peak noise in the elasticity and damping coefficient depended on the size of the window (Figure 3.4). Increasing the window size increases

³⁴ The effective mass of an oscillating cantilever in liquid is $> 10^{-12}$ kg. A single 2 MDa dextran molecule attached to a cantilever would cause a mass increase of about $3 \cdot 10^{-21}$ kg.

the time period available to calculate the frequency components of the motion of the cantilever, and thus results in reduced noise (Figure 3.4A, C) and, consequently, a better apparent S/N-ratio (Figure 3.4B, D).

Interestingly, the S/N-ratio depended on the type of AFM cantilever used. In Figure 3.4, the results of five types of cantilevers are shown. These cantilevers differ in their dimensions, spring constants, and resonance frequencies (see Table 3.1). Choosing

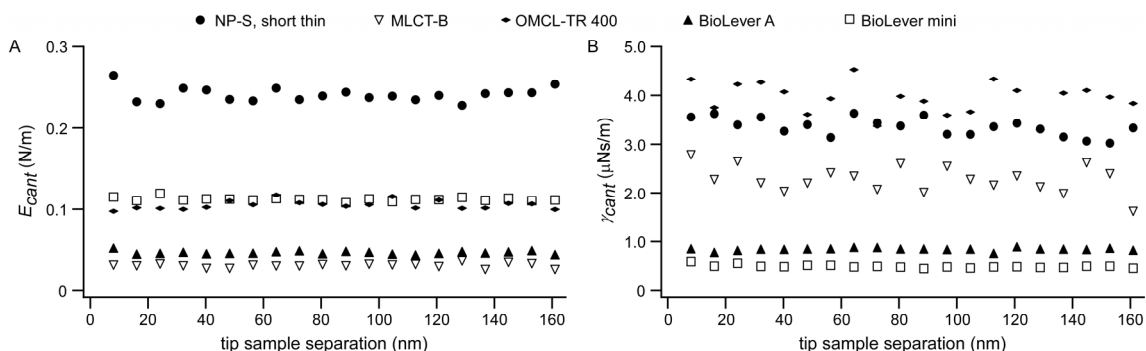


Figure 3.3 Distance dependence of visco-elastic parameters. The elasticity (A) and damping coefficient (B) of five cantilever types are shown as a function of tip-sample separation. Curves were recorded at 160 nm/s pulling velocity on a dextran surface and analyzed using a window size of 50 ms. The traces show no significant distance dependence of the elasticity and damping coefficient in the range of tip-sample separation studied here.

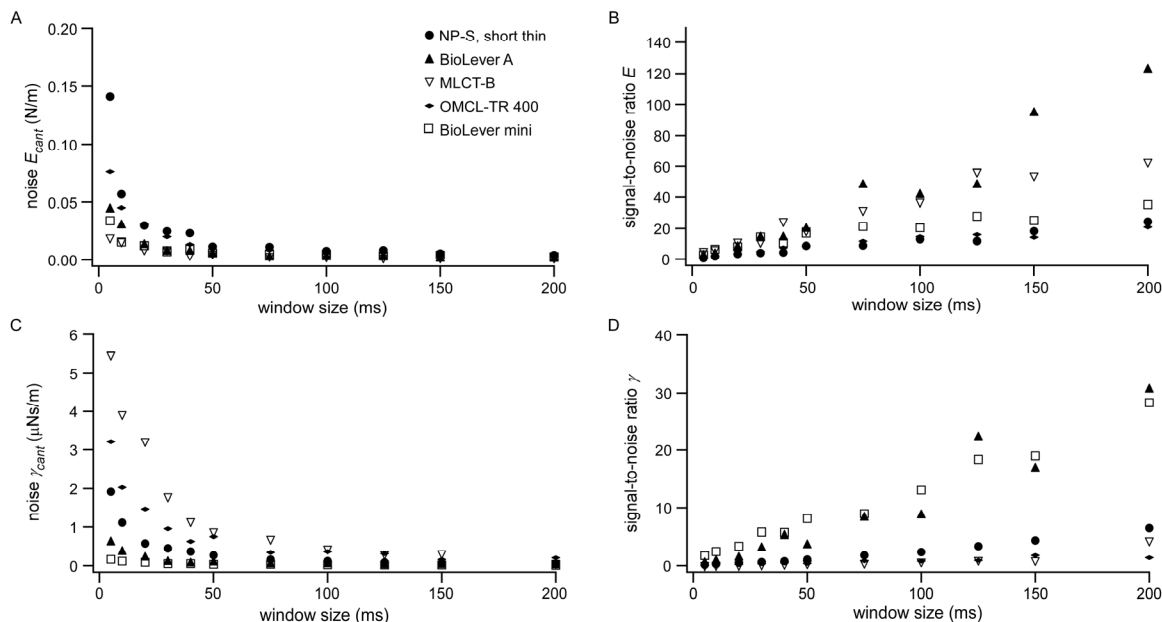


Figure 3.4 Signal-to-noise ratio depends on window size and cantilever type. The noise in measurement of elasticity (A) and damping coefficient (C) is shown for five different cantilevers as a function of the window size. As expected, increasing the time available for monitoring the cantilever motion and calculating the PSD reduces the noise. The apparent signal-to-noise ratios were calculated by comparing a peak elasticity and damping of $E_{mol} = 100$ pN/nm and $\gamma_{int} = 0.3$ μ Ns/m with the noise values from (A) and (C). While all cantilevers showed a similar performance in elasticity measurements (B) the damping information (D) could only be extracted from the measurements using the small rectangular cantilevers (BioLever A and BioLever mini).

a novel small cantilever (BioLever mini) with high resonance frequency (≈ 30 kHz in solution) significantly improved the S/N-ratio of the dynamic measurements. While all cantilevers had similar performance in measuring the elasticity (Figure 3.4A, B), only the BioLever mini had a sufficiently good S/N-ratio to resolve damping coefficients (Figure 3.4C, D). One probable reason for the better S/N-ratio of the BioLever mini is its significantly higher resonance frequency. However, other size-dependent effects must be responsible for the drastic difference in S/N-ratios. To further investigate this phenomenon, the noise of five types of cantilevers that span a wide range of sizes and resonance frequencies (see Table 3.1), was determined at a fixed window size of 75 ms and plotted as a function of cantilever damping coefficients and resonance frequencies (Figure 3.5). These data highlight that the damping coefficients and thus the size of the cantilevers have a very strong influence on their dynamic S/N-ratio. For the polysaccharide dextran, a reasonable trade-off between S/N-ratio and time-resolution was achieved using the BioLever mini and a window size of 8.3 ms. At a pulling speed of 160 nm/s per second, this window size yields one dynamic measurement every 1.3 nm. If the pulling speed is reduced tenfold (to 16 nm/s) as in a recent paper by Kawakami *et al.* [347], one could obtain one measurement per 1.3 nm with an improved S/N-ratio by a factor of \approx five.

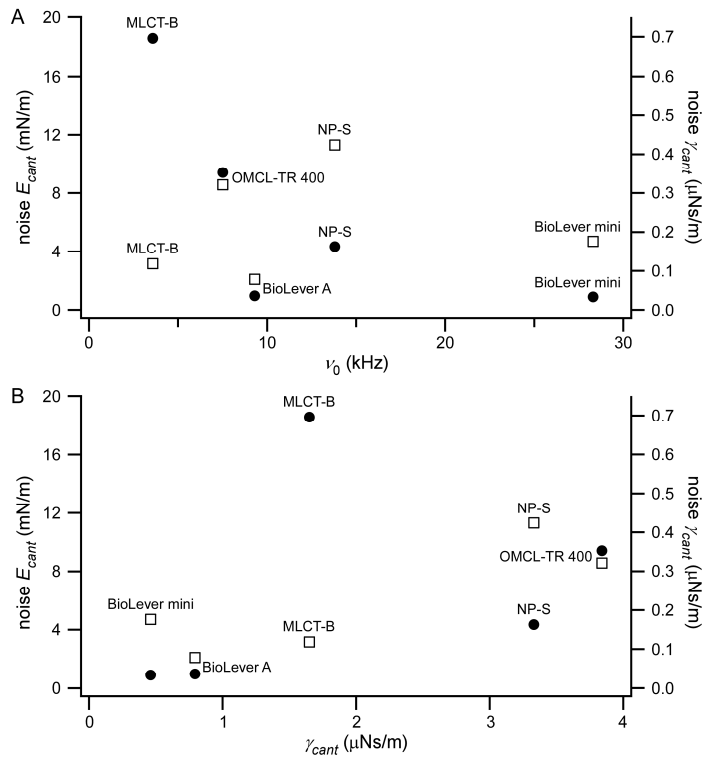


Figure 3.5 Cantilever sensitivity depends on resonance frequency (A) and cantilever damping (B). The peak noise in elasticity (open squares) and damping (filled circles) measurements was determined for different cantilevers, which are described in detail in section 3.2.2. Curves were recorded at 160 nm/s pulling velocity and analyzed as described for Figure 3.4 with a window size of 75 ms. Evidently, the noise of the cantilevers increases with size and damping but decreases with increasing resonance frequency. The damping coefficients of the cantilevers used for the abscissa in (B) were recorded 160 nm from the surface.

3.3.3 Visco-Elasticity of Dextran

Figure 3.6 shows the elasticity and damping coefficients associated with two dextran molecules. For direct comparison with the results obtained using other approaches, E_{mol} and γ_{mol} were plotted as a function of the applied force (Figure 3.6A, C). The curves were normalized to show the monomeric elasticity (E_{mon}) and damping coefficient (γ_{mon}) (Figure 3.6B, D), as has been recently described [347]. This is necessary as the extended dextran fragments typically differ in lengths and E_{mol} and γ_{mol} reciprocally scale with dextran length. The molecular response revealed the typical visco-elastic behavior of single dextran molecules undergoing the chair-boat transition. At an applied force of ≈ 0.3 nN, an increase in E_{mol} and γ_{mol} due to the stretching of the polysaccharide chain was observed. Broad maxima in E_{mol} and γ_{mol} were reached at a force of ≈ 0.6 nN before a decrease during the chair-boat transition. As at the low-force regime, further stretching of the polysaccharide chain increased E_{mol} and γ_{mol} . Thus, spring constant and damping factor increase along with increasing force and molecular extension. Hydrodynamic friction between fluid and polymer could be one source for increasing damping factors. If that was true, the damping factor would rise by

$$\gamma_{int} \approx 6\pi\eta_f \Delta x_{mol}(F)$$

3.6

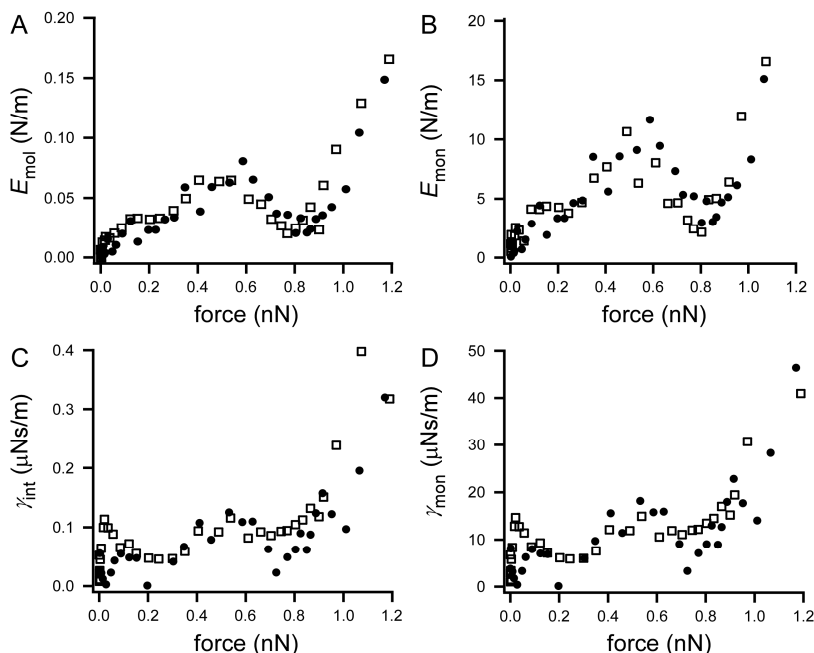


Figure 3.6 Dynamic response of single dextran molecules. The molecular elasticity (A) and damping coefficient (C) of two single dextran molecules are shown as a function of the applied force. The two molecules stretched had lengths corresponding to 145 (filled circles) and 129 (open squares) monomers and show the typical visco-elastic behavior of dextran. Broad maxima in the elasticity and damping are detected at a force of ≈ 0.6 nN prior to a decrease in elasticity and damping due to the chair-boat-transition. In (B) and (D) the curves from (A) and (C) were multiplied with the number of monomers to yield the response of an individual pyranose subunit.

where $\Delta x_{mol}(F)$, the force-dependent molecule extension, represents the effective hydrodynamic radius of the polymer [348]. This dependence is clearly not observed. Moreover, at molecular extensions of ≤ 100 nm typical for the experiments presented here, the damping factor should be in the order of 10^{-9} Ns/m, which is two orders of magnitude lower than the damping factors observed. Consequently, friction is supposed to originate from internal conformational changes [348]. More precisely, the rough energy landscape of dextran, which is due to the multitude of possible conformations of the pyranose ring, seems to be responsible for high local friction [427]. As mentioned above the visco-elastic properties of single dextran molecules measured are in good agreement to those previously reported [347,348].

Here, the (molecular) relaxation time, τ , which is given by the ratio of interaction-induced damping and elasticity following $\tau = \frac{\gamma_{int}}{E_{mol}}$, has been calculated (Figure 3.7).

Surprisingly, there is no clear dependence of the relaxation time on the applied force. In theory, the structural transition should be accompanied by a peak in the relaxation time [427], just as was observed for unfolding of bR [415]. In addition, the relaxation times found for dextran are much smaller than those of individual membrane proteins [415] although one would expect similar values.

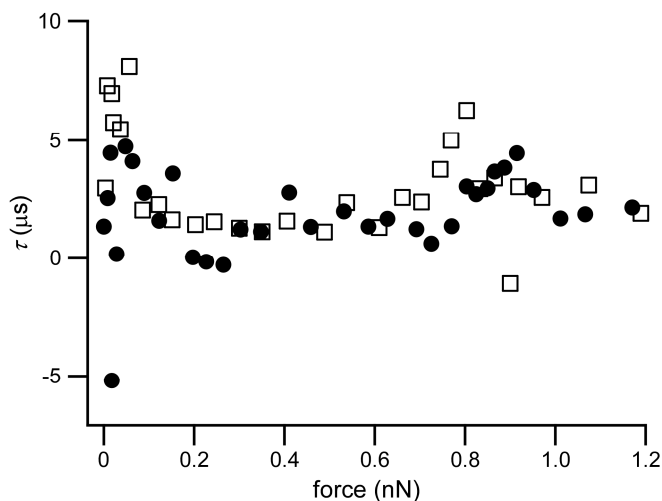


Figure 3.7 Molecular relaxation times calculated for the two dextran molecules of Figure 3.6. Unexpectedly, there is no clear dependency on the applied force and no maximum near 0.6 nN is visible.

Importantly, it seems that the molecular damping coefficients correlate with the molecular elasticities (Figure 3.6 and Figure 3.7). As mentioned above, such coupling of elastic and viscous interactions could indicate direct crosstalk of the elastic component into the apparent damping behavior [426].

3.4 CONCLUSIONS

The past decade has seen a dramatic increase in our understanding of the mechanical properties of biological macromolecules and their roles in biological processes [317,417]. In single-molecule force-extension experiments, researchers have studied the mechanical properties of biomolecules in response to external pulling forces [334,417,428]. In this chapter, it has been shown that the apparent dynamic visco-elastic properties of single bio-molecules can be calculated from the thermal motion of the AFM cantilever during conventional force-extension experiments. The results presented are in good agreement with those recently reported [347,348] but have been acquired with a time resolution of less than ten milliseconds. This is at least one order of magnitude faster than other experimental approaches that are based on the analysis of the PSD of cantilever motion [347,348]. Since the proposed approach only requires choice of the proper type of cantilever it could be directly applied to study protein and RNA unfolding and the dynamic properties of complex biomolecular systems.

DIGITAL FORCE-FEEDBACK FOR SINGLE-MOLECULE FORCE-CLAMP SPECTROSCOPY ON PROTEINS

4.1 INTRODUCTION

Protein folding is a challenging topic in biological research. For decades ensemble methods have been used to unravel the mechanisms and interactions underlying protein (un-)folding [429]. Albeit providing a plethora of information about the folding process, these methods represent an averaged view of the processes. Therefore, it is difficult to characterize rarely populated (un-)folding intermediates that, as a consequence of multidimensional folding funnels, are likely to occur in some of the multiple folding pathways (see section 1.2.1.1). New methodological approaches tackle this intriguing task.

Single-molecule techniques provide information on protein (un-)folding and reveal reaction pathways that cannot be revealed by ensemble measurements [428]. SMFS, as one of these techniques, probes both single water-soluble and membrane proteins to gain insights into e.g. the relative population of various (un-)folding pathways, energy landscapes, and interactions stabilizing the native protein (see section 2.4.2). In conventional SMFS, a protein is stretched at a constant velocity and the unfolding of domains results in a saw-tooth F-D pattern. DFS experiments, where the loading rate is modulated by varying the pulling velocity, are used to characterize the energy landscape (see section 2.3.2.4) that governs the mechanical behavior of complexes [318] or (membrane-)proteins [403,405,406]. In these experiments the force applied changes with time because the molecular handles (e.g. already unfolded polypeptide segments) used to tether the molecule between tip and support act as a non-linear entropic spring. For this reason, the loading rate experienced by the molecule is not constant during the experiment and complicates data interpretation.

Lately, Fernandez and co-workers introduced an alternative approach, the so-called force-clamp technique. Therein, a constant force is applied to a bond, complex,

or protein using an AFM-based force-clamp apparatus [331-333,410,412,430]. The life time of a bond or protein decays exponentially with the applied force [333,410,412]. The advantage of this technique is that life times and, maybe more importantly, life time distributions can be directly measured at well-defined loads [430]. Furthermore, force-clamping enables new kinds of experiments such as monitoring folding trajectories of single proteins under force to be performed [331,410].

In contrast to conventional SMFS, where the piezoelectric actuator is retracted from the tip with a constant velocity, force-clamp experiments require the surface to move in a cantilever force-dependent manner. Thereto, the cantilever deflection is monitored and compared to a user-defined set-point. The difference, the error signal, is fed into a feedback controller that adjusts the position of the piezoelectric actuator to reduce the difference. High-performance force-clamp instruments are typically custom-made and use custom analogue electronics for feedback control [332,333,410,412]. At the same time as the developments presented in this chapter were initiated, a software-based proportional-integral-differential (PID) controller was proposed [348]. Unlike analogue force-clamp machines, this instrument responded slowly to setpoint changes.

In this chapter, a simple, fast, and all-digital feedback loop system for use in force-feedback single-molecule experiments is presented. The performance is demonstrated by unfolding a protein construct consisting of five Ig27 domains (Ig27₅) and the integral membrane protein Na⁺:H⁺-antiporter NhaA from *Escherichia coli*. Importantly, it will be demonstrated that the system is capable of easily combining constant-velocity SMFS with the force-feedback mode and performing complex experimental cycles that include extending, relaxing, and holding single molecules.

4.2 EXPERIMENTAL PROCEDURES

4.2.1 Support Preparation

Steel discs of 12 mm diameter were etched for 1 min in concentrated hydrochloric acid, rinsed with deionized water, and cleaned with ethanol. Subsequently, teflon coated polyethylene foil patches 13 mm in diameter were glued to the steel discs using Loctite 406 superglue. Mica discs of 6.4 mm diameter were manually punched from large mica sheets and glued to the steel-supported teflon foil using Araldit Rapid (Carl Roth, Karlsruhe), a two-component adhesive. Before the experiments, layers of mica were cleaved off using adhesive tape. Thus, a clean and

over several hundreds of square micrometers atomically flat surface was exposed that was suitable for sample adsorption.

Template-stripped gold [431,432] was prepared by depositing a thin layer of gold onto freshly cleaved mica sheets using a SCD 050 sputtering device (Bal-Tec, Balzer, Principality of Liechtenstein). Gold layer deposition was performed at ambient temperature. Afterwards, the mica sheet was cut into small squares of ~ 12 - 15 mm size. Gold pieces were glued to HCl-etched steel discs with the gold surface facing the steel disc using Epo-Tek 377 (Polytec PT, Waldbronn) and cured at 150 °C for 1 h. Prior to experiments, the mica surface was mechanically removed, exposing a clean, flat gold surface.

4.2.2 Sample Preparation

Engineered Ig27_s [433], was adsorbed to template-stripped gold for 25 min in PBS (138 mM NaCl, 2.7 mM KCl, 10 mM phosphate, pH 7.4) buffer. AFM experiments with Ig27_s were performed in PBS. Native purple membrane from *H. salinarium* [434] was adsorbed to freshly cleaved mica in 300 mM KCl, 20 mM Tris-HCl, pH 7.8 [287]. This buffer solution was also used for the bR experiments [313]. Two-dimensional crystals of NhaA [435] were immobilized on freshly cleaved mica in 150 mM KCl, 10 % (v/v) glycerol, 25 mM K⁺-acetate, pH 4.0 for 20 min. Experiments on NhaA were performed in buffer solution containing 150 mM KCl, 50 mM NaCl, 20 mM Tris-HCl at pH 7.7. After AFM imaging of immobilized membrane protein patches an unperturbed area was selected to unfold individual proteins. The proteins used were kind gifts from D. A. Smith (Ig27_s), Leeds, D. Oesterhelt (bR), Munich, and C. Ziegler (NhaA), Frankfurt.

4.2.3 Force Spectroscopy Measurements

A commercial AFM (PicoForce, Nanoscope IV, Veeco, Santa Barbara, USA) was extended with two server-grade PCs equipped with 16 bit data acquisition electronics (E-6036 and M-6259, National Instruments, Munich, Germany) (Figure 4.1). For data capturing, the deflection and the z-piezo signal were digitized at 10 kHz using the M-series card and IgorPro 5.0 (Wavemetrics, Lake Oswego, USA). For force-feedback control, the deflection signal was first low-pass filtered at 1 kHz using a low noise pre-amplifier (SR560, Stanford Research, Sunnyvale, USA) before it was digitized and processed in the software-based PID controller (see below). To avoid two nested

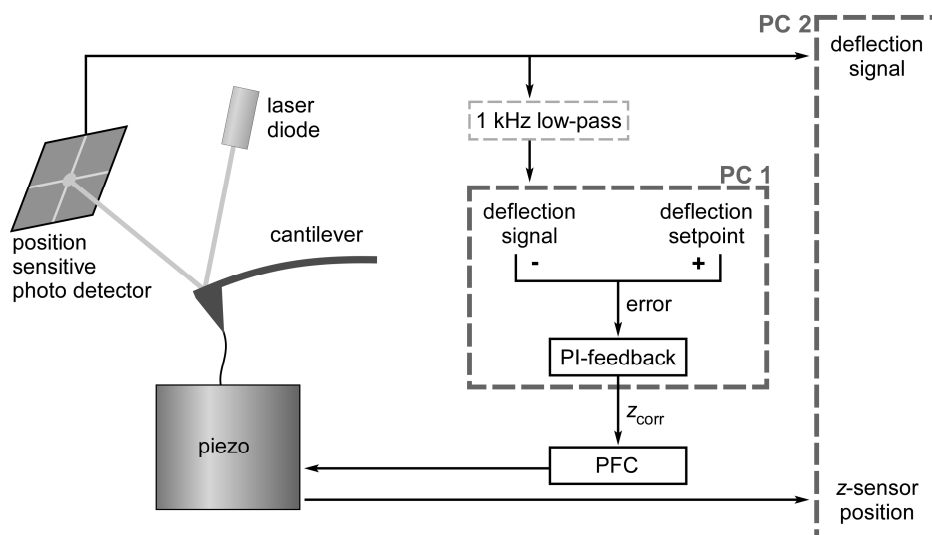


Figure 4.1 Schematic of the extended AFM setup for force-feedback control. The setup is based on a commercial PicoForce AFM. The signal from the photo detector was low-pass filtered and digitized in PC 1. The error between the deflection setpoint and the deflection signal was calculated and fed into the PI-controller. The resulting z -position correction signal, z_{corr} , was used to drive the z -piezo through the PicoForce AFM controller (PFC). PC 2 simultaneously acquired the deflection signal from the photo detector and the z -position signal from the capacitive sensor of the z -piezo.

feedback loops, the z -feedback loop of the commercial AFM was deactivated during the experiments.

For all force spectroscopy experiments V-shaped 100 μm long SiN_3 cantilevers with nominal spring constants of 90 pN/nm (OMCL-TR 400, Olympus, Tokyo, Japan) were used. The spring constant of each cantilever was measured in liquid using thermal fluctuation analysis [293,436] (see section 2.2.2.4) prior to experiments. Proteins were attached to the AFM tip by pushing it onto the surface with a contact force of 1 to 2 nN for 1 to 2 s. Although the nature of the resulting attachment is unknown, it is sufficiently strong to withstand stretching forces of ~ 2 nN [312-315,366,370,437-439]. After attachment, the cantilever was retracted 10 to 25 nm from the surface with a speed of 500 nm/s to overcome non-specific tip-surface interactions. Beyond this distance a defined force was applied to the protein molecule using the force-clamp mode. After a force-clamp measurement, the cantilever was separated another 400 nm from the surface to ensure that molecules still bound to the AFM stylus were detached. To reduce noise and thermal drift of the system, a glass bell was used to isolate the AFM from acoustic noise and temperature variations. In addition, the microscope was allowed to equilibrate for at least 1 h.

4.2.4 Data Analysis

Data analysis was performed using IgorPro 5.0. For Ig27₅, life times of structural intermediates were determined by measuring the length of the plateaus between the initial loading (Figure 4.2A, beginning of stage 1) and rupture events. For membrane proteins, such as NhaA, the life time was measured differently. As membrane proteins are anchored within the lipid membrane, the force is exclusively applied to structural elements directly connected to the cantilever tip. Other structural elements are not loaded until preceding elements unfold. Hence, the life time of a structural segment is the time between two consecutive rupturing events.

4.2.5 Software-Based PI(D) Controller

The PID controller was entirely software-based and programmed in IgorPro 5.0. The deflection signal from the microscope was low-pass filtered with a cut-off frequency of 1 kHz and acquired at 10 kHz in a voltage range from -5 V to +5 V using the E-series card (Figure 4.1). The deflection signal of the free cantilever was determined before each experimental cycle and served as the zero-force reference. In the feedback mode, the deflection signal was continuously monitored by a *do-while* loop. During each feedback cycle, the proportional error (P) between the set-point and the actual deflection was obtained by calculating the difference between the two values. The mean of the error (P) and the error calculated in the preceding cycle gave the integral error (I). The differential error (D) was the difference of the error (P) and the preceding error. The correction value for the z-piezo position, z_{corr} , is then given by

$$z_{corr} = pg \cdot P + ig \cdot I + dg \cdot D \quad 4.1$$

where pg , ig , and dg denote the proportional, integral, and differential gains, respectively. The gains are weighting factors that were adjusted experimentally. Each *do-while* loop took $\sim 200 \mu\text{s}$ to be completed, thus allowing the controller to update the z_{corr} signal at $\sim 5 \text{ kHz}$.

In the experiments shown here, dg was set 0, which lead to a PI-controller that was easier to tune. To prevent overshooting while compensating for large errors, an anti-reset-windup function was introduced. It sets $I=0$ if P was larger than a pre-defined threshold. The threshold value was adjusted empirically.

4.3 RESULTS AND DISCUSSION

4.3.1 PI(D)-Controller

A force-clamp apparatus was built around a commercial AFM through extension with two server-grade PCs for data acquisition and feedback control (Figure 4.1). The performance of any feedback controller depends on fine-tuning of the system, i.e. careful adjustment of the gains. Here, the differential gain, dg , was set to 0, simplifying the system as only proportional and integral gains had to be adjusted. Albeit differential control reduces overshooting, it hypersensitizes the system to oscillatory behavior, which makes it problematic to implement in AFM applications. Indeed, overshooting was observed in the first tests. This overshooting could be reduced by either lowering the gains and thus slowing down the response time of the system, or introducing an anti-reset-windup that activates the integral control only in the vicinity of the set-point. The latter almost completely eliminated overshooting while keeping the response time short (Figure 4.2A, inset). Proportional and integral gains were adjusted by evaluating the feedback performance in terms of response time and settling behavior.

For fine-tuning, unfolding events of Ig27 and NhaA were analyzed. Figure 4.2A shows a representative time-course of force and molecular extension (red and blue traces) for Ig27⁵. The unfolding of each Ig27 domain increased the molecule's length and shortly decreased the force applied to the molecule. The latter is caused by the finite response time of the feedback loop, i.e. the time needed to reach the force set-point. Analysis of such unfolding events revealed that the typical response time is in the order of ~ 6 ms (Figure 4.2A, inset), which is comparable to the performance of the custom-built analogue systems [333,412]. Occasionally, faster response times (> 3 ms) could be observed. Because it takes only ~ 200 μ s for the feedback loop to complete an iteration, i.e. the position of the piezoelectric actuator is updated at a frequency of ~ 5 kHz, it seems feasible that the response time of the feedback loop can be improved.

The digital feedback loop has several advantages. (i) Analogue feedback systems may introduce noise during signal processing which digital systems do not. Although analogue systems perform calculations faster, digital systems may be preferred, if sufficiently fast, because calculations performed by the digital feedback system are highly reproducible. (ii) Analogue systems are prone to drift, e.g. due to thermal fluctuations or aging of the components they are composed of. In contrast, the digital feedback loop is stable as no thermal drift or aging effects can occur. (iii) Digital

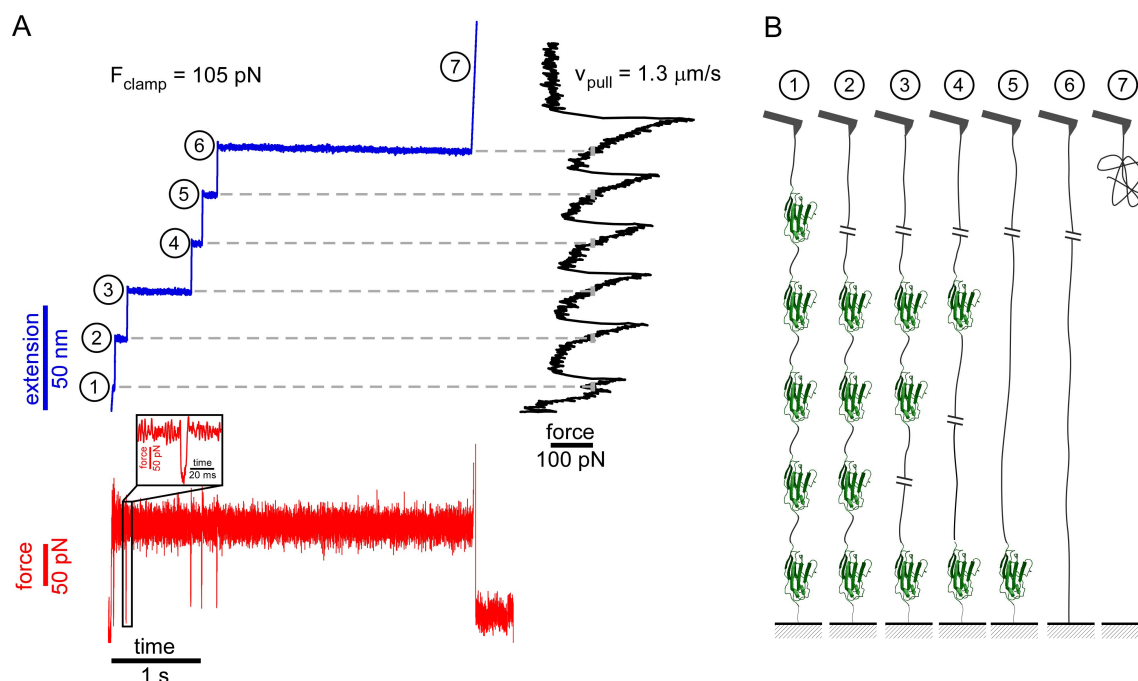


Figure 4.2 Mechanical unfolding of single Ig27_s molecules. (A) Time course of the unfolding of single Ig27 domains under constant force (blue trace: extension; red trace: force). Unfolding of each domain (encircled numbers) resulted in a step-wise increase of the molecular extension (blue trace) and in short peaks in the force trace (red). The inset shows a magnified region of the time course of the force signal detected during unfolding of a single Ig27 domain. Events corresponding to unfolding of Ig27 at constant velocity (black trace) are marked with dashed lines. The red and black traces were low-pass filtered using a cut-off frequency of 1 kHz. **(B)** Schematic representation of multi-domain Ig27 (PDB-ID: 1TIT) during mechanical unfolding. Here, a cartoon with broken lines is shown; in the real experiment the tip surface distance increases as in (A) (blue trace). Numbers shown correspond to those used in (A).

implementation of the feedback loop allows the system to be controlled through a software interface and the addition and removal of experimental features (such as filters or anti-reset-windup) without hardware changes. In summary, a digital setup makes AFM experiments very versatile and increases the flexibility of experiments by enabling different modules such as force-feedback and constant-velocity to be combined. For example, transmembrane α -helices G, F, E, D, C, and B of bR were unfolded and extracted prior to loading transmembrane α -helix A with a force of ~ 80 pN (using a z-ramp with constant velocity; Figure 4.3A, red trace). With a delay of 0.1 ms, the force-feedback was turned on and maintained the load on helix A until it was finally unfolded and extracted from the membrane (Figure 4.3, light blue and red segments). The modular design of digital feedback loops allows sophisticated mechanical single-molecule experiments in which single molecules are alternately stretched, relaxed, or clamped at defined forces or distances.

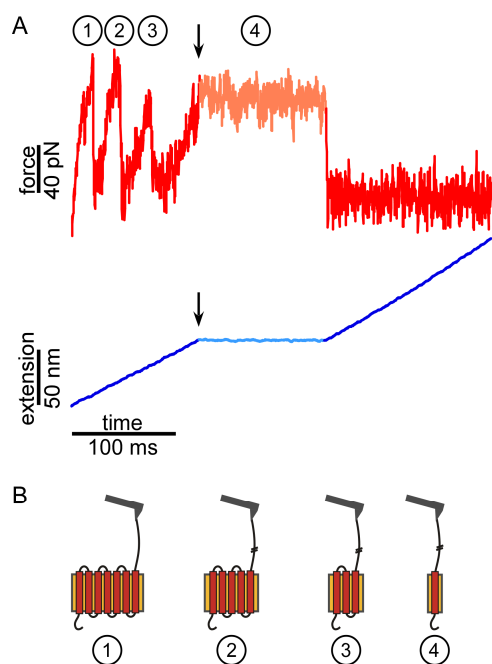


Figure 4.3 Combination of constant-velocity and force-feedback modules. (A) Force (red trace) and extension (blue trace) time course. Transmembrane α -helices G to B of a single bR molecule were unfolded at a constant pulling velocity of 500 nm/s (red trace, stages 1-3 correspond to unfolding of α -helices G and F (1), E and D (2), and C and B (3)). Then, the force-feedback was turned on (arrow) to probe the lifetime (stage 4, light red and blue segments) of the lipid membrane-embedded α -helix A. After α -helix A unfolded, the surface further retracted from the cantilever tip. (B) Schematic representation of the unfolding pathway of bR.

4.3.2 System Stability

To apply a constant force on the molecule during a force-clamp experiment the stability of the digital feedback system is crucial. The digital feedback loop itself is very stable since it has no hardware components that may introduce uncertainties. Nevertheless, some parts of the system, especially the cantilever, are susceptible to drift. This is important in the context of force-clamp applications as cantilever drift leads to significant errors in the force measurement. If the system is not in thermal equilibrium, temperature gradients within the AFM head and the liquid surrounding the cantilever will occur, e.g. due to heat generation by the laser. Therefore, the cantilever drifts, i.e. it slowly bends. This is caused by differences in thermal expansion of the cantilever material (e.g. silicon or silicon nitride) and the reflective coating (e.g. chromium, aluminum, and/or gold). This drift can be significantly reduced by allowing the system to thermally equilibrate. A glass bell creates an acoustically and thermally isolated compartment and allows the AFM to equilibrate. Even in such a thermally equilibrated system a considerable variety of drifting behaviors within a set of cantilevers can be observed [410]. Consequently, cantilevers were screened for low drift before later used in force-clamp measurements [331,333]. The drift of these cantilevers was neglectable in the time range of single experiments, which was ≈ 7 s. For longer-lasting experiments, drift-less cantilevers such as the recently developed torsion-levers [440] would be beneficial.

4.3.3 Force-Clamp Unfolding of Ig27₅

Multi-domain Ig27 mechanics has been extensively studied using SMFS, making it an ideal system for testing the feedback system. For later comparison with force-clamp data, Ig27 domains were first unfolded at a constant velocity of 1.3 $\mu\text{m/s}$ and saw-tooth patterned force-distance curves were obtained (Figure 4.2A, black trace). The peak spacing (~ 25 nm) and the peak forces (between 200 and 300 pN) were in good agreement with data reported previously [315]. Then, Ig27 domains were unfolded using the force-clamp protocol. Like the force-distance curves from constant-velocity SMFS, the extension curves obtained in the force-clamp mode showed a broad length distribution that is due to the attachment the AFM stylus at a various position along the polypeptide chain. Only curves having three or more steps of 23 nm were considered for further analysis. This step size is the extension observed during the unfolding of single Ig27 domains at 105 pN stretching force in conventional force spectra (Figure 4.2A, dashed lines; see also Ref. [332]).

The elongation curves of force-clamp experiments contain several regions of varying duration (Figure 4.2A, blue trace). While all extension curves showed the typical 23 nm steps, their evolution over time never looked the same, demonstrating that the unfolding of Ig27 domains is a stochastic process (see also Ref. [333]). The life times of individual domains of the molecule shown here varied from 20 ms to 1.2 s (Figure 4.2, state 1 and 5). After the last Ig27 domain had unfolded, the polypeptide was still tethered between AFM tip and support (figure 2A, state 6). In a last step, the molecule detached from the tip or the support (Figure 4.2A, state 7). Figure 4.2B schematically illustrates the consecutive but random unfolding of individual Ig27 domains. The extension curve from the force-clamp experiment nicely correlate with data obtained from constant-velocity SMFS experiments (Figure 4.2A, grey dashed lines).

4.3.4 Force-Clamp Unfolding of NhaA

Initial force spectroscopy data on unfolding of bR validated this approach for the study of interactions that govern stability and folding of membrane proteins [313,366]. Peaks in force spectra of bR, as well as other membrane proteins, correlate to the sequential unfolding of individual structural domains. Hence, detailed insights into stabilizing interactions were achieved at the sub-molecular level. Further applications of SMFS, such as DFS, or force modulation spectroscopy were used to probe stability and the unfolding pathways of bR at varying mechanical loads [405,415]. These data

together with the recent modeling of the unfolding process *in silico* [215,216] have contributed to the understanding of complex molecular interactions within membrane proteins and their assemblies. Another example of a membrane protein studied with SMFS is NhaA, a $\text{Na}^+:\text{H}^+$ antiporter from *E. coli*. Recent studies exploiting SMFS in the conventional constant-velocity mode allowed comprehensive analysis of molecular interactions within NhaA and revealed the on and off switching of the protein function [311,400]. Here, the first experiments probing the interactions of a membrane protein, i.e. NhaA, by force-clamp SFMS are presented.

Mechanical unfolding of individual NhaA molecules in constant-velocity SMFS experiments results in force-extension traces of ≈ 100 nm length that contains a characteristic pattern of force peaks [312] (Figure 4.4, black trace). Transmembrane domains of NhaA have certain probabilities to unfold individually or together with domains directly connected by the peptide backbone. Using the three-dimensional crystal structure of NhaA [441], it was possible to precisely assign individual peaks in the force spectra to structural domains.

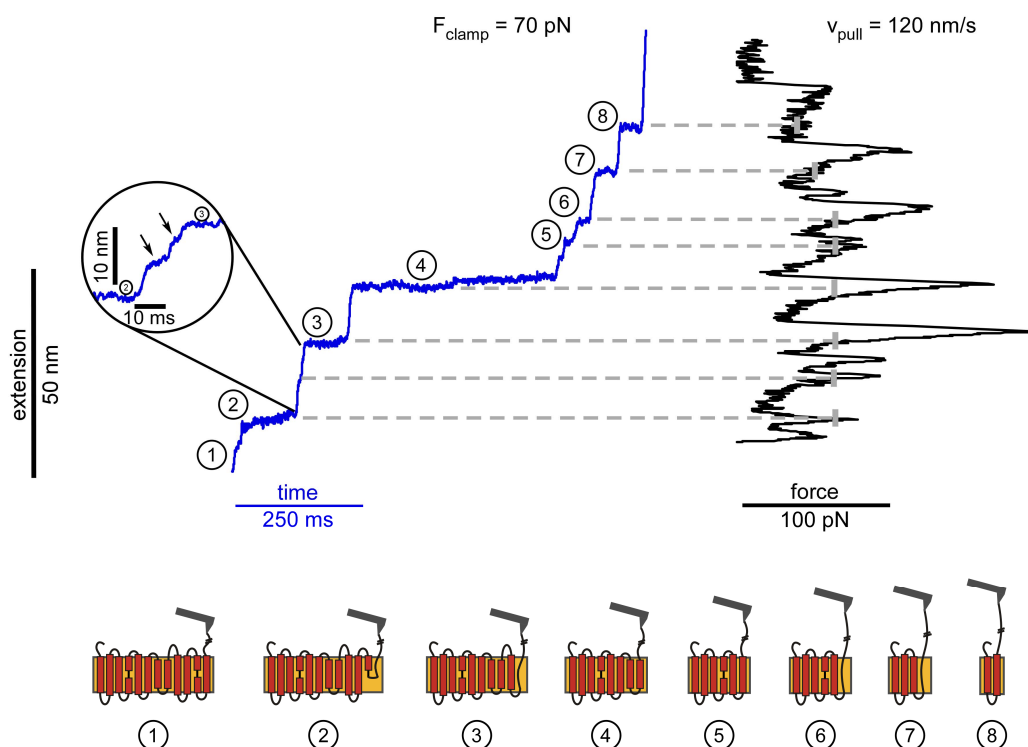


Figure 4.4 Force-induced unfolding pathways of NhaA. Top: A single NhaA molecule was attached to the AFM stylus with its C-terminus and subsequently unfolded applying a constant force (the blue trace shows the extension of the molecule) or stretching at a constant velocity (black trace represents a typical F-D trace). Corresponding unfolding intermediates are numbered and marked with dashed lines. The inset shows a magnified region of the constant force extension trace, indicating that certain structural domains exhibited only a marginal stability and life times shorter than 10 ms (arrows). The reconstructed unfolding pathway of a single NhaA molecule is given at the bottom.

Similar to titin unfolding experiments, extension traces obtained in force-clamp SMFS on NhaA varied in length, because the AFM stylus bound to the protein at various locations in its termini or extramembrane loops. Only traces ~ 100 nm in length were further considered, as they resulted from the sequential unfolding of NhaA molecules into a fully stretched conformation [312]. These F-D curves originate from proteins stretched from their C-terminus, because previous studies showed that the N-terminal end of NhaA is not accessible for the AFM tip at the conditions used [400]. A characteristic extension trace is shown in Figure 4.4 (blue trace). The trace contains several plateaus where the contour length of the polypeptide remains constant for 20-300 ms. Elongations indicate unfolding steps. However, the stability of some intermediate states was so low (< 10 ms) that they were hard to resolve (Figure 4.4, inset, marked with arrows).

By measuring the length of the polypeptide chain at every step, the unfolding pathways of NhaA under a constant force was reconstructed (Figure 4.4, bottom). Analysis of 12 extension traces shows that unfolding pathways followed by molecules under a constant load were similar to those observed in conventional SMFS experiments. This is not surprising. A mechanical load of the same order of magnitude and in the same direction (normal to the membrane plane) is applied to the protein. Thus, the same molecular interactions within the protein are probed. Comparing spectra of force-clamp and constant-velocity SMFS further validates this conclusion (Figure 4.4, dashed lines). Each stable intermediate detected in the force-clamp trace correlated with a peak in the force-extension spectrum of NhaA. As shown in the magnified region (Figure 4.4, inset, marked with arrows), when switching from state 2 to 3, NhaA passed through two short-living intermediate states. At the same extension the constant-velocity trace has the triple peak that is characteristic for the unfolding of transmembrane domains IX and X [312]. These domains contain multiple kinks and short non-helical regions that result in a low mechanical stability [441].

The short α -helical pair VII and VIII of NhaA has the highest stability in conventional SFMS and force-clamp experiments. Stage 4 (Figure 4.4) reflects unfolding of helix VIII, which is linked to helix VII by a 3 aa long loop and withstood a force of 70 pN for ~ 500 ms before cooperative unfolding as a helical pair. In 10 of 12 extension traces recorded on NhaA this domain had the longest life times at loading forces of 50-75 pN. However, careful analysis of the force-clamp data revealed an additional event prior to unfolding of this helical pair. A minor increase of 1.5 nm in the contour length was seen in the extension trace, but not in constant-velocity spectra.

Remarkably, this extension was not immediately followed by the unfolding of transmembrane α -helices indicating a stable conformation. The observed step probably reflects a conformational change of the transmembrane domains but further experiments should be designed to study the unfolding mechanism and kinetics in greater detail. Noteworthy are many small steps in the elongation trace of NhaA that made the curves appear noisy compared to Ig27₅ experiments.

4.4 CONCLUSIONS

Here, a software-based force-feedback loop was presented that upgrades a commercial AFM. This digital approach performs constant-force single-molecule experiments comparable to recently introduced hardware-based solutions. The digital feedback loop was successfully applied to unfold a multimeric Ig27 construct and the membrane protein NhaA. While the developed system works with a feedback frequency of ≈ 5 kHz, there is potential to increase the performance and reduce the response time well below the 5 ms, especially if more advanced electronics, such as freely programmable gate arrays, or faster piezo actuators with higher resonance frequencies are implemented. The advantage of this digital system is that it is modular. Particularly, combination of constant-velocity and force-feedback modules allow a variety of complex experiments in which single molecules are alternatively stretched, relaxed, or clamped.

LIGAND BINDING TRIGGERS ENERGY LANDSCAPE AND MECHANICAL PROPERTIES OF THE AMINO ACID ANTIPORTER STET

5.1 INTRODUCTION

The amino acid/polyamine/organocation (APC) superfamily comprises about 250 members that are present in all phyla from prokaryotes to higher eukaryotes. These membrane proteins are solute:cation symporters or solute:solute antiporters [261]. One APC subfamily, the L-amino acid transporter (LAT) family, includes to the light subunits of eukaryotic heteromeric amino acid transporters (HATs) [262,263]. HATs are composed of a light subunit that provides transport activity and a disulfide-linked heavy subunit required for plasma membrane localization. As outlined in section 1.3.2.2, HATs are involved in vital processes including amino acid homeostasis [266,267] and maintenance of the plasma redox balance [269]. Consequently, mutations in HATs lead to diseases [148,149,264,265] and overexpression of certain HATs supports unabated growth of some primary human tumors [270], making them an anti-cancer drug target.

So far, a high-resolution structure of a eukaryotic LAT family member is not available. However, studies on xCT revealed a 12 transmembrane α -helix topology with cytosolic N- and C-termini and a re-entrant loop structure between transmembrane α -helices II and III [442]. The first identified prokaryotic member of the LAT family, SteT from *B. subtilis*, is a serine:threonine antiporter and has a high sequence identity (~ 30 %) to the light subunits of eukaryotic HATs. Moreover, SteT exhibits a similar putative membrane topology (Figure 5.1) and sequential mode of obligate exchange [271]. Thus, it is appropriate to use SteT as a model to study the structure-function relationship of LAT family members.

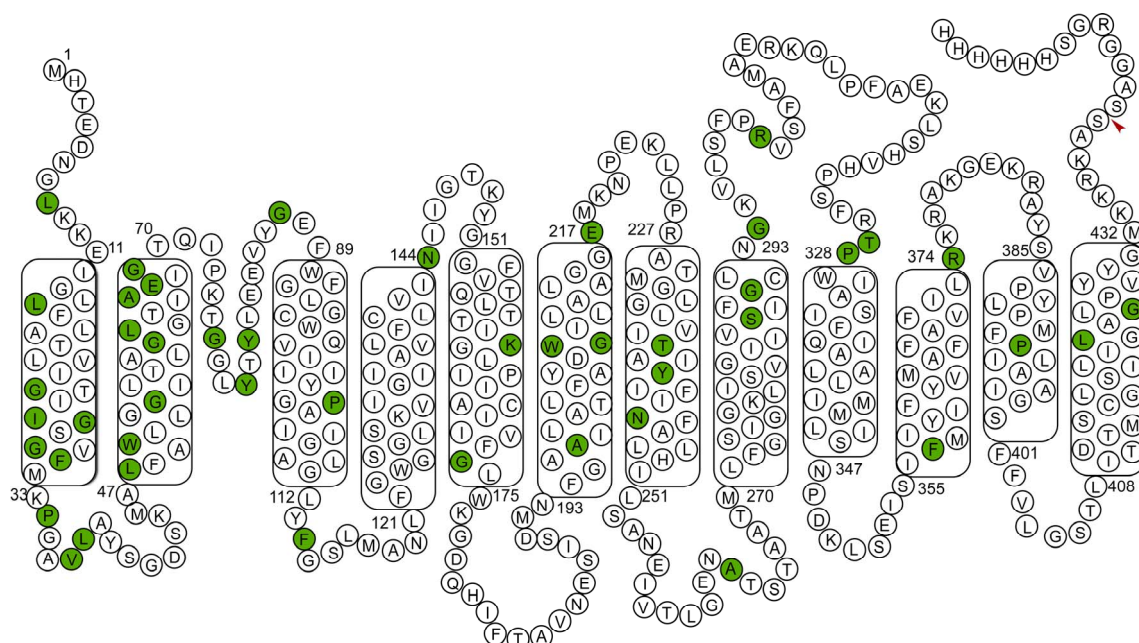


Figure 5.1 Secondary structure model of SteT. Based on comparison to xCT [442] and secondary structure prediction algorithms (e.g. the Phobius algorithm [443]), the topology of SteT was modeled showing twelve transmembrane α -helices and a re-entrant loop between transmembrane α -helices II and III. Residues conserved in SteT from *B. subtilis* and mammalian HATs are shaded in green and were identified by ClustalW multiple sequence alignment of SteT and the 50 highest scoring results of a Blast search among mammalian protein sequences using the SteT amino acid sequence as source. Amino acids are given in the one letter code. The red arrowhead in the C-terminal segment indicates the end of the native protein and the beginning of the genetically added tag used for protein purification.

According to current thinking, transport proteins undergo functionally related conformational changes. Transporters alternate between at least two conformations to expose their binding site(s) to the cytoplasmic and extracellular side of the plasma membrane [39,48,444-449]. Prior to conformational changes, substrates have to be recognized and bound. If substrates are amino acids, three main features can be used for specific selection and binding: (i) the negatively charged α -carboxyl group, (ii) the positively charged α -amino group, and (iii) the electrostatic, hydrophobic, or spatial properties of the side chain [39,450,451]. α -carboxyl and α -amino groups of L-amino acids, with the exception of proline, possess similar structural and chemical characteristics; however, their side chains are different in shape, size, and electrostatic properties. A combination of these features is assumed to specify which amino acid fits in the side chain binding pocket of an amino acid transporter. The two main substrates of SteT, L-serine and L-threonine are very similar, differing by only one side chain methylene group. SteT also transports aromatic L-amino acids (Trp, Tyr, and Phe) but with lower efficiencies [271].

In this study, SMFS has been applied to characterize molecular interactions that stabilize SteT in absence and in presence of its substrates, L-serine and L-threonine.

DFS has been exploited to characterize how substrate binding changes the energy landscape and the mechanical properties of the antiporter. It was observed that the overall stability of structural regions within SteT did not depend on substrate binding. However, substrate binding changed the energy landscape of these structures. In absence of substrate, all structural regions within SteT were stabilized by a narrow inner energy barrier and a second outer energy barrier. The unique properties of these energy barriers restricted the conformation of SteT, trapping the antiporter in a kinetically instable and mechanically rigid conformation. In contrast, substrate binding set SteT into a different energy minimum that significantly increased the kinetic stability and conformational flexibility of the antiporter.

5.2 EXPERIMENTAL PROCEDURES

5.2.1 Cloning, Overexpression, Purification, and Reconstitution into Proteoliposomes of SteT

SteT-containing proteoliposomes were kindly provided by F. Casagrande and D. Fotiadis (University of Berne). SteT was cloned and expressed by M. Palacin's laboratory at the University of Barcelona. Cloning, overexpression, and purification of SteT from *B. subtilis* with a C-terminally attached linker and His₆-tag (Figure 5.1, red arrowhead) have been previously described [271]. Briefly, purified SteT was solubilized in *n*-decyl- β -D-maltopyranoside (DM; Anatrace, Maumee, OH, USA) and mixed with 1,2-dimyristoyl-*sn*-glycero-3-phosphocholine (DMPC; Avanti Polar Lipids, Alabaster, AL, USA) solubilized in the same detergent (stock solution: 5 mg/ml DMPC, 1 % (w/v) DM, 150 mM NaCl, 10 % (v/v) glycerol, 0.01 % (w/v) NaN₃, 20 mM Tris-HCl, pH 8) to achieve a lipid-to-protein ratio (LPR) of 0.25 (w/w). The final SteT protein concentration was adjusted to 1.5 mg/ml. To reconstitute SteT into proteoliposomes the protein/lipid/detergent mixture was dialyzed against detergent-free buffer, i.e. 150 mM NaCl, 10 % glycerol (v/v), 250 mM betaine, 0.01 % (w/v) NaN₃, 20 mM Tris-HCl, pH 8 for about one week at room temperature.

5.2.2 SMFS and DFS

SMFS was performed using a Nanoscope IIIa AFM equipped with a PicoForce module and a PF scanner (Veeco Metrology, Santa Barbara, CA, USA). For a pulling velocity of 8720 nm/s, the AFM was extended with 16 bit data acquisition hardware (NI PCI-6221, National Instruments; Munich, Germany) that allowed data sampling

frequencies of up to 125 kHz using IgorPro 5 (WaveMetrics, Inc., Lake Oswego, OR, USA). Gold-coated 60 μm long silicon nitride (Si_3N_4) cantilevers (BioLever A, BL-RC150 VB, Olympus Ltd, Tokyo, Japan) had a nominal spring constant of 30 pN/nm and resonance frequency of ~ 8 kHz in water. Prior to experiments, the spring constant of each cantilever was determined in buffer solution using the equipartition theorem [293,436] (see section 2.2.2.4). SteT-containing proteoliposomes were adsorbed for 60–90 min at room temperature onto freshly cleaved mica (section 4.2.1) in 150 mM NaCl, 20 mM Tris-HCl, pH 8.0. To characterize substrate binding, the same buffer was supplemented with 5 mM L-serine or 5 mM L-threonine. After adsorption, the sample was rinsed several times with adsorption buffer to remove weakly attached membranes. Buffer solutions were prepared using nano-pure water (≥ 18 M Ω cm; purelab ultra, ELGA LabWater) and p.a. grade chemicals from Sigma or Merck. After buffer exchange, the AFM was thermally equilibrated for at least 30 min under a glass bell. Prior to SMFS, membranes containing densely packed SteT were located by contact mode AFM imaging. If necessary, the AFM stylus was used as a nano scalpel to remove aggregates or the upper layer of vesicles [398,452]. An unperturbed area of a membrane patch was selected and the AFM stylus was pushed onto the membrane at a force of ~ 750 pN for 0.5–1.0 s to promote unspecific attachment of the SteT polypeptide to the AFM stylus. In the following step, the cantilever was retracted from the surface at a constant velocity. The polypeptide tethering stylus and membrane was stretched, an increasing mechanical stretching force was applied, and unfolding of SteT was induced. Unfolding of SteT was monitored by simultaneously recording the cantilever deflection and the distance traveled by the piezo. The interaction force at each separation was calculated from the deflection using Hook's law resulting in F-D curves.

DFS experiments were performed at eight pulling velocities (145, 311, 654, 1090, 2180, 2910, 4360, and 8720 nm/s) using substrate-free SteT and SteT in the presence of L-serine or L-threonine. To minimize errors that may occur due to uncertainties in the cantilever spring constant calibration, SteT was unfolded using at least three different cantilevers for each pulling velocity. Table 5.1 summarizes the number of F-D curves recorded for each condition.

5.2.3 Data Selection and Analysis

In the past, a robust approach to select F-D curves that represent the complete unfolding of a membrane protein by a mechanical stretching force applied at its termini was developed [312,314,366,371]. Mechanically pulling the terminal end of a

membrane protein induces the sequential unfolding of its secondary structure elements beginning at the mechanically stressed terminus. Each structure that establishes an unfolding barrier is detected as a force peak in the F-D curve. The last force peak of a F-D curve denotes the length of the unfolded and stretched polypeptide that is anchored by the last membrane embedded structure [312,453]. When overcoming the stability of this last structural element, the membrane protein is completely unfolded and the entire polypeptide is extracted from the membrane. In other membrane proteins this last structural segment is the last membrane embedded transmembrane α -helix. For SteT it is assumed that this was also true. Accordingly, based on secondary structure prediction and the similar length of soluble N- and C-terminal peptides, stretched polypeptides would have a contour length of 380-440 amino acids (aa). Therefore, only F-D curves showing overall protein extension of 110-130 nm were selected. These curves were manually aligned to each other using the three characteristic force peaks observed at contour lengths of 70, 79, and 147 aa. Every peak of each F-D curve was fitted using the WLC model [320] with a persistence length of 0.4 nm and a monomer length per amino acid of 0.36 nm [315]. The WLC fit of each force peak gives the contour length as the number of unfolded and stretched amino acids. The obtained contour lengths and the corresponding rupture forces were statistically analyzed. Data analysis and calculations were performed using IgorPro 5 using built-in and custom-written procedures.

5.2.4 Compensation for Hydrodynamic Drag

At high pulling velocities, hydrodynamic friction of the cantilever³⁵ causes an underestimation of the unfolding force [454]. Hence, the measured unfolding forces, $F_{measured}$, were corrected to obtain the real unfolding force, F_{real} , using

$$F_{real} = F_{measured} + F_{fric} \frac{\kappa_{spacer}}{\kappa_{spacer} + \kappa_{cant}} \quad 5.1$$

with F_{fric} the friction force and κ_{spacer} the spring constant of the stretched polypeptide [455]. F_{fric} was half the difference between an approach and a retract F-D curve of a free cantilever [454]. The slope before peak rupturing was defined as κ_{spacer} and calculated from a WLC curve with the corresponding contour length. This correction was applied

³⁵ The friction force experienced by a cantilever depends on the pulling velocity and its size and geometry. Therefore, small cantilevers, such as the BioLever A used in this study experience less friction compared to previously used long V-shaped cantilevers.

to force spectroscopy data acquired at pulling velocities of 1090, 2180, 2910, 4360, and 8720 nm/s.

5.2.5 Calculation of x_u and k_0 from DFS Data

According to the Bell-Evans theory (for details refer to section 2.3.2.4) [380], the most probable unfolding force F^* plotted *versus* $\ln(r_f^*)$ describes the most prominent energy barrier within the force-driven unfolding process [373]. The relation between F^* and r_f^* can be described by

$$F^* = \frac{k_B T}{x_u} \ln \frac{x_u r_f^*}{k_B T k_0} \quad 5.2$$

where r_f^* is the most probable loading rate. The loading rate was calculated using $r_f = \kappa_{\text{spacer}} v_p$. Experimental loading rate and force histograms (Figure 5.2) were fitted with Gaussian distributions. The resulting F^* s were plotted *versus* r_f^* . x_u , and k_0 were obtained by fitting Equation 5.2 using a non-linear least-squares algorithm. Only forces and loading rates corresponding to the main peaks were considered.

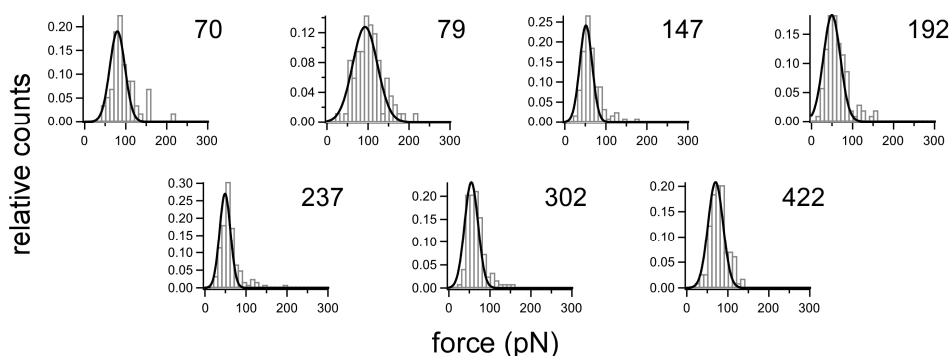


Figure 5.2 Experimental force histograms. Histograms show examples of experimentally determined force distributions. Data shown was recorded at 654 nm/s using substrate-free SteT. Black lines represent Gaussian fits to the force histograms. The numbers given at the top right of each histogram indicate the position of the peak within the F-D trace in aa.

5.2.6 Calculation of Transition Barrier Heights and Rigidity

The height of the free energy barrier, ΔG^\ddagger , separating the folded and unfolded state was assessed using an Arrhenius equation

$$\Delta G^\ddagger = -k_B T \ln(\tau_D k_0) \quad 5.3$$

where τ_D denotes the diffusive relaxation time [359]. Typical values for τ_D found for proteins are between 10^{-7} – 10^{-9} s [378,456]. Assuming $\tau_D = 10^{-8}$ s seems to be reasonable for determining the free energy barrier heights. This value has also been used for molecular dynamics simulations of protein folding [457]. Thus, a value of $\tau_D = 10^{-8}$ s was used throughout all calculations. Varying τ_D within the above-mentioned range,

changes the free energy of activation by < 15 %. Moreover, even if τ_D was wrong by orders of magnitude, the influence of the error of τ_D would be the same for all conditions and values and, hence, would not affect the qualitative results. Errors in ΔG^\ddagger were estimated by propagation of the errors of k_0 .

In absence of any information on the energy potential shape, simple parabolic potential was assumed and the spring constant of the bond, κ_{bond} , can be calculated using ΔG^\ddagger and x_u [317,458]

$$\kappa_{bond} = \frac{2\Delta G^\ddagger}{x_u^2} \quad 5.4$$

Errors in ΔG^\ddagger and x_u were propagated for error estimation.

5.3 RESULTS

5.3.1 Interactions of SteT In Presence and Absence of Substrates

SMFS was applied to determine the interactions stabilizing the serine:threonine antiporter SteT. Briefly, SteT proteoliposomes were imaged using contact mode AFM (Figure 5.3) and selected for SMFS. The AFM stylus was brought into contact with the proteoliposome to facilitate formation of a molecular linkage between individual SteT molecules and the AFM stylus (Figure 5.4A) [313]. Upon retraction of the stylus, the deflection and separation of the cantilever were recorded. Less than 5 % of F-D curves exhibited a saw tooth-like pattern. Due to unspecific interactions, the AFM stylus attached at several positions of the SteT polypeptide. Hence, the resulting F-D curves varied significantly in length and peak pattern. About 5 % of these F-D curves displayed a well-defined force peak pattern that extended over a length of 110 to 130 nm (Figure 5.4B). Each of these F-D curves was of a length that correlated with mechanical unfolding starting from one terminal end and showed a common pattern of seven major force peaks.

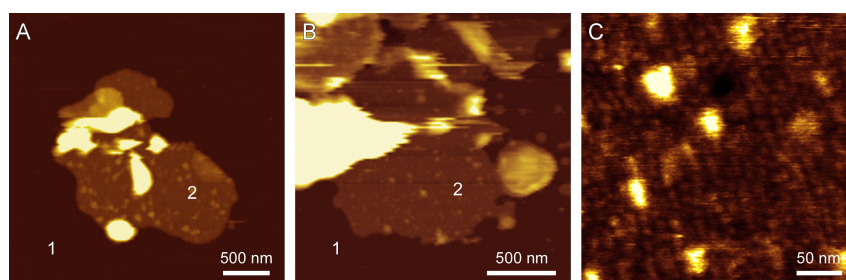


Figure 5.3 AFM topographs of SteT containing membranes. (A), (B) Overview of SteT containing membrane patches (2) adsorbed onto a mica surface (1). (C) SteT containing membranes at higher magnification. SteT is densely packed within the lipid membrane, although not arranged in a 2D crystalline array. The full color scale corresponds to 50 nm (in (A) and (B)) and 4 nm (C).

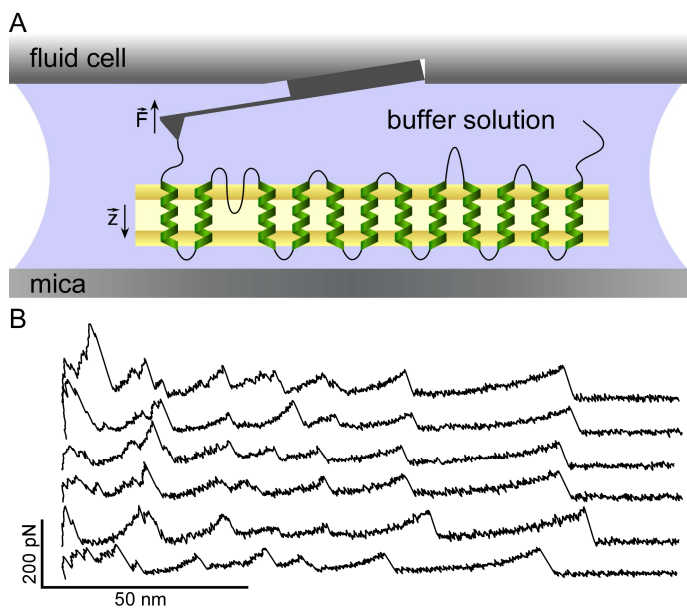


Figure 5.4 SMFS of SteT. (A) Pressing the AFM stylus onto the SteT-containing proteoliposomes facilitates adhesion of single transporter molecules to the AFM stylus. The resulting molecular bridge allows application of mechanical stress that initiates stepwise unfolding of SteT. Throughout experiments, sample and cantilever are fully immersed in buffer solution. (B) F-D curves recorded while unfolding single substrate-free SteT molecules at 654 nm/s in 150 mM NaCl, 20 mM Tris-HCl, pH 8.0.

First, F-D curves were recorded at $v_p = 654$ nm/s for substrate-free SteT ($n = 132$) and SteT in presence of 5 mM L-serine ($n = 128$) or 5 mM L-threonine ($n = 127$, Table 5.1). At first sight, the recorded F-D curves looked similar showing the common pattern of seven major force peaks (Figure 5.4B). However, individual F-D curves differed to some extent from each other. These differences were additional peaks and slightly different peak positions or amplitudes. To visualize common features, F-D curves were superimposed and converted to density plots (Figure 5.5A). All three superimpositions showed the common seven force peaks pattern. A characteristic double peak occurred at the contour lengths of ~ 70 and ~ 79 aa. This feature was followed by four peaks at contour lengths of ~ 147 , ~ 192 , ~ 237 , and ~ 302 aa. The last force peak was detected at ~ 422 aa (Table 5.2). Force peaks at contour length 147, 192, 237, and 302 aa showed comparable low forces. The peaks at 70 and 422 aa exhibited an intermediate force, while the segment located at 79 aa withstood the highest forces (Table 5.2, Figure 5.2). From the superimpositions, no substantial differences between the F-D spectra were revealed.

pulling velocity (nm/s)	number of analyzed F-D traces		
	substrate-free	5 mM L-serine	5 mM L-threonine
145	97	79	49
311	51	73	65
654	132	128	127
1090	101	86	68
2180	116	85	90
2910	106	109	86
4360	71	90	84
8720	71	81	109

Table 5.1 Number of SteT F-D curves analyzed for each pulling velocity and substrate condition.

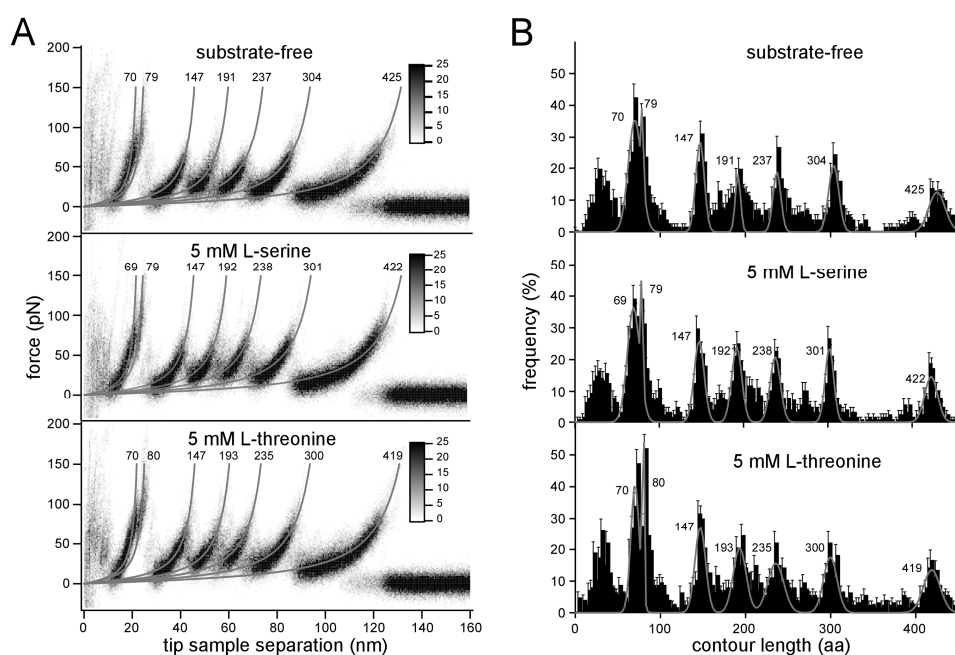


Figure 5.5 Superimpositions of F-D traces and analysis of peak appearance. (A) Superimpositions of F-D curves recorded while unfolding SteT in buffer lacking any substrate (top) and supplemented with 5 mM L-serine (middle) or 5 mM L-threonine (bottom). Superimpositions are represented as density plots each calculated from 60 F-D curves. Grey lines represent WLC curves with a persistence length of 0.4 nm and contour length (in amino acids) as indicated by the numbers next to the lines. The contour lengths were obtained from the Gaussian fits shown in (B). F-D curves were obtained at room temperature at a pulling velocity of 654 nm/s in buffer solution (150 mM NaCl, 20 mM Tris-HCl, pH 8.0, substrate as indicated). (B) Frequency of force peaks detected at different positions of the stretched polypeptide. Every force peak detected in individual F-D curves (B) was fitted using the WLC model, with the contour length of the stretched polypeptide as the only fitting parameter. The frequency at which the force peaks appeared is plotted in the histogram; substrate-free ($n = 132$), 5 mM L-serine ($n = 128$), and 5 mM L-threonine ($n = 127$). The bin size of the histograms is 3 aa and reflects the accuracy of fitting the WLC model [320] to individual force peaks. Error bars representing the standard error of the mean (SEM) were calculated using $SEM = (p(1-p)/n)^{1/2}$ with p the probability and n the total number of F-D curves. The width of each force peak distribution is given by the experimental noise, conformational variability of the structural segments and fitting accuracy of the force peaks [332,355,371,459,460]. The grey solid curve represents the sum of seven Gaussian fits to the seven main peaks from the histograms and superimpositions (A). Numbers next to peaks denote peak positions (measured in amino acids) obtained from Gaussian fits.

substrate-free SteT		L-serine		L-threonine	
contour length \pm SD (aa)	most probable force \pm SD (pN)	contour length \pm SD (aa)	most probable force \pm SD (pN)	contour length \pm SD (aa)	most probable force \pm SD (pN)
70.2 \pm 7.7	80 \pm 18	69.4 \pm 7.4	76 \pm 18	70.2 \pm 5.0	84 \pm 18
79.2 \pm 1.1	92 \pm 30	79.4 \pm 1.2	107 \pm 31	79.9 \pm 1.1	112 \pm 24
146.8 \pm 5.0	51 \pm 15	147.3 \pm 5.9	55 \pm 15	146.8 \pm 6.2	63 \pm 16
191.2 \pm 3.1	50 \pm 20	192.1 \pm 5.4	51 \pm 21	193.1 \pm 7.5	62 \pm 27
237.0 \pm 4.6	49 \pm 13	237.6 \pm 6.1	58 \pm 17	235.4 \pm 9.4	56 \pm 24
303.9 \pm 6.0	55 \pm 16	301.8 \pm 5.1	60 \pm 14	299.5 \pm 7.9	66 \pm 18
424.9 \pm 9.7	70 \pm 18	422.5 \pm 7.6	77 \pm 12	418.7 \pm 9.9	79 \pm 14

Table 5.2 Contour lengths and rupture forces of interactions stabilizing structural segments of SteT. Contour lengths represent most probable peak positions (measured in amino acids) obtained from Gaussian fits to the contour length distributions (Figure 5.5B). Forces represent most probable forces obtained from Gaussian fits to the experimental force distributions. Data were recorded at $v_p = 654$ nm/s.

5.3.2 Direction of Unfolding

Using SMFS, membrane proteins may be mechanically unfolded by pulling at either N- or C-terminal ends. Depending from which end unfolding is induced, F-D spectra show different patterns [312,453,461]. In the measurements, all F-D curves that exhibited lengths between 110 and 130 nm showed one common force peak pattern. This indicated that antiporters had been exclusively unfolded from one terminal end. According to the secondary structure predicted by the Phobius algorithm [443] the length of the N-terminal end corresponds to 11 aa, whereas the C-terminal end corresponds to 20 aa (including spacer and His₆-tag). The AFM stylus can pick up the terminal end of a membrane protein at random positions. Accordingly, the superimposition of the F-D curves should show starting points that are spread by the length of the terminal end pulled (Figure 5.5A). However, other secondary structure prediction algorithms like MEMSAT3 [462] showed different lengths of N- and C-terminal ends. Thus, in absence of a solid structural model, it was impossible to make a straightforward assignment of the terminal end from which mechanical unfolding of the antiporter was induced. Fortunately, for the following study the identity of the end is not vital.

5.3.3 Probability of Interactions

Each peak of a F-D curve reflects an interaction established by SteT. To quantify the probability of SteT to establish interactions in the absence and presence of substrate, every force peak of individual F-D curves was fitted using the WLC model

[320]. The resulting contour lengths are converted into the amino acid lengths of the polypeptide that had been unfolded and stretched above the membrane surface. Thereafter, the probability of a force peak appearing was plotted *versus* the length of the stretched polypeptide (Figure 5.5B). All histograms showed eight peaks. The first peaks occurring at contour lengths between 0 and 50 aa were detected at a distance at which unspecific interactions between stylus and membrane surface dominate the F-D spectra (Figure 5.4B). Accordingly, the superimpositions did not show defined force peaks in the corresponding region (Figure 5.5A). In contrast, the other peaks in the histograms correlated nicely to the well-defined force peaks in the superimpositions. To determine the most probable location of the force peaks (Table 5.2), Gaussians were fitted to the major peaks in the histograms (Figure 5.5B, grey lines). Interestingly, the position of the force peaks did not change in the presence or absence of substrate. Additionally, no significant changes in the force peak pattern could be detected upon addition of either substrate.

5.3.4 Substrate Binding Changes the Dynamic Energy Landscape of SteT

To examine how substrate binding influences the energy landscape of SteT, substrate-free SteT and SteT in the presence of 5 mM L-serine or 5 mM L-threonine was unfolded at pulling velocities ranging from 145 to 8720 nm/s. In agreement with theoretical considerations [373,380] and previous studies on soluble [403,463] and membrane proteins [368,369,405,406], the unfolding forces increased with pulling velocities. Plotting the most probable unfolding force, F^* , *versus* the logarithm of the most probable loading rate, r^* , (Figure 5.6) revealed insights into the energy profile underlying individual structural segments of SteT (Figure 2.10, Table 5.3). The dynamic force spectra of every structural segment of substrate-free SteT showed two linear regimes (Figure 5.6, left column). According to the Bell-Evans model [380] the existence of two linear regimes indicates that two barriers separate the folded from the unfolded state. At low loading rates, an outer barrier was probed, while at higher loading rates an inner barrier dominated the dynamic force spectrum. All structural segments exhibited inner barriers that showed ground-to-transition state distances, x_u , from 0.21 to 0.36 nm and unfolding rates, k_0 , from 2.2 to 27 s⁻¹. In contrast, their outer barriers showed much larger distances to the transition states ranging from 0.74 to 5 nm and much lower unfolding rates that ranged from $\sim 4 \cdot 10^{-42}$ to 0.1 s⁻¹ (Table 5.3).

On the contrary, the dynamic force spectra recorded in presence of L-serine (Figure 5.6, middle column) or L-threonine (Figure 5.6, right column) revealed a single

linear regime for every structural segment of SteT. This suggests that a single energy barrier stabilized the folded state of these structural segments in the ligand-bound state. For SteT in the presence of L-serine, x_u ranged from 0.38 to 1.34 nm and k_0 from $2.3 \cdot 10^{-8}$ to 1.6 s^{-1} . In the presence of L-threonine x_u ranged from 0.55 to 1.34 nm and k_0 from $1.5 \cdot 10^{-6}$ to 0.17 s^{-1} (Table 5.3). Except for the last structural segment, the energy barriers determined for SteT in presence of L-threonine showed slightly greater x_u values than in presence of L-serine. Depending on the substrate, the unfolding rate, k_0 , of some structural segments changed by more than three orders of magnitude (Table 5.3, highlighted in bold). Transition states and unfolding rates determined for SteT in presence of either substrate differed significantly from the values obtained for the inner barrier of substrate-free SteT.

Figure 5.6 Pulling velocity dependent response of interactions that stabilize individual segments of SteT. Fitting the r_f^* -dependent F^* (lines) using Equation 2 provides the parameters of the energy barriers that stabilize structural segments within SteT. x_u measures the distance from the energy well of the native state to the transition state, and k_0 describes the kinetic transition rate at which the structural segment unfolds at zero force. Error bars represent the SEM of force and loading rate, respectively, and are, if not visible, smaller than the symbols used. Fits were weighted using the SEM of the most probable force. Experiments were performed in 150 mM NaCl, 20 mM Tris-HCl, pH 8.0 in the absence of substrates (left column) or in presence of 5 mM L-serine (middle column) or 5 mM L-threonine (right column). Peak positions are given in amino acids.

Figure on next page →

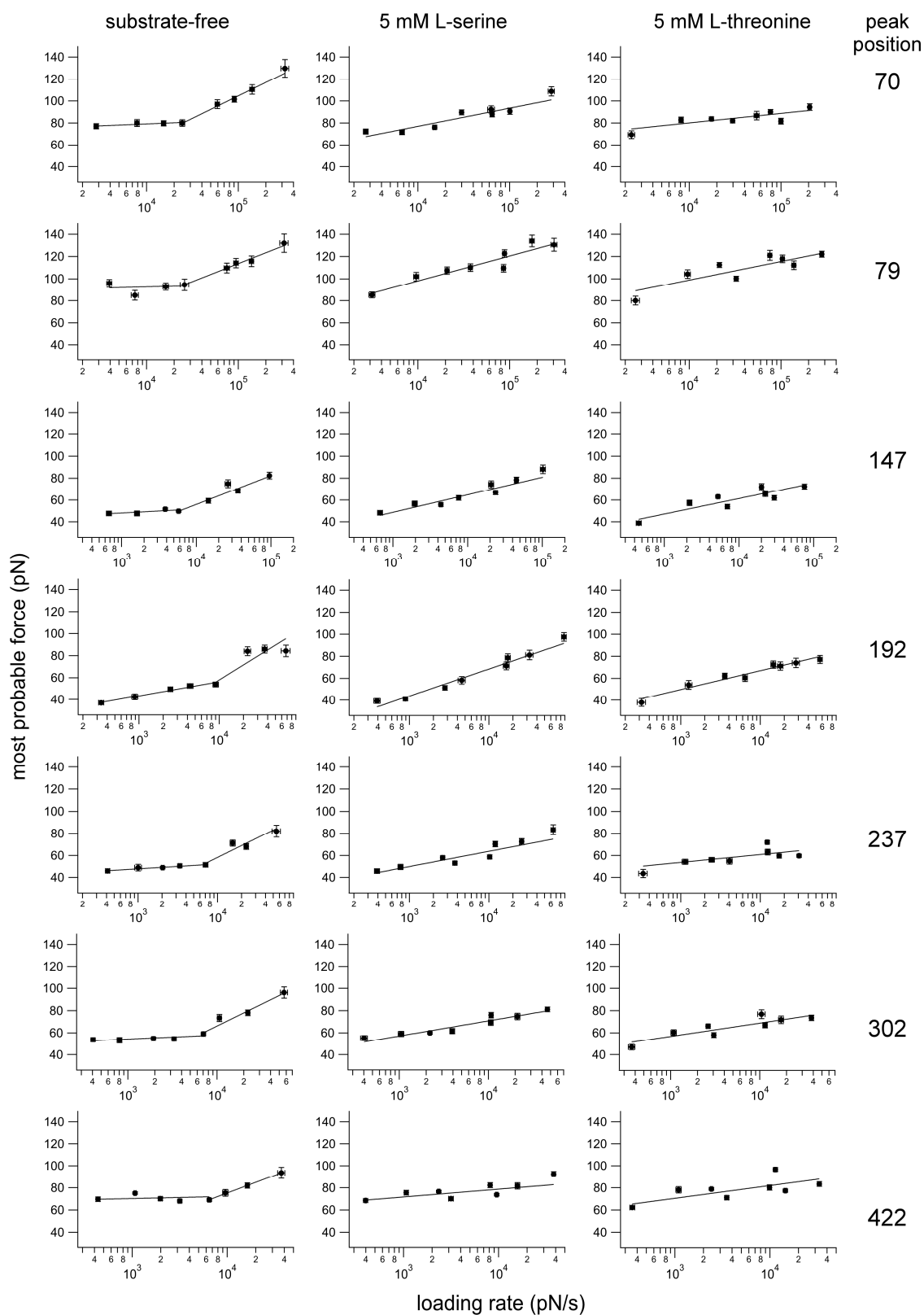


Figure 5.6

Chapter 5: Ligand Binding Changes the Energy Landscape

peak pos. (aa)	substrate-free ^{outer}	substrate-free ^{inner}	L-serine	L-threonine	substrate-free ^{outer}	substrate-free ^{inner}	L-serine	L-threonine
	$x_u \pm \text{SD (nm)}$				$k_0 \pm \text{SD (s}^{-1}\text{)}$			
70	2.71 ± 2.85	0.23 ± 0.03	0.57 ± 0.05	1.10 ± 0.22	1.4 ± 78 × 10 ⁻¹⁹	15.5 ± 9.	0.031 ± 0.030	1.5 ± 6.4 × 10⁻⁶
79	4.65 ± 14.5	0.29 ± 0.07	0.42 ± 0.04	0.57 ± 0.07	4.4 ± 1400 × 10 ⁻⁴²	2.2 ± 3.7	0.043 ± 0.040	1.6 ± 2.7 × 10 ⁻³
147	2.68 ± 1.82	0.36 ± 0.03	0.59 ± 0.05	0.67 ± 0.05	1.8 ± 39 × 10 ⁻¹¹	6.7 ± 2.4	0.14 ± 0.09	0.078 ± 0.049
192	0.74 ± 0.10	0.21 ± 0.02	0.38 ± 0.02	0.55 ± 0.06	7.7 ± 7.4 × 10 ⁻²	26.7 ± 8.0	1.6 ± 0.4	0.17 ± 0.14
237	2.15 ± 0.98	0.27 ± 0.04	0.69 ± 0.07	1.34 ± 0.26	7.3 ± 82 × 10 ⁻⁹	15.0 ± 6.5	0.040 ± 0.034	8.7 ± 31 × 10⁻⁶
302	2.58 ± 1.19	0.24 ± 0.03	0.69 ± 0.06	0.79 ± 0.09	1.0 ± 16 × 10 ⁻¹²	12.2 ± 4.2	0.011 ± 0.010	3.7 ± 4.9 × 10 ⁻³
422	4.98 ± 4.58	0.30 ± 0.05	1.34 ± 0.21	0.83 ± 0.07	1.4 ± 110 × 10 ⁻³⁴	3.3 ± 2.3	2.3 ± 8.5 × 10⁻⁸	1.4 ± 1.9 × 10⁻⁴
peak pos. (aa)	$\Delta G^\ddagger (k_B T)$				$\kappa_{bond} (\text{N/m})$			
70	62	16	22	32	0.07	2.41	0.55	0.22
79	114	18	22	25	0.04	1.72	1.00	0.64
147	43	17	21	21	0.05	1.06	0.49	0.39
192	21	15	18	20	0.32	2.84	1.01	0.55
237	37	16	22	30	0.07	1.84	0.38	0.14
302	46	16	23	24	0.06	2.27	0.40	0.32
422	97	17	36	27	0.03	1.64	0.17	0.33

Table 5.3 Parameters characterizing the energy barriers (x_u , k_0 , and ΔG^\ddagger) and spring constants (κ_{bond}) of stable structural segments of SteT. Parameters for the outer (substrate-free^{outer}) and inner (substrate-free^{inner}) barriers of substrate-free SteT and SteT in presence of 5 mM L-serine or 5 mM L-threonine. Errors represent standard deviations (SD). Changes in transition state, x_u , were considered significant when the values for $x_u \pm 2\text{SD}$ did not overlap. Changes in transition rate, k_0 , were considered significant when exceeding two orders of magnitude. Barrier heights, ΔG^\ddagger , and spring constants, κ_{bond} , were calculated as described in the section 5.2.

5.3.5 Correlation of x_u , k_0 , and ΔG^\ddagger

Taking all structural segments of SteT probed in absence and presence of substrate into account, we found a linear correlation ($R = 0.71$) between the position of the transition state x_u and the free energy of activation, ΔG^\ddagger (Figure 5.7A). Concomitant with an increase in ΔG^\ddagger the transition state shifted away from the energy minimum (higher x_u , Figure 5.7A, Table 5.3). For all structural segments x_u increased along with ΔG^\ddagger upon ligand binding, thus showing a Hammond-like behavior [368,407,464-467]. To further investigate the relationship between x_u and ΔG^\ddagger , the ratio $x_{u,\text{substrate}}/x_{u,\text{inner}}$ versus the ratio $\Delta G_{\text{substrate}}^\ddagger/\Delta G_{\text{inner}}^\ddagger$ was plotted for every structural segment (Figure 5.7B). Assuming a linear relationship between the ratios $x_{u,\text{substrate}}/x_{u,\text{inner}}$ and $\Delta G_{\text{substrate}}^\ddagger/\Delta G_{\text{inner}}^\ddagger$ [368], it becomes evident from the representative fits shown in Figure

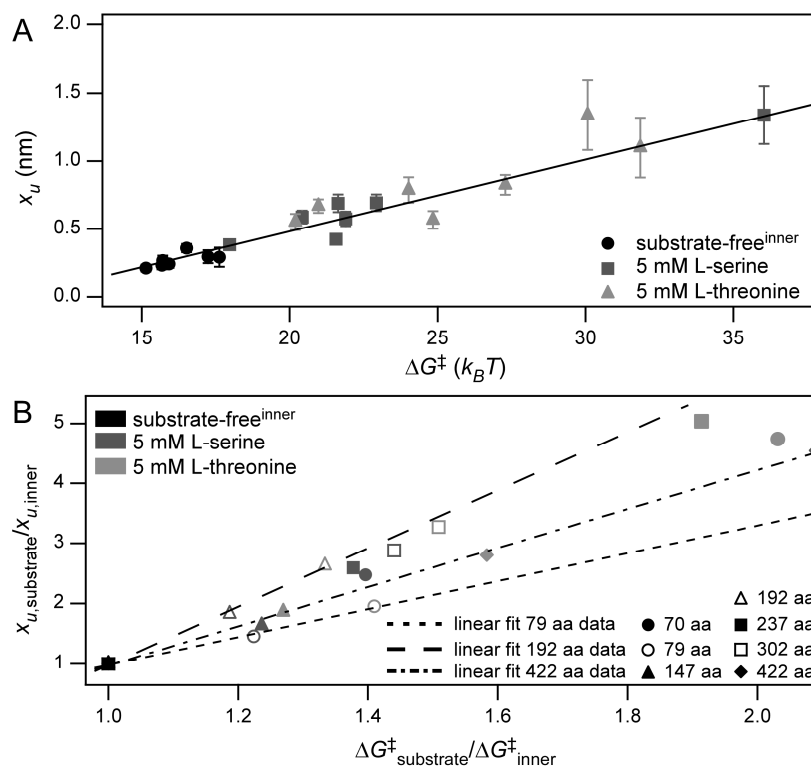


Figure 5.7 Correlation between x_u and ΔG^\ddagger . (A) Plotting x_u versus ΔG^\ddagger reveals their linear correlation for all structural segments of substrate-free SteT (inner barrier, black symbols) and SteT in presence of 5 mM L-serine (dark grey symbols) or 5 mM L-threonine (light grey symbols). Error bars represent standard deviations (SD). (B) Changes in x_u and ΔG^\ddagger for SteT in absence (inner barrier, black symbols) and presence of L-serine (dark grey symbols) or L-threonine (light grey symbols) with respect to the values for the inner barrier of substrate-free SteT. All structural segments revealed an apparent Hammond behavior, i.e. upon ligand binding x_u increased with increasing ΔG^\ddagger . Short-dashed, long-dashed, and dot-dashed lines represent linear fits to the values obtained for the structural segments at 79 (open circle), 192 (open triangle), and 422 aa (filled diamond), respectively. The different slopes of these fits (2.31, 4.85, and 3.25 for the short-dashed, long-dashed, and dot-dashed lines) show that ligand binding influenced each individual structural segment differently. Data taken from Table 5.3.

5.7B, that every structural segment showed a unique energetic sensitivity towards ligand binding as the slopes of the fits for the individual structural segments were different.

5.3.6 Mechanical Properties of SteT

Rigidity refers to the resistance of a material to structurally deform in response to a mechanical force. The rigidity of a protein depends on the curvature of the potential well of the energy profile, the height of the energy barrier, ΔG^\ddagger , and the distance x_u separating ground and transition state (Figure 2.10). The energy landscape describes the energy as a function of the conformational entropy of a protein structure [86,89,91]. Accordingly, decreasing (increasing) the width of an energy well that defines the conformational entropy of a protein structure allows the protein to adopt less (more) conformational sub-states. This decrease (increase) of conformational sub-states is usually described as decreasing (increasing) the conformational flexibility [140,317,455,468]. In absence of further information, a parabolic potential in vicinity of the energy minimum and a sharp transition barrier for all structural segments of SteT were assumed [317,468]. To approximate the rigidity of individual structural segments, their spring constants, k_{bond} , were calculated applying Equation 5.4. For substrate-free SteT, spring constants were calculated for each of the two energy barriers that stabilized a structural segment (Table 5.3). The outer barriers of these structural segments showed spring constants between 0.03 and 0.07 N/m, except for the segment correlated to the force peak at ~ 192 aa, which exhibited an increased spring constant of 0.32 N/m. In contrast, the inner barriers of these structural segments showed much higher spring constants ranging from 1.06 to 2.84 N/m. In presence of substrate, the spring constants of the individual structural segments ranging from 0.17 to 1.01 N/m for L-serine laid slightly above the spring constants for L-threonine, ranging from 0.14 to 0.64 N/m (Table 5.3, Figure 5.8). These spring constants indicated that the rigidity of the structural segments within SteT was generally lower in presence of substrate than that determined for the inner barriers and higher than that of the outer barriers of substrate-free SteT.

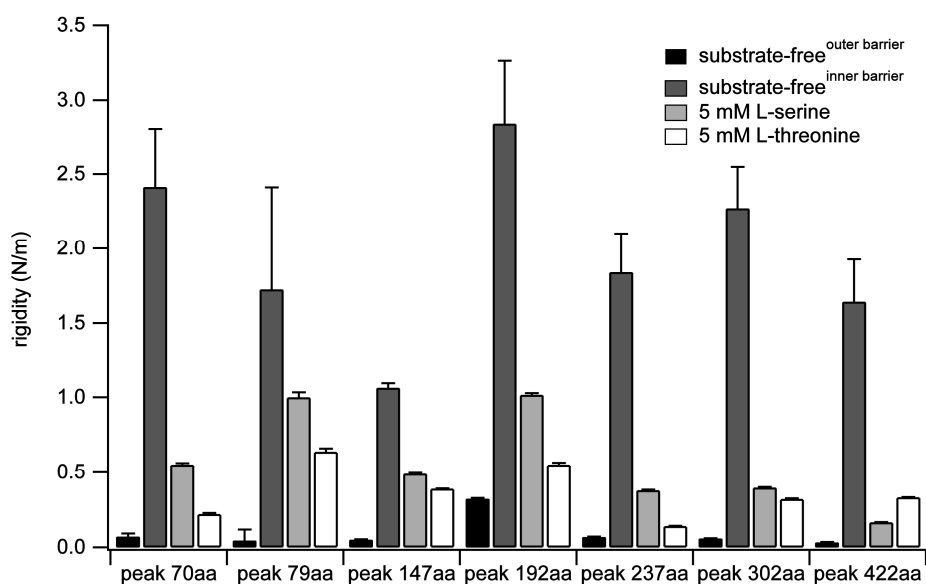


Figure 5.8 Rigidity of structural segments of SteT in absence and presence of substrate. For substrate-free SteT, rigidity of the outer and inner energy barriers is shown. Rigidity was estimated using Equation 5.4 to calculate the spring constant k_{bond} from x_u and ΔG^\ddagger obtained from DFS experiments. Errors were propagated from the errors of x_u and ΔG^\ddagger .

5.4 DISCUSSION

5.4.1 Amino Acid Binding by SteT Lacks Detectable Localized Interactions

Previously, SMFS has been applied to reveal the unfolding pathways of several membrane proteins, i.e. various rhodopsins [313,314,370-372] and different antiporters [311,312]. Here, SMFS was used to probe SteT, a member of the APC family. As with all membrane proteins investigated so far, the F-D spectra recorded upon mechanical unfolding of SteT showed a reproducible force peak pattern (Fig. 1C, D; Table 2). This characteristic F-D pattern can serve as a fingerprint of a membrane protein [437]. It was recently observed that the F-D spectra of the $\text{Na}^+:\text{H}^+$ antiporters NhaA from *E. coli* and MjNhaP1 from *Methanococcus jannaschii* showed an additional force peak upon ligand binding to the activated transporter which could be correlated to specific interactions established between Na^+ and deprotonated aspartic acid residues [311,400] in the Na^+ binding site [469]. In contrast, substrate binding to the antiporter SteT did not induce clear changes in the F-D pattern (Figure 5.5A, B). Thus, the binding of amino acids to an amino acid antiporter may be different than those of Na^+ binding to a $\text{Na}^+:\text{H}^+$ antiporter.

Unfortunately, a high-resolution structure of SteT or one of its homologues is not available. However, crystal structures of other amino acid transporters in complex with their amino acids have been determined [39,48]. These structures revealed various

ways for a transporter to bind an amino acid. For example in LeuT_{Aa}, a member of the neurotransmitter sodium symporter (NSS) family, amino acids of the partially unwound transmembrane α -helices I and VI coordinate the α -amino and α -carboxyl groups of leucine, while the leucine side chain resides in a hydrophobic pocket formed by transmembrane α -helices III, VI, and VIII [39]. Altogether, twelve amino acids from four transmembrane α -helices of LeuT_{Aa} were involved in leucine binding. Recent biochemical studies suggested that the cadaverine:L-lysine antiporter CadB from *E. coli*, an APC family member [261], forms a hydrophilic cavity using eight out of its twelve transmembrane α -helices [470]. Assuming that the substrate binding site is located within the translocation pathway, it seems feasible that multiple amino acid residues from several transmembrane α -helices contribute to ligand binding. This notion is supported by hydrophathy profile alignment of membrane transport proteins, which showed that APC transporters exhibit core structures similar to those of members of the NSS family [471]. Therefore, it may be assumed that the interactions established between ligand and SteT are distributed, such as observed for LeuT and CadB, and not highly localized, as in the case of Na⁺:H⁺ antiporters. Because SMFS measurements did not reveal discrete changes in the F-D spectra that would have indicated localized interactions of the substrate with SteT, it can be concluded that binding of L-serine and L-threonine establishes individually rather weak interactions with multiple amino acid residues.

5.4.2 SteT Unfolds Differently Compared to Other Membrane Proteins

Recent DFS studies showed that structural segments of bacteriorhodopsin, bovine rhodopsin, and NhaA are stabilized by single energy barriers [405,406,468]. On average, the transition state that separated the structural segments of these membrane proteins from their folded state was ~ 0.4 nm (x_u between 0.2 and 0.8 nm). Thus, it could be concluded that the structural segments had to be stretched by ~ 0.4 nm to induce their cooperative unfolding. This short distance leads to the assumption that rather short ranged inter- and intramolecular bonds had to be broken to induce unfolding and extraction of the structural segments of these membrane proteins. In contrast to this previous finding, the dynamic force spectra of substrate-free SteT were dominated by two linear regimes (Figure 5.6, left column), which indicated that every structural segment of SteT was stabilized by two energy barriers. The two energy barriers of substrate-free SteT exhibited quite different characteristics. The inner energy barrier was located close to the native basin (x_u between 0.21 and 0.36 nm), exhibited

fast transition rates (k_0 between 2.2 and 26.7 s⁻¹), and caused a high structural rigidity as judged by the spring constants (κ_{bond} between 1.06 and 2.84 N/m, Figure 5.8, Table 5.3). This indicates that the substrate-free SteT formed stiff and brittle structural segments that have been stabilized by short-ranged localized and directional interactions. The fast transition rates, faster than those measured for other membrane proteins [370,405,406], indicate a low kinetic stability of the structural segments. In contrast, the outer barrier was located far from the native basin (x_u between 0.74 and 4.98 nm), and exhibited slower transition rates (k_0 between 0.077 and 4.4·10⁻⁴² s⁻¹, Figure 5.8, Table 5.3). Thus, the structural segments of SteT showed an altered mechanical behavior when crossing the outer barrier compared to traversing the inner barrier.

Evans and Ludwig found two energy barriers at 0.7 and 1.2 nm when extracting biotinylated 1,2-distearoyl-*sn*-glycero-3-phosphoethanolamine (DSPE) from 1-stearoyl-2-oleoyl-*sn*-glycero-3-phosphocholine (SOPC) bilayers [472]. The authors concluded that the hydrophobic core of the membrane forms a barrier against the extraction of the hydrophobic lipid tail. If each leaflet of an SOPC membrane has a ~ 1.5 nm thick hydrophobic region [473-475], the transition state of outer energy barrier (~ 1.2 nm) correlates reasonably well with the thickness of the hydrophobic core [472]. The transition state position of the inner energy barrier (0.7 nm) was correlated with the position of the unsaturated bond in the oleoly chain [472]. Adapting this interpretation to membrane proteins, the relevant scale for hydrophobic interactions would approximate the thickness of the hydrophobic core of the lipid bilayer (~ 2.5 nm for DMPC [476]). Indeed, the distance of the transition states obtained for the outer barriers of structural segments at 70, 147, 237, and 302 aa were between 2 and 3 nm. In contrast, the structural segments located at 79 and 422 aa showed higher x_u values, ~ 4.7 and ~ 5.0 nm, that exceeded the thickness of the lipidic hydrophobic core. However, it should be considered that transmembrane α -helices of transporters, including APC superfamily members, can cross the membrane highly tilted [39,48,477]. Tilted helices bury longer polypeptide stretches within the membrane and, therefore, may cause larger x_u values. Thus, the narrow inner and the wide outer energy barriers observed for substrate-free SteT may characterize different unfolding processes. If this conclusion is correct, crossing the inner energy barrier may describe an unfolding step that has been induced by breaking specific short-ranged interactions e.g. stabilizing the tertiary or quaternary structure of individual segments. Because the transition rate of the inner barrier is quite substantial it may be assumed that this barrier can be also crossed in absence of a pulling force. In such a case the outer unfolding barrier would

establish a system that protects complete unfolding of the structural segment and thus might allow re-association of intramolecular bonds that have been broken. This outer barrier is kinetically much more stable compared to the kinetically unstable inner barrier. It may be further assumed that the outer barrier is stabilized by longer ranged interactions compared to the inner barrier. Applying a mechanical stress can force this structural segment to overcome its outer barrier to complete the unfolding process.

5.4.3 Substrate Binding Changes the Energy Landscape of SteT

To investigate how substrate binding changes the energy landscape of SteT, DFS in presence of L-serine and L-threonine was conducted. First of all, the position of the stable structural segments did not depend on the substrate binding, indicating that each structural segment unfolded independently and exhibited an intrinsic stability. However, comparison of the dynamic force spectra shows a dramatic change in the energy landscapes. The inner and outer energy barriers observed for substrate-free SteT changed to only one energy barrier in the presence of substrate. Substrate binding created energy barriers with transition states that were located between those determined for the inner and outer energy barriers of substrate-free SteT.

Distances between ground state and transition state are a measure of the conformational flexibility that a folded structure can adopt within the constricting energy well [478,479]. Thus, the shift from narrow inner barriers of substrate-free SteT to wider energy barriers in presence of substrate indicates an increased conformational flexibility of the structural segments of SteT. Since, in presence of L-serine or L-threonine, every structural segment of SteT changes its mechanical properties to favor functionally related structural changes of the antiporter (Figure 5.8, Table 5.3) this structural flexibility may be required to allow substrate transport. The alternate substrate access of an antiporter from one to the other membrane surface only occurs in the substrate-bound state [480]. Antiporters in the substrate-unbound state do not alternate access from one to the other membrane surface. Thus, the increased structural flexibility of SteT in the substrate-bound state results in an increased probability to alternate the substrate access from one to the other side of the membrane. In contrast, the substrate-free state of SteT is trapped in a more brittle and rigid conformation (Figure 5.9). It is suggested, that such restricted conformations favor the specific binding of substrates [481]. Substrate binding also lowers the unfolding rate of structural segments of SteT (compare k_0 values in Table 5.3). It can be concluded that substrate binding sets the structural segments into a deeper energy minimum [482],

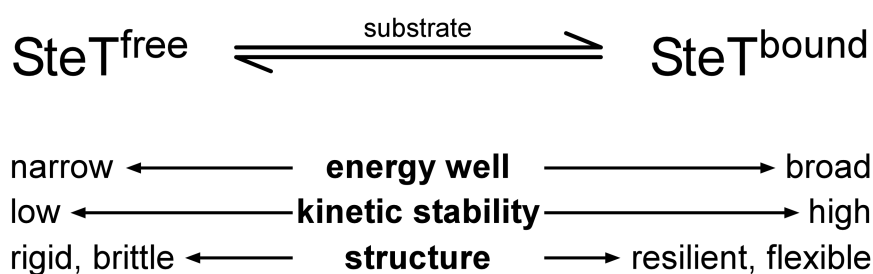


Figure 5.9 Energy landscape and mechanical properties of SteT changing upon substrate binding. In absence of substrate ($\text{SteT}^{\text{free}}$) the inner energy barrier of SteT shows a narrow energy well exhibiting a low kinetic stability that determines a rigid and brittle structure. The second outer energy barrier of $\text{SteT}^{\text{free}}$, is not shown. In presence of substrate ($\text{SteT}^{\text{bound}}$) the two energy barriers stabilizing every structural segment of SteT fuse into one single energy barrier that provides SteT with very different mechanical and kinetic characteristics. The energy barrier of $\text{SteT}^{\text{bound}}$ is broad and shows an increased kinetic stability that shapes resilient and flexible structural segments of SteT.

and thus, kinetically stabilizes SteT (Equation 5.3; compare k_0 and ΔG^\ddagger values in Table 5.3). Studies on soluble proteins showed that ligand binding can increase the midpoint of thermal unfolding transitions by several °C corresponding to a stabilization of the protein [483].

Albeit L-serine and L-threonine are structurally similar and show similar side chain properties, the additional methylene group in L-threonine seems to have some effect on the energy landscape of SteT. In presence of L-threonine, the energy barriers of the first six segments of SteT showed increased distances to their transition state, lower unfolding rates, and lower spring constants (Table 5.3). The last structural segment, detected at a contour length of 422 aa, revealed a smaller x_u and higher k_0 and κ_{bond} values in presence of L-threonine compared with L-serine. While the differences in x_u values were not significant, the unfolding rate for three structural segments (highlighted in bold in Table 5.3) changed significantly, demonstrating differing effects of the substrates on SteT. Functional studies on L-serine transport by SteT unveiled a slightly higher stimulating effect for L-threonine than for L-serine [271], indicating unlike SteT-substrate interactions for L-serine and L-threonine.

5.4.4 Hammond-Like Behavior Reflects Ground State Effects

According to Hammond's postulate [464] two similar structures should exhibit similar energies. For protein folding, this leads to correlation between the free energy of activation and the position of the transition state on the reaction coordinate [465]. Recently, DFS studies detected that the unfolding intermediates of bacteriorhodopsin at different temperatures and of different bacteriorhodopsin mutants show Hammond behavior [368,407]. Here, unfolding intermediates formed by the structural segments of SteT showed a Hammond-like behavior, i.e. the distance from the ground state to the

transition state increases with the free energy of activation. In the context of dynamic energy landscapes [478,482], Hammond behavior can be explained as follows. The DFS data shows that the force peaks denoting the unfolding intermediates of SteT did not change their position upon substrate binding. Thus, it can be concluded that substrate binding did not establish new strong localized interactions within SteT and did not change the unfolding intermediates of SteT. Nevertheless, analysis of the DFS data shows that the distance between the energy minimum and the transition state changes along with the free energy of activation. At first sight, this Hammond behavior points towards stabilization of the folded state. As pointed out by Sánchez and Kiefhaber [466,467] true Hammond behavior would require (structural) changes in the transition state while the ground and unfolded states would remain structurally unaffected and retain their position on the energy landscape. Since DFS reveals the distance between transition state and ground state, a ground state shifting away from a stable transition state would show the same effect as true Hammond behavior. Indeed, it was shown for soluble proteins that the transition state structure can be insensitive to changes in protein stability such as introduced by point mutations [466]. Doubtless, the ground state for SteT in absence and presence of substrate will be different. Combined molecular dynamics/Monte Carlo simulations showed ligand binding to cause a shift in the most frequently populated protein conformations and, thus, to redistribute proteins to a deeper energy well that has been created in the energy landscape upon ligand binding [482]. Consequently, the observed correlation between x_u and ΔG^\ddagger for SteT can be attributed to changes in the ground state and does not reflect true Hammond behavior. This implies that small differences in the substrate, e.g. a slightly longer amino acid side chain, could significantly alter energetics and conformations of the antiporter.

5.5 CONCLUSIONS

Inter- and intramolecular interactions shape the energy landscape that describes the conformational flexibility and kinetic stability of proteins. SMFS was used to investigate how substrate binding modifies the energy landscape of the serine:threonine antiporter SteT. Upon addition of substrate, SMFS did not detect large changes in the interactions that stabilized the structural segments of SteT. Therefore, substrate binding of SteT was mediated by multiple weak interactions rather than by a few strongly localized interactions. Although individually weak, together these interactions change the energy landscape of all structural segments. However, to which

extend substrate binding changes the energy barriers of individual structural segments remains intrinsic to the structural regions (Table 5.3, Figure 5.7B). From a structural point of view, it is hardly possible that the substrate interacts with all structural segments of the antiporter simultaneously. Thus, it remains to be determined which of these changes are mediated by direct interactions with the substrate and which ones result from indirect interactions.

In absence of substrate, the energy landscape showed that every structural segment of SteT was stabilized by two very different energy barriers. The co-existence of two energy barriers indicated that the structural segments were stabilized by two different mechanisms. The first energy barrier was dominated by short-range interactions that shaped a very narrow energy well and had a short lifetime. As a result, these structures have brittle mechanical properties that were kinetically less stable. This kinetic instability suggests a propensity of these structures to overcome the barrier stabilizing them in absence of any applied force. Such transitions would lead to the unfolding of the structural segment. However, each structural segment establishes a second energy barrier that shows an extended transition state and higher kinetic stability. In contrast to the inner barrier this outer barrier may be dominated by longer range interactions and permit reassociation of perturbed tertiary contacts.

In presence of substrate, the structural segment energy landscapes were simpler, having single energy barriers. Thus, ligand binding shifted the structural segments into a new, deeper energy well. Comparing the inner barriers of substrate-free SteT to the barriers of SteT in presence of substrate revealed that ligand binding kinetically stabilized SteT and changed its mechanical properties from a rigid and brittle structure to a more resilient and kinetically stable one (Figure 5.9). Whereas rigid structural segments constrain the conformational flexibility and, thus, favor the specificity required for specific amino acid binding, the enhanced conformational flexibility may be required for the antiporters to allow substrate binding at the other membrane surface and to facilitate substrate translocation.

PH-INDUCED CONFORMATIONAL CHANGES IN CX26 HEMICHANNELS MODULATED BY AMINOSULFONATES

6.1 INTRODUCTION

Gap junction channels (GJC) are dynamic macromolecular complexes capable of opening and closing the channel pore in response to a number of stimuli such as divalent cations, signaling molecules, phosphorylation, pH, and modulators of specific isoforms [484]. These regulated conduits for the passage of small molecules greatly influence homeostasis, development, ionic transmission, and other cellular processes. While substantial cell biological, biochemical, and biophysical evidence for the effects of these modulators exists, our knowledge about GJC at the structural level is limited, especially regarding the conformational changes occurring during pore gating in response to the various stimuli.

Each connexin channel is composed of two hexamers, the connexons, that dock at their opposed extracellular surfaces (see section 1.3). The cyclic arrangement of the subunits within the hexamers suggests that gating can occur by a rotation and translation of the transmembrane segments within all six monomers. It has been postulated that gating occurs as a "camera iris" shutter [485]. An alternate hypothesis has been proposed in which intra-connexin associations occur that either lead to a particle-receptor blockage at the cytoplasmic surface [225,486-488] or activate a physical gate near the extracellular surface ("loop gate") [489]. Recently, Sosinsky and co-workers unveiled a physically blocked cytoplasmic pore in a Cx26 mutant showing decreased permeability [488]. On the basis of the 3D crystal structure of wt Cx26, Maeda *et al.* [225] lately suggested that the N-terminal helix might be involved in formation of a blocking particle. This helix forms a funnel at the cytoplasmic entrance of the pore. Whether the proposed mechanisms correlate to the closure of fast and/or slow gates that have been characterized by electrophysiological methods (for a recent review see Ref. [238]) remains to be determined.

Intracellular acidification is one of the stimuli by which connexin channels open and close. Experimentally determined decreases in intracellular pH are known to decrease junctional electrical coupling in cardiomyocytes and in Purkinje fibers [236,490-492] as well as in teleost and amphibian embryos [493]. Stergiopoulos *et al.* showed that many, but not all connexins close in a pH sensitive manner when tested in the paired *Xenopus* oocyte system [494]. For example, Cx26 channels are highly pH sensitive in a physiological pH range but Cx32 are much less affected by pH changes. Homomeric hemichannels also displayed this pH regulation [495]. Differences in the pH regulation of gap junctions were attributed to the diversity of the primary sequence, particularly in certain regions such as the C-terminal tail, because the pH sensitivity of dodecameric channels could be modified only when they were composed of heterotypic combinations [495]. However, it is important to note that these experiments were done in whole cells and cannot distinguish between gating of the channel due to protonation of the connexin or protonation of modulators or ligands that bind to the connexin and then close the channel.

Bevans and Harris used a permeability assay system, the so-called transport specific fractionation (TSF, [496]), to test for functional pore size. Heteromeric Cx32/Cx26 connexons reconstituted into liposomes showed pH-dependent channel activity when suspended in aminosulfonate buffers³⁶. The pH sensitivity was directly attributed to binding of protonated aminosulfonates to Cx26 since homomeric Cx32 channels did not show this pH sensitivity [496,499]. However, it should be noted that Cx46 hemichannels in excised patches show pH sensitivity in the absence of any added cytosolic material [500].

Previously, Müller *et al.* had shown using high-resolution contact mode AFM imaging that force dissected Cx26 gap junction hemichannels reversibly open and close in response to Ca²⁺ acting as ligand [397]. As the cytoplasmic GJC surface proved to be too flexible for high-resolution imaging, Ca²⁺ induced conformational changes could be only observed on the more rigid extracellular hemichannel surfaces. The flexibility of the cytoplasmic surface is well documented not only by AFM studies [397,501,502] but also by electron microscopy and by other structural and biochemical methods (for a complete review of flexibility in the cytoplasmic domains see Ref [217]).

³⁶ The buffers used contained e.g. HEPES, TAPS, and MES as aminosulfonate compounds. One of the simplest of these aminosulfonate compounds is taurine, a naturally occurring ubiquitous cytoplasmic component [497,498].

In contrast to previous work, the extracellular surface was imaged at higher spatial resolution that allowed insight into the tertiary conformations of polypeptide loops connecting the transmembrane α -helices lining the connexon pore. Taking advantage of the AFM's capability to operate in physiological buffer solutions allowed the response of hemichannels on pH changes to be directly observed and visualized at extracellular connexon surfaces. This simplistic *in vitro* system allows to correlate the addition of modulating agents with the observed conformational changes. The high-resolution AFM topographs suggest that the extracellular connexin domains undergo an aminosulfonate-modulated conformational change that closes the connexon channel at the extracellular surface. This conformational change was fully reversible. From the high-resolution AFM topographs, a mechanism for closure of the extracellular "loop" gate was deduced, which is supposed to be different from the previously observed Ca^{2+} induced closure.

6.2 EXPERIMENTAL PROCEDURES

6.2.1 Cx26 Gap Junction Preparation

Gap junction membranes were isolated from stably transfected HeLa cells overexpressing Cx26 [503]³⁷. Gap junction membranes were prepared at the University of California, San Diego, USA, and kindly provided by G. Sosinsky and co-workers.

6.2.2 AFM Imaging

AFM topographs were recorded in buffer solution using contact mode. The AFM (Nanoscope E, Veeco, Santa Barbara, USA) was equipped with a fluid cell and 100 μm long oxide sharpened Si_3N_4 cantilevers (OMCL-TR 400, Olympus, Tokyo, Japan), which had a nominal spring constant of ≈ 80 pN/m. Prior to imaging, gap junction membranes were adsorbed to freshly cleaved mica (section 4.2.1) in buffer solution (200 mM NaCl, 2 mM EGTA, 1 mM PMSF, and HEPES (4-(2-hydroxyethyl)-1-piperazineethanesulfonic acid) at pH values as indicated in the text) [287,397]. High-resolution topographs were recorded at minimal contact forces of ≤ 50 pN, which were manually adjusted to compensate thermal drift [288,397]. Proportional and integral gains were adjusted manually to minimize the error (deflection) signal and to maximize the height signal [504]. When approaching a lateral resolution of ≈ 1 nm the

³⁷ The preparation procedure was slightly modified. HEPES buffer instead of Tris buffer was used, resulting in higher gap junction membrane yield and less contaminating material.

scanning speed of the AFM tip laid between 500 and 1.500 nm/s. Only topographs that showed identical structural features when comparing the simultaneously acquired trace and retrace direction scans were selected for further analysis. Topographs that showed asymmetric particles or indicated any kind of tip artifact were not analyzed.

6.2.3 Image Processing and Averaging

Topographs (512 × 512 pixels) were selected by the reproducibly imaged structural details of the protein and by comparing the simultaneously monitored height profiles acquired in trace and retrace direction. Correlation averaging was performed using the SEMPER image processing system [505]. A well-preserved unit cell was selected from the raw data and cross-correlated with the topograph [506]. Unit cells were extracted according to the peak coordinates of the cross-correlated topograph. Single particle averages were generated by translationally and rotationally aligning the unit cells to a reference connexon and then averaged. This correlation average was used as reference for refinement cycles [507]. Correlation averaged unit cells were six-fold symmetrized. To assess the standard deviation $\sigma_{k,l}$, individual unit cells were extracted according to the coordinates of their correlation peaks and were aligned rotationally as well as translationally before single particle averaging [508]. The standard deviation (SD) was then calculated from the averaged topograph $\mu_{k,l}$ for each pixel (k, l) for x^i particles [286]:

$$\sigma_{k,l}^2 = \frac{1}{N} \sum_{i=1}^N (x_{k,l}^i - \mu_{k,l})^2 \quad 6.1$$

These SD maps are displayed as an image in a one-to-one pixel correspondence with the correlation averaged topograph. The values range from 0.1 (black) to 0.35 nm (white) and the color table continuously ranges from black to white.

6.3 RESULTS

6.3.1 High-Resolution Imaging of the Extracellular Connexon Surface

Force dissection with AFM imaging provides high-resolution surface views of the extracellular surface. Figure 6.1A shows a gap junction plaque imaged by AFM in buffer solution. As reported previously by Müller *et al.* [397], Cx26 gap junctions exhibited a thickness of 17.5 ± 0.8 nm (average \pm SD, $n = 20$) while the surrounding lipid membranes were only 4.5 ± 0.6 nm high. These gap junction plaques exposed their cytoplasmic surfaces to the AFM tip while the extracellular surfaces were sandwiched

between the membranes embedding the connexons. To characterize the extracellular surface, the upper connexon layer of the plaque had to be mechanically removed by the scanning AFM tip (Figure 6.1B). At minimal forces of ≤ 50 pN applied to the scanning AFM cantilever, repetitive imaging is non-destructive and allows to reproducibly observe substructures of biological membranes in their native conformation [288]. However, at about 10 to 20-fold increased forces the scanning process caused mechanical removal of the upper layer of the gap junction plaque [397,452,509].

After removal of the upper layer, the exposed extracellular surface could be observed at high-resolution (Figure 6.1C). The AFM topograph showed the six-fold

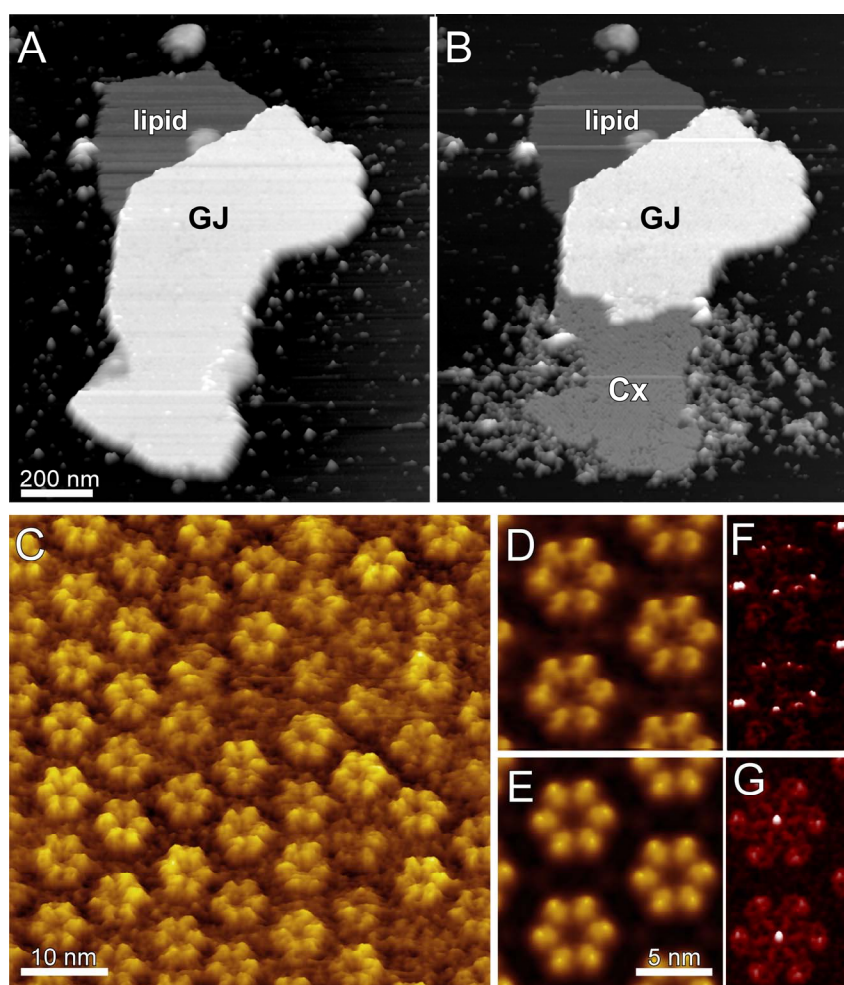


Figure 6.1 Force dissection of gap junction plaque and high-resolution AFM imaging. (A) Overview of a gap junction plaque (marked as GJ). (B) Same gap junction plaque but partially dissected, revealing a single-layered connexon membrane (marked as Cx). The gap junction membrane was dissected by enhancing the applied force from 50 pN (imaging force) to about 500-1000 pN during repeatedly scanning the sample. After removal the gap junction plaque was re-imaged. (C) High-resolution topograph showing substructural details of the extracellular connexon surface. Individual connexons showing six-fold symmetry were separated by 7.7 ± 0.3 nm. Correlation averaged connexon surface (D) and standard deviation (SD) map (F). Six-fold symmetrized correlation average (E) and SD map (G). AFM topographs were recorded in buffer solution (pH 6.0, 20 mM maleate, 70 mM NaCl, 2.5 mM KCl, 1 mM $MgCl_2$). Full color range of topographs corresponds to a vertical range of 25 nm (A and B), 3 nm (C, D, and E) that of the SD maps to 0.35 nm (F and G). All topographs are displayed as relief tilted by 5° .

symmetry of each connexon with its characteristic central pore. Each subunit of the connexon is thought to be formed by one connexin that showed substructural details [217]. The correlation average of the connexon surface (Figure 6.1D, E) showed their common structural details while the standard deviation (SD) map (Figure 6.1F, G) marked regions exhibiting an enhanced structural flexibility.

6.3.2 Observing pH-Induced Conformational Changes

pH-induced conformational changes on the extracellular connexon surface were first visualized at a constant electrolyte concentration (2mM EGTA, 1mM PMSF) and at a constant HEPES concentration of 10 mM (Figure 6.2). Prior to imaging, the membranes were absorbed onto the mica support using buffer containing 10mM HEPES, 2mM EGTA, 200mM NaCl, and 1mM PMSF. Connexons observed at pH 6.0 appeared very different to those observed at pH 7.0 and higher. However, it could happen that single connexons showed individual deviations among each other. For example, a small number of connexons (< 5 %) showed different channel diameters than others. To allow statistical relevant conclusions about the average structural conformation of a single connexon at a certain buffer condition single particle averages were calculated (Figure 6.2G, I, K, and M). The unprocessed topographs of single connexons and their corresponding averages did not show any significant differences in connexon shape or substructure. The majority of single connexons imaged (> 85 %) exhibited the same structural conformation as reflected by their average. Thus, it could be ruled out that the connexons imaged may have represented mixed populations of several structural states, but rather a single predominant configuration. Connexon averages were computed from AFM topographs recorded at pH 6.0 (Figure 6.2G), 6.5 (Figure 6.2I), 7.0 (Figure 6.2K), and 7.6 (Figure 6.2M). Averages calculated from connexons imaged at pH 8.0 and 8.5 did not show any significant deviation from that recorded at 7.6 and, therefore, are not shown. Regions of SD maps (Figure 6.2H, J, L, and N) exhibiting enhanced values indicated structural fluctuations of the connexon surface. All averages showed the 8° skew of the connexon lobes from the vertical axis characteristic of detergent treated samples [510]. While the overall appearance of the hexameric channel did not change, the diameter of the central channel significantly increased with increasing pH.

Besides measuring the channel diameters of averaged connexons, also those from single connexons were analyzed. The histograms suggest that the average channel diameter measured for a certain pH value reflects that of the majority (> 85 %) of the individual connexons (Figure 6.3). Under experimental conditions known to induce a closed channel [494,496], the channel entrance exhibited a maximum depth of 0.4 ± 0.1 nm with a diameter of only 0.6 ± 0.3 nm measured at full width half maximum (FWHM) height. The SD map of the average (Figure 6.2H) showed no maxima at the channel entrance suggesting that this area exhibited no enhanced structural flexibility. The surface structure of the connexon did not significantly change after increasing the pH to 6.5. However, the SD map of the closed connexon changed. The region at the

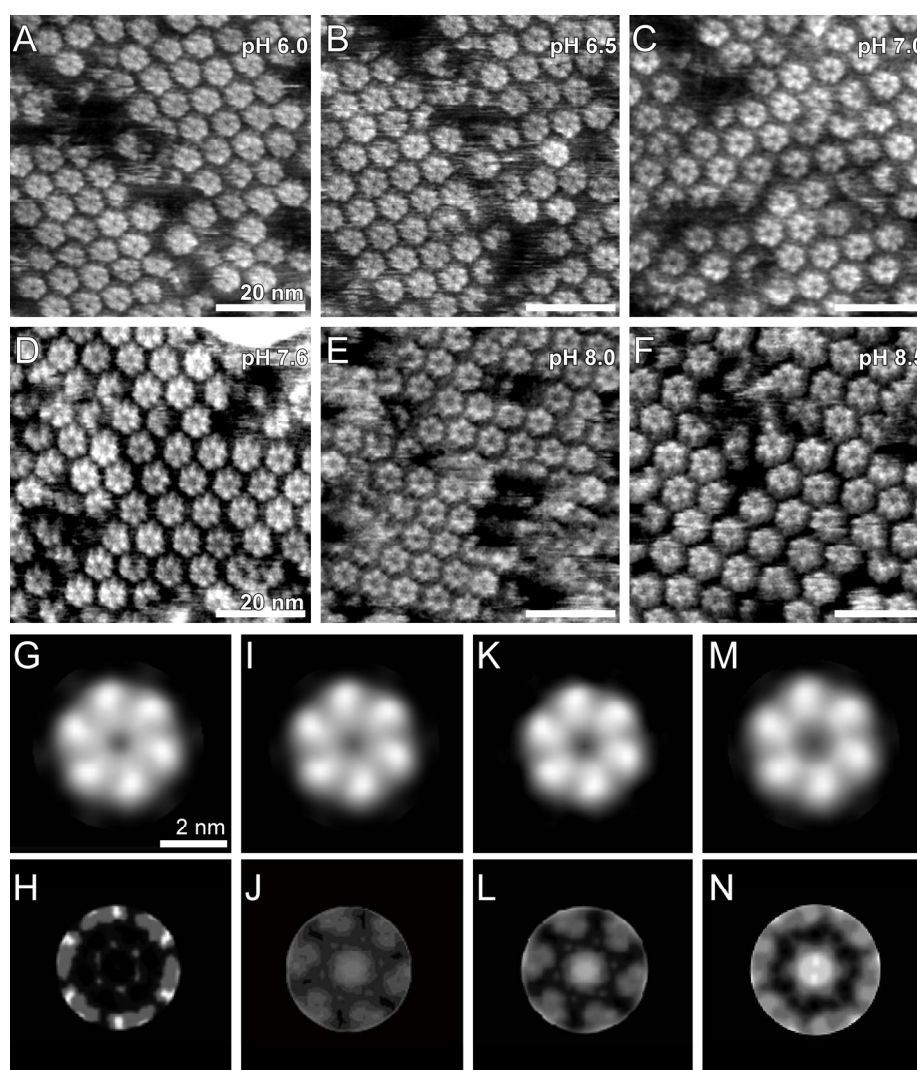


Figure 6.2 pH dependent conformational changes on the extracellular connexon surface. Connexons were imaged at pH 6.0 (A), pH 6.5 (B), pH 7.0 (C), pH 7.6 (D), pH 8 (E), and pH 8.5 (F). Correlation averages (G, I, K, and M) and SD maps (H, J, L, and N) were calculated from AFM topographs recorded at pH 6.0 (G and H), 6.5 (I and J), 7.0 (K and L), and 7.6 (M and N). The buffer solution in all experiments was 2 mM EGTA, 1 mM PMSF, and 10 mM HEPES. For each pH investigated, the adsorption and starting imaging buffer were identical. Full gray scale of topographs corresponds to a vertical range of 3 nm that of the SD maps to 0.35 nm.

channel entrance showed a slightly enhanced value of 0.15 nm (Figure 6.2J) indicating that the corresponding structures now exhibited some structural flexibility. This may also explain the slightly increased maximum depth of the channel (0.6 ± 0.2 nm; $n = 85$). At this pH the width of the channel entrance increased slightly to 0.9 ± 0.3 nm ($n = 91$). Increasing the pH to 7.0 further increased the width of the channel entrance (Figure 6.2K) to 1.3 ± 0.2 nm ($n = 85$). As a result of this opening, the AFM tip now could penetrate into the channel entrance detecting an average maximum depth of 1.2 ± 0.35 nm ($n = 40$). Furthermore, the SD map of the connexon surface (Figure 6.2L) increased its central maxima now indicating that the channel entrance had further increased its flexibility. At the same time the outer regions of the connexins were observed to slightly enhance flexibility as indicated by their SD increasing to 0.2 nm ($n = 40$). Increasing the pH to 7.6 (Figure 6.2D) finally widened the channel entrance (Figure 6.2M) to a diameter of 1.7 ± 0.3 nm ($n = 81$). Concomitant with the opening of the channel entrance, the SD map (Figure 6.2N) showed that this structural region further increased its flexibility to a maximum SD of 0.35 nm ($n = 40$). Interestingly, individual connexins showed an increased SD of 0.25 nm at their outer rims as well. Further increasing the pH to 8 (Figure 6.2E) and 8.5 (Figure 6.2F) did not significantly change the correlation averages or connexon structures of the extracellular surface (data not shown). It should be noted that "partially closed channels" had a diameter lying between that observed of fully opened and fully closed channels. AFM topographs showed that more than 85 % of the single hemichannels had no significant deviation in their channel diameter (Figure 6.3). This suggests that the partially closed hemichannels adopted a functional state that reflects an intermediate channel size between fully open and closed conformations and not a mixture of solely open and closed states.

To prove whether the observed conformational change was reversible the pH was decreased to 6.0 after the channels were fully opened at pH 9.0. The AFM recorded topographs showed that the previously opened pore now re-closed. That suggests a fully reversible conformational change. Cycles of pH changes were often repeated more than 4 times. Table 6.1 summarizes the data for the measurements of inner pore diameter and channel entrance depth for the different pH values.

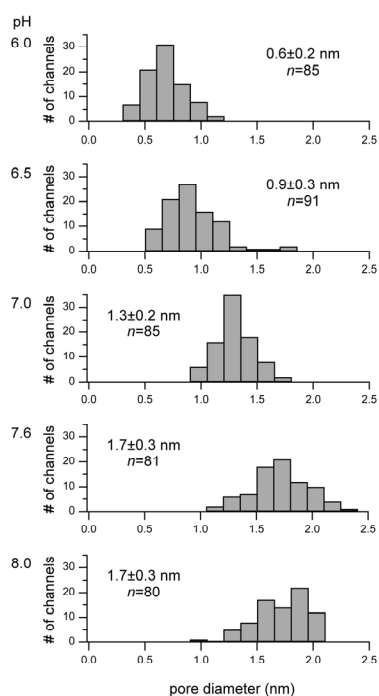


Figure 6.3 Histogram of pH-induced changes of channel diameters taken from AFM topographs of Cx26 connexons. Topographs were taken from Cx26 membranes in 10 mM HEPES buffered solutions such as described for Figure 6.2. At minimum 80 connexins were measured for each histogram. The histogram distributions indicate that the pH-induced increase of the channel diameter is best represented by a process in which the channels gradually switch from the closed to the fully open state.

pH	Maximum channel entrance depth (nm)	Channel entrance diameter (FWHM) (nm)
5.5	not determined	0.6 ± 0.3
6.0	0.4 ± 0.1	0.6 ± 0.3
6.5	0.5 ± 0.3	0.9 ± 0.3
7.0	1.0 ± 0.4	1.3 ± 0.2
7.6	1.1 ± 0.3	1.7 ± 0.3
8.0	0.9 ± 0.2	1.7 ± 0.3
8.5	0.9 ± 0.2	1.6 ± 0.3

Table 6.1 Summary of the data on the pH dependent channel entrance maximum depth and channel entrance diameter measured at the extracellular connexon surface.

6.3.3 Conformational Changes Are Not Dependent on HEPES Concentration

HEPES belongs to a class of aminosulfonate compounds that have been shown to act as modulators of the Cx26 channel [496]. Following the lead of Bevans and Harris [496], it was tested whether the observed conformational change is due solely to pH or to binding of aminosulfonates, which modulate a pH conformational change, to Cx26. Therefore, the HEPES concentration was increased to 50 mM and the extracellular connexon surface was imaged (Figure 6.4). Surprisingly, AFM topographs recorded at pH 8.0 (Figure 6.4A) and at pH 9 (Figure 6.4B) showed that the open state of the connexon channels was not influenced by the increase in protonated HEPES. For both pH conditions, the averages of the inner channel diameters measured from single connexons were 1.6 ± 0.3 nm ($n = 83$) such as observed for the open connexon conformation (Figure 6.2 and Figure 6.3).

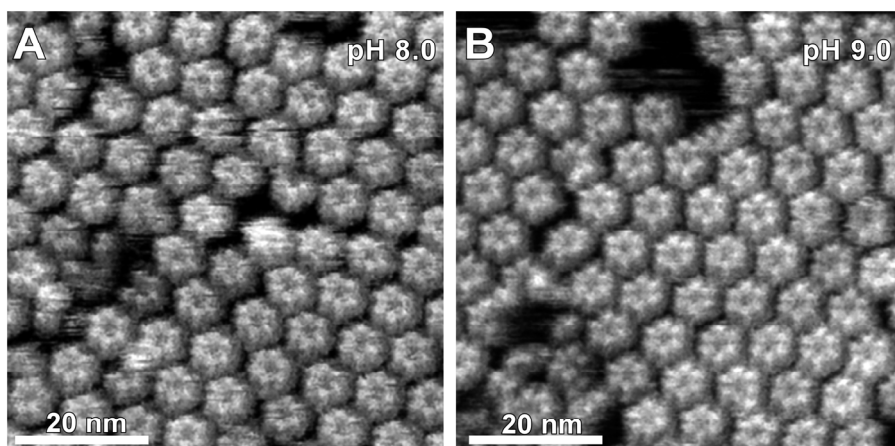


Figure 6.4 Connexon channels do not change conformation upon enhancing HEPES concentration. Extracellular surface of connexon Cx26 imaged at pH 8.0 (A) and pH 9.0 (B) buffered with 50 mM HEPES. The raw data showed no significant deviation from connexons imaged at pH ≥ 7.6 in 10 mM HEPES (compare with Figure 6.2). Full gray scale of topographs corresponds to a vertical range of 3 nm.

Additional experiments were performed in an effort to close open channels with higher HEPES concentrations at pH ≥ 7.6 . The sample was adsorbed to the mica surface at 50 mM HEPES, pH 7.6, and AFM imaging was performed with the same buffer. At this pH, the effective concentration of protonated HEPES would be maximal at ~ 25 mM. Under these conditions, the channels remained open. Open channels were also observed at HEPES concentrations up to 200 mM at pH 7.5 (data not shown). In each case, a positive control (10 mM HEPES, lowering the pH) was included to ensure the functionality of the sample. Alternatively, adsorption at pH 6.5 (50 mM HEPES) was performed to ensure HEPES binding and then increased the pH to 7.5 for AFM imaging. In this case, the topographs revealed open channels at pH 7.5 but partially closed channels at pH 6.5. Therefore, 10 mM may be the concentration at which binding is at saturation conditions in these experiments.

6.3.4 No Conformational Change Occurs in the Absence of Aminosulfonates

According to previous findings [496,499], the pH dependent gating of Cx26 could be only observed in presence of aminosulfonate-containing compounds. To test this hypothesis and to prove that the conformational change observed can be indeed correlated to the gating mechanism, connexin preparations were imaged at different pH buffered in non-aminosulfonate buffers. AFM topographs of maleate buffered connexons showed that they did not change their conformation at pH values of 6.0, 6.5, or 7.0 (Figure 6.5A-C). Similarly, the extracellular connexon surface apparently did not show a pH dependent change in their channel diameter if the aqueous solution was buffered with potassium phosphate (KH_2PO_4) (Figure 6.5D-F). All topographs (Figure

6.5A-F) and correlation averages (Figure 6.5G-N) have in common that the channel entrance appeared widely opened throughout the pH ranges imaged (compare to Figure 6.2).

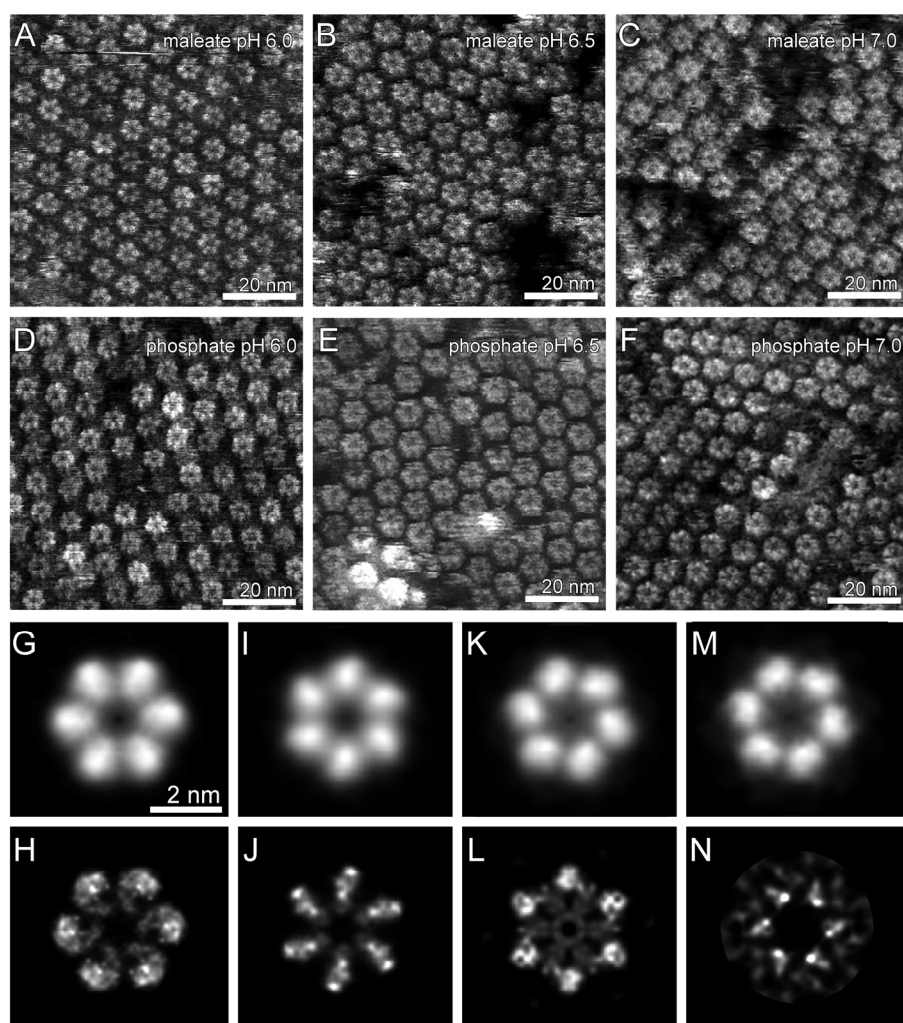


Figure 6.5 Cx26 channel remains open in absence of aminosulfonate. Extracellular connexon surface imaged at pH 6.0 (A), 6.5 (B) and 7.0 (C) in aqueous solution buffered with 20 mM maleate revealed an open state. Imaged at different pH values of 6.0 (D), 6.5 (E) and 7.0 (F) buffered by 20 mM phosphate, the extracellular connexon surface showed an open pore. Correlation averages (G, I, K, and M) and SD maps (H, J, L, and N) were calculated from the AFM topographs recorded at pH 6.0 buffered with 20 mM maleate (G and H), pH 7.0 buffered with 20 mM maleate (I and J), pH 6.0 buffered with 20 mM phosphate (K and L), and pH 7.0 buffered with 20 mM phosphate (M and N). Full gray scale of topographs corresponds to vertical range of 3 nm that of the SD maps to 0.35 nm.

6.3.5 Quantitative Analysis of the Channel Closure

The diameter of the average connexon decreased gradually with pH (Figure 6.6A). While the depth of the channel decreased concomitant with an increase in the width of the connexon lobes, the overall diameter of the connexon itself did not change (Figure 6.6B). This is also reflected in the difference image between the fully closed (pH

6.0, Figure 6.7A) and fully open (pH 7.6, Figure 6.7B) averages shown in Figure 6.7C. In this difference image, positive differences are displayed as red and negative differences as black. The medium red level reflects no differences. It is also clear from this difference image that the extracellular region of the subunits rotate by $\sim 6.5^\circ$ between the open and closed states (Figure 6.7A,B), thereby changing the diameter of the pore. A previously published hemichannel structure shows a narrowing of the connexon pore at the extracellular end that may be part of a physical gate closing upon acidification [511].

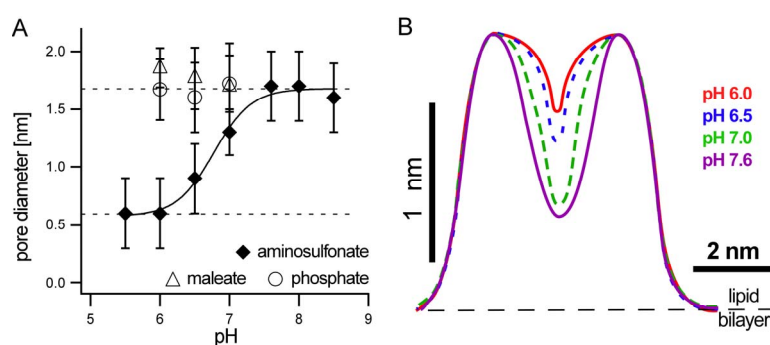


Figure 6.6 Analysis of pH-induced closure of Cx26 hemichannels. (A) Pore diameter versus pH for the three buffers tested here. Diameters were measured at FWHM depth of the channel. Each diameter is represented by its mean \pm standard deviation as measured from single connexons (see Table 1) that were imaged at different pH in aqueous solution buffered with 10 mM HEPES (closed diamonds), 20 mM maleate (open triangles), or 20 mM phosphate (open circles). (B) Two-dimensional profile of the channel pore at different the pH values. Note that while the channel entrance becomes shallower, the connexon diameter does not change significantly.

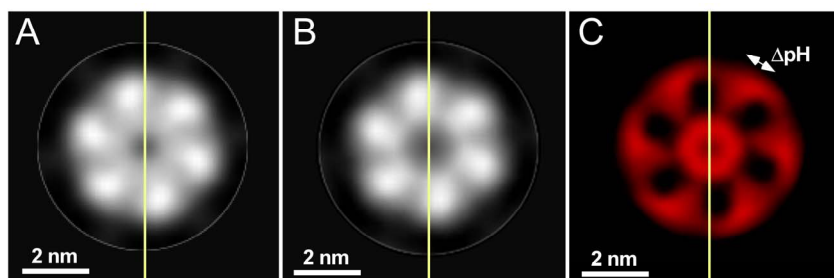


Figure 6.7 Model of pH-induced closure. This mechanism involves the conformational rotation of the connexon lobes between closed (A) and open (B) as well as internal rearrangements within extracellular vestibule that acts like a physical gate. (C) Difference map calculated between fully closed and fully open states. The differences are highlighted using a 7-step black to red scale where bright red shades reflect structures detected in the closed state but absent in the open one. Dark red reflects no differences and dark red to black shades indicate structures in the open state that were missing in the closed one.

6.4 DISCUSSION

In this study, the molecular mechanisms by which Cx26 hemichannels respond to H^+ ions has been examined. An AFM equipped with a buffer chamber allowed Cx26 membranes under physiological conditions to be observe at high-resolution.

Analogous to the TSF system of Harris and co-workers [512] or the excised patch experiments of Verselis and colleagues [240], this is a reductionist system. Limiting the number of variables in the imaging procedure makes the results complementary to other pH studies done in whole cells [237,494]. The data presented in this chapter show that Cx26 hemichannels close in response to acidification, but only in the presence of an aminosulfonate buffer suggesting that the aminosulfonate cation acts as a modulator or ligand to specific sites on the Cx26 protein. In addition, the data indicates that the aminosulfonate binding site is located on the cytoplasmic surface and that this signal is transduced to effect pore closure at the extracellular surface. It should be noted that the gating observed is not due to clustering of hemichannels in 2D crystals because Bevans and Harris first identified this effect in Cx26/Cx32 hemichannels inserted into liposomes at concentrations of ~ 1 hemichannel per liposome [496].

6.4.1 Aminosulfonates Are Required to Induce Closure During Acidification in Isolated Cx26 Gap Junction Hemichannels

The results presented confirm previous findings of Harris and Bevans [496] that aminosulfonate (HEPES) binding to Cx26 modulates the acidification-induced closure of hemichannels. The "titration" curves obtained for pH-induced closure (Figure 6.6A) closely follow the sigmoidal, gradual plots obtained by either electrophysiology [494] or permeability measurements [496]. It is yet unknown whether the sigmoidal shape indicates a cooperative mechanism among the six connexin subunits [513]. However, another AFM study of the Ca²⁺ induced closure of Cx43 hemichannels reconstituted into lipid vesicles reported an all-or-none effect [514].

Topographs recorded in non-aminosulfonate buffers do not reveal any pH dependent conformational change. Binding of aminosulfonates has been shown to occur at the C-terminus [515]. Incomplete binding of HEPES to the cytoplasmic domains that face the mica surface may explain why in topographs recorded at low pH a minority species of channels show a wider diameter ("open" state) while the majority of channels have a smaller opening ("closed" state) at their extracellular surface. It is possible that some connexins may have bound HEPES while others did not due to steric hindrance of the aminosulfonate-binding site on the C-terminus. Since non-aminosulfonate buffers could not induce pH dependent pore closure, binding of HEPES is required for pH-induced closure. If HEPES is sterically hindered from binding to the C-terminal tail or if the binding site has been altered by the interactions

of the cytoplasmic domains with the mica support, then increasing the HEPES concentration will have no effect.

In this study, gap junctions that were absorbed to mica at 10 mM HEPES and subsequently exposed to 50 or 200 mM HEPES did not close the pores. This is in contrast to the results of Bevans and Harris [496] where raising the protonated HEPES concentration closed the channel. The most likely explanation is that at this concentration and with homomeric Cx26 channels, enough HEPES binding sites are saturated to effect a conformational change.

6.4.2 pH Gating of Connexins

Chemical gating has been extensively studied in cell-cell channels [516,517]. Typically, CO₂ has been used as the acidification agent in whole cell experiments and the term is often used interchangeably with pH gating [238]. It has been proposed that calmodulin plays a role in modulating chemical gating [517] by acting as a "cork" to plug the channel entrance at the cytoplasmic surface. Here, the effects of direct acidification in presence of different buffers rather than with CO₂ were observed using AFM imaging.

Channel closure by H⁺ ions is a common gating mechanism among the connexin family. Some members such as Cx32 channels are more pH independent than Cx26 channels that are highly sensitive to pH changes within a physiological range. Other isoforms such as Cx43 or Cx45 show an intermediate sensitivity to acidification [494]. For cardiac connexins (Cx43, Cx40, and Cx45), Stergiopoulos *et al.* [494] demonstrated that truncation of the C-terminus significantly decreased the response of intact channels to acidification. In a study comparing Cx46 channels expressed in oocytes and Cx46 hemichannels in excised patches, Verselis and co-workers [240,500] showed that Cx46 hemichannels act similarly to intact channels and close reversibly with acidification. The site of action for H⁺ is localized to the cytoplasmic domains. The measured gating kinetics are slow (tens of milliseconds). It was also noted that a "pH inactivation" occurred whereby the number of hemichannels re-opening with increased pH decreased every cycle. Here, such an effect could be observed as well. Whereas the opening and closure of most Cx hemichannels was fully reversible, some individual channels remained in their closed state and re-opened much later than the others. Such pH cycles repeatedly watching the closure and opening of hemichannels could be repeated many times (> 4).

Connexons have unique functions (reviewed in [518]) that are different from the ones served in docked channels. It has been proposed that two docked hemichannels act in series [240] so the results obtained for connexons may be extrapolated to intercellular channels. Hemichannel plaques have been imaged with AFM in isolated preparations [519] and using freeze fracture and thin section electron microscopy in *Xenopus* oocytes expressing exogenous Cx50 [520]. *In vivo*, Cx26 hemichannels have been demonstrated to be expressed in transfected tissue culture cells [521] and in retinal horizontal cells [522,523]. In recent work by Harris and co-workers [515], HeLa cells were stably transfected with combinations of Cx26 and Cx32 with and without a C-terminal tag. Assayed by a parachute dye coupling assay, dye transfer through native heteromeric Cx26/Cx32 or Cx26/Cx32-tag intercellular channels was significantly reduced in the presence of 10 mM taurine in the media. HeLa cells possess a plasma membrane bound taurine transporter so that cytoplasmic taurine levels become elevated when taurine is added in excess to the cell culture medium. Tao *et al.* showed that tagged Cx26 heteromeric channels were unaffected by the increased taurine concentration. Presumably, the taurine binding site is located at the distal end of the C-terminus and the added tag sterically blocks binding [515]. Membrane-impermeable HEPES blocked the taurine-induced inhibition because it obstructs the taurine transporter. Following up with simple scrape-dye loading assays [524] on the Cx26 over-expressing HeLa cells used prepare the membrane patches for this AFM study, Sosinsky and co-workers also saw a decrease in dye transfer with 10 mM taurine in the media (G. E. Sosinsky, personal communication). Therefore, the pH gating observed here for "undocked" Cx26 hemichannels is relevant and may be comparable to that seen in Cx26 gap junction channels. In summary, these results suggest that the binding site is most likely on the cytoplasmic side since the extracellular domains in intercellular channels are typically inaccessible to ligands, such as peptides or antibodies.

6.4.3 Mechanism of Channel Closure at the Extracellular Surface Gate

Mechanisms to explain the opening and closing of connexin channels have been proposed based on the hypothesis that there are two different physical gates: one at the cytoplasmic surface and one at the extracellular surface. High-resolution topographs of the cytoplasmic surface of Cx26 indicate a unique surface domain structure [397] containing both the N and C termini and cytoplasmic loop. It is not known if the short C-terminus interacts with the cytoplasmic loop although C-terminal tagging of Cx26 in

heteromeric Cx26/Cx32 hemichannels and gap junctions eliminates the aminosulfonate-modulated pH dependent closure. Cx32, a much more pH insensitive connexin, is not affected by aminosulfonates [496] and presumably, does not contain an aminosulfonate binding site. Since the transmembrane and extracellular domains are highly conserved among connexins, the ligand-binding site would most likely reside in the variable C-terminus of Cx26. This part of the sequence is not conserved in Cx32. Therefore, a two-step process is proposed where the aminosulfonate first has to bind to a C-terminal domain before a pH-induced conformational change can occur.

Since the high-resolution topographs reveal only the topology of the extracellular surface [397], in the following what may be occurring at the extracellular gate is addressed. Two mechanisms have been postulated for gating of the extracellular gate of connexons. The first is that of Unwin and co-workers, whereby the pore closes by pivoting and tilting of the subunits from a stationary extracellular end [485,525]. This model postulates that there is very little change in the channel opening at the extracellular end but that rotation of individual subunits causes the channel diameter to become narrower. Concomitant, the channel length is slightly increased as well [229]. The second mechanism that includes two distinct gates, a fast and a slow reacting, respectively, was deduced from single channel conductance measurements of Cx46 hemichannels. It was proposed by Trexler *et al.* [489] that the fast gate was located closer to the cytoplasmic surface and the slow gate closer to the extracellular surface. The fast gate has been proposed to be the cytoplasmic gate that acts by a receptor/ligand mechanism [487]. The extracellular voltage gate was postulated to form a "loop gate" in isolated hemichannels and a cytoplasmic "cell-cell channel" gate for paired, docked connexons [489]. It was shown using an electrophysiological analysis, that these slow component currents seen in hemichannels were similar to those observed during early cell-cell channel docking events. The term "loop gate" was coined because Trexler *et al.* [489] proposed that the main structural elements involved in docking are the extracellular loops.

Comparison of the correlation averaged structures reveals a 6.5° rotation of the subunits between pH 6.0 and 7.6 (Figure 6.7A and B). While Unwin and co-workers [485,525] predicted this rotation of the subunits, there was no observable change in the connexon outer diameter as would have been predicted by the Unwin model. Such a consistency of the connexon diameter would argue for the "loop gate model". Evidence from substituted cysteine accessibility method (SCAM) studies have shown that the loop gate is extracellular to amino acid L35 in Cx46 and that the gate is localized at the

extracellular end of the channel [526]. However, the electrophysiological data cannot discern if there is a rotation of the subunits in concert with this extracellular gate. More recent three dimensional reconstructions [224,511] contain a constriction of the pore approximately 3/4 from the cytoplasmic surface opening. In both these 3D structures, the pore does not appear to be closed and the physiological state of the channel is ambiguous. In the structure by Unger and co-workers [224], the channel has been speculated to be in a closed or partially closed state because the crystals were obtained in the presence of oleamide, a compound that was demonstrated to close Cx43 channels in vivo [224]. The AFM topographs support the model of a physical gate close to the extracellular surface because additional to the pore diameter that decreases upon acidification also its depth is shallower as probed by the AFM tip (see Figure 6.6B and Table 6.1).

6.4.4 Connexon Extracellular Surface Is More Rigid When the Extracellular Gate Is Closed

As recently extensively reviewed [217], there are several lines of evidence that the extracellular domain is fairly rigid. Lately, the 3D structure of wt Cx26 revealed the structure of the extracellular domain [225] (also see section 1.3.1). In contrast to previous models, the extracellular loops E1 and E2 do not form two concentric β -barrels, as has been previously proposed [527]. Still, the extracellular loops E1 and E2 interdigitate with those from symmetry related partner connexins, a topology supported by the AFM images presented in this work. Our AFM topographs indicate that there is some flexibility dependent on the open state of the channel and that this flexibility is not homogenous. In the open state, this flexibility is highest at the channel entrance, minimal at the adjacent structures, and again higher at the outer rim of the structures. The fact that channel flexibility increases with diameter has been observed before with Ca^{2+} dependent closure [397].

6.4.5 The Relevance of pH Gating in Tissues and Organs

Tissue cells use intracellular acidification as a mechanism to invoke regulatory processes. With respect to gap junction function, two systems are worth noting because of their relevance to disease. The first is pH-dependent gating of Cx43 in heart gap junctions and the second, relevant to the isoform used in this study, is the effect of pH in the inner ear with implications for hearing dysfunction or loss.

Cx43 channels close in response to acidification [513]. This has implications for the functioning of cardiac tissue where Cx43 is the most frequent connexin. During ischemic events, a drop in intracellular pH (pH_i) occurs in heart [528] and brain tissue [529]. Cardiac ischemia leads to electrical uncoupling [530] as well as to dephosphorylation and internalization of Cx43 [531]. Gating of connexin channels by lowered pH_i is likely to contribute to arrhythmogenesis in acute myocardial infarction. Connexin channels close and thereby eliminate electrical coupling when the cytoplasm is acidified by the accumulation of lactic acid that is due to anaerobic metabolism [532]. However, this uncoupling of cells may serve a more important role of isolating normal from damaged heart tissue cells, thus limiting the spread of acute ischemic injury [533].

Cases of patients with hereditary non-syndromic deafness due to mutations in the Cx26 sequence have pointed towards the important role that these gap junction channels play in homeostasis and most likely in potassium ion recycling [534,535]. Cx26 and Cx30 are co-expressed in the epithelium and connective tissue of the cochlea. Cx26-based intercellular communication in the inner ear has been postulated to play a homeostatic role in hearing analogous to the function that Cx32 plays during action potential generation in nervous tissue [536,537]. It has been proposed that gap junctional communication restores the ionic balance after a nerve potential has been generated and that dysfunction of Cx26 channels results in exotoxicity leading to inner ear damage [538]. While the role of pH gating in the inner ear has not been well investigated, a study by Ikeda and Morizono suggested that CO_2 levels influence the acid-base regulation of inner ear fluids through the cochlear round window and that changes in CO_2 levels and pH can effect cochlear function [539]. In severe cases, this might lead to sensorineural hearing loss that has been demonstrated in cases of patients with secretory *otitis media* [540].

6.4.6 The Importance of Taurine in Tissues and Organs and Co-Expression with Cx26

The HEPES buffer used in this series of experiments belongs to a class of compounds known as aminosulfonates. The simplest of the aminosulfonates is α -aminoethanesulfonic acid, also known as taurine which is one of the most abundant low molecular weight organic compounds many animals [497]. In mammals, significant cytoplasmic taurine concentrations are ubiquitous. The highest concentrations are found in heart, brain, muscle, and particularly in retina. The concentration in these tissues is at millimolar levels; however, for HeLa cells the

expected concentration would be in the mid-micromolar range [497]. In many cell types, there are active taurine transporters in the plasma membrane [541]. It is interesting to note that heart and muscles do not contain Cx26, whereas astrocytes and leptomeningeal cells do contain this isoform [542]. This suggests that maybe an inverse relationship between tissues expressing Cx26 and those containing cytosolic millimolar amounts of taurine exists. Hence, tissues containing lower levels of taurine could modulate Cx26 channel function in much more regulated manner. It has been hypothesized that taurine functions to aid in osmoregulation, especially in excitable tissues rich in membranes [543] where high, transient ionic fluxes are accompanied by osmotic imbalances. Taurine modulates many Ca^{2+} dependent processes (for a review refer to Ref [497]) although this is thought to occur through indirect processes. Another function for taurine as an antioxidant has been proposed [544]. Harris and co-workers along with the experiments presented here have demonstrated a potential biological role for aminosulfonate binding to Cx26. A subject for further investigations is to explore whether other connexins highly expressed in excitable tissues show a taurine-modulated acidification-induced closure in whole cells where taurine can exist in millimolar concentrations and whether these isoforms can bind this compound or if taurine binding is unique to Cx26.

6.5 CONCLUSIONS

Gap junctions are highly regulated macromolecular assemblies. High-resolution AFM imaging was exploited to investigate the pH-induced closure of Cx26 connexons. In presence of aminosulfonate compounds such as HEPES, acidification of the buffer solution resulted in channel closure that could be observed on the extracellular side of the channel. This suggests that the responsible gate is located at or close to the extracellular surface. Single-particle analyses of topographs recorded at different pH conditions revealed that Cx26 connexons close and open gradually in response to pH changes. In concert with the unaffected outer connexon diameter at different pH, the results presented here support the "loop gate model" model. A slight rotation along the six-fold symmetry axis was found to be associated with channel gating.

In the absence of aminosulfonate compounds, however, acidification did not affect the channel diameter at all, underscoring the requirement of aminosulfonate compounds for pH gating of Cx26 connexons. Thus, the intracellular taurine

concentration could be exploited to tune the pH sensitivity of Cx26 gap junction channels *in vivo* in a tissue-specific manner.

OUTLOOK

Invented in 1986 [273], AFM is a fast emerging technology that has been the source for development of a huge variety of applications that are used to investigate both biological and non-biological specimens. Just like any other technique, AFM is constantly improving through progress on the level of instrumentation but also through the assays developed to address specific questions.

Surface imaging has been the original application of AFM. Since then and especially during the past few years AFM imaging has made great progress. Various imaging modes, such as non-contact [279] and multifrequency [545,546] imaging, and high-speed microscopes [547-553] have been developed. These microscopes are just about to reach the stage of being commercially available. Certainly, in the future, these methods will be of increasing importance, since they will allow to investigate more fragile specimens³⁸ or to study dynamic processes (such as Cx26 hemichannel pore closure) at time scales not accessible to present AFMs³⁹.

From the beginning 1990s on, the AFM has been increasingly used to measure forces, e.g. of ligand-receptor pairs [308,554], cell adhesion [307], DNA [335] and polymer stretching [319,323], and (membrane)protein unfolding [313,315]. These experiments provided intriguing insight into underlying interactions and mechanisms and how these are related to function of the investigated system. Since then, SMFS has proven to be a valuable tool for studying the unfolding and the interactions stabilizing membrane proteins as well as the underlying energy landscape. Moreover, functionally related changes within membrane proteins could be revealed [406,437] (chapter 5). The

³⁸ Multifrequency but especially non-contact AFM significantly reduce the force applied to the specimen during scanning, resulting in less sample deformation. Consequently, samples which would be disrupted by conventional AFM imaging techniques could be investigated using these novel approaches.

³⁹ Recording a high-resolution AFM topograph using contact mode AFM typically takes ~90-100 s, while high-speed AFM can reach imaging rates of > 10 images/s. Still, images recorded with a high speed AFM usually contain less pixels and still do not reach the resolution obtained by recent slow imaging modes.

following sections briefly describe possible future experiments that aim for a better understanding of transmembrane transport proteins and membrane protein folding.

7.1 EFFECT OF LIGANDS AND INHIBITORS ON TRANSPORT PROTEINS

Motivated by the studies of Kedrov *et al.* on the Na⁺:H⁺ antiporters NhaA and MjNhaP1 [311,400,401,406], the effect of ligand binding to the serine:threonine antiporter SteT has been investigated (chapter 5). Interestingly, the effects of ligand binding to SteT and NhaA or MjNhaP1 were different, which could be attributed to the marked differences in the nature of the ligands (amino acids and sodium ions). The disagreement of the effects that ligands have on transporters calls for further investigation. Thus, it would be desirable to test the impact of ligands but also inhibitors on the interactions stabilizing various transmembrane transport proteins and the underlying energy landscapes. To obtain a comprehensive impression of the consequences of ligands binding to transporters, several members of different transporter families should be investigated. However, testing a large number of different proteins, ligands, and inhibitors will require automating data collection and analysis.

Continuing the collaboration with the group of D. Fotiadis in Berne, a bacterial di- and tripeptide transporter will be the next protein to be studied. It will be interesting to see, whether di- and tripeptide binding will show different effects and what will be the impact of inhibitors like monomeric amino acids and tetrapeptides.

7.2 MEMBRANE PROTEIN FOLDING

Over the last decade, SMFS has been established as an appealing approach to study membrane protein unfolding, circumventing issues arising from classical (un)folding studies due to the hydrophobic nature of membrane proteins (see section 1.2.2). Conversely, SMFS has been rarely used to study folding of membrane proteins. Indeed, such folding studies are limited to bR and NhaA [312,399,408]. Moreover, although providing meaningful insight into *in vitro* folding mechanisms of these proteins, refolding was initiated from partially unfolded proteins, i.e. the last structural segment of the protein remained inserted into the membrane. As a result, the unfolded

peptide was strongly linked to the membrane and the remnant secondary structure as well as the surrounding proteins⁴⁰ could facilitate folding.

For systematic studies on how transmembrane α -helices insert into lipid membranes, reductionist systems are required that allow the role of individual amino acids on the insertion process to be deciphered. Wimley and White established a biophysical hydrophobicity scale for amino acids measuring the partitioning of small peptides between an aqueous and a hydrophobic phase [125]. Similarly, von Heijne and co-workers tested the impact of different amino acids on the capability of peptide segments to adopt a transmembrane topology using an *in vitro* translation system. This biological hydrophobicity scale agrees remarkably well with the biophysical Wimley-White scale [101,128] (see section 1.2.1.2 – The "Four-Step" Model). Still, a linking element is missing. While the biophysical approach probed small peptides, comparatively large peptide segments were probed to establish the biological scale. To date, no systematic study on the spontaneous insertion of oligopeptides into lipid membranes without an aiding translocon have been published.

Taking advantage of the single-molecule sensitivity of force spectroscopy, it might be possible to probe insertion of single transmembrane segment-forming peptides. For such an experiment, the peptide should be covalently attached to the AFM tip. However, synthesis of such hydrophobic peptides might be difficult. Moreover, problems like aggregation and cantilever modification will have to be tackled.

Conceptually, a modified AFM tip would be approached and held for a certain time close to the membrane surface to allow peptide binding to and insertion into the bilayer. Evaluating the probability of insertion of hydrophobic peptides with single amino acid replacements should give information of the energetic contribution of single amino acids to membrane insertion. It will be interesting to see how such a hydrophobicity scale relates to the Wimley-White and the biological scale. Moreover, recently, a theoretical framework estimating the association kinetics of single molecules tethered to AFM tips have been published [555]. Thus, such an experiment could at the same time shed light on the kinetics of peptide partitioning from the aqueous phase to the lipid bilayer.

⁴⁰ For all studies, 2D crystalline arrays of bR or NhaA were used. These crystalline arrays are highly enriched in protein which could affect the mechanism and thermodynamics of insertion and folding.

APPENDIX

GLOSSARY OF ABBREVIATIONS

°C	Degree Celsius
µm	Micrometer (10^{-6} m)
2D	Two-dimensional
3D	Three-dimensional
Å	Ångström (10^{-10} m)
aa	Amino acid
ABC	ATP binding cassette
AFM	Atomic force microscope
APC	Amino acid/polyamine/organocation
ATP	Adenosine triphosphate
<i>B. subtilis</i>	<i>Bacillus subtilis</i>
BFP	Biomembrane force probe
bR	Bacteriorhodopsin
CD	Circular dichroism
CFTR	Cystic fibrosis transmembrane conductance regulator
cm	Centimeter (10^{-2} m)
Da	Dalton ($1.66054 \cdot 10^{-27}$ kg)
DFS	Dynamic force spectroscopy
DLVO	Derjaguin-Landau-Verwey-Overbeek
DMPC	1,2-Dimyristoyl- <i>sn</i> -glycero-3-phosphocholine
DNA	Deoxyribonucleic acid
DOPC	1,2-Dioleoyl- <i>sn</i> -glycero-3-phosphocholine
DSPE	1,2-Distearoyl- <i>sn</i> -glycero-3-phosphoethanolamine
<i>E. coli</i>	<i>Escherichia coli</i>
EDL	Electrostatic double layer
EDTA	Ethylenediaminetetraacetic acid

eFJC	Extended freely jointed chain
EGTA	Ethylene glycol-bis(2-aminoethylether)- <i>N,N,N',N'</i> -tetraacetic acid
EM	Electron microscopy
eWLC	Extended wormlike chain
F-D	Force-distance
FJC	Freely jointed-chain
FRET	Förster resonance energy transfer
FTIR	Fourier transform infra red
FWHM	Full width at half maximum
GJC	Gap junction channel
GpA	Glycophorin A
GPCR	Guanine nucleotide-binding protein coupled receptor
h	Hour
HAT	Heteromeric amino acid transporter
HEPES	4-(2-hydroxyethyl)-1-piperazineethanesulfonic acid
I27	27 th immunoglobulin domain of the giant muscle protein titin
IgG	Immunoglobulin G
J	Joule
kcal	Kilocalories (10^3 cal; 1 cal = 4.1868 J)
kDa	Kilodalton
kHz	Kilohertz (10^3 Hz)
LacY	Lactose permease from <i>Escherichia coli</i>
LAT	L-amino acid transporter
LeuT _{Aa}	Leucine transporter from <i>Aquifex aeolicus</i>
LOT	Laser optical tweezers
<i>M. jannaschii</i>	<i>Methanococcus jannaschii</i>
MDa	Megadalton
MES	2-(N-Morpholino)ethanesulfonic acid
min	Minute
mm	Millimeter (10^{-3} m)
mM	Millimolar (10^{-3} mol/l)
MT	Magnetic tweezers
MΩ	Megaohm (10^6 Ω)
NhaA	Sodium:proton (Na ⁺ :H ⁺) antiporter from <i>Escherichia coli</i>
nm	Nanometer (10^{-9} m)

NMR	Nuclear magnetic resonance
PBS	Phosphate buffered saline
PC	Phosphatidylcholine
PDB	Protein data bank
PE	Phosphatidylethanolamine
PMSF	α -Toluenesulfonyl fluoride
pN	Piconewton (10^{-12} N)
POPC	1-Palmitoyl-2-oleoyl- <i>sn</i> -glycero-3-phosphocholine
PS	Phosphatidylserine
PSD	Power spectral density
PSPD	Position sensitive photo detector
RNA	Ribonucleic acid
s	Second
S/N	Signal-to-noise
SD	Standard deviation
SDS	Sodium dodecyl sulphate
SDSL-EPR	Site-directed spin labeling electron paramagnetic resonance
SEM	Standard error of the mean
SFA	Surface force apparatus
SM	Sphingomyeline
SMFS	Single-molecule force spectroscopy
SNOM	Scanning nearfield optical microscope
SOPC	1-Stearoyl-2-oleoyl- <i>sn</i> -glycero-3-phosphocholine
SPM	Scanning probe microscope
SSID	Site-specific infrared dichroism
SteT	Serine:threonine exchange transporter from <i>B. subtilis</i>
STM	Scanning tunneling microscope
TAPS	N-[Tris(hydroxymethyl)methyl]-3-aminopropanesulfonic acid
Tris	2-Amino-2-(hydroxymethyl)-1,3-propanediol
TROSY	Transverse relaxation optimized spectroscopy
TSF	Transport-specific fractionation
WLC	Wormlike chain
wt	Wild-type

Amino acids are abbreviated using the single letter code.

GLOSSARY OF SYMBOLS

Dimensions of units are given according to the Système International d'Unites, prefactors found in the text are not considered in this compilation of units.

$\langle x^2 \rangle$	Time-averaged mean-square cantilever displacement [m ²]
B	Measurement bandwidth [s ⁻¹]
$c_{e,i}$	Concentration of the i^{th} ion species of an electrolyte [M]
D	Differential error [V]
d	Distance between two surfaces [m]
dg	Differential gain
e	Elementary charge [C]
F	Force [N]
F^*	Most probable rupture/unfolding force [N]
H_a	Hamaker constant [J]
I	Integral error [V]
ig	Integral gain
$k(F)$	Force-dependent unfolding rate
k_0	Unfolding rate in absence of force [s ⁻¹]
k_B	Boltzmann constant ($1.38 \cdot 10^{-23}$ J/K)
L_c	Contour length [m]
L_{cant}	Length of a cantilever [m]
l_K	Kuhn length [m]
l_P	Persistence length [m]
m	Mass [kg]
M^*	Mass added to a cantilever [kg]
p	Pressure [Pa]
P	Proportional error [V]
pg	Proportional gain
Q	Quality factor
R	Radius of a cantilever tip [m]
Re	Reynolds number
r_f	Loading rate [N/s]
r_f^*	Most probable loading rate [N/s]
T	Temperature [K]

t	Time [s]
t_{ss}	Tip-sample separation [m]
U_{A-D}	Voltage [V] of each of the four (A-D) segments of the position sensitive photo detector
U_{PSPD}	Deflection output signal of the position sensitive photo detector [V]
v_p	Pulling velocity [m/s]
W_{cant}	Width of a cantilever [m]
x_{mol}	Molecule extension [m]
x_u	Distance between native and transition state corrected for deviations from the direction of force ($x_u = x_\beta \cos\theta$) [m]
x_β	Distance between native and transition state along the reaction coordinate [m]
Z_{corr}	Correction value for z-piezo position [V]
z_i	Valency the i^{th} ion species
z_p	Piezo movement [m]
γ	Damping coefficient [Ns/m]
Γ_i	Imaginary part of the complex hydrodynamic function
ΔG	Free energy change [J]
ΔG^\ddagger	Free energy of activation [J]
ϵ_0	Solute permittivity [C/(Vm)]
ϵ_e	Vacuum permittivity [C/(Vm)]
η_f	Fluid viscosity [Ns/m ²]
κ_{bond}	Elasticity of a bond or structural segment [N/m]
κ_{cant}	Cantilever spring constant [N/m]
$\kappa_{segment}$	Segment elasticity [N/m]
κ_{spacer}	Spring constant of the polymeric handle connecting cantilever tip and molecule (e.g. already unfolded polypeptide) [N/m]
λ_D	Debye length [m]
ρ_f	Fluid density [kg/m ³]
σ	Standard deviation (SD)
σ_i	Surface charge density [C/m ²]
τ	Molecular relaxation time [s]
τ_D	Diffuse relaxation time [s]
ν_0	Resonance frequency [s ⁻¹]
Φ	Specific polymer stiffness [N]

χ	Optical lever deflection sensitivity [m/V]
ψ	Surface potential [V]
ω_0	Angular resonance frequency [s^{-1}]; $\omega_0 = 2\pi\nu_0$

PUBLICATION LIST

Bippes, C.A., Zeltina, A., Casagrande, F., Ratera, M., Palacin, M. Müller, D.J. & Fotiadis, D. (2009) Substrate Binding Tunes Conformational Flexibility and Kinetic Stability of an Amino Acid Antiporter. *J Biol Chem* 284, 18651-18663

Bosshart, P.D., Casagrande, F., Frederix, P.L.T.M., Ratera, M., Bippes, C.A., Müller, D.J., Palacin, M. Engel, A. & Fotiadis, D. (2008) High-Throughput Single-Molecule Force Spectroscopy for Membrane Proteins. *Nanotechnology* 19, 384014

Yu, J.*, Bippes, C.A.*, Hand, G.M., Müller, D.J. & Sosinsky, G.E. (2007) Aminosulfonate Modulated pH Induced Conformational Changes in Connexin26 Hemichannels. *J Biol Chem* 282, 8895-8904

(* equal contribution)

Bippes, C.A., Janovjak, H., Kedrov, A. & Müller, D.J. (2006) Digital Force-feedback for Protein Unfolding Experiments Using Atomic Force Microscopy. *Nanotechnology* 17, 044022

Bippes, C.A., Humphris, A.D.L., Start, M., Müller, D.J. & Janovjak, H. (2005) Direct Measurement of Single-molecule Visco-Elasticity in Atomic Force Microscope Force-Extension Experiments. *Eur Biophys J* 65, 287-292

Kather, I., Bippes, C.A. & Schmid F.X. (2005) A Stable Disulfide-Free Gene-3-Protein of Phage fd Generated by *In Vitro* Evolution. *J Mol Biol* 354, 666-678

ACKNOWLEDGEMENTS

I would like to thank...

... Prof. Daniel Müller for making this work possible. Thank you, Daniel, for the supervision and the freedom in research that you granted me. You always had some advice and encouraging words when things seemed to get stuck. You told me how to guide and inspire people.

... Prof. Gina Sosinsky for the fantastic collaboration on the Cx26 project. You were always concerned about providing proper sample, discussing results, and suggesting further experiments.

... Prof. Dimitrios Fotiadis for the fantastic collaboration on the SteT project. Thank you for fighting for new protein preparations and the fruitful discussion of the data. I hope that the following project will perform at least as good as the one on SteT.

... Dr. Harald Janovjak for introducing me to AFM (especially force spectroscopy) and the support at the beginning of my time as Ph.D. student.

... Dr. Alexej Kedrov for being a good friend and his support and advice. You always had a helping hand and were willing to discuss projects, results, and other issues of daily life. You were always realistic. I really learnt a lot from you.

... Dr. David Cisneros for his advice, especially when I was starting to learn imaging.

... Dr. Jonne Helenius for all the things he told me. You were always prepared for discussion and giving advice.

... Susanne Wegmann for helping wherever and whenever she could.

... Adriana Klyszejko for joining me in fighting broken microscopes.

... Antra Zeltina for her hard work in helping me to collect data for the SteT project.

... Barbara Lindemann for her administrative work. You saved all of us a tremendous amount of daily paper work. Thank you for organizing my trips and dealing with companies and TU administration.

... the rest of the Müller Lab (including former members). Thank you for providing such a nice atmosphere and an inspiring working environment!

... my parents Inge and Klaus Bippes. I am grateful for your continuous support and encouragement in whatever I decided to do.

... Claudia for accompanying and supporting me in every possible way all the years.

BIBLIOGRAPHY

1. Voet, D. & Voet, J. G. (1994). *Biochemie*. 1 edit, VCH, Weinheim.
2. Alberts, B., Bray, D., Lewis, J., Raff, M., Roberts, K. & Watson, J. D. (1995). *Molekularbiologie der Zelle*. 3 edit, VCH Verlagsgesellschaft, Weinheim, Germany.
3. De Rosa, M., Gambacorta, A. & Gliozzi, A. (1986). Structure, biosynthesis, and physicochemical properties of archaeobacterial lipids. *Microbiol Mol Biol Rev* **50**, 70-80.
4. Albers, S. V., Van De Vossenberg, J. L., Driessen, A. J. & Konings, W. N. (2000). Adaptations of the archaeal cell membrane to heat stress. *Front Biosci* **5**, D813-820.
5. Van Meer, G., Voelker, D. R. & Feigenson, G. W. (2008). Membrane lipids: Where they are and how they behave. *Nat Rev Mol Cell Biol* **9**, 112-124.
6. Alberts, B., Johnson, A., Lewis, J., Raff, M., Roberts, K. & Walter, P. (2002). *Molecular biology of the cell*. 4 edit, Garland Science, New York, NY, USA.
7. Rothman, J. E. & Lenard, J. (1977). Membrane asymmetry. *Science* **195**, 743-753.
8. Zachowski, A. (1993). Phospholipids in animal eukaryotic membranes: Transverse asymmetry and movement. *Biochem J* **294** (Pt 1), 1-14.
9. Steinberg, S. F. (2008). Structural basis of protein kinase C isoform function. *Physiol Rev* **88**, 1341-1378.
10. Leever, S. J., Vanhaesebroeck, B. & Waterfield, M. D. (1999). Signalling through phosphoinositide 3-kinases: The lipids take centre stage. *Curr Opin Cell Biol* **11**, 219-225.
11. von Heijne, G. (1986). The distribution of positively charged residues in bacterial inner membrane proteins correlates with the transmembrane topology. *EMBO J* **5**, 3021-3027.
12. von Heijne, G. & Gavel, Y. (1988). Topogenic signals in integral membrane proteins. *Eur J Biochem* **174**, 671-678.
13. Gavel, Y., Steppuhn, J., Herrmann, T. & von Heijne, G. (1991). The positive-inside rule applies to thylakoid membrane proteins. *FEBS Lett* **282**, 41-46.
14. Gavel, Y. & von Heijne, G. (1992). The distribution of charged amino acids in mitochondrial inner-membrane proteins suggests different modes of membrane integration for nuclear and mitochondrially encoded proteins. *Eur J Biochem* **205**, 1207-1215.
15. Bogdanov, M., Mileykovskaya, E. & Dowhan, W. (2008). Lipids in the assembly of membrane proteins and organization of protein supercomplexes: Implications for lipid-linked disorders. *Subcell Biochem* **49**, 197-239.
16. Lee, A. G. (2004). How lipids affect the activities of integral membrane proteins. *Biochim Biophys Acta, Biomembr* **1666**, 62-87.
17. Opekarová, M. & Tanner, W. (2003). Specific lipid requirements of membrane proteins - a putative bottleneck in heterologous expression. *Biochim Biophys Acta, Biomembr* **1610**, 11-22.
18. Singer, S. J. & Nicolson, G. L. (1972). The fluid mosaic model of the structure of cell membranes. *Science* **175**, 720-731.
19. Engelman, D. M. (2005). Membranes are more mosaic than fluid. *Nature* **438**, 578-580.

20. Kusumi, A., Nakada, C., Ritchie, K., Murase, K., Suzuki, K., Murakoshi, H., Kasai, R. S., Kondo, J. & Fujiwara, T. (2005). Paradigm shift of the plasma membrane concept from the two-dimensional continuum fluid to the partitioned fluid: High-speed single-molecule tracking of membrane molecules. *Annu Rev Biophys Biomol Struct* **34**, 351-378.
21. Rütz, M.-L. & Hülser, D. F. (2001). Supramolecular dynamics of gap junctions. *Eur J Cell Biol* **80**, 20-30.
22. Schagger, H. & Pfeiffer, K. (2000). Supercomplexes in the respiratory chains of yeast and mammalian mitochondria. *EMBO J* **19**, 1777-1783.
23. Dekker, J. P. & Boekema, E. J. (2005). Supramolecular organization of thylakoid membrane proteins in green plants. *Biochim Biophys Acta, Bioenerg* **1706**, 12-39.
24. Simons, K. & Vaz, W. L. C. (2004). Model systems, lipid rafts, and cell membranes. *Annu Rev Biophys Biomol Struct* **33**, 269.
25. Wiener, M. & Sh, W. (1992). Structure of a fluid dioleoylphosphatidylcholine bilayer determined by joint refinement of X-ray and neutron diffraction data. III. Complete structure. *Biophys J* **61**, 434-447.
26. White, S. H. & Wimley, W. C. (1999). Membrane protein folding and stability: Physical principles. *Annu Rev Biophys Biomol Struct* **28**, 319-365.
27. Wallin, E. & von Heijne, G. (1998). Genome-wide analysis of integral membrane proteins from eubacterial, archaean, and eukaryotic organisms. *Protein Sci* **7**, 1029-1038.
28. White, S. H. (2004). The progress of membrane protein structure determination. *Protein Sci* **13**, 1948-1949.
29. Berman, H. M., Westbrook, J., Feng, Z., Gilliland, G., Bhat, T. N., Weissig, H., Shindyalov, I. N. & Bourne, P. E. (2000). The protein data bank. *Nucleic Acids Res* **28**, 235-242.
30. Raman, P., Cherezov, V. & Caffrey, M. (2006). The membrane protein data bank. *Cellular and Molecular Life Sciences (CMLS)* **63**, 36-51.
31. Cowan, S. W. & Rosenbusch, J. P. (1994). Folding pattern diversity of integral membrane proteins. *Science* **264**, 914-916.
32. Tamm, L. K., Hong, H. & Liang, B. (2004). Folding and assembly of β -barrel membrane proteins. *Biochim Biophys Acta, Biomembr* **1666**, 250-263.
33. Buchanan, S. K. (1999). β -barrel proteins from bacterial outer membranes: Structure, function and refolding. *Curr Opin Struct Biol* **9**, 455-461.
34. Koebnik, R., Locher, K. P. & Van Gelder, P. (2000). Structure and function of bacterial outer membrane proteins: Barrels in a nutshell. *Mol Microbiol* **37**, 239-253.
35. Wimley, W. C. (2003). The versatile β -barrel membrane protein. *Curr Opin Struct Biol* **13**, 404-411.
36. Galdiero, S., Galdiero, M. & Pedone, C. (2007). β -barrel membrane bacterial proteins: Structure, function, assembly and interaction with lipids. *Curr Protein Pept Sci* **8**, 63-82.
37. Song, L., Hobaugh, M. R., Shustak, C., Cheley, S., Bayley, H. & Gouaux, J. E. (1996). Structure of staphylococcal α -hemolysin, a heptameric transmembrane pore. *Science* **274**, 1859-1866.
38. Olson, R. & Gouaux, E. (2003). *Vibrio cholerae* cytolysin is composed of an α -hemolysin-like core. *Protein Sci* **12**, 379-383.
39. Yamashita, A., Singh, S. K., Kawate, T., Jin, Y. & Gouaux, E. (2005). Crystal structure of a bacterial homologue of Na^+/Cl^- -dependent neurotransmitter transporters. *Nature* **437**, 215-223.
40. Weiss, M. S. & Schulz, G. E. (1992). Structure of porin refined at 1.8 Å resolution. *J Mol Biol* **227**, 493-509.
41. White, S. H., Ladokhin, A. S., Jayasinghe, S. & Hristova, K. (2001). How membranes shape protein structure. *J Biol Chem* **276**, 32395-32398.
42. Ulmschneider, M. B., Sansom, M. S. P. & Nola, A. D. (2005). Properties of integral membrane protein structures: Derivation of an implicit membrane potential. *Proteins: Struct, Funct, Bioinf* **59**, 252-265.

43. von Heijne, G. (1981). Membrane proteins - the amino acid composition of membrane-penetrating segments. *Eur J Biochem* **120**, 275-278.
44. Popot, J.-L. & Engelman, D. M. (2000). Helical membrane protein folding, stability, and evolution. *Annu Rev Biochem* **69**, 881-922.
45. Bowie, J. U. (1997). Helix packing in membrane proteins. *J Mol Biol* **272**, 780-789.
46. Screpanti, E. & Hunte, C. (2007). Discontinuous membrane helices in transport proteins and their correlation with function. *J Struct Biol* **159**, 261-267.
47. Fu, D., Libson, A., Miercke, L. J., Weitzman, C., Nollert, P., Krucinski, J. & Stroud, R. M. (2000). Structure of a glycerol-conducting channel and the basis for its selectivity. *Science* **290**, 481-486.
48. Yernool, D., Boudker, O., Jin, Y. & Gouaux, E. (2004). Structure of a glutamate transporter homologue from *Pyrococcus horikoshii*. *Nature* **431**, 811-818.
49. Kanner, B. I., Bendahan, A., Pantanowitz, S. & Su, H. (1994). The number of amino acid residues in hydrophilic loops connecting transmembrane domains of the GABA transporter GAT-1 is critical for its function. *FEBS Lett* **356**, 191-194.
50. Killian, J. A. & von Heijne, G. (2000). How proteins adapt to a membrane-water interface. *Trends Biochem Sci* **25**, 429-434.
51. Pestourie, C., Cerchia, L., Gombert, K., Aissouni, Y., Boulay, J., De Franciscis, V., Libri, D., Tavitian, B. & Duconge, F. (2006). Comparison of different strategies to select aptamers against a transmembrane protein target. *Oligonucleotides* **16**, 323-335.
52. Yildirim, M. A., Goh, K.-I., Cusick, M. E., Barabasi, A.-L. & Vidal, M. (2007). Drug-target network. *Nat Biotechnol* **25**, 1119-1126.
53. Religa, T. L., Markson, J. S., Mayor, U., Freund, S. M. V. & Fersht, A. R. (2005). Solution structure of a protein denatured state and folding intermediate. *Nature* **437**, 1053-1056.
54. Zeeb, M. & Balbach, J. (2004). Protein folding studied by real-time NMR spectroscopy. *Methods* **34**, 65-74.
55. Hagerman, P. J., Schmid, F. X. & Baldwin, R. L. (1979). Refolding behavior of a kinetic intermediate observed in the low pH unfolding of ribonuclease A. *Biochemistry* **18**, 293-297.
56. Hamill, A. C., Wang, S.-C. & Lee, C. T. (2005). Probing lysozyme conformation with light reveals a new folding intermediate. *Biochemistry* **44**, 15139-15149.
57. Pelton, J. T. & Mclean, L. R. (2000). Spectroscopic methods for analysis of protein secondary structure. *Anal Chem* **277**, 167-176.
58. Wallace, B. A., Lees, J. G., Orry, A. J., Lobley, A. & Janes, R. W. (2003). Analyses of circular dichroism spectra of membrane proteins. *Protein Sci* **12**, 875-884.
59. Kelly, S. M. & Price, N. C. (1997). The application of circular dichroism to studies of protein folding and unfolding. *Biochimica et Biophysica Acta, Protein Structure and Molecular Enzymology* **1338**, 161-185.
60. Schuler, B. & Eaton, W. A. (2008). Protein folding studied by single-molecule FRET. *Curr Opin Struct Biol* **18**, 16-26.
61. Schuler, B., Lipman, E. A. & Eaton, W. A. (2002). Probing the free-energy surface for protein folding with single-molecule fluorescence spectroscopy. *Nature* **419**, 743-747.
62. Privalov, P. L. (1996). Intermediate states in protein folding. *J Mol Biol* **258**, 707-725.
63. Fabian, H. & Naumann, D. (2004). Methods to study protein folding by stopped-flow FT-IR. *Methods* **34**, 28-40.
64. Phillips, C. M., Mizutani, Y. & Hochstrasser, R. M. (1995). Ultrafast thermally induced unfolding of RNase A. *Proc Natl Acad Sci USA* **92**, 7292-7296.
65. Fierz, B. & Kiefhaber, T. (2007). End-to-end vs interior loop formation kinetics in unfolded polypeptide chains. *J Am Chem Soc* **129**, 672-679.
66. Fierz, B., Reiner, A. & Kiefhaber, T. (2009). Local conformational dynamics in α -helices measured by fast triplet transfer. *Proc Natl Acad Sci USA* **in press**.

67. Mayor, U., Guydosh, N. R., Johnson, C. M., Grossmann, J. G., Sato, S., Jas, G. S., Freund, S. M. V., Alonso, D. O. V., Daggett, V. & Fersht, A. R. (2003). The complete folding pathway of a protein from nanoseconds to microseconds. *Nature* **421**, 863-867.
68. Chung, H. S. & Tokmakoff, A. (2008). Temperature-dependent downhill unfolding of ubiquitin. I. Nanosecond-to-millisecond resolved nonlinear infrared spectroscopy. *Proteins: Struct, Funct, Bioinf* **72**, 474-487.
69. Woenckhaus, J., Köhling, R., Thiyagarajan, P., Littrell, K. C., Seifert, S., Royer, C. A. & Winter, R. (2001). Pressure-jump small-angle X-ray scattering detected kinetics of staphylococcal nuclease folding. *Biophys J* **80**, 1518-1523.
70. Panick, G. & Winter, R. (2000). Pressure-induced unfolding/refolding of ribonuclease A: Static and kinetic fourier transform infrared spectroscopy study. *Biochemistry* **39**, 1862-1869.
71. Jacob, M., Holtermann, G., Perl, D., Reinstein, J., Schindler, T., Geeves, M. A. & Schmid, F. X. (1999). Microsecond folding of the cold shock protein measured by a pressure-jump technique. *Biochemistry* **38**, 2882-2891.
72. Chen, E., Goldbeck, R. A. & Klinger, D. S. (1997). Nanosecond time-resolved spectroscopy of biomolecular processes. *Annu Rev Biophys Biomol Struct* **26**, 327-355.
73. Nölting, B., Golbik, R. & Fersht, A. R. (1995). Submillisecond events in protein folding. *Proc Natl Acad Sci USA* **92**, 10668-10672.
74. Fierz, B., Satzger, H., Root, C., Gilch, P., Zinth, W. & Kiefhaber, T. (2007). Loop formation in unfolded polypeptide chains on the picoseconds to microseconds time scale. *Proc Natl Acad Sci USA* **104**, 2163-2168.
75. Fersht, A. R., Matouschek, A. & Serrano, L. (1992). The folding of an enzyme : I. Theory of protein engineering analysis of stability and pathway of protein folding. *J Mol Biol* **224**, 771-782.
76. Snow, C. D., Sorin, E. J., Rhee, Y. M. & Pande, V. S. (2005). How well can simulation predict protein folding kinetics and thermodynamics? *Annu Rev Biophys Biomol Struct* **34**, 43-69.
77. Dill, K. A. (1990). Dominant forces in protein folding. *Biochemistry* **29**, 7133-7155.
78. Daggett, V. & Fersht, A. R. (2003). The present view of the mechanism of protein folding. *Nat Rev Mol Cell Biol* **4**, 497-502.
79. Anfinsen, C. B. (1973). Principles that govern the folding of protein chains. *Science* **181**, 223-230.
80. Anfinsen, C. B. & Haber, E. (1961). Studies on the reduction and re-formation of protein disulfide bonds. *J Biol Chem* **236**, 1361-1363.
81. Anfinsen, C. B., Haber, E., Sela, M. & White, F. H. (1961). The kinetics of formation of native ribonuclease during oxidation of the reduced polypeptide chain. *Proc Natl Acad Sci USA* **47**, 1309-1314.
82. Dill, K. A. (1985). Theory for the folding and stability of globular proteins. *Biochemistry* **24**, 1501-1509.
83. Zwanzig, R., Szabo, A. & Bagchi, B. (1992). Levinthal's paradox. *Proc Natl Acad Sci USA* **89**.
84. Levinthal, C. (1968). Are there pathways in protein folding? *J Chim Phys Phys-Chim Biol* **65**, 44-45.
85. Dill, K. (1999). Polymer principles and protein folding. *Protein Sci* **8**, 1166-1180.
86. Dill, K. A. & Chan, H. S. (1997). From Levinthal to pathways to funnels. *Nat Struct Biol* **4**, 10-19.
87. Onuchic, J. N., Luthey-Schulten, Z. & Wolynes, P. G. (1997). Theory of protein folding: The energy landscape perspective. *Annu. Rev. Phys. Chem.* **48**, 545-600.
88. Onuchic, J. N., Socci, N. D., Luthey-Schulten, Z. & Wolynes, P. G. (1996). Protein folding funnels: The nature of the transition state ensemble. *Folding and Design* **1**, 441-450.

89. Dill, K. A., Bromberg, S., Yue, K., Ftebig, K. M., Yee, D. P., Thomas, P. D. & Hue Sun Chan, K. A. D. (1995). Principles of protein folding - a perspective from simple exact models. *Protein Sci* **4**, 561-602.
90. Bryngelson, J. D., Onuchic, J. N., Socci, N. D. & Wolynes, P. G. (1995). Funnels, pathways, and the energy landscape of protein folding: A synthesis. *Proteins: Struct, Funct, Genet* **21**, 167-195.
91. Wolynes, P. G., Onuchic, J. N. & Thirumalai, D. (1995). Navigating the folding routes. *Science* **267**, 1619-1620.
92. Dempsey, C. E. (1990). The actions of melittin on membranes. *Biochim Biophys Acta* **1031**, 143-161.
93. Cramer, W. A., Heymann, J. B., Schendel, S. L., Deriy, B. N., Cohen, F. S., Elkins, P. A. & Stauffacher, C. V. (1995). Structure-function of the channel-forming colicins. *Annu Rev Biophys Biomol Struct* **24**, 611-641.
94. Zhan, H., Oh, K. J., Shin, Y.-K., Hubbell, W. L. & Collier, R. J. (1995). Interaction of the isolated transmembrane domain of diphtheria toxin with membranes. *Biochemistry* **34**, 4856-4863.
95. Rapoport, T. A. (2007). Protein translocation across the eukaryotic endoplasmic reticulum and bacterial plasma membranes. *Nature* **450**, 663-669.
96. Van Den Berg, B., Clemons, W. M. J., Collinson, I., Modis, Y., Hartmann, E., Harrison, S. C. & Rapoport, T. A. (2004). X-ray structure of a protein-conducting channel. *Nature* **427**.
97. White, S. H. (2007). Membrane protein insertion: The biology-physics nexus. *J Gen Physiol* **129**, 363-369.
98. White, S. H. & Heijne, G. V. (2004). The machinery of membrane protein assembly. *Curr Opin Struct Biol* **14**, 397-404.
99. White, S. H. & von Heijne, G. (2008). How translocons select transmembrane helices. *Ann Rev Biophys* **37**, 23-42.
100. Heinrich, S. U., Mothes, W., Brunner, J. & Rapoport, T. A. (2000). The Sec61p complex mediates the integrative of a membrane protein by allowing lipid partitioning of the transmembrane domain. *Cell* **102**, 233-244.
101. Hessa, T., Kim, H., Bihlmaier, K., Lundin, C., Boekel, J., Andersson, H., Nilsson, I., White, S. H. & von Heijne, G. (2005). Recognition of transmembrane helices by the endoplasmic reticulum translocon. *Nature* **433**, 377-381.
102. Heinrich, S. U. & Rapoport, T. A. (2003). Cooperation of transmembrane segments during the integration of a double-spanning protein into the ER membrane. *EMBO J* **22**, 3654-3663.
103. Sadlish, H., Pitonzo, D., Johnson, A. E. & Skach, W. R. (2005). Sequential triage of transmembrane segments by Sec61alpha during biogenesis of a native multispansing membrane protein. *Nat Struct Mol Biol* **12**, 870-878.
104. Bowie, J. U. (2005). Solving the membrane protein folding problem. *Nature* **438**, 581-589.
105. Booth, P. J., Templar, R. H., Curran, A. R. & Allen, S. J. (2001). Can we identify the forces that drive the folding of integral membrane proteins? *Biochem. Soc. Trans.* **29**, 408-413.
106. Booth, P. J., Templar, R. H., Meijberg, W., Allen, S. J., Curran, A. R. & Lorch, M. (2001). In vitro studies of membrane protein folding. *Crit. Rev. Biochem. Mol. Biol.* **36**, 501-603.
107. Wimley, W. C. & White, S. H. (2000). Designing transmembrane alpha-helices that insert spontaneously. *Biochemistry* **39**, 4432-4442.
108. Huang, K. S., Bayley, H., Liao, M. J., London, E. & Khorana, H. G. (1981). Refolding of an integral membrane protein. Denaturation, renaturation, and reconstitution of intact bacteriorhodopsin and two proteolytic fragments. *J Biol Chem* **256**, 3802-3809.
109. Liao, M. J., London, E. & Khorana, H. G. (1983). Regeneration of the native bacteriorhodopsin structure from two chymotryptic fragments. *J Biol Chem* **258**, 9949-9955.
110. Popot, J.-L., Gerchman, S.-E. & Engelman, D. M. (1987). Refolding of bacteriorhodopsin in lipid bilayers: A thermodynamically controlled two-stage process. *J Mol Biol* **198**, 655-676.

111. Popot, J. L. & Engelman, D. M. (1990). Membrane protein folding and oligomerization: The two-stage model. *Biochemistry* **29**, 4031-4037.
112. Engelman, D. M., Chen, Y., Chin, C.-N., Curran, A. R., Dixon, A. M., Dupuy, A. D., Lee, A. S., Lehnert, U., Matthews, E. E., Reshetnyak, Y. K., Senes, A. & Popot, J.-L. (2003). Membrane protein folding: Beyond the two stage model. *FEBS Lett* **555**, 122-125.
113. MacKenzie, K. R., Prestegard, J. H. & Engelman, D. M. (1997). A transmembrane helix dimer: Structure and implications. *Science* **276**, 131-133.
114. Russ, W. P. & Engelman, D. M. (2000). The GxxxG motif: A framework for transmembrane helix-helix association. *J Mol Biol* **296**, 911-919.
115. Senes, A., Gerstein, M. & Engelman, D. M. (2000). Statistical analysis of amino acid patterns in transmembrane helices: The GxxxG motif occurs frequently and in association with β -branched residues at neighboring positions. *J Mol Biol* **296**, 921-936.
116. Hermansson, M. & von Heijne, G. (2003). Inter-helical hydrogen bond formation during membrane protein integration into the ER membrane. *J Mol Biol* **334**, 803-809.
117. Gratkowski, H., Lear, J. D. & Degrado, W. F. (2001). Polar side chains drive the association of model transmembrane peptides. *Proc Natl Acad Sci USA* **98**, 880-885.
118. Choma, C., Gratkowski, H., Lear, J. D. & Degrado, W. F. (2000). Asparagine-mediated self-association of a model transmembrane helix. *Nat Struct Biol* **7**, 161-166.
119. Zhou, F. X., Merianos, H. J., Brunger, A. T. & Engelman, D. M. (2001). Polar residues drive association of polyleucine transmembrane helices. *Proc Natl Acad Sci USA* **98**, 2250-2255.
120. Partridge, A. W., Therien, A. G. & Deber, C. M. (2004). Missense mutations in transmembrane domains of proteins: Phenotypic propensity of polar residues for human disease. *Proteins* **54**, 648-656.
121. Meindl-Beinker, N. M., Lundin, C., Nilsson, I., White, S. H. & von Heijne, G. (2006). Asn- and Asp-mediated interactions between transmembrane helices during translocon-mediated membrane protein assembly. *EMBO Rep* **7**, 1111-1116.
122. Jacobs, R. E. & White, S. H. (1989). The nature of the hydrophobic binding of small peptides at the bilayer interface: Implications for the insertion of transbilayer helices. *Biochemistry* **28**, 3421-3437.
123. Nymeyer, H., Woolf, T. B. & Garcia, A. E. (2005). Folding is not required for bilayer insertion: Replica exchange simulations of an alpha-helical peptide with an explicit lipid bilayer. *Proteins: Struct, Funct, Bioinf* **59**, 783-790.
124. Wimley, W. C., Creamer, T. P. & White, S. H. (1996). Solvation energies of amino acid side chains and backbone in a family of host-guest pentapeptides. *Biochemistry* **35**, 5109-5124.
125. Wimley, W. C. & White, S. H. (1996). Experimentally determined hydrophobicity scale for proteins at membrane interfaces. *Nat Struct Biol* **3**, 842-848.
126. Hessa, T., White, S. H. & von Heijne, G. (2005). Membrane insertion of a potassium-channel voltage sensor. *Science* **307**, 1427.
127. Engelman, D. M. & Steitz, T. A. (1981). The spontaneous insertion of proteins into and across membranes: The helical hairpin hypothesis. *Cell* **23**, 411-422.
128. Hessa, T., Meindl-Beinker, N. M., Bernsel, A., Kim, H., Sato, Y., Lerch-Bader, M., Nilsson, I., White, S. H. & von Heijne, G. (2007). Molecular code for transmembrane-helix recognition by the Sec61 translocon. *Nature* **450**, 1026-1030.
129. Guijarro, J. I. A., Sunde, M., Jones, J. A., Campbell, I. D. & Dobson, C. M. (1998). Amyloid fibril formation by an SH3 domain. *Proc Natl Acad Sci USA* **95**, 4224-4228.
130. McParland, V. J., Kad, N. M., Kalverda, A. P., Brown, A., Kirwin-Jones, P., Hunter, M. G., Sunde, M. & Radford, S. E. (2000). Partially unfolded states of β -microglobulin and amyloid formation in vitro. *Biochemistry* **39**, 8735-8746.
131. Litvinovich, S. V., Brew, S. A., Aota, S., Akiyama, S. K., Haudenschild, C. & Ingham, K. C. (1998). Formation of amyloid-like fibrils by self-association of a partially unfolded fibronectin type III module. *J Mol Biol* **280**, 245-258.

132. Fändrich, M., Fletcher, M. A. & Dobson, C. M. (2001). Amyloid fibrils from muscle myoglobin. *Nature* **410**, 165-166.
133. Ferrao-Gonzales, A. D., Souto, S. O., Silva, J. L. & Foguel, D. (2000). The preaggregated state of an amyloidogenic protein: Hydrostatic pressure converts native transthyretin into the amyloidogenic state. *Proc Natl Acad Sci USA* **97**, 6445-6450.
134. De Felice, F. G., Vieira, M. N. N., Meirelles, M. N. L., Morozova-Roche, L. A., Dobson, C. M. & Ferreira, S. T. (2004). Formation of amyloid aggregates from human lysozyme and its disease-associated variants using hydrostatic pressure. *FASEB J*, 03-1072fje.
135. Chiti, F., Webster, P., Taddei, N., Clark, A., Stefani, M., Ramponi, G. & Dobson, C. M. (1999). Designing conditions for in vitro formation of amyloid protofilaments and fibrils. *Proc Natl Acad Sci USA* **96**, 3590-3594.
136. Schmittschmitt, J. P. & Scholtz, J. M. (2003). The role of protein stability, solubility, and net charge in amyloid fibril formation. *Protein Sci* **12**, 2374-2378.
137. Chiti, F. & Dobson, C. M. (2009). Amyloid formation by globular proteins under native conditions. *Nat Chem Biol* **5**, 15-22.
138. Chiti, F. & Dobson, C. M. (2006). Protein misfolding, functional amyloid, and human disease. *Annu Rev Biochem* **75**, 333-366.
139. Dobson, C. M. (2003). Protein folding and misfolding. *Nature* **426**, 884-890.
140. Sanders, C. R. & Nagy, J. K. (2000). Misfolding of membrane proteins in health and disease: The lady or the tiger? *Curr Opin Struct Biol* **10**, 438-442.
141. Qu, B.-H., Strickland, E. & Thomas, P. J. (1997). Cystic fibrosis: A disease of altered protein folding. *J Bioenerg Biomembr* **29**, 483-490.
142. Seibert, F. S., Loo, T. W., Clarke, D. M. & Riordan, J. R. (1997). Cystic fibrosis: Channel, catalytic, and folding properties of the CFTR protein. *J Bioenerg Biomembr* **29**, 429-442.
143. Sung, C.-H., Schneider, B. A., Agarwal, N., Papermaster, D. S. & Nathans, J. (1991). Functional heterogeneity of mutant rhodopsins responsible for autosomal dominant retinitis pigmentosa. *Proc Natl Acad Sci USA* **88**, 8840-8844.
144. Sung, C.-H., Davenport, C. M. & Nathans, J. (1993). Rhodopsin mutations responsible for autosomal dominant retinitis pigmentosa. *J Biol Chem* **268**, 26645-26649.
145. Kaushal, S. & Khorana, H. G. (1994). Structure and function in rhodopsin. 7. Point mutations associated with autosomal dominant retinitis pigmentosa. *Biochemistry* **33**, 6121-6128.
146. Tamarappoo, B. K., Yang, B. & Verkman, A. S. (1999). Misfolding of mutant aquaporin-2 water channels in nephrogenic diabetes insipidus. *J Biol Chem* **274**, 34825-34831.
147. Nichols, C. G. (2006). KATP channels as molecular sensors of cellular metabolism. *Nature* **44**, 470-476.
148. Calonge, M. J., Gasparini, P., Chillaron, J., Chillon, M., Gallucci, M., Rousaud, F., Zelante, L., Testar, X., Dallapiccola, B., Di Silverio, F. & Et Al. (1994). Cystinuria caused by mutations in rBAT, a gene involved in the transport of cystine. *Nat Genet* **6**, 420-425.
149. Feliubadalo, L., Font, M., Purroy, J., Rousaud, F., Estivill, X., Nunes, V., Golomb, E., Centola, M., Aksentijevich, I., Kreiss, Y., Goldman, B., Pras, M., Kastner, D. L., Pras, E., Gasparini, P., Bisceglia, L., Beccia, E., Gallucci, M., De Sanctis, L., Ponzzone, A., Rizzoni, G. F., Zelante, L., Bassi, M. T., George, A. L., Jr., Manzoni, M., De Grandi, A., Riboni, M., Endsley, J. K., Ballabio, A., Borsani, G., Reig, N., Fernandez, E., Estevez, R., Pineda, M., Torrents, D., Camps, M., Lloberas, J., Zorzano, A. & Palacin, M. (1999). Non-type I cystinuria caused by mutations in SLC7A9, encoding a subunit (b⁰⁺AT) of rBAT. *Nat Genet* **23**, 52-57.
150. Kelsell, D. P., Dunlop, J., Stevens, H. P., Lench, N. J., Liang, J. N., Parry, G., Mueller, R. F. & Leigh, I. M. (1997). Connexin26 mutations in hereditary non-syndromic sensorineural deafness. *Nature* **387**, 80-83.
151. Ward, C. L. & Kopito, R. R. (1994). Intracellular turnover of cystic fibrosis transmembrane conductance regulator. Inefficient processing and rapid degradation of wild-type and mutant proteins. *J Biol Chem* **269**, 25710-25718.

152. Vembar, S. S. & Brodsky, J. L. (2008). One step at a time: Endoplasmic reticulum-associated degradation. *Nat Rev Mol Cell Biol* **9**, 944-957.
153. Nikles, D. & Tampé, R. (2007). Targeted degradation of ABC transporters in health and disease. *J Bioenerg Biomembr* **39**, 489-497.
154. Denning, G. M., Anderson, M. P., Amara, J. F. M., J., Smith, A. E. & Welsh, M. J. (1992). Processing of mutant cystic fibrosis transmembrane conductance regulator is temperature-sensitive. *Nature* **358**, 761-764.
155. Bogdanov, M. & Dowhan, W. (1999). Lipid-assisted protein folding. *J Biol Chem* **274**, 36827-36830.
156. Hunt, J. F., Earnest, T. N., Bousche, O., Kalghatgi, K., Reilly, K., Horvath, C., Rothschild, K. J. & Engelman, D. M. (1997). A biophysical study of integral membrane protein folding. *Biochemistry* **36**, 15156-15176.
157. Zhou, Y. & Bowie, J. U. (2000). Building a thermostable membrane protein. *J Biol Chem* **275**, 6975-6979.
158. Eidelman, O., Barnoy, S., Razin, M., Zhang, J., Mcphie, P., Lee, G., Huang, Z., Sorscher, E. J. & Pollard, H. B. (2002). Role for phospholipid interaction in the trafficking defect of $\Delta F508$ -CFTR. *Biochemistry* **41**, 11161-11170.
159. Welch, W. J. (2004). Role of quality control pathways in human diseases involving protein misfolding. *Semin Cell Dev Biol* **15**, 31-38.
160. Cheung, J. C. & Deber, C. M. (2008). Misfolding of the cystic fibrosis transmembrane conductance regulator and disease. *Biochemistry* **47**, 1465-1473.
161. Sitia, R. & Braakman, I. (2003). Quality control in the endoplasmic reticulum protein factory. *Nature* **426**, 891-894.
162. Cutting, G.: *Cystic fibrosis mutation database*. <<http://www.genet.sickkids.on.ca/cftr/Home.html>>, last updated: 02 March 2007
163. Martin, P. E., L Coleman, S., Casalotti, S. O., Forge, A. & Evans, W. H. (1999). Properties of connexin26 gap junctional proteins derived from mutations associated with non-syndromal hereditary deafness. *Hum Mol Genet* **8**, 2369-2376.
164. Rees, D. C., Komiya, H., Yeates, T. O., Allen, J. P. & Feher, G. (1989). The bacterial photosynthetic reaction center as a model for membrane proteins. *Annu Rev Biochem* **58**, 607-633.
165. Booth, P. J. (2003). The trials and tribulations of membrane protein folding in vitro. *Biochim Biophys Acta, Biomembr* **1610**, 51-56.
166. Seddon, A. M., Curnow, P. & Booth, P. J. (2004). Membrane proteins, lipids and detergents: Not just a soap opera. *Biochim Biophys Acta, Biomembr* **1666**, 105-117.
167. Loll, P. J. (2003). Membrane protein structural biology: The high throughput challenge. *J Struct Biol* **142**, 144-153.
168. Yoshikawa, S., Tera, T., Takahashi, Y., Tsukihara, T. & Caughey, W. S. (1988). Crystalline cytochrome c oxidase of bovine heart mitochondrial membrane: Composition and X-ray diffraction studies. *Proc Natl Acad Sci USA* **85**, 1354-1358.
169. Becher, B. M. & Cassim, S. Y. (1975). Improved isolation procedures for the purple membrane of *Halobacterium halobium*. *Prep Biochem Biotechnol* **5**, 161 - 178.
170. Knepper, M. A. (1994). The aquaporin family of molecular water channels. *Proc Natl Acad Sci USA* **91**, 6255-6258.
171. Tate, C. G. (2001). Overexpression of mammalian integral membrane proteins for structural studies. *FEBS Lett* **504**, 94-98.
172. Wagner, S., Bader, M. L., Drew, D. & De Gier, J.-W. (2006). Rationalizing membrane protein overexpression. *Trends Biotechnol* **24**, 364-371.

173. Otto, J. C., Dewitt, D. L. & Smith, W. L. (1993). N-glycosylation of prostaglandin endoperoxide synthases-1 and -2 and their orientations in the endoplasmic reticulum. *J Biol Chem* **268**, 18234-18242.
174. Bowie, J. U. (2001). Stabilizing membrane proteins. *Curr Opin Struct Biol* **11**, 397-402.
175. Hunte, C. & Richers, S. (2008). Lipids and membrane protein structures. *Curr Opin Struct Biol* **18**, 406-411.
176. Renthal, R. (2006). An unfolding story of helical transmembrane proteins. *Biochemistry* **45**, 14559-14566.
177. Taneva, S. G., Caaveiro, J. M., Muga, A. & Goñi, F. M. (1995). A pathway for the thermal destabilization of bacteriorhodopsin. *FEBS Lett* **367**, 297-300.
178. Haltia, T. & Freire, E. (1995). Forces and factors that contribute to the structural stability of membrane proteins. *Biochim Biophys Acta, Rev Biomembr* **1241**, 295-322.
179. Luecke, H. (1999). Structural changes in bacteriorhodopsin during ion transport at 2 Å resolution. *Science* **286**, 255-260.
180. Cherezov, V., Rosenbaum, D. M., Hanson, M. A., Rasmussen, S. G. F., Thian, F. S., Kobilka, T. S., Choi, H.-J., Kuhn, P., Weis, W. I., Kobilka, B. K. & Stevens, R. C. (2007). High-resolution crystal structure of an engineered human β_2 -adrenergic G protein-coupled receptor. *Science* **318**, 1258-1265.
181. Rasmussen, S. G. F., Choi, H.-J., Rosenbaum, D. M., Kobilka, T. S., Thian, F. S., Edwards, P. C., Burghammer, M., Ratnala, V. R. P., Sanishvili, R., Fischetti, R. F., Schertler, G. F. X., Weis, W. I. & Kobilka, B. K. (2007). Crystal structure of the human β_2 adrenergic G-protein-coupled receptor. *Nature* **450**, 383-387.
182. Ruska, E. (1987). The development of the electron microscope and of electron microscopy. *Bioscience Reports* **7**, 607-629.
183. Unwin, P. N. T. & Henderson, R. (1975). Molecular structure determination by electron microscopy of unstained crystalline specimens. *J Mol Biol* **94**, 425-432.
184. Saibil, H. (2000). Macromolecular structure determination by cryo-electron microscopy. *Acta Crystallographica Section D* **56**, 1215-1222.
185. Murata, K., Mitsuoka, K., Hirai, T., Walz, T., Agre, P., Heymann, J. B., Engel, A. & Fujiyoshi, Y. (2000). Structural determinants of water permeation through aquaporin-1. *Nature* **407**, 599-605.
186. Frank, J. (2002). Single-particle imaging of macromolecules by cryo-electron microscopy. *Annu Rev Biophys Biomol Struct* **31**, 303-319.
187. Pervushin, K., Riek, R., Wider, G., Senn, H. & Wüthrich, K. (1997). Attenuated T2 relaxation by mutual cancellation of dipole-dipole coupling and chemical shift anisotropy indicates an avenue to NMR structures of very large biological macromolecules in solution. *Proc Natl Acad Sci USA* **94**, 12366-12371.
188. Arora, A. & Tamm, L. K. (2001). Biophysical approaches to membrane protein structure determination. *Curr Opin Struct Biol* **11**, 540-547.
189. Opella, S. J. & Marassi, F. M. (2004). Structure determination of membrane proteins by NMR spectroscopy. *Chem Rev* **104**, 3587-3606.
190. Altenbach, C., Marti, T., Khorana, H. G. & Hubbell, W. L. (1990). Transmembrane protein structure: Spin labeling of bacteriorhodopsin mutants. *Science* **248**, 1088-1092.
191. Altenbach, C., Greenhalgh, D. A., Khorana, H. G. & Hubbell, W. L. (1994). A collision gradient method to determine the immersion depth of nitroxides in lipid bilayers: Application to spin-labeled mutants of bacteriorhodopsin. *Proc Natl Acad Sci USA* **91**, 1667-1671.
192. Hilger, D., Polyhach, Y., Padan, E., Jung, H. & Jeschke, G. (2007). High-resolution structure of a Na⁺/H⁺ antiporter dimer obtained by pulsed EPR distance measurements. *Biophys J*.
193. Rabenstein, M. S. & Shin, Y.-K. (1995). Determination of the distance between two spin labels attached to a macromolecule. *Proc Natl Acad Sci USA* **92**, 8239-8243.

194. Wu, J., Bvoss, J., Hubbell, W. L. & Kaback, H. R. (1996). Site-directed spin labeling and chemical crosslinking demonstrate that helix V is close to helices VII and VIII in the lactose permease of *Escherichia coli*. *Proc Natl Acad Sci USA* **93**, 10123-10127.
195. Farrens, D. L., Altenbach, C., Yang, K., Hubbell, W. L. & Khorana, H. G. (1996). Requirement of rigid-body motion of transmembrane helices for light activation of rhodopsin. *Science* **274**, 768-770.
196. Borbat, P. P., Mchaourab, H. S. & Freed, J. H. (2002). Protein structure determination using long-distance constraints from double-quantum coherence ESR: Study of T4 lasozyme. *J Am Chem Soc* **124**, 5304-5314.
197. Arkin, I. T., MacKenzie, K. R. & Brünger, A. T. (1997). Site-directed dichroism as a method for obtaining rotational and orientational constraints for oriented polymers. *J Am Chem Soc* **119**, 8973-8980.
198. Vogel, H., Nilsson, L., Rigler, R., Meder, S., Boheim, G., Beck, W., Kurth, H.-H. & Jung, G. (1993). Structural fluctuations between two conformational states of a transmembrane helical peptide are related to its channel-forming properties in planar lipid membranes. *Eur J Biochem* **212**, 305-313.
199. Gerwert, K. (1999). Molecular reaction mechanisms of proteins monitored by time-resolved FTIR-spectroscopy. *Biol Chem* **380**, 931-935.
200. Wang, J. & El-Sayed, M. A. (1999). Temperature jump-induced secondary structural change of the membrane protein bacteriorhodopsin in the premelting temperature region: A nanosecond time-resolved fourier transform infrared study. *Biophys J* **76**, 2777-2783.
201. Sharom, F. J., Liu, R. & Romsicki, Y. (1998). Spectroscopic and biophysical approaches for studying the structure and function of the P-glycoprotein multidrug transporter. *Biochem Cell Biol* **76**, 695-708.
202. Brouillette, C. G., Muccio, D. D. & Finney, T. K. (1987). pH dependence of bacteriorhodopsin thermal unfolding. *Biochemistry* **26**, 7431-7438.
203. Edrington 5th, T. C., Bennett, M. & Albert, A. D. (2008). Calorimetric studies of bovine rod outer segment disk membranes support a monomeric unit for both rhodopsin and opsin. *Biophys J* **95**, 2859-2866.
204. Bukauskas, F. F., Vogel, R. & Weingart, R. (1997). Biophysical properties of heterotypic gap junctions newly formed between two types of insect cells. *J Physiol (Camb)* **499**, 701-713.
205. Dunlop, J., Bowlby, M., Peri, R., Vasilyev, D. & Arias, R. (2008). High-throughput electrophysiology: An emerging paradigm for ion-channel screening and physiology. *Nat Rev Drug Discovery* **7**, 358-368.
206. Karpen, J. W. & Ruiz, M. (2002). Ion channels: Does each subunit do something on its own? *Trends Biochem Sci* **27**, 402-409.
207. Martin, P. E. M., Mambetisaeva, E. T., Archer, D. A., George, C. H. & Evans, W. H. (2000). Analysis of gap junction assembly using mutated connexins detected in Charcot-Marie-Tooth X-linked disease. *J Neurochem* **74**, 711-720.
208. Yoshimura, T., Satake, M., Ohnishi, A., Tsutsumi, Y. & Fujikura, Y. (1998). Mutations of connexin32 in Charcot-Marie-Tooth disease type X interfere with cell-to-cell communication but not cell proliferation and myelin-specific gene expression. *J Neurosci Res* **51**, 154-161.
209. Kristensen, A. S., Larsen, M. B., Johnsen, L. B. & Wiborg, O. (2004). Mutational scanning of the human serotonin transporter reveals fast translocating serotonin transporter mutants. *Eur J Neurosci* **19**, 1513-1523.
210. Le Gouill, C., Parent, J.-L., Caron, C.-A., Gaudreau, R., Volkov, L., Rola-Pleszczynski, M. & Stankova, J. (1999). Selective modulation of wild type receptor functions by mutants of G-protein-coupled receptors. *J Biol Chem* **274**, 12548-12554.
211. Fanelli, F. & De Benedetti, P. G. (2005). Computational modeling approaches to structure-function analysis of G protein-coupled receptors. *Chem Rev* **105**, 3297-3351.

212. Oliveira, L., Hulsen, T., Lutje Hulshik, D., Paiva, A. C. M. & Vriend, G. (2004). Heavier-than-air flying machines are impossible. *FEBS Lett* **564**, 269-273.
213. Wang, Y. & Tajkhorshid, E. (2008). Electrostatic funneling of substrate in mitochondrial inner membrane carriers. *Proc Natl Acad Sci USA* **105**, 9598-9603.
214. De Groot, B. L., Frigato, T., Helms, V. & Grubmüller, H. (2003). The mechanism of proton exclusion in the aquaporin-1 water channel. *J Mol Biol* **333**, 279-293.
215. Cieplak, M., Filipek, S., Janovjak, H. & Krzysko, K. A. (2006). Pulling single bacteriorhodopsin out of a membrane: Comparison of simulation and experiment. *Biochim Biophys Acta, Biomembr* **1758**, 537-544.
216. Seeber, M., Fanelli, F., Paci, E. & Caflisch, A. (2006). Sequential unfolding of individual helices of bacterioopsin observed in molecular dynamics simulations of extraction from the purple membrane. *Biophys J* **91**, 3276-3284.
217. Sosinsky, G. E. & Nicholson, B. J. (2005). Structural organization of gap junction channels. *Biochim Biophys Acta, Biomembr* **1711**, 99-125.
218. Prochnow, N. & Dermietzel, R. (2008). Connexons and cell adhesion: A romantic phase. *Histochem Cell Biol* **130**, 71-77.
219. Loewenstein, W. R. (1981). Junctional intercellular communication: The cell-to-cell membrane channel. *Physiol Rev* **61**, 829-913.
220. Gerido, D. A. & White, T. W. (2004). Connexin disorders of the ear, skin, and lens. *Biochim Biophys Acta, Biomembr* **1662**, 159-170.
221. Willecke, K., Eiberger, J., Degen, J., Eckardt, D., Romualdi, A., Güldenagel, M., Deutsch, U. & Söhl, G. (2002). Structural and functional diversity of connexin genes in the mouse and human genome. *Biol Chem* **383**, 725-737.
222. Milks, L. C., Kumar, N. M., Houghten, R., Unwin, N. & Gilula, N. B. (1988). Topology of the 32-kD liver gap junction protein determined by site-directed antibody localizations. *EMBO J* **7**, 2967-2975.
223. Unger, V. M., Kumar, N. M., Gilula, N. B. & Yeager, M. (1997). Projection structure of a gap junction channel at 7 Å resolution. *Nat Struct Biol* **4**, 39-42.
224. Unger, V. M., Kumar, N. M., Gilula, N. B. & Yeager, M. (1999). Three-dimensional structure of a recombinant gap junction membrane channel. *Science* **283**, 1176-1180.
225. Maeda, S., Nakagawa, S., Suga, M., Yamashita, E., Oshima, A., Fujiyoshi, Y. & Tsukihara, T. (2009). Structure of the connexin 26 gap junction channel at 3.5 Å resolution. *Nature* **458**, 597-602.
226. Caspar, D. L. D., Goodenough, D. A., Makowski, L. & Phillips, W. C. (1977). Gap junctions structures I: Correlated electron microscopy and X-ray diffraction. *J Cell Biol* **74**, 605-628.
227. Makowski, L., Caspar, D. L. D., Phillips, W. C. & Goodenough, D. A. (1977). Gap junction structure: II. Analysis of the X-ray diffraction data. *J Cell Biol* **75**, 629-645.
228. Tibbitts, T. T., Caspar, D. L., Phillips, W. C. & Goodenough, D. A. (1990). Diffraction diagnosis of protein folding in gap junction connexons. *Biophys J* **57**, 1025-1036.
229. Unwin, P. & Ennis, P. (1983). Calcium-mediated changes in gap junction structure: Evidence from the low angle X-ray pattern. *J Cell Biol* **97**, 1459-1466.
230. Duffy, H. S., Sorgen, P. L., Girvin, M. E., O'Donnell, P., Coombs, W., Taffet, S. M., Delmar, M. & Spray, D. C. (2002). pH-dependent intramolecular binding and structure involving Cx43 cytoplasmic domains. *J Biol Chem* **277**, 36706-36714.
231. Purnick, P. E. M., Benjamin, D. C., Verselis, V. K., Bargiello, T. A. & Dowd, T. L. (2000). Structure of the amino terminus of a gap junction protein. *Arch Biochem Biophys* **381**, 181-190.
232. Sorgen, P. L., Duffy, H. S., Cahill, S. M., Coombs, W., Spray, D. C., Delmar, M. & Girvin, M. E. (2002). Sequence-specific resonance assignment of the carboxyl terminal domain of connexin 43. *J Biomol NMR* **23**, 245-246.

233. Sorgen, P. L., Duffy, H. S., Sahoo, P., Coombs, W., Delmar, M. & Spray, D. C. (2004). Structural changes in the carboxyl terminus of the gap junction protein connexin43 indicates signaling between binding domains for c-Src and zonula occludens-1. *J Biol Chem* **279**, 54695-54701.
234. Sorgen, P. L., Duffy, H. S., Spray, D. C. & Delmar, M. (2004). pH-dependent dimerization of the carboxyl terminal domain of Cx43. *Biophys J* **87**, 574-581.
235. Goodenough, D. A., Goliger, J. A. & Paul, D. L. (1996). Connexins, connexons, and intercellular communication. *Annu Rev Biochem* **65**, 475-502.
236. Noma, A. & Tsuboi, N. (1987). Dependence of junctional conductance on proton, calcium and magnesium ions in cardiac paired cells of guinea-pig. *J Physiol (Camb)* **382**, 193-211.
237. Bukauskas, F. F. & Peracchia, C. (1997). Two distinct gating mechanisms in gap junction channels: CO₂-sensitive and voltage-sensitive. *Biophys J* **72**, 2137-2142.
238. Bukauskas, F. F. & Verselis, V. K. (2004). Gap junction channel gating. *Biochim Biophys Acta* **1662**, 42-60.
239. Verselis, V. K., Ginter, C. S. & Bargiello, T. A. (1994). Opposite voltage gating polarities of two closely related connexins. *Nature* **368**, 348-351.
240. Verselis, V. K., Trexler, E. B. & Bukauskas, F. F. (2000). Connexin hemichannels and cell-cell channels: Comparison of properties. *Braz J Med Biol Res* **33**, 379-389.
241. Hervé, J.-C., Bourmeyster, N., Sarrouilhe, D. & Duffy, H. S. (2007). Gap junctional complexes: From partners to functions. *Progress in Biophysics and Molecular Biology* **94**, 29-65.
242. Harris, A. L. (2007). Connexin channel permeability to cytoplasmic molecules. *Prog Biophys Mol Biol* **94**, 120-143.
243. Kelsell, D. P., Dunlop, J. & Hodgins, M. B. (2001). Human diseases: Clues to tracking the connexin code? *Trends Cell Biol* **11**, 2-6.
244. Nickel, R. & Forge, A. (2008). Gap junctions and connexins in the inner ear: Their roles in homeostasis and deafness. *Curr Opin Otolaryngol Head Neck Surg* **16**, 452-457.
245. Apps, S. A., Rankin, W. A. & Krumis, A. P. (2007). Connexin 26 mutations in autosomal recessive deafness disorders: A review. *Int J Audiol* **46**, 75-81.
246. Mese, G., Londin, E. & Mui, R. (2004). Altered gating properties of functional Cx26 mutants associated with recessive non-syndromic hearing loss. *Hum Genet* **115**, 191-199.
247. Kikuchi, T., Adams, J. C. & Miyabe, Y. (2000). Potassium ion recycling pathway via gap junction systems in the mammalian cochlea and its interruptions in hereditary nonsyndromic deafness. *Med Electron Microsc* **33**, 51-56.
248. Mazereeuw-Hautier, J., Bitoun, E. & Chevrant-Breton, J. (2007). Keratitis-ichthyosis-deafness syndrome: Disease expression and spectrum of connexin 26 (GJB2) mutations in 14 patients. *Br J Dermatol* **156**, 1015-1019.
249. Ikegami, T., Lin, C. & Kato, M. (1998). Four novel mutations of the connexin 32 gene in four Japanese families with Charcot-Marie-Tooth disease type 1. *Am J Med Genet* **80**, 352-355.
250. Alldredge, B. (2008). Clinical connexions. *J Clin Pathol (Lond)* **61**, 885-890.
251. Krulwich, T. A., Ito, M., Gilmour, R. & Guffanti, A. A. (1997). Mechanisms of cytoplasmic pH regulation in alkaliphilic strains of bacillus. *Extremophiles* **1**, 163-170.
252. Gong, S., Richard, H. & Foster, J. W. (2003). YjdE (AdiC) is the arginine:agmatine antiporter essential for arginine-dependent acid resistance in *Escherichia coli*. *J Bacteriol* **185**, 4402-4409.
253. Iyer, R., Williams, C. & Miller, C. (2003). Arginine-agmatine antiporter in extreme acid resistance in *Escherichia coli*. *J Bacteriol* **185**, 6556-6561.
254. Foster, J. W. (2004). *Escherichia coli* acid resistance: Tales of an amateur acidophile. *Nat Rev Micro* **2**, 898-907.
255. Anantharam, V., Allison, M. J. & Maloney, P. C. (1989). Oxalate:formate exchange. The basis for energy coupling in oxalobacter. *J Biol Chem* **264**, 7244-7250.
256. Abe, K., Hayashi, H. & Maloney, P. C. (1996). Exchange of aspartate and alanine. *J Biol Chem* **271**, 3079-3084.

257. Lolkema, J. S., Poolman, B. & Konings, W. N. (1998). Bacterial solute uptake and efflux systems. *Curr Opin Microbiol* **1**, 248-253.
258. Jung, H., Prich, T. & Hilger, D. (2007). Secondary transport of amino acids in prokaryotes. *J Membr Biol* **213**, 119-133.
259. Smith, Q. R. (2000). Transport of glutamate and other amino acids at the blood-brain barrier. *J Nutr* **130**, 1016-.
260. Reeds, P. J. (2000). Dispensable and indispensable amino acids for humans. *J Nutr* **130**, 1835S-1840.
261. Jack, D. L., Paulsen, I. T. & Saier Jr, M. H. (2000). The amino acid/polyamine/organocation (APC) superfamily of transporters specific for amino acids, polyamines and organocations. *Microbiology* **146**, 1797-1814.
262. Palacin, M., Nunes, V., Font-Llitjos, M., Jimenez-Vidal, M., Fort, J., Gasol, E., Pineda, M., Feliubadalo, L., Chillaron, J. & Zorzano, A. (2005). The genetics of heteromeric amino acid transporters. *Physiology* **20**, 112-124.
263. Verrey, F., Jack, D. L., Paulsen, I. T., M.H. Saier, J. & Pfeiffer, R. (1999). New glycoprotein-associated amino acid transporters. *J Membr Biol* **172**, 181-192.
264. Borsani, G., Bassi, M. T., Sperandeo, M. P., De Grandi, A., Buoninconti, A., Riboni, M., Manzoni, M., Incerti, B., Pepe, A., Andria, G., Ballabio, A. & Sebastio, G. (1999). SLC7A7, encoding a putative permease-related protein, is mutated in patients with lysinuric protein intolerance. *Nat Genet* **21**, 297-301.
265. Torrents, D., Mykkanen, J., Pineda, M., Feliubadalo, L., Estevez, R., De Cid, R., Sanjurjo, P., Zorzano, A., Nunes, V., Huoponen, K., Reinikainen, A., Simell, O., Savontaus, M. L., Aula, P. & Palacin, M. (1999). Identification of SLC7A7, encoding y⁺LAT-1, as the lysinuric protein intolerance gene. *Nat Genet* **21**, 293-296.
266. Bassi, M. T., Gasol, E., Manzoni, M., Pineda, M., Riboni, M., Martin, R., Zorzano, A., Borsani, G. & Palacin, M. (2001). Identification and characterisation of human xCT that co-expresses, with 4F2 heavy chain, the amino acid transport activity system x_c. *Pflug Arch Eur J Physiol* **442**, 286-296.
267. Sato, H., Tamba, M., Ishii, T. & Bannai, S. (1999). Cloning and expression of a plasma membrane cystine/glutamate exchange transporter composed of two distinct proteins. *J Biol Chem* **274**, 11455-11458.
268. Baker, D. A., Mcfarland, K., Lake, R. W., Shen, H., Tang, X. C., Toda, S. & Kalivas, P. W. (2003). Neuroadaptations in cystine-glutamate exchange underlie cocaine relapse. *Nat Neurosci* **6**, 743-749.
269. Sato, H., Shiiya, A., Kimata, M., Maebara, K., Tamba, M., Sakakura, Y., Makino, N., Sugiyama, F., Yagami, K., Moriguchi, T., Takahashi, S. & Bannai, S. (2005). Redox imbalance in cystine/glutamate transporter-deficient mice. *J Biol Chem* **280**, 37423-37429.
270. Fuchs, B. C. & Bode, B. P. (2005). Amino acid transporters ASCT2 and LAT1 in cancer: Partners in crime? *Semin Cancer Biol* **15**, 254-266.
271. Reig, N., Del Rio, C., Casagrande, F., Ratera, M., Gelpi, J. L., Torrents, D., Henderson, P. J. F., Xie, H., Baldwin, S. A., Zorzano, A., Fotiadis, D. & Palacin, M. (2007). Functional and structural characterization of the first prokaryotic member of the L-amino acid transporter (LAT) family: A model for APC transporters. *J Biol Chem* **282**, 13270-13281.
272. Binnig, G., Rohrer, H., Gerber, C. & Weibel, E. (1982). Tunneling through a controllable vacuum gap. *Appl. Phys. Lett.* **40**, 178-180.
273. Binnig, G., Quate, C. F. & Gerber, C. (1986). Atomic force microscope. *Phys Rev Lett* **56**, 930.
274. Nonnenmacher, M., O'boyle, M. P. & Wickramasinghe, H. K. (1991). Kelvin probe force microscopy. *Appl. Phys. Lett.* **58**, 2921-2923.
275. Martin, Y. & Wickramasinghe, H. K. (1987). Magnetic imaging by "force microscopy" with 1000 Å resolution. *Appl. Phys. Lett.* **50**, 1455-1457.

276. Lewis, A., Isaacson, M., Harootunian, A. & Muray, A. (1984). Development of a 500 Å spatial resolution light microscope: I. Light is efficiently transmitted through $\lambda/16$ diameter apertures. *Ultramicroscopy* **13**, 227-231.
277. Friedbacher, G. & Fuchs, H. (1999). Classification of scanning probe microscopies. *Pure Appl Chem* **71**, 1337-1357.
278. Giessibl, F. J. (1995). Atomic resolution of the silicon (111)-(7x7) surface by atomic force microscopy. *Science* **267**, 68-71.
279. Hoogenboom, B. W., Hug, H. J., Pellmont, Y., Martin, S., Frederix, P. L. T. M., Fotiadis, D. & Engel, A. (2006). Quantitative dynamic-mode scanning force microscopy in liquid. *Appl. Phys. Lett.* **88**, 193109-193103.
280. Meyer, G. & Amer, N. M. (1988). Novel optical approach to atomic force microscopy. *Appl. Phys. Lett.* **53**, 1045.
281. Viani, M. B., Schaffer, T. E., Chand, A., Rief, M., Gaub, H. E. & Hansma, P. K. (1999). Small cantilevers for force spectroscopy of single molecules. *J Appl Phys* **86**, 2258-2262.
282. Israelachvili, J. N. (1991). *Intermolecular and surface forces*. 2 edit, Academic Press, San Diego, CA, USA.
283. Muller, D. J. & Engel, A. (1997). The height of biomolecules measured with the atomic force microscope depends on electrostatic interactions. *Biophys J* **73**, 1633-1644.
284. Butt, H.-J. (1992). Measuring local surface charge densities in electrolyte solutions with a scanning force microscope. *Biophys J* **63**, 578-582.
285. Muller, D. J., Janovjak, H., Lehto, T., Kuerschner, L. & Anderson, K. (2002). Observing structure, function and assembly of single proteins by AFM. *Progress in Biophysics and Molecular Biology* **79**, 1-43.
286. Schabert, F. A. & Engel, A. (1994). Reproducible acquisition of *Escherichia coli* porin surface topographs by atomic force microscopy. *Biophys J* **67**, 2394-3403.
287. Muller, D. J., Amrein, M. & Engel, A. (1997). Adsorption of biological molecules to a solid support for scanning probe microscopy. *J Struct Biol* **119**, 172-188.
288. Muller, D. J., Fotiadis, D., Scheuring, S., Müller, S. A. & Engel, A. (1999). Electrostatically balanced subnanometer imaging of biological specimens by atomic force microscope. *Biophys J* **76**, 1101-1111.
289. Hutter, J. L. & Bechhoefer, J. (1993). Calibration of atomic-force microscope tips. *Rev Sci Instrum* **64**, 3342-3342.
290. Landau, L. D. & Lifshitz, E. M. (1980). *Statistical physics*. 3 edit, Elsevier, Burlington, MA, USA.
291. Evans, E. (2001). Probing the relation between force-lifetime-and chemistry in single molecular bonds. *Annu Rev Biophys Biomol Struct* **30**, 105-128.
292. Yasumura, K. Y., Stowe, T. D., Chow, E. M., Pfafman, T., Kenny, T. W., Stipe, B. C. & Rugar, D. (2000). Quality factors in micron- and submicron-thick cantilevers. *Microelectromechanical Systems, Journal of* **9**, 117-125.
293. Butt, H.-J. & Jaschke, M. (1995). Calculation of thermal noise in atomic force microscopy. *Nanotechnology* **6**, 1-7.
294. Cleveland, J. P., Manne, S., Bocek, D. & Hansma, P. K. (1993). A nondestructive method for determining the spring constant of cantilevers for scanning force microscopy. *Rev Sci Instrum* **64**, 403-405.
295. Sader, J. E., Larson, I., Mulvaney, P. & White, L. R. (1995). Method for the calibration of atomic force microscope cantilevers. *Rev Sci Instrum* **66**, 3789-3798.
296. Sader, J. E., Chon, J. W. M. & Mulvaney, P. (1999). Calibration of rectangular atomic force microscope cantilevers. *Rev Sci Instrum* **70**, 3967-3969.
297. Sader, J. E. (1998). Frequency response of cantilever beams immersed in viscous fluids with applications to the atomic force microscope. *J Appl Phys* **84**, 64-76.

298. Sader, J. E.: *Atomic force microscope cantilevers (calibration method of Sader)*. <<http://www.ampc.ms.unimelb.edu.au/afm/index.html>>, last updated: 19 December 2008
299. Scheuring, S., Ringler, P., Borgnia, M., Stahlberg, H., Muller, D. J., Agre, P. & Engel, A. (1999). High resolution AFM topographs of the *Escherichia coli* water channel aquaporin Z. *EMBO J* **18**, 4981-4987.
300. Muller, D. J., Heymann, J. B., Oesterhelt, F., Möller, C., Gaub, H., Büldt, G. & Engel, A. (2000). Atomic force microscopy of native purple membrane. *Biochim Biophys Acta, Bioenerg* **1460**, 27-38.
301. Muller, D. J., Fotiadis, D. & Engel, A. (1998). Mapping flexible protein domains at subnanometer resolution with the atomic force microscope. *FEBS Lett* **430**, 105-111.
302. Muller, D. J., Engel, A., Carrascosa, J. L. & Velez, M. (1997). The bacteriophage phi29 head-tail connector imaged at high resolution with the atomic force microscope in buffer solution. *EMBO J* **16**, 2547-2553.
303. García, R. & Pérez, R. (2002). Dynamic atomic force microscopy methods. *Surf Sci Rep* **47**, 197-301.
304. Moller, C., Allen, M., Elings, V., Engel, A. & Muller, D. J. (1999). Tapping-mode atomic force microscopy produces faithful high-resolution images of protein surfaces. *Biophys J* **77**, 1150-1158.
305. Elie-Caille, C., Severin, F., Helenius, J., Howard, J., Muller, D. J. & Hyman, A. A. (2007). Straight GDP-tubulin protofilaments form in the presence of taxol. *Curr Biol* **17**, 1765-1770.
306. Jiang, F., Horber, H., Howard, J. & Muller, D. J. (2004). Assembly of collagen into microribbons: Effects of pH and electrolytes. *J Struct Biol* **148**, 268-278.
307. Benoit, M., Gabriel, D., Gerisch, G. & Gaub, H. E. (2000). Discrete interactions in cell adhesion measured by single-molecule force spectroscopy. *Nat Cell Biol* **2**, 313-317.
308. Florin, E., Moy, V. & Gaub, H. (1994). Adhesion forces between individual ligand-receptor pairs. *Science* **264**, 415-417.
309. Bustamante, C., Bryant, Z. & Smith, S. B. (2003). Ten years of tension: Single-molecule DNA mechanics. *Nature* **421**, 423-427.
310. Moffitt, J. R., Chemla, Y. R., Smith, S. B. & Bustamante, C. (2008). Recent advances in optical tweezers. *Annu Rev Biochem* **77**, 205-228.
311. Kedrov, A., Wegmann, S., Smits, S. H. J., Goswami, P., Baumann, H. & Muller, D. J. (2007). Detecting molecular interactions that stabilize, activate and guide ligand-binding of the sodium/proton antiporter MjNhaP1 from *Methanococcus jannaschii*. *J Struct Biol* **159**, 290-301.
312. Kedrov, A., Ziegler, C., Janovjak, H., Kühlbrandt, W. & Muller, D. J. (2004). Controlled unfolding and refolding of a single sodium-proton antiporter using atomic force microscopy. *J Mol Biol* **340**, 1143-1152.
313. Oesterhelt, F., Oesterhelt, D., Pfeiffer, M., Engel, A., Gaub, H. E. & Muller, D. J. (2000). Unfolding pathways of individual bacteriorhodopsins. *Science* **288**, 143-146.
314. Cisneros, D. A., Oesterhelt, D. & Muller, D. J. (2005). Probing origins of molecular interactions stabilizing the membrane proteins halorhodopsin and bacteriorhodopsin. *Structure* **13**, 235-242.
315. Rief, M., Gautel, M., Oesterhelt, F., Fernandez, J. M. & Gaub, H. E. (1997). Reversible unfolding of individual titin immunoglobulin domains by AFM. *Science* **276**, 1109-1112.
316. Oberhauser, A. F., Marszalek, P. E., Erickson, H. P. & Fernandez, J. M. (1998). The molecular elasticity of the extracellular matrix protein tenascin. *Nature* **393**, 181-185.
317. Howard, J. (2001). *Mechanics of motor proteins and the cytoskeleton*, Sinauer Associates, Sunderland, MA, USA.
318. Merkel, R., Nassoy, P., Leung, A., Ritchie, K. & Evans, E. (1999). Energy landscapes of receptor-ligand bonds explored with dynamic force spectroscopy. *Nature* **397**, 50-53.

319. Rief, M., Oesterhelt, F., Heymann, B. & Gaub, H. E. (1997). Single molecule force spectroscopy on polysaccharides by atomic force microscopy. *Science* **275**, 1295-1297.
320. Bustamante, C., Marko, J. F., Siggia, E. D. & Smith, S. (1994). Entropic elasticity of lambda-phage DNA. *Science* **265**, 1599-1600.
321. Clausen-Schaumann, H., Seitz, M., Krautbauer, R. & Gaub, H. E. (2000). Force spectroscopy with single bio-molecules. *Curr Opin Chem Biol* **4**, 524-530.
322. Cui, Y. & Bustamante, C. (2000). Pulling a single chromatin fiber reveals the forces that maintain its higher-order structure. *Proc Natl Acad Sci USA* **97**, 127-132.
323. Oesterhelt, F., Rief, M. & Gaub, H. E. (1999). Single molecule force spectroscopy by AFM indicates helical structure of poly(ethylene-glycol) in water. *New Journal of Physics* **1**, 6.1-6.11.
324. Evans, E., Ritchie, K. & Merkel, R. (1995). Sensitive force technique to probe molecular adhesion and structural linkages at biological interfaces. *Biophys J* **68**, 2580-2587.
325. Ashkin, A. (1970). Acceleration and trapping of particles by radiation pressure. *Phys Rev Lett* **24**, 156.
326. Ashkin, A., Dziedzic, J. M., Bjorkholm, J. E. & Chu, S. (1986). Observation of a single-beam gradient force optical trap for dielectric particles. *Opt Lett* **11**, 288.
327. Leckband, D. (2000). Measuring the forces that control protein interactions. *Annu Rev Biophys Biomol Struct* **29**, 1-26.
328. Gosse, C. & Croquette, V. (2002). Magnetic tweezers: Micromanipulation and force measurement at the molecular level. *Biophys J* **82**, 3314-3329.
329. Israelachvili, J. N. & Adams, G. E. (1978). Measurement of forces between two mica surfaces in aqueous electrolyte solutions in the range 0-100 nm. *J Chem Soc, Faraday Trans* **74**, 975-1001.
330. Leckband, D. & Israelachvili, J. (2001). Intermolecular forces in biology. *Q Rev Biophys* **34**, 105-267.
331. Fernandez, J. M. & Li, H. (2004). Force-clamp spectroscopy monitors the folding trajectory of a single protein. *Science* **303**, 1674-1678.
332. Oberhauser, A. F., Hansma, P. K., Carrion-Vazquez, M. & Fernandez, J. M. (2001). Stepwise unfolding of titin under force-clamp atomic force microscopy. *Proc Natl Acad Sci USA* **98**, 468-472.
333. Schlierf, M., Li, H. & Fernandez, J. M. (2004). The unfolding kinetics of ubiquitin captured with single-molecule force-clamp techniques. *Proc Natl Acad Sci USA* **101**, 7299-7304.
334. Janshoff, A., Neitzert, M., Oberdörfer, Y. & Fuchs, H. (2000). Force spectroscopy of molecular systems - single molecule spectroscopy of polymers and biomolecules. *Angew Chem* **39**, 3212-3237.
335. Lee, G. U., Chrisey, L. A. & Colton, R. J. (1994). Direct measurement of the forces between complementary strands of DNA. *Science* **266**, 771-773.
336. Smith, S. B., Cui, Y. & Bustamante, C. (1996). Overstretching B-DNA: The elastic response of individual double-stranded and single-stranded DNA molecules. *Science* **271**, 795-799.
337. Marszalek, P. E., Li, H. & Fernandez, J. M. (2001). Fingerprinting polysaccharides with single-molecule atomic force microscopy. *Nat Biotechnol* **19**, 258-262.
338. Marszalek, P. E., Oberhauser, A. F., Pang, Y.-P. & Fernandez, J. M. (1998). Polysaccharide elasticity governed by chair-boat transitions of the glucopyranose ring. *Nature* **396**, 661-664.
339. Kratky, O. & Porod, G. (1949). Röntgenuntersuchung gelöster Fadenmoleküle. *Recueil des Travaux Chimiques des Pays-Bas* **68**, 1106-1122.
340. Marko, J. F. & Siggia, E. D. (1995). Stretching DNA. *Macromolecules* **28**, 8759-8770.
341. Smith, S. B., Finzi, L. & Bustamante, C. (1992). Direct mechanical measurements of the elasticity of single DNA molecules by using magnetic beads. *Science* **258**, 1122-1126.
342. Bouchiat, C., Wang, M. D., Allemand, J. F., Strick, T., Block, S. M. & Croquette, V. (1999). Estimating the persistence length of a worm-like chain molecule from force-extension measurements. *Biophys J* **76**, 409-413.

343. Baumann, C. G., Smith, S. B., Bloomfield, V. A. & Bustamante, C. (1997). Ionic effects on the elasticity of single DNA molecules. *Proc Natl Acad Sci USA* **94**, 6185-6190.
344. Wang, M. D., Yin, H., Landick, T., Gelles, J. & Block, S. M. (1997). Stretching DNA with optical tweezers. *Biophys J* **72**, 1335-1346.
345. Brady, J. W. (1986). Molecular dynamics simulations of α -D-glucose. *J Am Chem Soc* **108**, 8153-8160.
346. Humphris, A. D. L., Tamayo, J. & Miles, M. J. (2000). Active quality factor control in liquids for force spectroscopy. *Langmuir* **16**, 7891-7894.
347. Kawakami, M., Byrne, K., Khatri, B. S., Mcleish, T. C. B., Radford, S. E. & Smith, D. A. (2005). Viscoelastic measurements of single molecules on a millisecond time scale by magnetically driven oscillation of an atomic force microscope cantilever. *Langmuir* **21**, 4765-4772.
348. Kawakami, M., Byrne, K., Khatri, B., Mcleish, T. C., Radford, S. E. & Smith, D. A. (2004). Viscoelastic properties of single polysaccharide molecules determined by analysis of thermally driven oscillations of an atomic force microscope cantilever. *Langmuir* **20**, 9299-9303.
349. Walther, K. A., Brujic, J., Li, H. & Fernandez, J. M. (2006). Sub-angstrom conformational changes of a single molecule captured by AFM variance analysis. *Biophys J* **90**, 3806-3812.
350. Fukuda, N., Granzier, H. L., Ishiwata, S. I. & Kurihara, S. (2008). Physiological functions of the giant elastic protein titin in mammalian striated muscle. *J Physiol Sci* **58**, 151-159.
351. Granzier, H. & Labeit, S. (2007). Structure-function relations of the giant elastic protein titin in striated and smooth muscle cells. *Muscle Nerve* **36**, 740-755.
352. Gao, M., Lu, H. & Schulten, K. (2002). Unfolding of titin domains studied by molecular dynamics simulations. *J Muscle Res Cell Motil* **23**, 513-521.
353. Wang, K., Forbes, J. G. & Jin, A. J. (2001). Single molecule measurements of titin elasticity. *Prog Biophys Mol Biol* **77**, 1-44.
354. Marszalek, P. E., Lu, H., Li, H., Carrion-Vazquez, M., Oberhauser, A. F., Schulten, K. & Fernandez, J. M. (1999). Mechanical unfolding intermediates in titin modules. *Nature* **402**, 100-103.
355. Oberhauser, A. F., Marszalek, P. E., Carrion-Vazquez, M. & Fernandez, J. M. (1999). Single protein misfolding events captured by atomic force microscopy. *Nat Struct Mol Biol* **6**, 1025-1028.
356. Linke, W. & Grützner, A. (2008). Pulling single molecules of titin by AFM—recent advances and physiological implications. *Pflueg Arch Eur J Physiol* **456**, 101-115.
357. Sharma, D., Perisic, O., Peng, Q., Cao, Y., Lam, C., Lu, H. & Li, H. (2007). Single-molecule force spectroscopy reveals a mechanically stable protein fold and the rational tuning of its mechanical stability. *Proc Natl Acad Sci USA* **104**, 9278-9283.
358. Jollymore, A., Lethias, C., Peng, Q., Cao, Y. & Li, H. (2009). Nanomechanical properties of tenascin-X revealed by single-molecule force spectroscopy. *J Mol Biol* **385**, 1277-1286.
359. Dietz, H. & Rief, M. (2004). Exploring the energy landscape of GFP by single-molecule mechanical experiments. *Proc Natl Acad Sci USA* **101**, 16192-16197.
360. Bertz, M. & Rief, M. (2008). Mechanical unfoldons as building blocks of maltose-binding protein. *J Mol Biol* **378**, 447-458.
361. Ainaravapu, S. R. K., Li, L., Badilla, C. L. & Fernandez, J. M. (2005). Ligand binding modulates the mechanical stability of dihydrofolate reductase (DHFR). *Biophys J* **89**, 3337-3344.
362. Falb, M., Müller, K., Königsmaier, L., Oberwinkler, T., Horn, P., von Gronau, S., Gonzalez, O., Pfeiffer, F., Bornberg-Bauer, E. & Oesterhelt, D. (2008). Metabolism of halophilic archaea. *Extremophiles* **12**, 177-196.
363. Ng, W. V., Kennedy, S. P., Mahairas, G. G., Berquist, B., Pan, M., Shukla, H. D., Lasky, S. R., Baliga, N. S., Thorsson, V., Sbrogna, J., Swartzell, S., Weir, D., Hall, J., Dahl, T. A., Welti, R., Goo, Y. A., Leithauser, B., Keller, K., Cruz, R., Danson, M. J., Hough, D. W., Maddocks, D. G., Jablonski, P. E., Krebs, M. P., Angevine, C. M., Dale, H., Isenbarger, T. A., Peck, R. F., Pohlschroder, M., Spudich, J. L., Jung, K.-H., Alam, M., Freitas, T., Hou, S., Daniels, C. J.,

- Dennis, P. P., Omer, A. D., Eberhardt, H., Lowe, T. M., Liang, P., Riley, M., Hood, L. & Dassarma, S. (2000). Genome sequence of *Halobacterium* species NRC-1. *Proc Natl Acad Sci USA* **97**, 12176-12181.
364. Luecke, H., Schobert, B., Richter, H. T., Cartailler, J. P. & Lanyi, J. K. (1999). Structure of bacteriorhodopsin at 1.55 Å resolution. *J Mol Biol* **291**, 899-911.
365. Lanyi, J. K. (2004). Bacteriorhodopsin. *Annu. Rev. Physiol.* **66**, 665-688.
366. Muller, D. J., Kessler, M., Oesterhelt, F., Möller, C., Oesterhelt, D. & Gaub, H. (2002). Stability of bacteriorhodopsin alpha-helices and loops analyzed by single-molecule force spectroscopy. *Biophys J* **83**, 3578-3588.
367. Janovjak, H., Kessler, M., Oesterhelt, D., Gaub, H. & Muller, D. J. (2003). Unfolding pathways of native bacteriorhodopsin depend on temperature. *EMBO J* **22**, 5220-5229.
368. Sapra, K. T., Balasubramanian, G. P., Labudde, D., Bowie, J. U. & Muller, D. J. (2008). Point mutations in membrane proteins reshape energy landscape and populate different unfolding pathways. *J Mol Biol* **376**, 1076-1090.
369. Sapra, K. T., Doehner, J., Renugopalakrishnan, V., Padros, E. & Muller, D. J. (2008). Role of extracellular glutamic acids in the stability and energy landscape of bacteriorhodopsin. *Biophys J* **95**, 3407-3418.
370. Sapra, K. T., Park, P. S., Filipek, S., Engel, A., Muller, D. J. & Palczewski, K. (2006). Detecting molecular interactions that stabilize native bovine rhodopsin. *J Mol Biol* **358**, 255-269.
371. Cisneros, D. A., Oberbarnscheidt, L., Pannier, A., Klare, J. P., Helenius, J., Engelhard, M., Oesterhelt, F. & Muller, D. J. (2008). Transducer binding establishes localized interactions to tune sensory rhodopsin II. *Structure* **16**, 1206-1213.
372. Klyszejko, A. L., Shastri, S., Mari, S. A., Grubmuller, H., Muller, D. J. & Glaubitz, C. (2007). Folding and assembly of proteorhodopsin. *J Mol Biol* **376**, 35-41.
373. Evans, E. & Ritchie, K. (1997). Dynamic strength of molecular adhesion bonds. *Biophys J* **72**, 1541-1555.
374. Baldwin, R. L. & Rose, G. D. (1999). Is protein folding hierarchic? I. Local structure and peptide folding. *Trends Biochem Sci* **24**, 26-33.
375. Baldwin, R. L. & Rose, G. D. (1999). Is protein folding hierarchic? II. Folding intermediates and transition states. *Trends Biochem Sci* **24**, 77-83.
376. Hänggi, P., Talkner, P. & Borkovec, M. (1990). Reaction-rate theory: Fifty years after Kramers. *Reviews of Modern Physics* **62**, 251-341.
377. Kramers, H. A. (1940). Brownian motion in a field of force and the diffusion model of chemical reactions. *Physica* **7**, 284-304.
378. Bieri, O., Wirz, J., Hellrung, B., Schutkowski, M., Drewello, M. & Kiefhaber, T. (1999). The speed limit for protein folding measured by triplet-triplet energy transfer. *Proc Natl Acad Sci USA* **96**, 9597-9601.
379. Bell, G. I. (1978). Models for the specific adhesion of cells to cells. *Science* **200**, 618-627.
380. Evans, E. (1998). Energy landscapes of biomolecular adhesion and receptor anchoring at interfaces explored with dynamic force spectroscopy. *Faraday Discuss.* **11**, 1-16.
381. Hinterdorfer, P., Baumgartner, W., Gruber, H. J., Schilcher, K. & Schindler, H. (1996). Detection and localization of individual antibody-antigen recognition events by atomic force microscopy. *Proc Natl Acad Sci USA* **93**, 3477-3481.
382. Onuchic, J. N., Wolynes, P. G., Luthey-Schulten, Z. & Socci, N. D. (1995). Toward an outline of the topography of a realistic protein-folding funnel. *Proc Natl Acad Sci USA* **92**, 3626-3630.
383. Buzhynskyy, N., Hite, R. K., Walz, T. & Scheuring, S. (2007). The supramolecular architecture of junctional microdomains in native lens membranes. *EMBO Rep* **8**, 51-55.
384. Buzhynskyy, N., Girmens, J.-F., Faigle, W. & Scheuring, S. (2007). Human cataract lens membrane at subnanometer resolution. *J Mol Biol* **374**, 162-169.

385. Fotiadis, D., Jastrzebska, B., Philippsen, A., Muller, D. J., Palczewski, K. & Engel, A. (2006). Structure of the rhodopsin dimer: A working model for G-protein-coupled receptors. *Curr Opin Struct Biol* **16**, 252-259.
386. Muller, D. J., Schabert, F. A., Büldt, G. & Engel, A. (1995). Imaging purple membranes in aqueous solutions at sub-nanometer resolution by atomic force microscopy. *Biophys J* **68**, 1681-1686.
387. Scheuring, S. & Sturgis, J. N. (2005). Chromatic adaptation of photosynthetic membranes. *Science* **309**, 484-487.
388. Scheuring, S., Gonçalves, R. P., Prima, V. & Sturgis, J. N. (2006). The photosynthetic apparatus of *Rhodospseudomonas palustris*: Structures and organization. *J Mol Biol* **358**, 83-96.
389. Muller, D. J., Dencher, N. A., Meier, T., Dimroth, P., Suda, K., Stahlberg, H., Engel, A., Seelert, H. & Matthey, U. (2001). ATP synthase: Constrained stoichiometry of the transmembrane rotor. *FEBS Lett* **504**, 219-222.
390. Pogoryelov, D., Reichen, C., Klyszejko, A. L., Brunisholz, R., Muller, D. J., Dimroth, P. & Meier, T. (2007). The oligomeric state of c rings from cyanobacterial F₁-ATP synthases varies from 13 to 15. *J Bacteriol* **189**, 5895-5902.
391. Pogoryelov, D., Yu, J., Meier, T., Vonck, J., Dimroth, P. & Muller, D. J. (2005). The c15 ring of the *Spirulina platensis* F₁-ATP synthase: F₁/F₀ symmetry mismatch is not obligatory. *EMBO Rep* **6**, 1040-1044.
392. Stahlberg, H., Muller, D. J., Suda, K., Fotiadis, D., Engel, A., Meier, T., Matthey, U. & Dimroth, P. (2001). Bacterial Na⁺-ATP synthase has an undecameric rotor. *EMBO Rep* **2**, 229-233.
393. Seelert, H., Poetsch, A., Dencher, N. A., Engel, A., Stahlberg, H. & Muller, D. J. (2000). Structural biology. Proton-powered turbine of a plant motor. *Nature* **405**, 418-419.
394. Fritz, M., Klyszejko, A. L., Morgner, N., Vonck, J., Brutschy, B., Muller, D. J., Meier, T. & Müller, V. (2008). An intermediate step in the evolution of ATPases - a hybrid F₀-V₀ rotor in a bacterial Na⁺ F₁F₀ ATP synthase. *FEBS J* **275**, 1999-2007.
395. Muller, D. J., Engel, A., Matthey, U., Meier, T., Dimroth, P. & Suda, K. (2003). Observing membrane protein diffusion at subnanometer resolution. *J Mol Biol* **327**, 925-930.
396. Muller, D. J. & Engel, A. (1999). Voltage and pH-induced channel closure of porin OmpF visualized by atomic force microscopy. *J Mol Biol* **285**, 1347-1351.
397. Muller, D. J., Hand, G. M., Engel, A. & Sosinsky, G. E. (2002). Conformational changes in surface structures of isolated connexin 26 gap junctions. *EMBO J* **21**, 3598-3607.
398. Yu, J., Bippes, C. A., Hand, G. M., Muller, D. J. & Sosinsky, G. E. (2007). Aminosulfonate modulated pH-induced conformational changes in connexin26 hemichannels. *J Biol Chem* **282**, 8895-8904.
399. Kedrov, A., Janovjak, H., Ziegler, C., Kuhlbrandt, W. & Muller, D. J. (2006). Observing folding pathways and kinetics of a single sodium-proton antiporter from *Escherichia coli*. *J Mol Biol* **355**, 2-8.
400. Kedrov, A., Krieg, M., Ziegler, C., Kuhlbrandt, W. & Muller, D. J. (2005). Locating ligand binding and activation of a single antiporter. *EMBO Rep* **6**, 668-674.
401. Kedrov, A., Ziegler, C. & Muller, D. J. (2006). Differentiating ligand and inhibitor interactions of a single antiporter. *J Mol Biol* **362**, 925-932.
402. Cao, Y., Balamurali, M. M., Sharma, D. & Li, H. (2007). A functional single-molecule binding assay via force spectroscopy. *Proc Natl Acad Sci USA* **104**, 15677-15681.
403. Williams, P. M., Fowler, S. B., Best, R. B., Toca-Herrera, J. L., Scott, K., Steward, A. & Clarke, J. (2003). Hidden complexity in the mechanical properties of titin. *Nature* **422**, 446-449.
404. Chyan, C.-L., Lin, F.-C., Peng, H., Yuan, J.-M., Chang, C.-H., Lin, S.-H. & Yang, G. (2004). Reversible mechanical unfolding of single ubiquitin molecules. *Biophys J* **87**, 3995-4006.
405. Janovjak, H., Struckmeier, J., Hubain, M., Kedrov, A., Kessler, M. & Muller, D. J. (2004). Probing the energy landscape of the membrane protein bacteriorhodopsin. *Structure* **12**, 871-879.

406. Kedrov, A., Appel, M., Baumann, H., Ziegler, C. & Muller, D. J. (2008). Examining the dynamic energy landscape of an antiporter upon inhibitor binding. *J Mol Biol* **375**, 1258-1266.
407. Janovjak, H., Knaus, H. & Muller, D. J. (2007). Transmembrane helices have rough energy surfaces. *J Am Chem Soc* **129**, 246-247.
408. Kessler, M., Gottschalk, K. E., Janovjak, H., Muller, D. J. & Gaub, H. E. (2006). Bacteriorhodopsin folds into the membrane against an external force. *J Mol Biol* **357**, 644-654.
409. Garcia-Manyes, S., Brujic, J., Badilla, C. L. & Fernandez, J. M. (2007). Force-clamp spectroscopy of single protein monomers reveal the individual unfolding and folding pathways of I27 and ubiquitin. *Biophys J* **93**, 2436-2446.
410. Bullard, B., Garcia, T., Benes, V., Leake, M. C., Linke, W. A. & Oberhauser, A. F. (2006). The molecular elasticity of the insect flight muscle proteins projectin and kettin. *Proc Natl Acad Sci USA*.
411. Ainaravapu, S. R. K., Brujic, J., Huang, H. H., Wiita, A. P., Lu, H., Li, L., Walther, K. A., Carrion-Vazquez, M., Li, H. & Fernandez, J. M. (2006). Contour length and refolding rate of a small protein controlled by engineered disulfide bonds. *Biophys J* **92**, 225-233.
412. Wiita, A. P., Ainaravapu, S. R. K., Huang, H. H. & Fernandez, J. M. (2006). Force-dependent chemical kinetics of disulfide bond reduction observed with single-molecule techniques. *Proc Natl Acad Sci USA*, 0511035103.
413. Kawakami, M., Byrne, K., Brockwell, D., Radford, S. & Smith, A. (2006). Viscoelastic study of the mechanical unfolding of a protein by AFM. *Biophys J* **91**, L16-L18.
414. Kawakami, M., Byrne, K., Khatri, B. S., Mcleish, T. C. B. & Smith, D. A. (2006). Viscoelastic properties of single poly(ethylene glycol) molecules. *ChemPhysChem* **7**, 1710-1716.
415. Janovjak, H., Muller, D. J. & Humphris, A. D. L. (2005). Molecular force modulation spectroscopy revealing the dynamic response of single bacteriorhodopsins. *Biophys J* **88**, 1423-1431.
416. Humphris, A. D. L., Antognozzi, M., McMaster, T. J. & Miles, M. J. (2002). Transverse dynamic force spectroscopy: A novel approach to determining the complex stiffness of a single molecule. *Langmuir* **18**, 1729-1733.
417. Bustamante, C., Chemla, Y. R., Forde, N. R. & Izhaky, D. (2004). Mechanical processes in biochemistry. *Annu Rev Biochem* **73**, 705-748.
418. Liu, Y. Z., Leuba, S. H. & Lindsay, S. M. (1999). Relationship between stiffness and force in single molecule pulling experiments. *Langmuir* **15**, 8547-8548.
419. Chtcheglova, L. A., Shubeita, G. T., Sekatskii, S. K. & Dietler, G. (2004). Force spectroscopy with a small dithering of AFM tip: A method of direct and continuous measurement of the spring constant of single molecules and molecular complexes. *Biophys J* **86**, 1177-1184.
420. Forbes, J. G. & Wang, K. (2004). Simultaneous dynamic stiffness and extension profiles of single titin molecules: Nanomechanical evidence for unfolding intermediates. *J Vac Sci Technol, A* **22**, 1439-1443.
421. Kienberger, F., Pastushenko, V. P., Kada, G., Gruber, H. J., Riener, C., Schindler, H. & Hinterdorfer, P. (2000). Static and dynamical properties of single poly(ethylene glycol) molecules investigated by force spectroscopy. *Single Molecule* **1**, 123-128.
422. Toda, A., Kitazawa, M. & Yagi, A. (2004). Silicon tip cantilevers for force microscopy in water with resonance of 20 kHz or above. *Jap J Appl Phys* **43**, 4671-4675.
423. Sarid, D. (1994). *Scanning force microscopy*, Oxford University Press, New York, NY, USA.
424. Roters, A. & Johannsmann, D. (1996). Distance-dependent noise measurements in scanning force microscopy. *J Phys: Condens Matter* **8**, 7561-7577.
425. Pethica, J. B. & Oliver, W. C. (1987). Tip surface interactions in STM and AFM. *Phys Scr* **T19A**, 61-66.
426. Stark, R. W., Schitter, G., Guckenberger, R. & Stemmer, A. (2004). State-space model of freely vibrating and surface-coupled cantilever dynamics in atomic force microscopy. *Phys Rev B: Condens Matter Mater Phys* **69**, 085412.

427. Khatri, B. S., Kawakami, M., Byrne, K., Smith, A. & Mcleish, T. C. B. (2007). Entropy and barrier-controlled fluctuations determine conformational viscoelasticity of single biomolecules. *Biophys J* **92**, 1825-1835.
428. Zhuang, X. & Rief, M. (2003). Single-molecule folding. *Curr Opin Struct Biol* **13**, 88-97.
429. Radford, S. E. (2000). Protein folding: Progress made and promises ahead. *Trends Biochem Sci* **25**, 611-618.
430. Brujic, J., Hermans Z., R. I., Walther, K. A. & Fernandez, J. M. (2006). Single-molecule force spectroscopy reveals signatures of glassy dynamics in the energy landscape of ubiquitin. *Nat Phys* **2**, 282-286.
431. Hegner, M., Wagner, P. & Semenza, G. (1993). Ultralarge atomically flat template-stripped Au surfaces for scanning probe microscopy. *Surf Sci* **291**, 39-46.
432. Wagner, P., Hegner, M., Güntherodt, H.-J. & Semenza, G. (1995). Formation and in situ modification of monolayers chemisorbed on ultraflat template-stripped gold surfaces. *Langmuir* **11**, 3867-3876.
433. Brockwell, D. J., Beddard, G. S., Clarkson, J., Zinober, R. C., Blake, A. W., Trinick, J., Olmsted, P. D., Smith, D. A. & Radford, S. E. (2002). The effect of core destabilization on the mechanical resistance of I27. *Biophys J* **83**, 458-472.
434. Oesterhelt, D. (1998). The structure and mechanism of the family of retinal proteins from halophilic archaea. *Curr Opin Struct Biol* **8**, 489-500.
435. Williams, K. A., Geldmacher-Kaufer, U., Padan, E., Schuldiner, S. & Kühlbrandt, W. (1999). Projection structure of NhaA, a secondary transporter from *Escherichia coli*, at 4.0 Å resolution. *EMBO J* **18**, 3558-3563.
436. Florin, E.-L., Rief, M., Lehmann, H., Ludwig, M., Dornmair, C., Moy, V. T. & Gaub, H. E. (1995). Sensing specific molecular interactions with the atomic force microscope. *Biosens Bioelectron* **10**, 895-901.
437. Kedrov, A., Janovjak, H., Sapra, K. T. & Muller, D. J. (2007). Deciphering molecular interactions of native membrane proteins by single-molecule force spectroscopy. *Annu Rev Biophys Biomol Struct* **36**, 233-260.
438. Muller, D. J. & Engel, A. (2007). Atomic force microscopy and spectroscopy of native membrane proteins. *Nat Protoc* **2**, 2191-2197.
439. Muller, D. J. (2008). AFM: A nanotool in membrane biology. *Biochemistry* **47**, 7986-7998.
440. Beyder, A. & Sachs, F. (2006). Microfabricated torsion levers optimized for low force and high-frequency operation in fluids. *Ultramicroscopy* **106**, 838-846.
441. Hunte, C., Screpanti, E., Venturi, M., Rimon, A., Padan, E. & Michel, H. (2005). Structure of a Na⁺/H⁺ antiporter and insights into mechanism of action and regulation by pH. *Nature* **435**, 1197-1202.
442. Gasol, E., Jimenez-Vidal, M., Chillaron, J., Zorzano, A. & Palacin, M. (2004). Membrane topology of system x_c light subunit reveals a re-entrant loop with substrate-restricted accessibility. *J Biol Chem* **279**, 31228-31236.
443. Kall, L., Krogh, A. & Sonnhammer, E. L. (2007). Advantages of combined transmembrane topology and signal peptide prediction--the phobius web server. *Nucleic Acids Res* **35**, W429-432.
444. Sobczak, I. & Lolkema, J. S. (2004). Alternating access and a pore-loop structure in the Na⁺-citrate transporter CitS of *Klebsiella pneumoniae*. *J Biol Chem* **279**, 31113-31120.
445. Ward, A., Reyes, C. L., Yu, J., Roth, C. B. & Chang, G. (2007). Flexibility in the ABC transporter MsbA: Alternating access with a twist. *Proc Natl Acad Sci USA* **104**, 19005-19010.
446. Weyand, S., Shimamura, T., Yajima, S., Suzuki, S. I., Mirza, O., Krusong, K., Carpenter, E. P., Rutherford, N. G., Hadden, J. M., O'reilly, J., Ma, P., Saidijam, M., Patching, S. G., Hope, R. J., Norbertczak, H. T., Roach, P. C. J., Iwata, S., Henderson, P. J. F. & Cameron, A. D. (2008). Structure and molecular mechanism of a nucleobase-cation-symport-1 family transporter. *Science* **322**, 709-713.

447. Law, C. J., Maloney, P. C. & Wang, D.-N. (2008). Ins and outs of major facilitator superfamily antiporters. *Annu Rev Microbiol* **62**, 289-305.
448. Arkin, I. T., Xu, H., Jensen, M. O., Arbely, E., Bennett, E. R., Bowers, K. J., Chow, E., Dror, R. O., Eastwood, M. P., Flitman-Tene, R., Gregersen, B. A., Klepeis, J. L., Kolossvary, I., Shan, Y. & Shaw, D. E. (2007). Mechanism of Na⁺/H⁺ antiporting. *Science* **317**, 799-803.
449. Hollenstein, K., Dawson, R. J. P. & Locher, K. P. (2007). Structure and mechanism of ABC transporter proteins. *Curr Opin Struct Biol* **17**, 412-418.
450. Hu, Y., Fan, C.-P., Fu, G., Zhu, D., Jin, Q. & Wang, D.-C. (2008). Crystal structure of a glutamate/aspartate binding protein complexed with a glutamate molecule: Structural basis of ligand specificity at atomic resolution. *J Mol Biol* **382**, 99-111.
451. Uchino, H., Kanai, Y., Kim, D. K., Wempe, M. F., Chairoungdua, A., Morimoto, E., Anders, M. W. & Endou, H. (2002). Transport of amino acid-related compounds mediated by L-type amino acid transporter 1 (LAT1): Insights into the mechanisms of substrate recognition. *Mol Pharmacol* **61**, 729-737.
452. Fotiadis, D., Scheuring, S., Müller, S. A., Engel, A. & Muller, D. J. (2002). Imaging and manipulation of biological structures with the AFM. *Micron* **33**, 385-397.
453. Kessler, M. & Gaub, H. E. (2006). Unfolding barriers in bacteriorhodopsin probed from the cytoplasmic and the extracellular side by AFM. *Structure* **14**, 521-527.
454. Janovjak, H., Struckmeier, J. & Muller, D. J. (2005). Hydrodynamic effects in fast AFM single-molecule force measurements. *Eur Biophys J* **34**, 91-96.
455. Schlierf, M. & Rief, M. (2005). Temperature softening of a protein in single-molecule experiments. *J Mol Biol* **354**, 497-503.
456. Krieger, F., Fierz, B., Bieri, O., Drewello, M. & Kiefhaber, T. (2003). Dynamics of unfolded polypeptide chains as model for the earliest steps in protein folding. *J Mol Biol* **332**, 265-274.
457. Gräter, F. & Grubmüller, H. (2007). Fluctuations of primary ubiquitin folding intermediates in a force clamp. *J Struct Biol* **157**, 557-569.
458. Dietz, H., Berkemeier, F., Bertz, M. & Rief, M. (2006). Anisotropic deformation response of single protein molecules. *Proc Natl Acad Sci USA* **103**, 12724-12728.
459. Li, L., Huang, H. H.-L., Badilla, C. L. & Fernandez, J. M. (2005). Mechanical unfolding intermediates observed by single-molecule force spectroscopy in a fibronectin type III module. *J Mol Biol* **345**, 817-826.
460. Peng, Q. & Li, H. (2008). Atomic force microscopy reveals parallel mechanical unfolding pathways of T4 lysozyme: Evidence for a kinetic partitioning mechanism. *Proc Natl Acad Sci USA* **105**, 1885-1890.
461. Bosshart, P. D., Casagrande, F., Frederix, P. L. T. M., Ratera, M., Bippes, C. A., Muller, D. J., Palacin, M., Engel, A. & Fotiadis, D. (2008). High-throughput single-molecule force spectroscopy for membrane proteins. *Nanotechnology*, 384014.
462. McGuffin, L. J., Bryson, K. & Jones, D. T. (2000). The PSIPRED protein structure prediction server. *Bioinformatics* **16**, 404-405.
463. Carrion-Vazquez, M., Oberhauser, A. F., Fowler, S. B., Marszalek, P. E., Broedel, S. E., Clarke, J. & Fernandez, J. M. (1999). Mechanical and chemical unfolding of a single protein: A comparison. *Proc Natl Acad Sci USA* **96**, 3694-3699.
464. Hammond, G. S. (1955). A correlation of reaction rates. *J Am Chem Soc* **77**, 334-338.
465. Matouschek, A. & Fersht, A. R. (1993). Application of physical organic chemistry to engineered mutants of proteins: Hammond postulate behavior in the transition state of protein folding. *Proc Natl Acad Sci USA* **90**, 7814-7818.
466. Sánchez, I. E. & Kiefhaber, T. (2003). Hammond behavior versus ground state effects in protein folding: Evidence for narrow free energy barriers and residual structure in unfolded states. *J Mol Biol* **327**, 867-884.
467. Sánchez, I. E. & Kiefhaber, T. (2003). Non-linear rate-equilibrium free energy relationships and hammond behavior in protein folding. *Biophys. Chem.* **100**, 397-407.

468. Sapra, K. T., Park, P. S. H., Palczewski, K. & Muller, D. J. (2008). Mechanical properties of bovine rhodopsin and bacteriorhodopsin: Possible roles in folding and function. *Langmuir* **24**, 1330-1337.
469. Inoue, H., Noumi, T., Tsuchiya, T. & Kanazawa, H. (1995). Essential aspartic acid residues, Asp-133, Asp-163 and Asp-164, in the transmembrane helices of a Na⁺/H⁺ antiporter (NhaA) from *Escherichia coli*. *FEBS Lett* **363**, 264-268.
470. Soksawatmaekhin, W., Uemura, T., Fukiwake, N., Kashiwagi, K. & Igarashi, K. (2006). Identification of the cadaverine recognition site on the cadaverine-lysine antiporter CadB. *J Biol Chem* **281**, 29213-29220.
471. Lolkema, J. S. & Slotboom, D. J. (2008). The major amino acid transporter superfamily has a similar core structure as Na⁺-galactose and Na⁺-leucine transporters. *Mol Membr Biol* **25**, 567-570.
472. Evans, E. & Ludwig, F. (2000). Dynamic strengths of molecular anchoring and material cohesion in fluid biomembranes. *J Phys: Condens Matter* **12**, A315-A320.
473. Allende, D., Simon, S. A. & Mcintosh, T. J. (2005). Melittin-induced bilayer leakage depends on lipid material properties: Evidence for toroidal pores. *Biophys J* **88**, 1828-1837.
474. Aranda-Espinoza, H., Bermudez, H., Bates, F. S. & Discher, D. E. (2001). Electromechanical limits of polymersomes. *Phys Rev Lett* **87**, 208301.
475. Rawicz, W., Olbrich, K. C., Mcintosh, T., Needham, D. & Evans, E. (2000). Effect of chain length and unsaturation on elasticity of lipid bilayers. *Biophys J* **79**, 328-339.
476. Gruszecki, W. I. & Sielewiesiuk, J. (1990). Orientation of xanthophylls in phosphatidylcholine multibilayers. *Biochim Biophys Acta, Biomembr* **1023**, 405-412.
477. Casagrande, F., Ratera, M., Schenk, A. D., Chami, M., Valencia, E., Lopez, J. M., Torrents, D., Engel, A., Palacin, M. & Fotiadis, D. (2008). Projection structure of a member of the amino acid/polyamine/organocation transporter superfamily. *J Biol Chem* **283**, 33240-33248.
478. Kumar, S., Ma, B., Tsai, C. J., Sinha, N. & Nussinov, R. (2000). Folding and binding cascades: Dynamic landscapes and population shifts. *Protein Sci* **9**, 10-19.
479. Oliveberg, M. & Wolynes, P. G. (2005). The experimental survey of protein-folding energy landscapes. *Q Rev Biophys* **38**, 245-288.
480. West, I. C. (1997). Ligand conduction and the gated-pore mechanism of transmembrane transport. *Biochim Biophys Acta, Rev Biomembr* **1331**, 213-234.
481. Tsai, C. J., Kumar, S., Ma, B. & Nussinov, R. (1999). Folding funnels, binding funnels, and protein function. *Protein Sci* **8**, 1181-1190.
482. Okazaki, K.-I. & Takada, S. (2008). Dynamic energy landscape view of coupled binding and protein conformational change: Induced-fit versus population-shift mechanisms. *Proc Natl Acad Sci USA* **105**, 11182-11187.
483. Prajapati, R. S., Indu, S. & Varadarajan, R. (2007). Identification and thermodynamic characterization of molten globule states of periplasmic binding proteins. *Biochemistry* **46**, 10339-10352.
484. Harris, A. L. (2001). Emerging issues of connexin channels: Biophysics fills the gap. *Q Rev Biophys* **34**, 325-472.
485. Unwin, P. N. T. & Ennis, P. D. (1984). Two configurations of a channel-forming membrane protein. *Nature* **307**, 609-613.
486. Delmar, M., Stergiopoulos, K., Homma, N., Calero, G., Morley, G., Ek-Vitorin, J. F. & Taffet, S. M. (2000). A molecular model for the chemical regulation of connexin43 channels: The "Ball and chain" Hypothesis. In *Gap junctions. Molecular basis of cell communication in health and disease* (Peracchia, C., ed.), Vol. 49, pp. 223-248. Academic Press, San Diego.
487. Ek-Vitorin, J., Calero, G., Morley, G., Coombs, W., Taffet, S. & Delmar, M. (1996). pH regulation of connexin43: Molecular analysis of the gating particle. *Biophys J* **71**, 1273-1284.

488. Oshima, A., Tani, K., Hiroaki, Y., Fujiyoshi, Y. & Sosinsky, G. E. (2007). Three-dimensional structure of a human connexin26 gap junction channel reveals a plug in the vestibule. *Proc Natl Acad Sci USA*, 0703704104.
489. Trexler, E. B., Bennett, M. V. L., Bargiello, T. A. & Verselis, V. K. (1996). Voltage gating and permeation in a gap junction hemichannel. *Proc Natl Acad Sci USA* **93**, 5836-5841.
490. Spray, D. C. & Burt, J. M. (1990). Structure-activity relations of the cardiac gap junction channel. *Am J Physiol Cell Physiol* **258**, C195-205.
491. Reber, W. R. & Weingart, R. (1982). Ungulate cardiac purkinje fibres: The influence of intracellular pH on the electrical cell-to-cell coupling. *J Physiol (Camb)* **328**, 87-104.
492. Burt, J. M. (1987). Block of intercellular communication: Interaction of intracellular H⁺ and Ca²⁺. *Am J Physiol Cell Physiol* **253**, C607-612.
493. Spray, D. C., Harris, A. L. & Bennett, M. V. L. (1981). Gap junctional conductance is a simple and sensitive function of intracellular pH. *Science* **211**, 712-715.
494. Stergiopoulos, K., Alvarado, J. L., Mastroianni, M., Ek-Vitorin, J. F., Taffet, S. M. & Delmar, M. (1999). Hetero-domain interactions as a mechanism for the regulation of connexin channels. *Circ. Res.* **84**, 1144-1155.
495. Francis, D., Stergiopoulos, K., Ek-Vitorin, J. F., Cao, F. L., Taffet, S. M. & Delmar, M. (1999). Connexin diversity and gap junction regulation by pH. *Dev Genet* **24**, 123-136.
496. Bevans, C. G. & Harris, A. L. (1999). Regulation of connexin channels by pH. Direct action of the protonated form of taurine and other aminosulfonates. *J Biol Chem* **274**, 3711-3719.
497. Huxtable, R. J. (1992). Physiological actions of taurine. *Physiol Rev* **72**, 101-163.
498. Wright, C. E., Tallan, H. H. & Lin, Y. Y. (1986). Taurine: Biological update. *Annu Rev Biochem* **55**, 427-453.
499. Tao, L. & Harris, A. L. (2004). Biochemical requirements for inhibition of connexin26-containing channels by natural and synthetic taurine analogs. *J Biol Chem* **279**, 38544-38554.
500. Trexler, B. E., Bukauskas, F. F., Bennett, M. V. L., Bargiello, T. A. & Verselis, V. K. (1999). Rapid and direct effects of pH on connexins revealed by the connexin46 hemichannel preparation. *J Gen Physiol* **113**, 721-742.
501. Hoh, J. H., Sosinsky, G. E., Revel, J. P. & Hansma, P. K. (1993). Structure of the extracellular surface of the gap junction by atomic force microscopy. *Biophys J* **65**, 149-163.
502. Liu, F., Arce, F. T., Ramachandran, S. & Lal, R. (2006). Nanomechanics of hemichannel conformations: Connexin flexibility underlying channel opening and closing. *J Biol Chem*, M605048200.
503. Hand, G. M., Muller, D. J., Nicholson, B. J., Engel, A. & Sosinsky, G. E. (2002). Isolation and characterization of gap junctions from tissue culture cells. *J Mol Biol* **315**, 587-600.
504. Putman, C. A. J., Van Der Werft, K., De Grooth, B. G., Van Hulst, N. F., Greve, J. & Hansma, P. K. (1992). A new imaging mode in the atomic force microscopy based on the error signal. *SPIE* **1639**, 198-204.
505. Saxton, W. O., Pitt, T. J. & Horner, M. (1979). Digital image processing: The semper system. *Ultramicroscopy* **4**, 343-354.
506. Saxton, W. O. & Baumeister, W. (1982). The correlation averaging of a regularly arranged bacterial cell envelope protein. *J Microsc (Oxf)* **127**, 127-138.
507. Saxton, W. O., Baumeister, W. & Hahn, M. (1984). Three-dimensional reconstruction of imperfect two-dimensional crystals. *Ultramicroscopy* **13**, 57-70.
508. Frank, J., Breaudiere, J. P., Carazo, J. M., Verschoor, A. & Wagenknecht, T. (1988). Classification of images of biomolecular assemblies: A study of ribosomes and ribosomal subunits of *Escherichia coli*. *J Microsc (Oxf)* **150 (Pt 2)**, 99-115.
509. Hoh, J. H., Lal, R., John, S. A., Revel, J.-P. & Arnsdorf, M. F. (1991). Atomic force microscopy and dissection of gap junctions. *Science* **235**, 1405-1408.

510. Baker, T. S., Caspar, D. L. D., Hollingshead, C. J. & Goodenough, D. A. (1983). Gap junction structures. Iv. Asymmetric features revealed by low-irradiation microscopy. *J Cell Biol* **96**, 204-216.
511. Perkins, G., Goodenough, D. & Sosinsky, G. (1997). Three-dimensional structure of the gap junction connexon. *Biophys J* **72**, 533-544.
512. Harris, A. L., Walter, A., Paul, D., Goodenough, D. A. & Zimmerberg, J. (1992). Ion channels in single bilayers induced by rat connexin32. *Mol Brain Res* **15**, 269-280.
513. Morley, G. E., Taffet, S. M. & Delmar, M. (1996). Intramolecular interactions mediate pH regulation of connexin43 channels. *Biophys J* **70**, 1294-1302.
514. Thimm, J., Mechler, A., Lin, H., Rhee, S. & Lal, R. (2005). Calcium-dependent open/closed conformations and interfacial energy maps of reconstituted hemichannels. *J Biol Chem* **280**, 10646-10654.
515. Tao, L. & Harris, A. L. (2005). *49th Annual Meeting of the Biophysical-Society, Long Beach, CA.*
516. Peracchia, C. (2004). Chemical gating of gap junction channels: Roles of calcium, pH and calmodulin. *Biochim Biophys Acta, Biomembr* **1662**, 61-80.
517. Peracchia, C., Young, K. C., Wang, X. G., Chen, J. T. & Peracchia, L. L. (2003). The voltage gates of connexin channels are sensitive to CO₂. *Cell Communication & Adhesion* **10**, 233-237.
518. Saez, J. C., Retamal, M. A., Basilio, D., Bukauskas, F. F. & Bennett, M. V. L. (2005). Connexin-based gap junction hemichannels: Gating mechanisms. *Biochim Biophys Acta, Biomembr* **1711**, 215-224.
519. Lal, R., John, S. A., Laird, D. W. & Arnsdorf, M. F. (1995). Heart gap junction preparations reveal hemiplaques by atomic force microscopy. *Am J Physiol Cell Physiol* **268**, C968-977.
520. Zampighi, G. A., Loo, D. D. F., Kreman, M., Eskandari, S. & Wright, E. M. (1999). Functional and morphological correlates of connexin50 expressed in *Xenopus laevis* oocytes. *J Gen Physiol* **113**, 507-524.
521. Van Nhieu, G. T., Clair, C., Bruzzone, R., Mesnil, M., Sansonetti, P. & Combettes, L. (2003). Connexin-dependent inter-cellular communication increases invasion and dissemination of *Shigella* in epithelial cells. *Nat Cell Biol* **5**, 720-726.
522. Kamermans, M., Fahrenfort, I., Schultz, K., Janssen-Bienhold, U., Sjoerdsma, T. & Weiler, R. (2001). Hemichannel-mediated inhibition in the outer retina. *Science* **292**, 1178-1180.
523. Pottek, M., Hoppenstedt, W., Janssen-Bienhold, U., Schultz, K., Perlman, I. & Weiler, R. (2003). Contribution of connexin26 to electrical feedback inhibition in the turtle retina. *J Comp Neurol* **466**, 468-477.
524. El-Fouly, M. H., Trosko, J. E. & Chang, C. C. (1987). Scrape-loading and dye transfer. A rapid and simple technique to study gap junctional intercellular communication. *Exp Cell Res* **168**, 422-430.
525. Unwin, P. N. T. & Zampighi, G. (1980). Structure of the junction between communicating cells. *Nature* **283**, 545-549.
526. Pfahnl, A. & Dahl, G. (1998). Localization of a voltage gate in connexin46 gap junction hemichannels. *Biophys J* **75**, 2323-2331.
527. Foote, C. I., Zhou, L., Zhu, X. & Nicholson, B. J. (1998). The pattern of disulfide linkages in the extracellular loop regions of connexin 32 suggests a model for the docking interface of gap junctions. *J Cell Biol* **140**, 1187-1197.
528. Owens, L. M., Fralix, T. A., Murphy, E., Cascio, W. E. & Gettes, L. S. (1996). Correlation of ischemia-induced extracellular and intracellular ion changes to cell-to-cell electrical uncoupling in isolated blood-perfused rabbit hearts. *Circulation* **94**, 10-13.
529. Yokota, H., Yamamoto, Y., Naoe, Y., Fuse, A., Sato, H., Unemoto, K. & Kurokawa, A. (2000). Measurements of cortical cellular pH by intracranial tonometer in severe head injury. *Critical Care Medicine* **28**, 3275-3280.

530. Kleber, A. G., Riegger, C. B. & Janse, M. J. (1987). Electrical uncoupling and increase of extracellular resistance after induction of ischemia in isolated, arterially perfused rabbit papillary muscle. *Circ. Res.* **61**, 271-279.
531. Beardslee, M. A., Lerner, D. L., Tadros, P. N., Laing, J. G., Beyer, E. C., Yamada, K. A., Kleber, A. G., Schuessler, R. B. & Saffitz, J. E. (2000). Dephosphorylation and intracellular redistribution of ventricular connexin43 during electrical uncoupling induced by ischemia. *Circ. Res.* **87**, 656-662.
532. Nattel, S. (2004). The clinical relevance of connexin gating: How to control communication in the heart. *Heart Rhythm* **1**, 234.
533. Saltman, A. E., Aksehirli, T. O., Valiunas, V., Gaudette, G. R., Matsuyama, N., Brink, P. & Krukenkamp, I. B. (2002). Gap junction uncoupling protects the heart against ischemia. *J Thorac Cardiovasc Surg* **124**, 371-376.
534. Petit, C., Levilliers, J. & Hardelin, J. P. (2001). Molecular genetics of hearing loss. *Annu Rev Genet* **35**, 589-646.
535. Chang, E. H., Van Camp, G. & Smith, R. J. (2003). The role of connexins in human disease. *Ear Hear* **24**, 314-323.
536. Kamasawa, N., Sik, A., Morita, M., Yasumura, T., Davidson, K. G., Nagy, J. I. & Rash, J. E. (2005). Connexin-47 and connexin-32 in gap junctions of oligodendrocyte somata, myelin sheaths, paranodal loops and Schmidt-Lanterman incisures: Implications for ionic homeostasis and potassium siphoning. *Neuroscience* **136**, 65-86.
537. Paul, D. L. (1995). New functions for gap junctions. *Curr Opin Cell Biol* **7**, 665-672.
538. Beltramello, M., Piazza, V., Bukauskas, F. F., Pozzan, T. & Mammano, F. (2005). Impaired permeability to Ins(1,4,5)P3 in a mutant connexin underlies recessive hereditary deafness. *Nat Cell Biol* **7**, 63-69.
539. Ikeda, K. & Morizono, T. (1989). Effects of carbon dioxide in the middle ear cavity upon the cochlear potentials and cochlear pH. *Acta Otolaryngol* **108**, 88-93.
540. Paparella, M. M., Morizono, T., Le, C. T., Mancini, F., Sipila, P., Choo, Y. B., Liden, G. & Kim, C. S. (1984). Sensorineural hearing loss in otitis media. *Ann Otol Rhinol Laryngol* **93**, 623-629.
541. Tappaz, M. L. (2004). Taurine biosynthetic enzymes and taurine transporter: Molecular identification and regulations. *Neurochem Res* **29**, 83-96.
542. Nagy, J. I., Li, X., Rempel, J., Stelmack, G., Patel, D., Staines, W. A., Yasumura, T. & Rash, J. E. (2001). Connexin26 in adult rodent central nervous system: Demonstration at astrocytic gap junctions and colocalization with connexin30 and connexin43. *The Journal of Comparative Neurology* **441**, 302-323.
543. Jacobsen, J. G. & Smith, L. H. (1968). Biochemistry and physiology of taurine and taurine derivatives. *Physiol Rev* **48**, 424-511.
544. Pasantés-Morales, H., Wright, C. E. & Gaull, G. E. (1985). Taurine protection of lymphoblastoid cells from iron-ascorbate induced damage. *Biochem. Pharmacol.* **34**, 2205-2207.
545. Lozano, J. R. & Garcia, R. (2008). Theory of multifrequency atomic force microscopy. *Phys Rev Lett* **100**, 076102-076104.
546. Patil, S., Martinez, N. F., Lozano, J. R. & Garcia, R. (2007). Force microscopy imaging of individual protein molecules with sub-pico newton force sensitivity. *J Mol Recognit* **20**, 516-523.
547. Ando, T., Kodera, N., Naito, Y., Kinoshita, T., Furuta, K. Y. & Toyoshima, Y. Y. (2003). A high-speed atomic force microscope for studying biological macromolecules in action. *ChemPhysChem* **4**, 1196-1202.
548. Ando, T., Kodera, N., Takai, E., Maruyama, D., Saito, K. & Toda, A. (2001). A high-speed atomic force microscope for studying biological macromolecules. *Proc Natl Acad Sci USA* **98**, 12468-12472.

549. Ando, T., Uchihashi, T., Kodera, N., Yamamoto, D., Miyagi, A., Taniguchi, M. & Yamashita, H. (2008). High-speed AFM and nano-visualization of biomolecular processes. *Pflüg Arch Eur J Physiol* **456**, 211-225.
550. Ando, T., Uchihashi, T., Kodera, N., Yamamoto, D., Taniguchi, M., Miyagi, A. & Yamashita, H. (2007). High-speed atomic force microscopy for observing dynamic biomolecular processes. *J Mol Recognit* **20**, 448-458.
551. Humphris, A. D. L., Miles, M. J. & Hobbs, J. K. (2005). A mechanical microscope: High-speed atomic force microscopy. *Appl. Phys. Lett.* **86**, 034106-034103.
552. Fantner, G. E., Schitter, G., Kindt, J. H., Ivanov, T., Ivanova, K., Patel, R., Holten-Andersen, N., Adams, J., Thurner, P. J., Rangelow, I. W. & Hansma, P. K. (2006). Components for high speed atomic force microscopy. *Ultramicroscopy* **106**, 881-887.
553. Schitter, G., Astrom, K. J., Demartini, B. E., Thurner, P. J., Turner, K. L. & Hansma, P. K. (2007). Design and modeling of a high-speed AFM-scanner. *IEEE Trans Contr Sys* **15**, 906-915.
554. Lee, G. U., Kidwell, D. A. & Colton, R. J. (1994). Sensing discrete streptavidin biotin interactions with atomic-force microscopy. *Langmuir* **10**, 354-357.
555. Guo, S., Lad, N., Ray, C. & Akhremitchev, B. B. (2009). Association kinetics from single molecule force spectroscopy measurements. *Biophys J* **96**, 3412-3422.

Erklärung

Hiermit versichere ich, dass ich die vorliegende Arbeit ohne unzulässige Hilfe Dritter und ohne Benutzung anderer als der angegebenen Hilfsmittel angefertigt habe; die aus fremden Quellen direkt oder indirekt übernommenen Gedanken sind als solche kenntlich gemacht. Die Arbeit wurde bisher weder im Inland noch im Ausland in gleicher oder ähnlicher Form einer anderen Prüfungsbehörde vorgelegt.

Diese Arbeit wurde in der Zeit von November 2004 bis November 2008 unter der wissenschaftlichen Betreuung von Herrn Prof. Dr. Daniel J. Müller am Biotechnologischen Zentrum der Technischen Universität Dresden angefertigt.

Dresden, den 18.05.2009